Continuum results for light hadrons from 2+1 flavour Domain Wall QCD

Christopher Kelly

A thesis submitted in fulfilment of the requirements
for the degree of Doctor of Philosophy
to the
University of Edinburgh
2010

Abstract

This thesis presents a first study of the continuum limit of light hadronic physics using a lattice gauge theory simulation with good chiral symmetry. The results are interpreted and extrapolated using both the chiral effective theory and analytic models. Matrix elements of operators of the effective weak Hamiltonian are calculated.

The thesis details a combined chiral and continuum extrapolation of two ensemble sets of 2+1 flavour Domain Wall QCD data with inverse lattice spacings around 1.73 and 2.32 GeV. A novel procedure of matching lattice data at unphysical quark masses is used to define the scaling trajectory to the continuum limit.

Quantities studied include the pion and kaon masses and decay constants, the average up/down quark mass, the strange quark mass, and the neutral kaon mixing parameter B_K. The latter is an important theoretical input to the ϵ_K band in the unitarity triangle of the CKM matrix. A subset of recent results of ref. [1] in the chiral effective theory needed to perform our fits are re-derived.

New methods for the improved determination of the B_K matrix element (and other correlation functions), and also for the renormalisation of the relevant four-quark operator for B_K are presented.

Declaration

This thesis was composed by myself and presents work that I performed as a member of the RBC&UKQCD collaborations. This work has not been submitted for any other award or professional qualification.

The analyses documented within this work were performed on a set of Domain Wall fermion ensembles generated by RBC&UKQCD. I was one of several people who generated the correlation functions on the $32^3 \times 64$ ensembles. My earlier work resulted in a change of the method used for these measurements to the single wall source approach. I was responsible for the measurement of light hadronic matrix elements on the $m_l = 0.006$ ensemble, which represents the UKQCD collaboration's contribution to the data on the $32^3 \times 64$ ensemble set. In addition I wrote the parallel and offline contraction code for the non-perturbative renormalisation of four-quark $\Delta S = 2$ operators with volume sources and non-exceptional kinematics. I generated all of the amputated vertex functions currently used for the non-perturbative renormalisation of both the four-quark operators and the bilinear operators on the $32^3 \times 64$ and $24^3 \times 64$ ensemble sets. All of my analysis code uses the UKHadron libraries, which were principally developed by Peter Boyle. I took a lead role in the maintenance and development of this code base, adding a suite of features including the jackknife and superjackboot resampling procedures; the code for handling the reweighting of the strange sea-quark mass; and the code for the optimised generation and storage of the Bessel functions used for the finite-volume chiral fit forms. Using these tools I developed the iterative algorithms that simultaneously take the chiral and continuum limit of the $32^3 \times 64$ and $24^3 \times 64$ ensemble sets. The $SU(2)$ chiral fit forms were based on the work of David Antonio, which I extended with the addition of finite volume corrections and $\mathcal{O}(a^2)$ scaling terms.

Some of the results presented here appear in:

- "***Use of stochastic sources for the lattice determination of light quark physics***" [2], JHEP 0808 (2008) 086 [arXiv:0804.1501 [hep-lat]].

  This paper documents my investigation of stochastic source techniques in

collaboration with Peter Boyle and Andreas Jüttner. I performed all of the generation and analysis of the data. The results of this work are reproduced in chapter 5.

- "***Continuum Limit Physics from 2+1 Flavor DomainWall QCD***" [3], (not yet published).

  Also conference proceedings:

  "***Continuum results for light hadrons from 2+1 flavor DWF ensembles***" [4], PoS LAT2009 (2009) 087 [arXiv:0911.1309].

  These papers document the combined analysis of the $32^3 \times 64$ and $24^3 \times 64$ ensemble sets. I performed one of two independent analyses of the $32^3 \times 64$ ensembles and of the (extended) $24^3 \times 64$ ensembles, measuring the residual mass, axial renormalisation coefficient, pseudoscalar masses and decay constants, and Omega baryon masses. I reproduced Min Li's earlier analysis of the Sommer scale r_0 on both ensemble sets and extended it to include the reweighting in the strange sea-quark mass. I developed the code and performed the lead analysis of the simultaneous chiral and continuum extrapolation of the above quantities. This analysis has been verified by Robert Mawhinney but without performing the full superjackknife procedure and the smooth interpolation of the reweighted data. In addition I generated the data for the non-perturbative renormalisation of the quark masses and performed an independent re-analysis of the renormalisation of the quark masses into $\overline{\mathrm{MS}}$, albeit using only the one-loop perturbation theory rather than the two-loop results that will be published in the paper. Analyses of these data were performed by several others, including Dirk Broemmel and Yasumichi Aoki. As yet I have performed the only analysis of the continuum limit of r_0 and r_1. These analyses are the topics of chapters 6, 7 and 8.

- "***Continuum Limit of B_K from 2+1 Flavor Domain Wall QCD***" [5], (not yet published).

  Also conference proceedings:

  "***Scaling of B_K for 2+1 flavour domain wall fermions from 24^3 and $32^3 \times 64$ lattices***" [6], PoS LATTICE 2008 (2008) 270

These papers detail the analysis of the continuum limit of B_K. I performed one of the two independent analyses of the B_K data on $32^3 \times 64$ and $24^3 \times 64$ ensemble sets. I wrote the code and generated the data for the non-perturbative renormalisation of this quantity and performed one of the several independent analyses of the results. However in this case all of the analyses made use of my amputation code. As yet I have performed the only analysis of the continuum limit.

I have also contributed to other published works that are not presented in this thesis:

- "***The pion's electromagnetic form factor at small momentum transfer in full lattice QCD***" [7], JHEP 0807 (2008) 112 [arXiv:0804.3971 [hep-lat]].
- "$K \to \pi$ ***form factors with reduced model dependence***" [8], [arXiv:1004.0886].

Christopher Kelly
July 2010

Acknowledgements

I would like to thank Peter Boyle for his guidance and supervision over the last four years and in particular for his comments and suggestions on this mighty tome. I am also very grateful to the STFC for funding my PhD.

I would also like to thank the members of the Edinburgh PPT group that have aided me over the course of my PhD, including Luigi Del Debbio, James Zanotti and Richard Kenway, and in particular Jan Wennekers, who sadly passed away in December 2009.

I also thank my colleagues in the RBC&UKQCD collaborations, particularly Chris Sachrajda, Dirk Broemmel, Andreas Jüttner, Norman Christ and Robert Mawhinney.

Lastly, I thank Amy for her love and support.

Contents

List of Figures

List of Tables

Chapter 1

The Standard Model

The Standard Model (SM) is a highly successful model that describes the behaviour of all known fundamental particles (plus the Higgs boson) under the strong, weak and electromagnetic forces. The model contains three generations (pairings) of leptons and fermions. In the quark sector these are, in order of increasing quark mass: up and down, strange and charm, bottom and top. In addition, the model contains the QCD and electro-weak gauge bosons associated with a local $SU(3)_c \times SU(2)_L \times U(1)_V$ symmetry, and the scalar Higgs boson that induces masses for the heavy gauge bosons and the fermion fields via spontaneous symmetry breaking. These are described below.

1.1 The QCD sector

QCD is the non-Abelian gauge theory that describes the strong interactions. It arises due to a local invariance (gauge symmetry) of the quark fields under the Lie gauge group $SU(3)_C$ acting upon the colour degree of freedom. The quark fields transform under the fundamental 3-representation and the conjugate 'barred' fields $\bar{q}$ transform under the $\bar{3}$-representation. The Lagrangian of the QCD sector is

$$\mathcal{L}_{\text{QCD}} = \sum_f \bar{q}_f (i \not{D} - m_f) q_f - \frac{1}{4} F^a_{\mu\nu} F^{a\,\mu\nu} \,, \tag{1.1}$$

where the sum is performed over quark flavours f. Here the quark mass term arising from the spontaneous symmetry breaking in the Higgs sector has been included. The covariant derivative,

$$D_\mu q = (\partial_\mu + i g A^a_\mu t^a) q \,, \tag{1.2}$$

contains interactions between the quarks and the *gluon* (gauge) fields A^a_μ. There are eight gluon fields $a = 1 \ldots 8$ corresponding to the eight generators $t^a = \frac{\lambda^a}{2}$ of the Lie algebra. Here λ_i are the Gell-Mann matrices and $F^a_{\mu\nu}$ is the *field strength tensor*, defined as

$$F^a_{\mu\nu} = \partial_\mu A^a_\nu - \partial_\nu A^a_\mu + g f^{abc} A^b_\mu A^c_\nu \,, \tag{1.3}$$

where g is the QCD coupling and f^{abc} are the structure constants of $SU(3)$: $[t^a, t^b] = if^{abc}t^c$.

As discussed in chapter 2, the QCD coupling g is large at the hadronic energy scale. The resulting non-linear behaviour is believed to give rise to the *confinement* of quarks into meson and baryon bound states. In this regime, the standard techniques of perturbation theory cannot be used and the theory must be computationally simulated using lattice techniques. Some insight can also be gained through the chiral effective theory (chapter 3.2) which describes QCD around the *chiral limit*, in which the Lagrangian is symmetric under the *chiral symmetry*.

1.1.1 Chiral symmetry

In the massless (*chiral*) limit of QCD with N quark flavours, the Lagrangian is symmetric under a global $SU(N)_L \times SU(N)_R \times U(1)_V$ *flavour* symmetry, known as the *chiral symmetry*, under which the left and right handed quark flavours transform independently under the $SU(N)$ Lie group in the fundamental representation. Here the $U(1)$ vector symmetry allows for the classification of hadronic bound states into mesons and baryons and gives rise to baryon number conservation. The classical theory has an additional $U(1)_A$ axial symmetry, but this is broken in the interacting theory by the *axial anomaly* which arises due to topological effects [9]. The conserved currents of the $SU(N)_L \times SU(N)_R$ symmetry are the $N^2 - 1$ vector and axial currents, defined as

$$V_\mu^a = \bar{q}\gamma_\mu t^a q \quad \text{and} \quad A_\mu^a = \bar{q}\gamma_\mu\gamma_5 t^a q \tag{1.4}$$

respectively. As a result of the symmetry, hadrons should be able to be grouped into degenerate representations of $SU(N)_L \times SU(N)_R$. Importantly this implies degenerate sets of particles with opposite parity. The parity symmetry is discussed in detail in section 1.2.2.

Experimentally, hadrons containing up, down, and strange quarks, demonstrate the ability to be grouped into approximately degenerate sets corresponding to representations of $SU(3)$. These are the familiar meson nonets (actually an octet and a singlet) and the baryon octet and decuplet. No parity partners are observed, thus the $SU(3)_L \times SU(3)_R$ symmetry is broken. The charge Q_V^a associated with the V_0^a component of vector current remains a conserved quantity [10] in the chiral limit, implying the continued invariance of the theory under the associated $SU(3)_V$ vector symmetry.

Hadrons containing just up and down quarks can also be grouped into near-degenerate representations of $SU(2)$, which is a subgroup of $SU(3)$. This is known as *isospin symmetry*. These groupings include the pion triplet (π^+, π^0, π^-) and the

nucleon doublet (p, n).

The approximate nature of the degeneracy under $SU(2)_V$ and $SU(3)_V$ is a result of the differences between the quark masses. For example, assuming degenerate up/down quark masses and discounting electromagnetic effects, the pion triplet is degenerate. This is shown explicitly using the chiral effective theory in section 3.2.3. Only when the quark mass degeneracy is lifted does the $SU(N)_V$ vector symmetry break. As a result of the symmetry breaking, the $SU(2)$ isospin symmetry is a better approximation than the $SU(3)$ symmetry, because the mass splitting between the up and down quarks is much smaller than between those and the strange quark.

1.1.2 Chiral symmetry breaking

In the massless theory, the breaking of the chiral symmetry can occur if the ground state of the system (the vacuum state) is not symmetric under the full symmetry group. This is known as *spontaneous* symmetry breaking (SSB). A sufficient but not necessary condition for this to occur is a non-zero vacuum expectation value of the singlet scalar quark condensate $\langle S_0 \rangle = \langle \bar{q}q \rangle = \langle \bar{u}u + \bar{d}d + \bar{s}s \rangle$. A non-zero quark condensate may arise due to the presence of exact zero eigen-modes of the Dirac operator $\not{D}\psi = 0$ [11], which occur due to the non-trivial topology of the non-Abelian gauge fields according to the Atiyah-Singer index theorem [12].

Goldstone's theorem [13][14][15] states that for every broken generator of the spontaneously broken theory there exists a massless *Goldstone Boson*. $SU(N)$ has N^2-1 generators, thus the symmetry breaking is expected to generate N^2-1 Goldstone bosons.

The addition of a mass term for the quarks generates an *explicit* breaking of the $SU(N)_L \times SU(N)_R$ symmetry. This gives rise to a mass term for the what are now *pseudo*-Goldstone bosons (PGBs), which is proportional to the coefficient of the symmetry breaking term at leading order (i.e. the quark mass). This will be demonstrated using the chiral effective theory in section 3.2.3. The NLO corrections to the Goldstone boson masses are also calculated in section 3.2.3.

For three flavour QCD, taking into account the continued conservation of the vector charge, the broken generators must be those corresponding to the axial charge Q_A^a. The symmetry behaviour of the resulting PGBs ϕ must reflect the properties of the generators, i.e. they must be odd under parity and obey the commutation relation

$$\left[Q_V^a, \phi^b(x)\right] = if^{abc}\phi^c(x)\,. \tag{1.5}$$

The PGBs are therefore pseudoscalar and transform as an octet ($3^2 - 1 = 8$) under the remaining $SU(3)_V$ symmetry. The pseudoscalar pion/kaon octet is an ideal candidate

for this, as the masses of the particles are small in comparison to the corresponding vector (spin 1, odd under parity) quantities.

With $\langle \bar{q}q \rangle \neq 0$, the commutation relation of the axial charge with the pseudoscalar fields,

$$\langle 0|i \left[Q_a^A(t), P_a(y) \right] |0\rangle = \frac{2}{3} \langle \bar{q}q \rangle \,, \tag{1.6}$$

is non-zero. Inserting a complete set of states between the axial charge and the pseudoscalar fields, it is clear that both terms must have a non-zero overlap with the vacuum state. In particular this means that

$$\langle 0|A_\mu^a(0)|\phi^b\rangle = ip_\mu f_{PS} \delta^{ab} \tag{1.7}$$

is non-zero. Here f_{PS} is the the pseudoscalar decay constant. In section 6.4, this quantity is obtained for pion and kaon states via lattice simulation.

1.2 The electro-weak and Higgs sectors

In the Glashow, Weinberg and Salam (GWS) model [16][17][18], the electro-weak interactions arise from the spontaneous breaking of an invariance of the free-quark Lagrangian under a local $SU(2)_L \times U(1)_Y$ symmetry.

The $SU(2)_L$ symmetry acts on pairs of left-handed quark and lepton fields,

$$\begin{pmatrix} \nu_e \\ e^- \end{pmatrix}_L \quad \begin{pmatrix} \nu_\mu \\ \mu^- \end{pmatrix}_L \quad \begin{pmatrix} \nu_\tau \\ \tau^- \end{pmatrix}_L \quad \begin{pmatrix} u \\ d' \end{pmatrix}_L \quad \begin{pmatrix} c \\ s' \end{pmatrix}_L \quad \begin{pmatrix} t \\ b' \end{pmatrix}_L \,, \tag{1.8}$$

where d',s' and b' are weak flavour-eigenstates. These are connected to the familiar mass eigenstates d, s and b through the CKM matrix, described below. $SU(2)$ has three generators (the Pauli matrices), hence there are three gauge bosons, labelled A_μ^a for $a = 1 \ldots 3$.

The $U(1)_Y$ gauge symmetry gives rise to a force similar to electromagnetism but with a conserved *hypercharge* Y in place of the electric charge. It has a single vector gauge boson B_μ.

According to the Higgs mechanism [19][20][21][22], an additional scalar field ϕ (the Higg's boson) with a non-zero vacuum expectation value $v = \langle \phi \rangle$ results in the vacuum state losing its invariance under the full $SU(2)_L \times U(1)_Y$ symmetry group. This causes the symmetry to spontaneously break to a simple $U(1)_Q$ symmetry group, corresponding to electromagnetism. Here Q stands for the electric charge. Under the spontaneous breaking, the gauge bosons A_μ^a and B_μ mix to form four vector bosons: the charged $W_\mu^\pm$, the uncharged Z_μ^0, and the photon A_μ fields. The Higgs mechanism generates mass terms for the quarks and the W and Z bosons that are proportional to

the vaccuum expectation value v of the Higgs field. These terms are invariant under the $SU(2)_L$ symmetry. The full set of interaction vertices between the quarks, photons, $W^{\pm}$ and Z bosons can be found in ref. [23]. Out of these, only the *charged current* interactions,

$$\mathcal{L}_{CC} = \frac{g_2}{2\sqrt{2}} \left(J_\mu^+ W^{+\mu} + J_\mu^- W^{-\mu} \right) \tag{1.9}$$

are relevant to this work. Here g_2 is the $SU(2)_L$ coupling and

$$J_\mu^+ = (\bar{u}d')_{V-A} + (\bar{c}s')_{V-A} + (\bar{t}b')_{V-A} + (\bar{\nu}_e e)_{V-A} + (\bar{\nu}_\mu \mu)_{V-A} + (\bar{\nu}_\tau \tau)_{V-A}\,, \tag{1.10}$$

is the charged current. The quantity $(\bar{u}d')_{V-A} = \bar{u}\frac{1}{2}\gamma_\mu(1-\gamma^5)d'$ is the vector (V) minus axial-vector (A) quark bilinear vertex. These interactions allow flavour changing within the quark generations.

1.2.1 The CKM matrix

The CKM matrix relates the weak flavour-eigenstates to the mass eigenstates:

$$\begin{pmatrix} d' \\ s' \\ b' \end{pmatrix} = \begin{pmatrix} V_{ud} & V_{us} & V_{ub} \\ V_{cd} & V_{cs} & V_{cb} \\ V_{td} & V_{ts} & V_{tb} \end{pmatrix} \begin{pmatrix} d \\ s \\ b \end{pmatrix} = \hat{V}_{\mathrm{CKM}} \begin{pmatrix} d \\ s \\ b \end{pmatrix}\,, \tag{1.11}$$

where V_{ij} are complex numbers. In the Standard Model, the CKM matrix is unitary and as such has only four free parameters. In the *standard parameterisation* these are the (real) angles θ_{12}, θ_{13}, θ_{23} and the phase $\delta : 0 \leq \delta \leq 2\pi$. The matrix can then be written as

$$\hat{V}_{\mathrm{CKM}} = \begin{pmatrix} c_{12}c_{13} & s_{12}c_{13} & s_{13}e^{-i\delta} \\ -s_{12}c_{23} - c_{12}s_{23}s_{13}e^{i\delta} & c_{12}c_{23} - s_{12}s_{23}s_{13}e^{i\delta} & s_{23}c_{13} \\ s_{12}s_{23} - c_{12}c_{23}s_{13}e^{i\delta} & -s_{23}c_{12} - s_{12}c_{23}s_{13}e^{i\delta} & c_{23}c_{13} \end{pmatrix}\,, \tag{1.12}$$

where $c_{ij} = \cos\theta_{ij}$ and $s_{ij} = \sin\theta_{ij}$.

An alternate form is provided by the *Wolfenstein parameterisation*, which defines four parameters (λ, A, ρ, η) that are related to those of the standard parameterisation as follows:

$$\lambda = s_{12}, \quad A = \frac{s_{23}}{s_{12}s_{12}}, \quad \rho = \frac{s_{13}}{s_{12}s_{13}}\cos\delta, \quad \eta = \frac{s_{13}}{s_{12}s_{13}}\sin\delta\,. \tag{1.13}$$

Unitarity of the CKM matrix implies

$$V_{ud}V_{ub}^* + V_{cd}V_{cb}^* + V_{td}V_{tb}^* = 0\,. \tag{1.14}$$

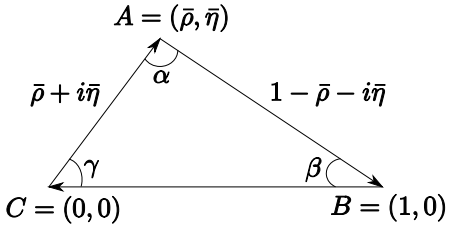

Figure 1.1: The Unitarity Triangle.

Type	J^{PC}	Operator
Scalar	0^{++}	$\bar{\psi}\psi$, $\bar{\psi}\gamma^0\psi$
Pseudoscalar	0^{-+}	$i\bar{\psi}\gamma^5\psi$, $\bar{\psi}\gamma^0\gamma^5\psi$
Vector	1^{--}	$\bar{\psi}\gamma^i\psi$
Axial Vector	1^{++}	$\bar{\psi}\gamma^i\gamma^5\psi$

Table 1.1: Parity eigenstate bilinear composite operators of fermion fields. Here $i = 1 \ldots 3$. The second column shows the spin, parity and charge conjugation eigenvalues (J, P and C respectively) in the form J^{PC}.

To $\mathcal{O}(\lambda^7)$ this relationship can be visualised as a closed triangle of base length unity in the complex $(\bar{\rho}, \bar{\eta})$ plane, where $\bar{\rho} = \rho(1 - \frac{1}{2}\lambda^2)$ and $\bar{\eta} = \eta(1 - \frac{1}{2}\lambda^2)$. This is known as the *unitarity triangle*, and is shown in figure 1.1.

1.2.2 Charge and Parity symmetries

The Parity (P) transformation acts upon a vector $\vec{x}$ as $\{\hat{\mathcal{P}} : \vec{x} \to \vec{x}\,' = -\vec{x}\}$.

A parity transformation upon the coordinates of a field can be accomplished with a unitary operator P. The integer-spin fields ϕ are eigenstates of parity

$$\phi'(\vec{x}\,', t) = P\phi(\vec{x}, t)P = p\phi(\vec{x}, t) \tag{1.15}$$

with discrete eigenvalues $p \in \{1, -1\}$. Table 1.1 lists the parity eigenvalues according to to the spin of the field. The spin-half fermion fields on the other hand are not eigenstates of parity:

$$\psi'(\vec{x}\,', t) = P\psi(\vec{x}, t)P = \eta_a\gamma^0\psi(-\vec{x}, t), \quad \bar{\psi}'(\vec{x}\,', t) = P\bar{\psi}(\vec{x}, t)P = \eta_a^*\bar{\psi}(-\vec{x}, t)\gamma^0\,. \tag{1.16}$$

Here η_a is a phase with $\eta_a^2 = \pm 1$. However, parity eigenstates can be formed from bilinear composite operators of fermion fields. These are given in the third column of table 1.1. These operators are used to pick out states of chosen spin and parity in lattice simulations (cf. secs. 4.2.3 and 6.3).

Charge conjugation (C) is the operation of replacing a particle with its correspond-

ing anti-particle. Under C the fermion fields transform as

$$C\psi C = -i(\bar{\psi}\gamma^0\gamma^2)^T \quad \text{and} \quad C\bar{\psi}C = -i(\gamma^0\gamma^2\psi)^T\,. \tag{1.17}$$

The bilinear parity eigenstates of table 1.1 are also eigenstates of charge conjugation. Their eigenvalues are also listed in the second column.

Electromagnetism and QCD are symmetric under both charge conjugation and parity. However in the weak interactions, the $V-A$ bilinear structure of the vertices breaks parity and charge conjugation as the vector bilinear transforms with the opposite sign to the axial-vector bilinear under both symmetries. The product of the charge conjugation and parity operations (CP) was initially thought to be conserved by the weak interactions as both the vector and axial bilinears are eigenstates of CP with eigenvalue +1. However studies of the kaon sector showed the presence of CP-violating interactions [24]. Such interactions can only appear through the complex phase δ in the CKM matrix. As the two-generation quark model does not admit a phase, the observation of CP-violation gave a clear signal of the existence of a third generation of quarks, years before the discovery of the bottom quark [25]. The precision measurement of CP-violation in the Standard Model is of great interest, as many Beyond the Standard Model (BSM) theories, including supersymmetric models [26], introduce additional sources of CP-violation that might be detected by comparing theory to experiment.

Note that the product CPT of the charge conjugation, parity and time reversal symmetries does appear to be a symmetry of the Standard Model, as breaking it would imply the breaking of Lorentz invariance [27].

1.2.3 Flavour Changing Neutral Currents

The weak interactions allow for loop-induced decays that do not conserve quark flavour and yet have no overall flow of electric charge. These are known as *flavour-changing neutral currents* (FCNC). At one-loop level these can be described by *penguin*

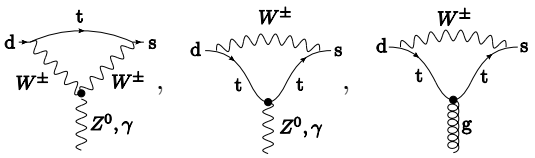

(1.18)

and *box* diagrams

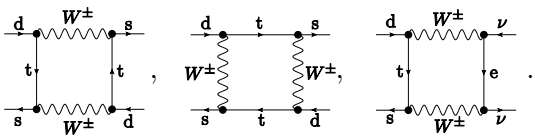

(1.19)

The first two diagrams of eqn. 1.19 produce a net flavour change of $\Delta S = 2$. Such diagrams allow for the mixing between neutral kaon and anti-kaon states.

1.2.4 CP-violation in the kaon sector

Due to neutral kaon mixing, the time evolution of the neutral kaon state vectors,

$$i\frac{\partial\psi(t)}{\partial t} = \hat{H}\psi(t), \quad \text{where} \quad \psi(t) = \begin{pmatrix} |K^0(t)\rangle \\ |\bar{K}^0(t)\rangle \end{pmatrix}, \tag{1.20}$$

is governed by a matrix valued Hamiltonian [28],

$$\hat{H} = \hat{M} - i\frac{\hat{\Gamma}}{2}, \tag{1.21}$$

which contains contributions from virtual $\hat{M}$ and real $\hat{\Gamma}$ intermediate states. These are Hermitian 2×2 matrices which are single-valued along the diagonal; $M_{11} = M_{22}$ and $\Gamma_{11} = \Gamma_{22}$ due to CPT symmetry [23].

The eigenstates of the Hamiltonian are

$$K_{L,S} = \frac{(1+\bar{\epsilon})K^0 \pm (1-\bar{\epsilon})\bar{K}^0}{\sqrt{2(1+|\bar{\epsilon}|^2)}}, \tag{1.22}$$

where $\bar{\epsilon}$ is a small complex number defined through the relation

$$\frac{1-\bar{\epsilon}}{1+\bar{\epsilon}} = \sqrt{\frac{M_{12}^* - i\frac{1}{2}\Gamma_{12}^*}{M_{12} - i\frac{1}{2}\Gamma_{12}}}. \tag{1.23}$$

The eigenstates K_L and K_S are known as "K-long" and "K-short" respectively, referring to their decay lifetime.

The eigenstates of the CP operator are denoted K_1 and K_2, and are defined as

$$\begin{aligned} K_1 &= \frac{1}{\sqrt{2}}(K^0 - \bar{K}^0), \quad \text{where} \quad CP|K_1\rangle = |K_1\rangle \qquad \text{and} \\ K_2 &= \frac{1}{\sqrt{2}}(K^0 + \bar{K}^0), \quad \text{where} \quad CP|K_2\rangle = -|K_2\rangle\,. \end{aligned} \tag{1.24}$$

The weak eigenstates can therefore be rewritten in terms of the CP eigenstates as

$$K_S = \frac{K_1 + \bar{\epsilon}\bar{K}_2}{\sqrt{2(1+|\bar{\epsilon}|^2)}} \quad \text{and} \quad K_L = \frac{K_2 + \bar{\epsilon}\bar{K}_1}{\sqrt{2(1+|\bar{\epsilon}|^2)}}. \tag{1.25}$$

Assuming CP-symmetry, K_1 can only decay to the CP-even 2π final state and K_2 can only decay to the CP-odd 3π final state. Due to phase-space considerations, the $K_2 \to 3\pi$ decay occurs at a much slower rate than the $K_1 \to 2\pi$ decay. As a result the

K_L weak eigenstate, which mostly comprises K_2, has a much longer lifetime than K_S which contains mostly K_1.

The admixture of K_1 and K_2 via the parameter $\bar{\epsilon}$ in the weak eigenstates allows for *indirect* CP-violation. This was first observed by Cronin and Fitch [24] in 1964, which resulted in them being awarded the 1980 Nobel Prize in Physics.

$\bar{\epsilon}$ is not a physical quantity, as it depends on the phase conventions chosen for the K^0 and $\bar{K}^0$ states. Removing the phase dependence, a physical quantity ϵ can be defined as

$$\epsilon = \bar{\epsilon} + i\xi, \quad \text{where} \quad \xi = \frac{\mathrm{Im}A_0}{\mathrm{Re}A_0}\,, \tag{1.26}$$

A_0 is the $K \to (\pi\pi)_{I=0}$ decay amplitude and I is the isospin. Note that the combination of two pions can also form an $I = 2$ state (the $I = 1$ state is forbidden as it has zero Clebsch-Gordon coefficients). ϵ can be measured experimentally with great accuracy [29] via the ratio of amplitudes

$$\epsilon = \frac{A\left(K_L \to (\pi\pi)_{I=0}\right)}{A\left(K_S \to (\pi\pi)_{I=0}\right)}\,. \tag{1.27}$$

It is related to the kaon Hamiltonian through the relation

$$\epsilon = \frac{\exp(i\pi/4)}{\sqrt{2}\Delta M_K}\left(\mathrm{Im}M_{12} + 2\xi\mathrm{Re}M_{12}\right)\,, \tag{1.28}$$

where $\Delta M_K = M(K_L) - M(K_S)$ is the mass difference. In section 8.7, the quantity B_K, which can be related to M_{12} (cf. sec. 3.1.4), is obtained non-perturbatively. In combination with the experimental value of ϵ, this can be used to determine the CP-violating phase δ.

Note that the Standard Model CP-violating phase also allows for *direct* CP-violation, parameterised by a quantity ϵ', in which a K_2 CP-eigenstate decays to two pions or a K_1 CP-eigenstate to three pions. This was first observed in 1988 at the NA31 experiment [30] at CERN by measuring the ratio of the decay rates of K_S and K_L into charged and neutral pions. Later measurements at the NA48 experiment [31] at CERN and KTeV at Fermilab [32] confirmed the earlier results.

Chapter 2

Renormalisation

Quantum field theories contain only local interactions, that is to say interactions between field variables at a point in space and those at infinitesimal separations. However, the correlation length over which particles interact in physical situations is large, spanning a region containing an infinite number of field variables. This chapter addresses the question of how this long-distance behaviour can arise from the short-range dynamics.

2.1 Regularisation and the continuum limit

In order to study the behaviour of a theory as a function of scale it is necessary to introduce an *ultraviolet regulator* in order to reduce the number of field variables per unit volume to a finite quantity. After calculations are performed in the regularised theory, the regulator is removed by taking the *the continuum limit*.

Common techniques include *lattice* regularisation, *momentum cutoff* regularisation and *dimensional regularisation*. In the lattice scheme, space is discretised onto a four-dimensional grid, and the continuum limit is reached by taking the lattice spacing to zero. This scheme is discussed at length in chapter 4. The momentum cutoff scheme introduces a limit Λ on the maximum momentum of particles in the theory. Here the continuum limit is reached by taking the cutoff to infinity. This scheme is the simplest conceptually, and is used extensively in this chapter. Finally, dimensional regularisation reduces the number of spatial dimensions to $4-\epsilon$, where ϵ is small, rendering formerly divergent momentum integrals finite. An example of the use of this scheme is given in section 3.2.3.

All regularisation schemes introduce an energy scale, known as the *regularisation scale*, in some way; in the lattice scheme this scale is the inverse of the lattice spacing, and in the momentum cutoff scheme the scale is the cutoff itself. In dimensional regularisation, the scale appears in the modification of the canonical scaling of the parameters. For example a dimensionless coupling in $d = 4$ dimensions has a canonical dimension of $-\epsilon$ in $d = 4-\epsilon$ dimensions (cf. section 3.2.3).

In order to retain a finite physical correlation length in the continuum limit, the dimensionless correlation length, measured in units of the regularisation scale, must diverge. This is the behaviour associated with a second order phase transition. As a result, all quantum field theories must be tuned to criticality in order to display any long-distance interacting behaviour. This tuning is known as renormalisation.

2.2 Wilson's Renormalisation Group

The behaviour of a theory at different length scales can be determined by *renormalisation group* (RG) transformations $\mathcal{T}$ of the action S_Λ which is regularised with a momentum cutoff Λ, to the *Wilsonian effective action* $S_{\Lambda'}$ with a lower cutoff Λ'. This transformation is obtained by integrating the *exact renormalisation group equation* (ERGE)[33],

$$-\Lambda\frac{\partial S_\Lambda}{\partial\Lambda} = (\mathcal{G}_{\rm dil} + \mathcal{G}_{\rm tra}\{\Psi\})\, S_\Lambda\,, \tag{2.1}$$

where $d\Lambda < 0$, and the operators $\mathcal{G}_{\rm dil}$ and $\mathcal{G}_{\rm tra}$ will be defined shortly. Integrating from Λ to Λ' gives

$$S_{\Lambda'} = \mathcal{T}\left(S_\Lambda,\, \Lambda'/\Lambda\right) = -\int_\Lambda^{\Lambda'} \frac{d\hat{\Lambda}}{\hat{\Lambda}}\, (\mathcal{G}_{\rm dil} + \mathcal{G}_{\rm tra}\{\Psi\})\, S_{\hat{\Lambda}}\,. \tag{2.2}$$

The operation $\mathcal{G}_{\rm tra}\{\Psi\}S_\Lambda$ replaces S_Λ with the action $S_{\Lambda-|d\Lambda|}$ obtained in the limit $\delta\Lambda \to 0$ of the *shell integration* of the path integral over field variables with momentum k in the range $\Lambda - |\delta\Lambda| < |k| \leq \Lambda$. The function Ψ depends on the method by which the momentum cutoff is introduced. The operation $\mathcal{G}_{\rm dil}S_\Lambda$ rescales the length coordinates of the action $x \to x - dx = (1 - \frac{|d\Lambda|}{\Lambda})x$, and also rescales the fields to maintain the form of the kinetic term. This is known as a *dilatation*. The fields are rescaled in this way in order to fix the invariance of the transformation under field rescalings, which is known as the *reparameterisation invariance* [34].

Notice that the function $\mathcal{T}$ depends only on the ratio Λ'/Λ. As a result, the RG transformation is *self-similar* [35][36]:

$$\mathcal{T}\left(S_\Lambda,\, \Lambda''/\Lambda\right) = \mathcal{T}\left(\mathcal{T}\left(S_\Lambda\,, \Lambda''/\Lambda'\right),\, \Lambda'/\Lambda\right)\,. \tag{2.3}$$

This means that $S_{\Lambda'}$ can also be obtained by a single shell integration over the range $\Lambda' < |k| \leq \Lambda$ followed by a dilatation that fixes the form of the kinetic term and rescales the coordinates $x \to x' = \frac{\Lambda'}{\Lambda}x$. This allows non-perturbative renormalisation group analyses to be performed using coarse steps. Such techniques are used in the improvement of lattice actions (cf. sections 2.4 and 4.1.2). However, in perturbation theory the transformation is only self-similar if known to all orders. As a result, coarser

steps amplify the truncation errors [37], and smaller steps are necessary.

As an illustration of the outcome of a renormalisation group transformation, consider the transformation of the scalar theory from $\Lambda \to b\Lambda$, where $b < 1$. This demonstration follows Wilson's original paper [38].

It will be shown that the functional forms of the actions S_Λ and $S_{b\Lambda}$ differ, thus it is necessary to adopt a notation for actions of fixed functional form. These are represented by a lower-case $s^{\cdots}_{\Lambda,\ldots}[\ldots]$, where the subscript indicates the cutoff dependencies, the superscript labels the form and the square brackets contain the field parameters. In this notation, the Euclidean scalar action is

$$S_\Lambda = s^0_\Lambda[\phi] + s^{\mathrm{src}}_\Lambda[\phi, J]\,, \tag{2.4}$$

where $J = J(x)$ is a source term, $\phi(k) = 0$ for $|k| > \Lambda$,

$$s^0_\Lambda[\phi] = \int d^4x\, \frac{1}{2}\left(\partial_\mu\phi\right)^2 + \frac{1}{2}m^2\phi^4 + \frac{1}{4!}\lambda\phi^4\,, \tag{2.5}$$

and

$$s^{\mathrm{src}}_\Lambda[\phi, J] = \int d^4x\; J\phi\,. \tag{2.6}$$

Here the position dependence of the source and fields has been suppressed for clarity. The generating functional

$$Z_\Lambda[J] = \int \mathcal{D}\phi\, e^{-S_\Lambda} = \left(\prod_{k<\Lambda}\int d\phi(k)\right) e^{-S_\Lambda} \tag{2.7}$$

is not modified under the RG transformation and thus remains dependent only on the initial cutoff throughout. The Euclidean metric is used to prevent light-like momenta with small k^2 from having large components.

As it stands, the theory has two scales: the mass m and the cutoff Λ. However, it can be rewritten in terms of a dimensionless mass $\hat{m}^2 = m^2/\Lambda^2$ by replacing

$$\frac{1}{2}m^2\phi^4 \to \frac{1}{2}\Lambda^2\hat{m}^2\phi^4 \tag{2.8}$$

without loss of generality. This exposes the canonical scaling of the mass term and places it on the same footing as the other dimensionless couplings. It will be shown below that the dimensionless mass is not constant but in fact changes with the cutoff via an additional dependence on other dimensionless couplings. Eventually the cutoff will be removed, hence a new scale must be introduced in order to retain the dimensionality of the mass term. This is discussed further in the next section.

Splitting the path integral over low momentum modes $\phi_l(k_l)$ with $|k_l| < b\Lambda$ and

high momentum modes $\phi_h(k_h)$ with $b\Lambda \leq |k_h| < \Lambda$, the generating functional becomes

$$Z_\Lambda[J] = \int \mathcal{D}\phi_l \int \mathcal{D}\phi_h \exp\Big\{ - s^0_{\Lambda,b\Lambda}[\phi_l + \phi_h] - s^{\rm src}_{\Lambda,b\Lambda}[\phi_l + \phi_h, J] \Big\} . \tag{2.9}$$

Defining

$$s^{\rm src}_{\Lambda,b\Lambda}[\phi_l + \phi_h, J] = s^{\rm src}_{b\Lambda}[\phi_l, J_l] + s^{\rm src}_{\Lambda}[\phi_h, J_h] , \tag{2.10}$$

eqn. 2.9 can be rewritten as

$$\begin{aligned} Z_\Lambda[J_l, J_h] \;&= \int \mathcal{D}\phi_l \exp\Big\{ - s^0_{b\Lambda}[\phi_l] - s^{\rm src}_{b\Lambda}[\phi_l, J_l] \Big\} \\ &\quad \times \int \mathcal{D}\phi_h \exp\Big\{ - s^{\rm kin}_{\Lambda}[\phi_h] - s^{\rm src}_{\Lambda}[\phi_h, J_h] - s^{\rm int}_{\Lambda,b\Lambda}[\phi_l, \phi_h] \Big\} , \end{aligned} \tag{2.11}$$

where

$$s^{\rm kin}_\Lambda[\phi_h] = \int d^4x \; \frac{1}{2} (\partial_\mu \phi_h)^2 \tag{2.12}$$

and

$$\begin{aligned} s^{\rm int}_{\Lambda,b\Lambda}[\phi_l, \phi_h] \;&= \int d^4x \; \frac{1}{2}\Lambda^2 \hat{m}^2 \phi_h^2 + \frac{1}{4!}\lambda \phi_h^4 + \partial_\mu \phi_l \partial_\mu \phi_h \\ &\quad + \Lambda^2 \hat{m}^2 \phi_l \phi_h + \frac{1}{6}\lambda \phi_l^3 \phi_h + \frac{1}{4}\lambda \phi_l^2 \phi_h^2 + \frac{1}{6}\lambda \phi_l \phi_h^3 . \end{aligned} \tag{2.13}$$

Here it is assumed that $\hat{m}^2 \ll 1$, and thus the mass can also be treated as a perturbation. Replacing ϕ_h with a functional derivative of the high-momentum field source, the integral can be split:

$$\begin{aligned} Z_\Lambda[J_l, J_h] \;&= \int \mathcal{D}\phi_l \exp\Big\{ - s^0_{b\Lambda}[\phi_l] - s^{\rm src}_{b\Lambda}[\phi_l, J_l] - s^{\rm int}_{b\Lambda}[\phi_l, \frac{\delta}{\delta J_h}] \Big\} \\ &\quad \times \int \mathcal{D}\phi_h \exp\Big\{ - s^{\rm kin}_{\Lambda}[\phi_h] - s^{\rm src}_{\Lambda}[\phi_h, J_h] \Big\} , \end{aligned} \tag{2.14}$$

and the high-momentum field integral can be performed, giving

$$\begin{aligned} Z_\Lambda[J_l, J_h] \;&= \int \mathcal{D}\phi_l \exp\Big\{ - s^0_{b\Lambda}[\phi_l] - s^{\rm src}_{b\Lambda}[\phi_l, J_l] - s^{\rm int}_{b\Lambda}[\phi_l, \frac{\delta}{\delta J_h}] \Big\} \\ &\quad \times \exp\left\{ -\frac{1}{2} \int d^4x \, d^4y \; J_h(x) \Delta_h(x,y) J_h(y) \right\} , \end{aligned} \tag{2.15}$$

where Δ is the high-momentum propagator,

$$\Delta_h(x,y) = \int \frac{d^4k}{(2\pi)^d} e^{ik(x-y)} \frac{\Theta(k)}{k^2} , \quad \text{with} \quad \Theta(k) = \begin{cases} 1 & \text{if } b\Lambda \leq |k| < \Lambda \\ 0 & \text{otherwise} \end{cases} . \tag{2.16}$$

Defining

$$s^{\Delta}_{b\Lambda}[\phi_l] = \log\left(\exp\Big\{ - s^{\rm int}_{b\Lambda}[\phi_l, \frac{\delta}{\delta J_h}]\Big\} \underbrace{\exp\left\{ -\frac{1}{2}\int d^4x\, d^4y\, J_h(x)\Delta_h(x,y)J_h(y)\right\}}_{P[J_h]} \right)_{J_h=0}, \tag{2.17}$$

in which the high-momentum field source is set to zero after the functional derivatives are applied, gives

$$Z_\Lambda[J_l] = \int \mathcal{D}\phi_l \exp\Big\{ - s^0_{b\Lambda}[\phi_l] - s^{\rm src}_{b\Lambda}[\phi_l, J_l] - s^{\Delta}_{b\Lambda}[\phi_l]\Big\}, \tag{2.18}$$

from which the Wilsonian effective action can be identified as

$$S_{b\Lambda} = s^0_{b\Lambda}[\phi_l] + s^{\rm src}_{b\Lambda}[\phi_l, J_l] + s^{\Delta}_{b\Lambda}[\phi_l]\,. \tag{2.19}$$

By Taylor expanding the first term of the logarithm in eqn. 2.17,

$$\exp\left\{-s^{\rm int}_{b\Lambda}[\phi_l, \frac{\delta}{\delta J_h}]\right\} = 1 - s^{\rm int}_{b\Lambda}[\phi_l, \frac{\delta}{\delta J_h}] + \frac{1}{2}\left(s^{\rm int}_{b\Lambda}[\phi_l, \frac{\delta}{\delta J_h}]\right)^2 \dots, \tag{2.20}$$

and applying this to the second term $P[J_h]$, it becomes clear that $s^{\Delta}_{b\Lambda}$ contains an infinite series of additional operators of the low-momentum fields. For example, the following term arises at leading order in the expansion:

$$\frac{1}{4}\lambda\phi_l^2(x)\left(\frac{\delta}{\delta J_h(x)}\right)^2 P[J_h] \xrightarrow{J_h\to 0} -\frac{1}{4}\lambda\phi_l^2(x)\Delta_h(x,x) = \quad . \tag{2.21}$$

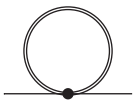

The loop integral can be solved by converting to 4−spherical polar coordinates:

$$\Delta_h(x,x) = \int_{b\Lambda\le|k|<\Lambda} \frac{d^4k}{(2\pi)^d}\frac{1}{k^2} = \int d\Omega_4 \int_{b\Lambda}^{\Lambda} \frac{dl}{(2\pi)^d} l^3 \frac{1}{l^2}\,, \quad \text{with} \quad \int d\Omega_4 = 2\pi^2 \quad . \tag{2.22}$$

Here Ω_4 is the angular component of the 4-dimensional hypersphere, and l is the radial component. The result,

$$\Delta_h(x,x) = \frac{\Lambda^2}{16\pi^2}(1-b^2)\,, \tag{2.23}$$

is position independent, thus eqn. 2.21 acts as an additive mass term in the Lagrangian of ϕ_l:

$$\frac{1}{2}\Lambda^2\hat{m}^2 \xrightarrow{\Lambda\to b\Lambda} \frac{1}{2}b^2\Lambda^2\left(\hat{m}^2 + \Delta\hat{m}^2\right), \quad \text{where} \quad \Delta\hat{m}^2 = \frac{\lambda}{32\pi^2}(\frac{1}{b^2}-1)\,, \tag{2.24}$$

and $\hat{m} = m/(b\Lambda)$ on the right-hand side, written in terms of the new cutoff.

In general, this procedure generates corrections to all of the terms in the Lagrangian of the low energy modes. It also generates an infinite series of higher-dimension operators. For example the term $\left(\int d^4x\, \phi_l^3(x) \frac{\delta}{\delta J_h(x)}\right)^2 P[J_h]$ will generate a six-point interaction term of the form

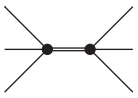 . (2.25)

This non-local term should be expanded as a series of local derivative terms according to the operator product expansion (cf. section 3.1.1), but that is beyond the scope of this section, suffice to say that at leading order it will give a correction ΔC to the dimension 6 term ϕ_l^6, which formerly had a coefficient of zero.

The Wilsonian effective action $S_{b\Lambda}$ is appropriate for describing interactions at energy scales lower than $b\Lambda$. Its terms are compared to those of the original action S_Λ below, ordered in the increasing canonical dimension of the operator:

$$\begin{aligned}
\tfrac{1}{2}\Lambda^2\hat{m}^2\phi^2 &\rightarrow \tfrac{1}{2}b^2\Lambda^2(\hat{m}^2+\Delta\hat{m}^2)\phi^2 \\
\tfrac{1}{2}(\partial_\mu\phi)^2 &\rightarrow \tfrac{1}{2}(1+\Delta Z)(\partial_\mu\phi)^2 \\
\tfrac{1}{4!}\lambda\phi^4 &\rightarrow \tfrac{1}{4!}(\lambda+\Delta\lambda)\phi^4 \\
\Lambda^{-2}\,0\phi^6 &\rightarrow b^{-2}\Lambda^{-2}\Delta\hat{C}\phi^6 \\
\Lambda^{-4}\,0(\partial_\mu\phi)^4 &\rightarrow b^{-4}\Lambda^{-4}\Delta\hat{D}(\partial_\mu\phi)^4 \\
&\vdots
\end{aligned} \tag{2.26}$$

The terms ΔZ, $\Delta\hat{m}^2$, etc are referred to as *counterterms*. Here the higher-dimension terms have had their canonical scaling exposed as with the mass term above. Notice that all of the additional terms preserve the $Z(2)$ symmetry, $\phi \rightarrow -\phi$, of the initial Lagrangian. For example there is no ϕ^3 term. If the original Lagrangian had additional symmetries, the Wilsonian effective Lagrangian would also retain these. This is very important to the discussion of effective theories in chapter 3.

The remaining dilatation can be accomplished by rescaling $b\Lambda \rightarrow \Lambda$, $k \rightarrow k' = k/b$, $x \rightarrow x' = xb$ and $\phi \rightarrow \phi' = \left[b^{-2}(1+\Delta Z)\right]^{\frac{1}{2}}\phi$. The integral over ϕ_l' measured in the rescaled units is then over the region $|k| < \Lambda$.

Under the integral, the theory describes a *renormalisation group flow* through the infinite-dimensional space of couplings. As the transformations do not modify the path integral in any way, the flows describe curves of *constant physics*.

2.3 Asymptotic freedom of QCD

The analysis of the previous section demonstrates that the so-called 'constants' of a quantum field theory, even if dimensionless, are in fact dependent on the energy scale

of the interactions being considered.

In the early 1970s it was discovered that the coupling in non-abelian Yang-Mills theories such as QCD tends to zero in the ultraviolet [39]. This is known as *asymptotic freedom*. In the low energy regime, asymptotically free theories become strongly coupled, which in QCD results in the binding of quarks into hadrons. In this regime the standard techniques of perturbation theory break down, and other methods such as lattice QCD must be used.

One manifestation of asymptotic freedom is the linear long-distance behaviour of the static inter-quark potential, which occurs due to the binding of the strongly-coupled gluons into flux tubes [40][41][42][43][44] with a potential energy that rises linearly with the separation of the quarks, giving a constant binding force. This generally conjectured behaviour is observed in the lattice simulations in section 6.7. Only when the potential energy is large enough to generate a quark-antiquark pair does the flux tube break. As a result, isolated quarks can never be observed in nature. This is known as *confinement*.

2.4 The continuum limit of QCD

A point in parameter space that is defined at the original cutoff Λ is referred to as a *bare theory*. In order to be a valid description of QCD in the continuum limit $\Lambda \to \infty$, a bare theory must satisfy the following three criteria:

1. The gauge coupling must tend to zero in the ultraviolet due to asymptotic freedom.

2. The dimensionless correlation length in units of Λ must be infinite.

3. The physical theory must arise naturally, and thus should not require the tuning of a large number of parameters.

The true physical theory is represented by a single renormalisation group flow, specified by an infinite set of parameters at each point. Clearly in order for the physical theory to arise naturally, something more is needed. The missing ingredient is the existence of a *free-field* or *Gaussian fixed point*: a stationary point of the renormalisation group transformation at which all parameters are zero.

The first of the conditions is satisfied by any flow that passes infinitesimally close to the Gaussian fixed point in the ultraviolet. In this context, the fixed point is referred to as an *ultraviolet fixed point*. The aforementioned flows are referred to as *renormalised trajectories*, and can be found by tuning to the edge of the *critical manifold* [45] or *domain* [38] of points that evolve onto the fixed point. Usually the critical manifold encompasses a large multi-dimensional subspace of points local to the fixed point.

The dimensions of this subspace are referred to as *irrelevant directions*. Only in the typically small number of *relevant directions*, orthogonal to the critical manifold, is tuning required to find a renormalised trajectory. The divergence of the dimensionless correlation length requires that the quark mass, which defines the distance that a quark can propagate, is finite at high energies, and therefore that the dimensionless quark mass tends to zero. This is also satisfied by the close-approach to the Gaussian fixed point in the ultraviolet. The fixed point and its critical manifold therefore exist in the subspace of theories with divergent dimensionless correlation length, which is known as the *critical surface* [38].

The relevant parameters of the Gaussian fixed point of single-flavour QCD are the dimensionless quark mass $\hat{m}$ and the coupling constant g. There is therefore a one-dimensional family of renormalised trajectories. Renormalised trajectories are attractive, meaning that nearby flows converge upon them asymptotically [46]. This enables them to be parameterised by points on a line in the $(g, \hat{m})$ plane at fixed mass or coupling. For example, fixing the coupling and varying the mass picks out a series of different renormalised trajectories.

Figure 2.1 contains a sketch of two renormalised trajectories of the Gaussian fixed point. The first renormalised trajectory, figure 2.1(a), runs in the plane of the coupling and a dimensionless irrelevant coupling $\hat{I}$, and is picked out by tuning the mass to zero at fixed coupling g_1. In this particular case, the same trajectory can be found by tuning the mass to zero at any coupling (e.g. g_2). This trajectory represents the chiral limit of QCD. Figure 2.1(b) shows a more general scenario. Here the renormalised trajectory runs in the (g, m) plane initially before flowing away in the direction of the irrelevant coupling. It is picked out by tuning the mass to m_1 at fixed coupling g_1. At a coupling g_2 the same trajectory is reached by tuning the the mass to $\hat{m}_2$. The curve of mass versus coupling required to reach a particular renormalised trajectory is known as a *scaling curve*.

In the region of the Gaussian fixed-point, a perturbative expansion of the regularised path integral in the weak coupling can be performed. In order to take the continuum limit, the scaling curve of points that converge to the physical renormalised trajectory must be picked out. This is achieved by tuning the bare theory, or equivalently the counter-terms of the relevant couplings, order-by-order to the critical manifold as the cutoff is removed, in such a way as to fix the mass and coupling at an arbitrary *renormalisation scale*. The values of the *renormalised parameters* are chosen through a set of *renormalisation conditions*, which define the choice of renormalised trajectory. Unsurprisingly this procedure is known as *renormalisation*. The regulator is required in order to be able to manipulate, and subsequently remove, divergent terms arising from unbounded loop momenta. The renormalisation scale becomes the scale against which

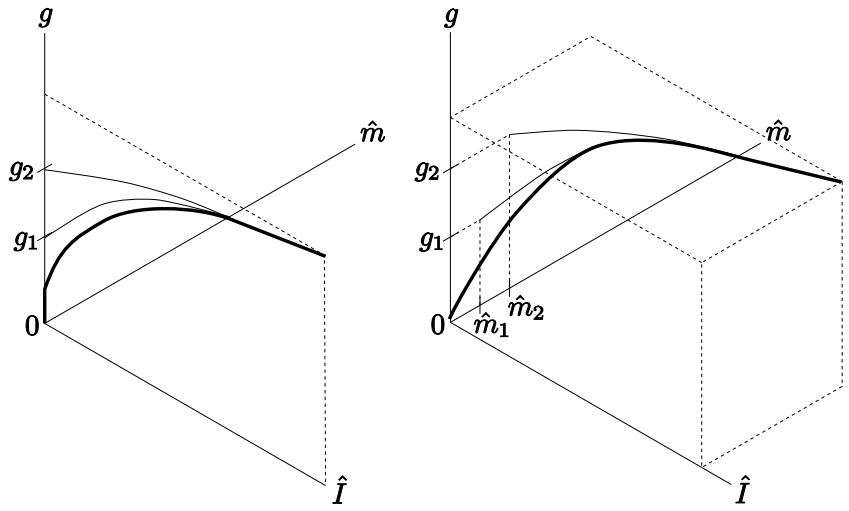

(a) Massless renormalised trajectory (b) A massive renormalised trajectory

Figure 2.1: Two renormalised trajectories (dark curves) of the Gaussian fixed point of QCD, plotted against the coupling g, dimensionless mass $\hat{m}$ and a dimensionless irrelevant parameter $\hat{I}$. Also shown are a series of RG flows that converge upon the renormalised trajectories.

all dimensionful quantities are defined. An example of perturbative renormalisation, using the $\overline{\text{MS}}$ scheme in dimensional regularisation, is given in section 3.2.3.

When simulating at a finite cutoff scale far below the Gaussian fixed point, it is necessary to tune to a renormalised trajectory rather than to the critical manifold itself. Whereas the tuning to the critical manifold requires the specification of two parameters, the so-called *perfect action* that defines a renormalised trajectory must specify the full infinite set of couplings. Clearly this cannot be performed exactly, but attempts have been made to approximate such a theory [47]. The benefit of this approach is that a perfect action exactly describes continuum physics even at finite cutoff.

The alternative to explicitly tuning to a renormalised trajectory is to take the cutoff to infinity while following a scaling curve of points in a finite subspace of parameters that converge to the chosen renormalised trajectory. Here it is more convenient to parameterise the renormalised trajectory in terms of a set of dimensionless physical quantities or ratios of quantities $\{\mathcal{R}\}$ (eg. m_π/m_Ω), one for each free parameter of the theory. The scaling curve is then defined by the parameters of a set of simulations with bare masses and couplings tuned such that their simulated values of $\{\mathcal{R}\}$ match those of the renormalised trajectory. Notice that in this procedure, the tuning of the mass and gauge coupling to the scaling curve does not require a choice of physical scale. The scale is assigned later by assigning a dimensionful value to a previously dimensionless physical quantity $\mathcal{D}$ on the renormalised trajectory. For example, in chapter 8 the scale is set through the continuum value of the Omega baryon. The cutoff scale of each

simulated point on the scaling curve can then be determined by comparing the value of $\mathcal{D}$ to the physical value, after which predictions for physical quantities in the continuum can be obtained by extrapolating to the limit of infinite cutoff. The down-side to this approach is that multiple simulations are required to perform this extrapolation. This procedure is presented in more detail in chapter 8.

The rate at which a theory defined on the scaling curve converges to the renormalised trajectory can be improved by moving the bare theory closer to the renormalised trajectory in the space of irrelevant couplings. This allows the theory at finite cutoff to more accurately reproduce continuum physics. In lattice QCD this is known as Symanzik improvement [48][49].

If no ultraviolet fixed point exists, trajectories can still be found that flow from the critical surface. Like the renormalised trajectories, specifying such a flow requires the fixing of an infinite number of parameters. However, here the flow is not attractive and thus all parameters must be fixed exactly. Such a theory is *non-renormalisable*. Effective theories (chapter 3) are examples of such theories.

2.5 The Callan-Symanzik Equation

Once the continuum limit has been taken, the renormalisation group flow from the ultraviolet to the infrared parallels the renormalised trajectory. After setting the scale using either an explicit renormalisation scale or by imposing that a physical quantity such as the Omega baryon mass matches its physical value, an energy scale μ can be assigned to all points along the renormalised trajectory. It then becomes possible to determine the scale dependence of the couplings.

The scaling of the mass and gauge coupling can be determined at high energies using perturbation theory, to a precision that depends on the magnitude of the couplings and the order of the perturbative expansion. The renormalised action offers a convenient expansion point, as the couplings and scale are easily determined from the renormalisation conditions. The scaling behaviour of the renormalised couplings, which are the relevant parameters of the ultraviolet fixed point, can be determined simply by varying the renormalisation scale at which the renormalisation coefficients are determined. The determination of the scaling behaviour of the irrelevant operators is the topic of the next section. As the form of the renormalisation group transformation depends only on the relative change in the cutoff (cf. eqn. 2.3), the scaling functions (the beta-function and the anomalous dimensions - see below) obtained by varying the ratio of the renormalisation scale to the cutoff of the bare theory are applicable between any two values of the cutoff within the perturbative regime [37], although at lower scales the calculation must be performed at higher orders to maintain a given

accuracy.

One parameter that has not been mentioned is the field renormalisation Z, which is the coefficient of the kinetic term. Under renormalisation group transformations, this quantity is fixed to unity through a rescaling of the fields. However it must be recognised that the field strength is changing behind the scenes. This becomes clear when considering the behaviour of Green's functions under changes in the renormalisation scale μ along the renormalised trajectory.

As a Green's function consists of products of field variables, its value can only change as a function of scale through the field strength renormalisation. A small change of scale which shifts this quantity by a factor $1 + \delta Z$ will result in a shift in the value of an n-point Green's function $G^{(n)}$ by

$$G^{(n)} \to (1 + n\delta Z)G^{(n)} \,. \tag{2.27}$$

In QCD, the change in the field strength renormalisation Z arises alongside a change in the mass δm and the coupling δg. Treating Z as a function of the mass, coupling and scale $Z = Z(\mu, m, g)$, the shift in $G^{(n)}$ becomes

$$\delta G^{(n)} = \left(\delta\mu \frac{\partial}{\partial \mu} + \delta g \frac{\partial}{\partial g} + \delta m \frac{\partial}{\partial m} \right) G^{(n)} = n\delta Z G^{(n)} \,, \tag{2.28}$$

which can be rewritten as

$$\left(\mu \frac{\partial}{\partial \mu} + \beta \frac{\partial}{\partial g} + \gamma_m m \frac{\partial}{\partial m} + n\gamma \right) G^{(n)}(\{x_i\}; \mu, g, m) = 0 \,, \tag{2.29}$$

where in the limit $\delta\mu \to 0$,

$$\beta = \mu \frac{\partial g}{\partial \mu} \quad \gamma_m = \mu \frac{\partial \log m}{\partial \mu} \quad \gamma = -\mu \frac{\partial Z}{\partial \mu} \,. \tag{2.30}$$

Equation 2.29 is the *Callan-Symanzik Equation*. β, γ and γ_m are the *beta-function*, the *anomalous dimension of the field* and the *mass anomalous dimension* respectively. These quantities contain the scale dependence of the couplings.

2.6 Renormalisation of composite operators

A general quantum field theory calculation involves Green's functions containing isolated field operators, as these are related through the LSZ formalism [50] to physical scattering amplitudes. Sometimes it is also necessary to consider Green's functions of *local composite operators*, defined as normal ordered products (cf. section 4.2.3) of field variables at a single point in space, which are not relevant operators of

the ultraviolet fixed point, yet need to be evaluated against the background of the theory. Such measurements are necessary when measuring correlation functions of effective interactions, for example the B_K four-quark matrix element against the QCD background (c.f. section 3.1.3).

The insertion of a single composite operator $\mathcal{O}$ into a Green's function of spatially-separated fields,

$$\langle \mathcal{T}\psi(r_0)\dots\psi(r_m)\bar{\psi}(s_0)\dots\bar{\psi}(s_n)\mathcal{O}(x)\rangle\,, \tag{2.31}$$

can be generated by introducing a position dependent source term $Q(x)$ into the generating functional:

$$Z[J,Q] = \int \mathcal{D}\bar{\psi}\mathcal{D}\psi \exp\left(iS[\bar{\psi},\psi] + i\int d^4x\left[Q(x)\mathcal{O}(x) + J(x)\bar{\psi}(x) + \bar{J}(x)\psi(x)\right]\right). \tag{2.32}$$

Considered as an additional term in the action, it is clear that the operator will require renormalisation in order to remain finite as the cutoff is removed. Introducing a renormalisation coefficient $Z_{\mathcal{O}}$, the renormalised action becomes

$$S_r[\bar{\psi},\psi,Q] = S_r[\bar{\psi},\psi] + Z_{\mathcal{O}}\int d^4x\, Q(x)\mathcal{O}(x)\,. \tag{2.33}$$

In general the composite operator will mix under renormalisation with all operators of equal and lower canonical dimension that transform in the same way under the symmetries of the Lagrangian [51]. This occurs naturally along the renormalisation group flow through parameter space. As a result one must renormalise a (usually finite) set of operators by introducing source terms of the form

$$Z^i_j Q^j(x)\mathcal{O}_i(x) \tag{2.34}$$

into the renormalised action.

With a single composite operator insertion $Z^i_j\mathcal{O}_i$, a Green's function $G^{(n;1)}$ scales by an additional product of factors $\prod_i(1+\delta Z^i_j)$ which enter in the same way as the field strength renormalisation in eqn. 2.27:

$$G^{(n;1)} \to (1 + n\delta Z + \sum_i \delta Z^i_j)G^{(n;1)}\,. \tag{2.35}$$

This results in a series of additional anomalous dimensions entering into the Callan-Symanzik equation:

$$\gamma^i_j = \mu\frac{\partial}{\partial\mu}\log Z^i_j\,. \tag{2.36}$$

As the composite operators are typically irrelevant operators of the ultraviolet fixed

point, the action is non-renormalisable until the source is set to zero. This means that an infinite number of renormalisation coefficients are required in order to make finite all Green's functions containing an arbitrary number of operator insertions. Only those operators that are relevant to the ultraviolet fixed point can be renormalised with a single renormalisation coefficient for an arbitrary number of operator insertions.

The non-renormalisability occurs due to the presence of additional divergences that arise when the composite operators coincide spatially. Consider the approach of two general composite operators in the renormalised Green's function

$$G_R^{(m+n;2)} = (Z)^{m+n} Z_i^k Z_j^l \langle \mathcal{T}\psi(r_0)\dots\psi(r_m)\bar{\psi}(s_0)\dots\bar{\psi}(s_n)\mathcal{O}_k(x)\mathcal{O}_l(y)\rangle\,, \tag{2.37}$$

where the possibility of operator mixing has been allowed. In the limit of close approach $x \to y$, the operators can be expanded into a series of single renormalised composite operators [52]

$$Z_m^j Z_n^k f^i_{(p,q)\,jk} \partial_x^p \partial_y^q \mathcal{O}_i(x)\delta(x-y) \tag{2.38}$$

with increasing numbers of derivatives p and q, by applying the operator product expansion (cf. section 3.1.1). This series of *contact terms* must be subtracted in order to properly renormalise the Green's function. The coefficients $f^i_{(p,q)\,jk}$ are divergent, and can be non-zero even in the free-field case [52]. The fully renormalised Green's function is given as

$$\begin{aligned} G_R^{(m+n;2)} \quad &= (Z)^{m+n} Z_i^k Z_j^l \Big\{ \langle \mathcal{T}\psi(r_0)\dots\psi(r_m)\bar{\psi}(s_0)\dots\bar{\psi}(s_n)\mathcal{O}_k(x)\mathcal{O}_l(y)\rangle \\ &\qquad + f^a_{(p,q)\,kl} \partial_x^p \partial_y^q \Big(\langle \mathcal{T}\psi(r_0)\dots\psi(r_m)\bar{\psi}(s_0)\dots\bar{\psi}(s_n)\mathcal{O}_a(x)\rangle \delta(x-y) \Big) \Big\}\,. \end{aligned} \tag{2.39}$$

The contact terms can be generated through the addition of a term

$$Z_m^j Z_n^k f^i_{(p,q)\,jk} \partial^p Q_j \partial^q Q_k \mathcal{O}_i \tag{2.40}$$

into the generating functional.

With a larger number of insertions, more divergences arise that are cancelled by further contact terms involving more powers of derivatives and sources. If the canonical dimension of the source is non-negative the series converges, as only a limited number of such terms can be written that satisfy the dimensionality. For example for dimension 2 operators, for which the source term has canonical dimension 2, the series terminates on the term $f^0_{jk} Q^j Q^k$ where $\mathcal{O}_0 = \mathbf{1}$. This term does not render the theory non-renormalisable. For dimension 6 operators, the source has dimension -2 and the series never converges. Consequently, in order to renormalise all Green's functions with an arbitrary number of operator insertions, an infinite amount of counterterms

are required. This demonstrates that dimension 6 operators are non-renormalisable [53].

In this thesis, only insertions of single composite operators are considered, for which multiplicative renormalisation is all that is required. In chapter 7, the renormalisation of the four-quark vertices of the weak effective theory (section 3.1) that contribute to neutral kaon mixing are discussed at length.

Chapter 3

Effective Theories

In the Standard Model there are a large number of scales, from the quark mass scale of a few MeV, through the hadronic scale at a few hundred MeV, to the top mass scale at hundreds of GeV. For physics at a particular energy scale, the effects of interactions at much larger scales are typically small unless the corresponding operators are relevant operators of the controlling ultraviolet fixed point of the theory. As a result, much of the low energy dynamics can be studied in isolation, with the high energy dynamics entering only as higher order corrections. The result is as an *effective field theory* (EFT) (in the literature, the word 'field' is often dropped).

This chapter focuses on the development of two effective theories that are used to study low energy hadronic behaviour in lattice simulations. The first is the effective theory of the weak interactions, which is analysed in the framework of the operator product expansion. The second is the chiral effective theory, which is an attempt to understand the low energy behaviour of hadrons about the massless chiral limit.

3.1 Weak Decays and The Operator Product Expansion

Hadronic interactions typically occur at energy scales of $\mathcal{O}(1\,\mathrm{GeV})$. At these scales the weak interactions, which are mediated by W bosons of mass $M_W \sim 80$ GeV, are essentially point-like. This motivates the formulation of a low-energy effective theory in which the non-local weak interactions are approximated by local operators.

3.1.1 Formal development

Wilson's procedure [38] offers a conceptually clear framework for understanding effective theories. This approach was used in section 2.2 to introduce the renormalisation group. In this procedure, the field content of a theory with a momentum cutoff Λ is split into low- and high-frequency modes about an arbitrary scale λ, and a shell integration of the generating functional over the high-frequency modes is performed. This section outlines the application of this procedure to the weak interactions with a cutoff set below M_W. Particular emphasis is placed on dealing with non-local diagrams such as

eqn. 2.25 that involve high-momentum propagators.

The generating functional of the weak interactions is

$$Z[\bar{j}, j, J_\mu^+, J_\mu^-] = \int \prod_q (\mathcal{D}\bar{q}\mathcal{D}q)\, \mathcal{D}W^+ \mathcal{D}W^- \exp\left(i \int d^4x \mathcal{L}(x)\right) , \tag{3.1}$$

where

$$\begin{aligned}
\mathcal{L} &= \mathcal{L}_W^{\text{free}} + \mathcal{L}_{\text{quark}}^{\text{free}} + \mathcal{L}^{\text{int}} , \\
\mathcal{L}_W^{\text{free}} &= -\frac{1}{2}(\partial_\mu W_\nu^+ - \partial_\nu W_\mu^+)(\partial^\mu W^{-,\nu} - \partial^\nu W^{-,\mu}) + M_W^2 W_\mu^+ W^{-,\mu} \\
&\qquad + \frac{g_2}{2\sqrt{2}} \left(J_\mu^+ W^{+,\mu} + J_\mu^- W^{-,\mu}\right) , \\
\mathcal{L}_{\text{quark}}^{\text{free}} &= \sum_q \bar{q}(i\gamma^\mu \partial_\mu - m_q)q + \bar{j}q + \bar{q}j , \text{ and} \\
\mathcal{L}^{\text{int}} &= \sum_{p,n} \frac{g_2}{2\sqrt{2}} \left((V-A)_{pn\,\mu}^+ W^{+,\mu} + (V-A)_{pn\,\mu}^- W^{-,\mu}\right) .
\end{aligned} \tag{3.2}$$

Here $\bar{j}$, j, J_μ^+ and J_μ^- are sources for the quark, antiquark, W^+ and W^- fields respectively,

$$(V-A)_{pn\,\mu}^+ = V_{pn}\bar{p}\gamma_\mu(1-\gamma_5)n, \quad \text{and} \quad (V-A)_{pn\,\mu}^- = \left((V-A)_{pn\,\mu}^+\right)^\dagger , \tag{3.3}$$

where $p \in (u, c, t)$ and $n \in (d, s, b)$. The unitary gauge has been used for the W fields and the mass term generated by the Higgs mechanism has been included. The coefficient of the W sources $\frac{g_2}{2\sqrt{2}}$ is included for later convenience.

Following the procedure outlined in section 2.2, the interaction Lagrangian $\mathcal{L}^{\text{int}}$ is restated in terms of functional derivatives of the sources $J^\pm$ as

$$\mathcal{L}^{\text{int}} = \sum_{p,n} (V-A)_{pn\,\mu}^+ \frac{\delta}{\delta J_\mu^+} + (V-A)_{pn\,\mu}^- \frac{\delta}{\delta J_\mu^-} , \tag{3.4}$$

allowing the generating functional of free W bosons, [23]

$$Z_W[J^-, J^+] = \int \mathcal{D}W^+ \mathcal{D}W^- \exp\left(i \int d^4x \mathcal{L}_W^{\text{free}}(x)\right) , \tag{3.5}$$

to be separated out. Up to a total derivative, the action can be rewritten in a quadratic form,

$$\begin{aligned}
\int d^4x\, \mathcal{L}_W^{\text{free}}(x) &= \int d^4x\, d^4y\, W_\mu(x)^+ \Big(\delta(x-y)[g^{\mu\nu}(\partial^2 + M_W^2) - \partial^\mu\partial^\nu]\Big) W_\nu^-(y) \\
&\qquad + \delta(x-y)\frac{g_2}{2\sqrt{2}}\Big(J_\mu^+(x)W^{+,\mu}(x) + J_\mu^-(x)W^{-,\mu}(x)\Big) ,
\end{aligned} \tag{3.6}$$

which can be integrated within the generating functional of eqn. 3.5, giving

$$Z_W \sim \exp\left(-i\int d^4x\, d^4y\, \frac{g_2^2}{8} J_\mu^-(x)\Delta^{\mu\nu}(x,y)J_\nu^+(y)\right), \tag{3.7}$$

where $\Delta^{\mu\nu}(x,y)$ is the W propagator,

$$\Delta^{\mu\nu}(x,y) = \int \frac{d^4k}{(2\pi)^4} e^{-ik(x-y)} \frac{-1}{k^2 - M_W^2}\left(g_{\mu\nu} - \frac{k_\mu k_\nu}{M_W^2}\right). \tag{3.8}$$

The fields are now split into high- and low-frequency modes about λ and the high-momentum modes are integrated out of the path integral. At energy scales below M_W, the W boson is not an on-shell degree of freedom; it appears only as an internal virtual particle. The process of integrating out high-frequency modes therefore removes the W as a degree of freedom entirely. For the quark fields, the procedure is as follows. Following section 2.2, split the quark fields about λ as $q = q_l + q_h$ [54] and split the source terms as $j = j_l + j_h$. As the high- and low-frequency components (q_h and q_l resp.) commute, the terms in the Lagrangian coupling the modes can be rewritten in terms of $\delta/\delta j_h$ and $\delta/\delta\bar{j}_h$ and the high-frequency modes can be integrated out in isolation, as with the W fields above:

$$\begin{aligned} Z_h[\bar{J}_h, J_h] &= \int \mathcal{D}\bar{q}_h \mathcal{D}q_h \exp\left\{ i\int d^4x \left(\mathcal{L}^{\text{free}}_{\text{quark}}\big(\bar{q}_h(x), q_h(x)\big) + \bar{j}_h(x)q_h(x) + \bar{q}_h(x)j_h(x)\right)\right\} \\ &= \frac{1}{\sqrt{\det(\mathcal{G}_h^{-1})}} \exp\left\{\frac{1}{2}\int d^4x\, d^4y\, \bar{j}_h(x)\mathcal{G}_h(x,y)j_h(y)\right\}, \end{aligned} \tag{3.9}$$

where $\mathcal{G}_h$ is the propagator of the high-momentum quark fields. Finally the functional derivatives in the interaction terms can be allowed to act upon the generating functionals of the W and the high-frequency quarks, generating an infinite set of terms involving the propagators of the W boson and the high-frequency quarks. The sources $J_\mu^\pm$, $\bar{j}_h$ and j_h can now be set to zero as these fields cannot form on-shell external states.

At leading order in g_2^2, the procedure above generates the effective vertex

$$\mathcal{L}^{(1)}_{\text{eff}}(x) = \int d^4y \frac{g_2^2}{8}\big(V_{pn}\bar{p}_l(x)\gamma_\mu(1-\gamma_5)n_l(x)\big)\Delta^{\mu\nu}(x,y)\big(V_{p'n'}\bar{p}'_l(y)\gamma_\mu(1-\gamma_5)n'_l(y)\big) \tag{3.10}$$

which is non-local in the fields. As the energy scale of these modes $k^2 \ll M_W^2$, the W propagator can be expanded in terms of the small quantity $\frac{k^2}{M_W^2}$. To leading order,

$$\Delta^{\mu\nu}(x,y) = \int \frac{d^4k}{(2\pi)^4} e^{-ik(x-y)} \frac{g_{\mu\nu}}{M_W^2} + \mathcal{O}\left(k^2/M_W^2\right) \approx \frac{g_{\mu\nu}}{M_W^2}\delta^4(x-y). \tag{3.11}$$

Inserting this into eqn. 3.10 and performing the integral over y, one obtains the local effective Lagrangian

$$\mathcal{L}^{(1)}_{\text{eff}} = \frac{-G_F}{\sqrt{2}} V^*_{pn} V_{p'n'} (\bar{n}p)_{V-A} (\bar{p}'n')_{V-A} \,, \tag{3.12}$$

where $(\bar{n}p)_{V-A} = \bar{n}\gamma^\mu(1-\gamma^5)p$, and $G_F = \frac{\sqrt{2}}{8}\frac{g_2^2}{M_W^2}$ is Fermi's constant.

The expansion of non-local effective operators as a sum over local operators is called the *operator product expansion* (OPE). Higher order terms in the expansion of the propagator contain factors of the internal momentum k, which equate to derivatives of the quark fields in position-space. These have a higher canonical mass dimension. In general the OPE generates an infinite set of local operators

$$\sum_i C_i(x)\mathcal{O}_i(x) \tag{3.13}$$

of increasing mass dimension. Here C_i are known as *Wilson coefficients*. When applied to the Weak interactions the higher dimension terms can usually be neglected as M_W is very large. However, for some physical processes it is useful to understand the behaviour of a non-local interaction near the *light-cone*, at which $(x-y)^2 \approx 0$. This condition can be satisfied even when the components of $x-y$ are not small. In this situation, the importance of the operators in the OPE is not governed solely by the mass dimension d, but the difference between this and the spin J of the operator. As a result, higher dimension, higher spin operators can play a major role. The quantity $d-J$ is referred to as the *twist* [55]. Higher twist operators are important in, for example, studies of deep-inelastic scattering [56][57], parton [58] and meson [59] structure functions.

At next-to-leading order in the expansion under G_F, there are a series of effective vertices involving two insertions of the W propagator. These include $\Delta S = 2$ effective vertices of the form

$$G_F^2 M_W^4 \lambda_i \lambda_j \int d^4k \Big(\bar{d}_l \gamma^\mu (1-\gamma^5) \mathcal{G}_h^i(k) \gamma^\alpha (1-\gamma^5) s_l\Big) \Delta^{\mu\nu}(k) \Delta^{\alpha\beta}(k) \times \Big(\bar{d}_l \gamma^\nu (1-\gamma^5) \mathcal{G}_h^j(k) \gamma^\beta (1-\gamma^5) s_l\Big) \,, \tag{3.14}$$

where external momenta and numeric coefficients have been ignored. Here $\mathcal{G}_h^i$ is the propagator of the heavy internal quark i, and $\lambda_i = V^*_{is}V_{id}$. At leading order in the OPE, this has the form [23]

$$\text{Box}(\Delta S = 2) = -\sum_{ij} \lambda_i \lambda_j \frac{G_F^2}{16\pi^2} M_W^2 F(x_i, x_j) (\bar{s}d)_{V-A} (\bar{s}d)_{V-A} \,, \tag{3.15}$$

where $F(x_i, x_j)$ is the Wilson coefficient and x_i is the ratio of the internal quark mass m_i to the W mass; $x_i = \frac{m_i^2}{M_W^2}$.

The evaluation of the Wilson coefficient F of eqn. 3.15 requires the integration of a high-frequency quark loop. Here, the loop momenta are bounded by the cutoff Λ. Unfortunately, the sharp cutoff destroys the underlying gauge invariance of the theory as $p_\mu = i\partial_\mu$ is not gauge covariant (unlike the covariant derivative D_μ). It is also not Lorentz invariant as the cutoff is frame dependent. Alternate symmetry preserving cutoff regularisations use a smooth cutoff [60][61] or a modification of the effective Lagrangian [62], but these are difficult to implement.

A much more convenient symmetry preserving regularisation is the *dimensional regularisation* (DIMREG) scheme [63], in which divergent integrals are made finite by generalising to $d = 4 - \epsilon$ dimensions. Here the generalisation of γ^5 to $4 - \epsilon$ dimensions can be handled in several ways. The simplest (but algebraically inconsistent) scheme, known as *naive dimensional regularisation* (NDR) [64][65], treats γ^5 as in the four-dimensional theory, as anticommuting with all other gamma-matrices. An example of the use of DIMREG/NDR can be found in section 3.2.3.

The strategy for generating the effective theory of the weak interactions in DIMREG/NDR is to move from the high- to low-energy regime while successively integrating out the heavy degrees of freedom (first the top, then the W) as the corresponding mass threshold is crossed. At each threshold M, the theory below the threshold is *matched* to the theory above order-by-order in perturbation theory. This is achieved by renormalising both theories in DIMREG/NDR at a scale $\mu \approx M$ and demanding that both give the same result for a sufficient number of quantities to determine the Wilson coefficients. The result is a so-called *continuum effective field theory* [66]. This procedure has been used to generate the heavy quark effective theory (see for example [67]) in which slow-moving heavy quarks are integrated out of QCD. The approach is also reminiscent of the calculation of counterterms in renormalised perturbation theory.

3.1.2 $K^0 \to \bar{K}^0$ mixing

In section 1.2.3, the flavour changing neutral current interactions were introduced. These allow for the mixing of neutral kaon and anti-kaon states and thus allow indirect CP-violation in the Standard Model. The leading order effective vertex parameterising these interactions in the effective theory is given by eqn. 3.15. The corresponding 1-loop box diagrams in the full theory are treated in DIMREG according to the continuum EFT prescription. In fact the integrals are not divergent. Comparing the result to

eqn. 3.15 gives the Wilson coefficient F. Using the unitarity of the CKM matrix,

$$\lambda_u + \lambda_c + \lambda_t = 0\,, \tag{3.16}$$

(recall from eqn. 3.14 that $\lambda_i = V_{is}^* V_{id}$), the sum of Wilson coefficients can be written as

$$\sum_{i,j\in\{u,c,t\}} \lambda_i \lambda_j F(x_i, x_j) = \sum_{i,j\in\{c,t\}} \lambda_i \lambda_j S_0(x_i, x_j)\,, \tag{3.17}$$

where

$$S_0(x_i, x_j) = F(x_i, x_j) + F(x_u, x_u) - F(x_i, x_u) - F(x_j, x_u)\,. \tag{3.18}$$

The Wilson coefficient S_0 is now summed only over the charm and top quark masses. In general only the terms $F(x_i, x_j)$ for $i, j \in \{c, t\}$ are included as the up quark mass is much smaller than M_W ($x_u \sim 1.4 \times 10^{-9}$). The result is [68]

$$\begin{aligned} S_0(x_i, x_j) \quad = -x_i x_i \Bigg\{ & \frac{1}{x_i - x_j}\left[\frac{1}{4} - \frac{3}{2}\frac{1}{x_i - 1} - \frac{3}{4}\frac{1}{(x_i-1)^2}\right] \ln x_i + (x_i \leftrightarrow x_j) \\ & - \frac{3}{4}\frac{1}{(x_i-1)(x_j-1)} \Bigg\}\,. \end{aligned} \tag{3.19}$$

3.1.3 QCD effects and Wilson Coefficients

In continuum EFT, the leading $\mathcal{O}(\alpha_s)$ QCD corrections to the Wilson coefficients S_0 are evaluated by calculating the following diagrams in the effective theory,

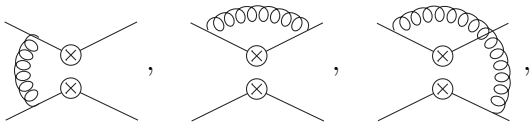

(3.20)

and then matching the results to the two-loop diagrams [70]

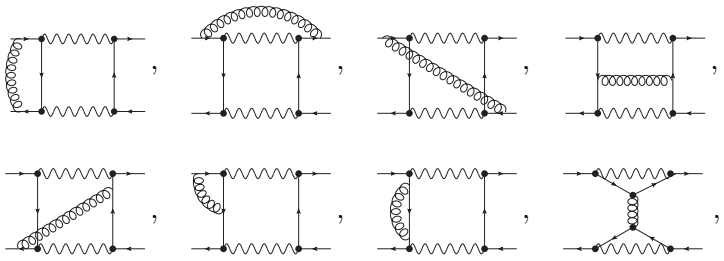

(3.21)

plus their symmetric counterparts, in the full theory at the threshold scale M_W. Here $\alpha_s = \frac{g^2}{4\pi}$, where g is the QCD coupling. The renormalisation of the effective vertex is performed by including it as a composite operator in the framework of QCD. It thus requires an additional counterterm for the vertex (c.f. section 2.6).

After matching, the result is specified at a generic renormalisation scale μ by evolving the Wilson coefficients down from M_W to μ using the renormalisation group running. This must be performed in stages as the running may cross quark mass-thresholds. Taking a typical $\mu \lesssim m_c \approx 1$ GeV, the running passes from the five-quark to the four-quark and finally the three-quark regime. The renormalisation group running of $S(\mu)$ in the N-flavour regime is given by its anomalous dimension γ_N

$$\frac{dS(\mu)}{d\ln\mu} = \gamma_N(\mu)S(\mu)\,, \quad \text{where} \quad \gamma_N(\mu) = \frac{1}{Z_N}\frac{dZ_N}{d\ln\mu}\,, \tag{3.22}$$

and Z_N is the renormalisation coefficient. The anomalous dimension can be expanded in powers of the QCD coupling g as

$$\gamma_N = \frac{g^2}{16\pi^2}\gamma_N^{(0)} + \frac{g^4}{(16\pi^2)^2}\gamma_N^{(1)} + \dots\,, \tag{3.23}$$

where [71]

$$\gamma_N^{(0)} = 4 \quad \text{and} \quad \gamma_N^{(1)} = -7 + \frac{4}{9}N\,. \tag{3.24}$$

Of course g also runs according to the beta function (eqn. 2.30)

$$\beta_N(\mu) = -\frac{g^3}{16\pi^2}\beta_N^{(0)} - \frac{g^5}{(16\pi^2)^2}\beta_N^{(1)} + \dots\,, \tag{3.25}$$

where

$$\beta_N^{(0)} = 11 - \frac{2}{3}N \quad \text{and} \quad \beta_N^{(1)} = 102 - \frac{24}{3}N\,. \tag{3.26}$$

Defining

$$d_N^{(0)} = \frac{\gamma_N^{(0)}}{2\beta_N^{(0)}} \quad \text{and} \quad J_N = \frac{\gamma_N^{(1)}}{2\beta_N^{(0)}} - \frac{d_N^{(0)}}{\beta_N^{(0)}}\beta_N^{(1)}\,, \tag{3.27}$$

and denoting $\alpha^{(N)} = \frac{g^2}{4\pi}$ in the N-flavour regime, the sum over Wilson coefficients eqn. 3.17 becomes [70][72]

$$\begin{aligned}\sum_{i,j\in\{c,t\}} \lambda_i\lambda_j S(x_i,x_j;\mu) = \quad & \left[\lambda_c^2\eta_1 S_0(x_c,x_c) + \lambda_t^2\eta_2 S_0(x_t,x_t) + 2\lambda_t\lambda_c\eta_3 S_0(x_t,x_c)\right] \\ & \times \left[\alpha_s^{(3)}(\mu)\right]^{-d_3^{(0)}} \times \left[1 + \frac{\alpha_s^{(3)}(\mu)}{4\pi}J_3\right] + \text{h.c}\,.\end{aligned} \tag{3.28}$$

Here η_i are numeric coefficients [70][72][73][74][75]:

$$\eta_1 = 1.38(20)\,, \quad \eta_2 = 0.57(1)\,, \quad \eta_3 = 0.47(4)\,, \tag{3.29}$$

where the error represents theoretical uncertainties due to leftover μ dependences at

$\mathcal{O}(\alpha_s^2)$, and at the QCD scale in the $\overline{\text{MS}}$ scheme, $\Lambda_{\overline{\text{MS}}}$ [23]. The leading order box effective vertex is then

$$\text{Box}(\Delta S = 2) = -\sum_{i,j\in\{c,t\}} \lambda_i \lambda_j \frac{G_F^2}{16\pi^2} M_W^2 S(x_i, x_j; \mu)(\bar{s}d)_{V-A}(\bar{s}d)_{V-A}\,. \tag{3.30}$$

3.1.4 The neutral kaon mixing parameter B_K

The FCNC interactions comprise the component of the Hamiltonian of the neutral kaon system (eqn. 1.21) that describes virtual intermediate states [23]:

$$\langle \bar{K}^0 | \mathcal{H}_{\text{eff}}(\Delta S = 2) | K^0 \rangle = 2 m_K M_{12}^*\,. \tag{3.31}$$

Here $\mathcal{H}_{\text{eff}}(\Delta S = 2)$ is minus the term in the effective Lagrangian (eqn. 3.30). Define the expectation value of the four-quark operator as

$$\langle (\bar{s}d)_{V-A}(\bar{s}d)_{V-A} \rangle = \frac{8}{3} B_K(\mu) f_K^2 m_K^2\,, \tag{3.32}$$

where f_K is the kaon decay constant that parameterises the decay of charged kaons to the vacuum via the axial current A_μ:

$$\langle 0 | A_\mu | K^+(k) \rangle = k_\mu f_K\,. \tag{3.33}$$

Then

$$M_{12}^* = \frac{G_F^2}{12\pi^2} B_K(\mu) f_K^2 m_K M_W^2 \sum_{i,j\in\{c,t\}} \lambda_i \lambda_j S(x_i, x_j; \mu)\,. \tag{3.34}$$

B_K is known as the *neutral kaon mixing parameter* or the *kaon bag parameter*. It is a renormalisation scheme dependent quantity that parameterises the low-energy non-perturbative component of the mixing.

It is useful to define B_K in the *Renormalisation Group Invariant* (RGI) scheme, in which it has no renormalisation scale dependence. The scheme change factor for $B_K(\mu)$ is determined as follows. The perturbative Wilson coefficients, denoted $C(\mu)$ here, are run to a high energy scale M by applying a conversion factor [76] as follows,

$$w[\mu] w^{-1}[M] C(\mu) = C(M)\,. \tag{3.35}$$

The form of w at NLO can be obtained from eqn. 3.28:

$$w[\mu] = \left(\alpha_s^{(3)}(\mu)\right)^{-d_3^{(0)}} \left(1 + \frac{\alpha_s^{(3)}(\mu)}{4\pi} J_3(\mu)\right)\,. \tag{3.36}$$

Here the running is typically taken from the $N_f = 3$ theory, even above the charm threshold. The product of $B_K(\mu)$ and its Wilson coefficients is renormalisation scheme independent, therefore

$$B_K(\mu)C(\mu) = B_K(\mu)w^{-1}[\mu]w[M]C(M) = \hat{B}_K\hat{C}\,, \tag{3.37}$$

where $\hat{B}_K$ and $\hat{C}$ are the bag parameter and the Wilson coefficients in the RGI scheme. Separating the components according to their scale dependence, the RGI quantities can be identified as

$$\hat{C} = w[M]C(M) \quad \text{and} \quad \hat{B}_K = B_K(\mu)w^{-1}[\mu]\,. \tag{3.38}$$

In practise, quantities matched to the RGI scheme using perturbation theory at a fixed order retain a small scale dependence due to the truncation of the perturbative series. This effect can be reduced by using perturbation theory at a higher order or by performing the matching at a higher energy at which the perturbative series converges more quickly.

Using eqn. 1.28, M_{12} can be used to determine the ϵ-parameter of indirect CP-violation. As this is very well known experimentally [29], the right-hand side of eqn. 3.34 can be solved for the Standard Model CP-violating phase δ (c.f. section 1.2.1) to a high accuracy by inserting values for $|V_{us}|$, $|V_{ub}|$, $|V_{cb}|$, m_t and B_K. Precision values of B_K are currently only attainable via lattice QCD. The determination of this parameter is the focus of sections 6.6 and 8.7.

3.2 Chiral Effective Theory

The chiral effective theory, or *chiral perturbation theory* (ChPT), attempts to describe QCD near the chiral limit (cf. section 1.1.1). In this low-energy regime, quarks are bound into hadrons and the relevant degrees of freedom are the colour-singlet pseudoscalar states. There are in fact two formulations of the chiral effective theory, describing the $SU(3)_L \times SU(3)_R \times U(1)_V$ and the $SU(2)_L \times SU(2)_R \times U(1)_V$ chiral limits. These are referred to as $SU(3)$ and $SU(2)$ ChPT respectively. The former is the interacting theory of pions and kaons, whereas the latter contains only the pions.

Both approaches to generating effective theories that were described in section 3.1.1 are *top-down* approaches, in which the low-energy theory is generated systematically by identifying and removing high-energy degrees of freedom. For the chiral effective theory, the physics is entirely non-perturbative, and the relevant low-energy degrees of freedom are composite particles that cannot be identified from the bare theory. Instead, notice that the effective Lagrangian contains all operators compatible with the symmetries

of the bare Lagrangian. Therefore, the effective theory can simply be written down and the couplings obtained by matching the effective theory to the full theory in the continuum EFT framework. This is a *bottom-up* approach. The coupling constants of the chiral effective theory are known as *low-energy constants* (LECs). These can be obtained only by matching the theory to experimental or simulated lattice data. Recent lattice simulations [1] have indicated that at next-to-leading order, $SU(3)$ ChPT does not adequately describe pion and kaon dynamics at the strange quark mass scale. The two flavour effective theory appears to provide a much better description of the pion sector, hence only this version is considered for this work. The kaon sector is included by coupling $SU(2)$ ChPT to a heavy meson effective theory, as described in section 3.2.5. In chapter 8 many of the LECs of the LO and NLO two-flavour effective Lagrangians are determined via lattice simulation.

3.2.1 The lowest order effective Lagrangian

In order to make use of the effective theory, some power counting scheme must be devised to enable the terms to be ordered according to their magnitude. For the effective theory of the weak interactions, a perturbative series was formed in terms of the small coupling G_F. In the chiral effective theory, the only small parameters are the quark masses and the external momenta (derivatives of fields). These form the basis of Weinberg's power counting scheme [77]. With the rule that a mass term M^2 is counted at the same order as two derivatives, and noting that only even powers of the momenta arise because of Lorentz invariance, the power counting assigns a dimension

$$D = 2 + \sum_{n=1}^{\infty} 2(n-1)N_{2n} + 2N_L \tag{3.39}$$

to a given diagram, where N_L is the number of loops, and N_{2n} is the number of vertices originating from the Lagrangian $\mathcal{L}_{2n}$.

The lowest order Lagrangian $\mathcal{L}_2$ contains only terms with two derivatives and one mass term. Nevertheless this still contains an infinite number of terms, as the power counting places no restrictions on the number of pion fields in a given term. Fortunately this set is restricted by the necessity of being invariant under $SU(2)_L \times SU(2)_R$. A compact form of $\mathcal{L}_2$ can be written in terms of the variable $U(x) = \exp\left(2i\frac{\phi(x)}{f}\right)$, where the LEC f has mass dimension unity and

$$\phi = \exp\left\{i\frac{1}{\sqrt{2}}\phi_i\sigma_i\right\} = \frac{1}{\sqrt{2}}\begin{pmatrix} \phi_3 & \phi_1 - i\phi_2 \\ \phi_1 + i\phi_2 & -\phi_3 \end{pmatrix} = \begin{pmatrix} \pi^0/\sqrt{2} & \pi^+ \\ \pi^- & -\pi^0/\sqrt{2} \end{pmatrix}. \tag{3.40}$$

Here σ_i are the Pauli matrices. Under the group element $g = (R, L) \in SU(2)_L \times$

$SU(2)_R$, this transforms as $U \to RUL^\dagger$.

For a degenerate up/down quark mass m_l, the leading order Lagrangian $\mathcal{L}_2$ has the form

$$\mathcal{L}_2 = \frac{f^2}{8}\mathrm{Tr}\left(\partial_\mu U \partial^\mu U^\dagger\right) + \frac{f^2}{8}\mathrm{Tr}\left(\hat{\chi}U^\dagger + U\hat{\chi}^\dagger\right), \quad \text{where} \quad \hat{\chi} = 2B\,\mathrm{diag}(m_l, m_l)\,. \tag{3.41}$$

The trace over the terms containing only U ensures the invariance under $SU(2)_L \times SU(2)_R$. The quark mass terms have been introduced as explicit symmetry breaking parameters with a magnitude proportional to the quark mass, as discussed in section 1.1.2. Here B is a LEC of mass dimension unity. These terms are not invariant under $SU(2)_L \times SU(2)_R$ by construction.

Here the conventions for ϕ and f are those of ref.[1]. In these conventions the LEC f, which is the LO value of the pion decay constant (defined in sec. 1.1.2), is defined such that $f_\pi \sim 130$ MeV. Other conventions use $F = \frac{1}{\sqrt{2}}f$ giving $F_\pi \sim 90$ MeV [78].

3.2.2 The NLO chiral Lagrangian

The chiral Lagrangian $\mathcal{L}_4$ at $\mathcal{O}(p^4)$ can be derived by considering all products of U, $\partial_\mu U$ and $\hat{\chi}$ at this order in the power counting, and winnowing those based on chiral symmetry, Lorentz invariance and parity. The result is [79]

$$\begin{aligned}\mathcal{L}_4 = \;& l_1\left\{\mathrm{Tr}\left[\partial_\mu U(\partial^\mu U)^\dagger\right]\right\}^2 + l_2\mathrm{Tr}\left[\partial_\mu U(\partial_\nu U)^\dagger\right]\mathrm{Tr}\left[\partial^\mu U(\partial^\nu U)^\dagger\right] \\ & + l_3\mathrm{Tr}\left[\partial_\mu U(\partial^\mu U)^\dagger\partial_\nu U(\partial^\nu U)^\dagger\right] + l_4\mathrm{Tr}\left[\partial_\mu U(\partial^\mu U)^\dagger\right]\mathrm{Tr}\left(\hat{\chi}U^\dagger + U\hat{\chi}^\dagger\right) \\ & + l_5\mathrm{Tr}\left[\partial_\mu U(\partial^\mu U)^\dagger\left(\hat{\chi}U^\dagger + U\hat{\chi}^\dagger\right)\right] + l_6\left[\mathrm{Tr}\left(\hat{\chi}U^\dagger + U\hat{\chi}^\dagger\right)\right]^2 \\ & + l_7\left[\mathrm{Tr}\left(\hat{\chi}U^\dagger - U\hat{\chi}^\dagger\right)\right]^2 + l_8\mathrm{Tr}\left(\hat{\chi}U^\dagger\hat{\chi}U^\dagger + U\hat{\chi}^\dagger U\hat{\chi}^\dagger\right) + h_2\mathrm{Tr}\left(\chi^\dagger\chi\right),\end{aligned} \tag{3.42}$$

where l_i are the NLO low-energy constants and terms coupling U to external fields [78] have been ignored.

3.2.3 Calculation of the pion mass at NLO

As an example of a calculation in the chiral effective theory, this section contains a full re-derivation of the mass of the neutral pion $\pi^0 = \phi_3$ at next-to-leading order. This is obtained from the self-energy corrections to the pion propagator.

At $\mathcal{O}(p^4)$, Weinberg's power counting equation (with $D = 4$) gives

$$4 = 2 + 2N_L + 2N_4\,, \tag{3.43}$$

where N_L is the number of loops and N_4 is the number of vertices from $\mathcal{L}_4$. Here the

terms in $N_{2n} = N_6 \ldots$ have been set to zero as the coefficients $2n-2$ for $n > 2$ cannot satisfy the equation for positive integer N_{2n}. The coefficient of N_2 is always zero. As a result, at $\mathcal{O}(p^4)$ the pion self-energy contains tree-level and 1-loop diagrams from $\mathcal{L}_2$ ($N_L = 1, N_4 = 0$) and tree-level diagrams from $\mathcal{L}_4$ ($N_L = 0, N_4 = 1$).

Tree-level corrections from $\mathcal{L}_2$

Expanding $\mathcal{L}_2$ in U up to fourth order,

$$U = \mathbb{I} + \left(2i\frac{\phi}{f}\right) + \frac{1}{2!}\left(2i\frac{\phi}{f}\right)^2 + \frac{1}{3!}\left(2i\frac{\phi}{f}\right)^3 + \frac{1}{4!}\left(2i\frac{\phi}{f}\right)^4 + \mathcal{O}(\phi^5)\,, \tag{3.44}$$

and keeping only the terms containing two ϕ_3 fields, one obtains the standard kinetic and mass terms,

$$\mathcal{L}_2^{\text{free}} = \frac{1}{2}\partial_\mu\phi_3\partial^\mu\phi_3 - \frac{1}{2}\chi_l\phi_3^2\,, \tag{3.45}$$

and a set of interaction terms which will be discussed shortly. Here

$$(m_{\phi_3})^2_{\mathcal{O}(p^2)} = \chi_l \equiv 2Bm_l \tag{3.46}$$

is the square of the neutral pion mass at leading order. The same terms arise for the other components of ϕ, thus the Goldstone bosons are degenerate. In this thesis, the (unitary) pion mass with light quarks of mass m_l is denoted m_{ll} in order to be consistent with the notation of section 3.2.4.

The degeneracy of the pion masses at leading order is retained even when the quark mass degeneracy is broken. Modifying the mass matrix $\hat{\chi} \to 2B\,\text{diag}(m_u, m_d)$, the masses become

$$(m_{ud})^2_{\mathcal{O}(p^2)} = \frac{1}{2}(\chi_u + \chi_d) = B(m_u + m_d)\,. \tag{3.47}$$

For simplicity and for use in current lattice simulations, the remainder of this calculation is performed with degenerate quarks.

1-loop corrections from $\mathcal{L}_2$

When considering corrections to the pion propagator, only one-particle irreducible diagrams need be considered. At one-loop these are tadpole diagrams,

$$-i\Sigma_{\mathcal{L}_2}(p^2) = \Bigg($$ 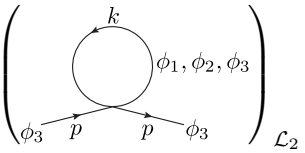

$$\Bigg)_{\mathcal{L}_2}\,, \tag{3.48}$$

where p is the momentum of the incoming and outgoing ϕ_3 particles and k is the loop momentum. The loop can contain any of the three components of $\vec{\phi}$.

The four-point terms containing two ϕ_3 fields are separated according to their field content as

$$V_{3333} \equiv \frac{1}{12f^2}\chi_l\phi_3^4 \tag{3.49}$$

and

$$V_{33jj} \equiv \frac{1}{3f^2}\Big(-(\partial_\mu\phi_3)^2\phi_j^2 - \phi_3^2(\partial_\mu\phi_j)^2 + 2(\partial_\mu\phi_3)\phi_3(\partial^\mu\phi_j)\phi_j + \frac{1}{2}\chi_l\phi_3^2\phi_j^2\Big)\,. \tag{3.50}$$

Momentum-space Feynman rules are derived following the standard procedure of multiplying by i, replacing partial derivatives $\partial_\mu\phi_i(p_i)$ with $-ip_i$ and symmetrising over permutations of like fields. All momenta are considered to be flowing towards the vertex. The results are

$V_{3333} \quad \rightarrow$ 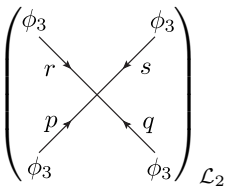

$= \dfrac{2i}{f^2}\chi_l\,,$

and

$V_{33jj} \quad \rightarrow$ 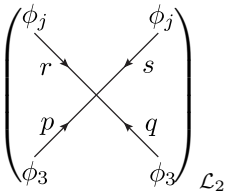

$= \dfrac{4i}{3f^2}\left(p\cdot q + r\cdot s - \dfrac{1}{2}(p+q)_\mu(r+s)^\mu + \dfrac{1}{2}\chi_l\right).$

(3.51)

Here the index $j \in \{1, 2\}$. The first diagram contains a symmetry factor of 4! from the number of ways of associating a field ϕ_3 with a leg of the vertex. Symmetry factors of 4 arise from the 2×2 ways of arranging the fields in the first, second and last term of the second diagram in a similar way.

Setting $q = -p$ and $r = -s = k$ in the Feynman rules, and employing the fact that the ϕ field propagators are identical, the three diagrams of eqn. 3.48 can be combined to give

$$-i\Sigma_{\mathcal{L}_2}(p^2) = \frac{-8}{3f^2}\int\frac{d^4k}{(2\pi)^4}\frac{1}{k^2-\chi_l}\left(-p^2-k^2+\frac{5}{4}\chi_l\right). \tag{3.52}$$

Following the continuum EFT prescription, the integral is dimensionally regularised by generalising to $d = 4 - \epsilon$ dimensions, where ϵ is small. After a Wick rotation $p_0 \rightarrow$

$-ip_0$, $p^2 \to -p^2$ to Euclidean space, the dimensionally regularised mass correction is

$$-i\Sigma^{(d)}_{\mathcal{L}_2}(p^2) = \frac{-8i}{3f^2}\left(\int \frac{d^dk}{(2\pi)^d}\frac{\left(p^2+\frac{5}{4}\chi_l\right)}{k^2+\chi_l} + \int \frac{d^dk}{(2\pi)^d}\frac{k^2}{k^2+\chi_l}\right). \tag{3.53}$$

Transforming to d-spherical coordinates, the integral in the first term assumes the form

$$\int \frac{d^dk}{(2\pi)^d}\frac{1}{k^2+\chi_l} = \int d\Omega_d \int \frac{dl}{(2\pi)^d}\frac{l^{d-1}}{l^2+\chi_l}\,. \tag{3.54}$$

Defining $x = \dfrac{\chi_l}{l^2+\chi_l}$ such that $l^2 = \chi_l(\dfrac{1}{x}-1)$ and $dl = -\dfrac{(l^2+\chi_l)^2}{2l\chi_l}dx$, eqn. 3.54 becomes

$$\frac{-1}{2(2\pi)^d\chi_l^{1-\frac{d}{2}}}\int d\Omega_d \int_0^1 dx\, x^{-\frac{d}{2}}(1-x)^{\frac{d}{2}-1}\,, \tag{3.55}$$

which contains the the *beta function*, defined as

$$B(\alpha,\beta) \equiv \int_0^1 dx x^{\alpha-1}(1-x)^{\beta-1} = \frac{\Gamma(\alpha)\Gamma(\beta)}{\Gamma(\alpha+\beta)}\,. \tag{3.56}$$

Here Γ is the *gamma function*, which continues the definition of the factorial function to non-integers. The angular integral is a standard result:

$$\int d\Omega_d = \frac{2(\pi)^{\frac{d}{2}}}{\Gamma(\frac{d}{2})}\,. \tag{3.57}$$

Equation 3.55 therefore integrates to

$$\frac{-1}{(4\pi)^{\frac{d}{2}}\chi_l^{1-\frac{d}{2}}}\Gamma(1-\frac{d}{2})\,, \tag{3.58}$$

where the identity $\Gamma(1) = 0! = 1$ has been used. Replacing d with $4-\epsilon$ and expanding $\Gamma(-1+\frac{\epsilon}{2})$ about its pole at -1, this reduces to

$$\Gamma(-1+\frac{\epsilon}{2}) = -\frac{2}{\epsilon}+\gamma-1+\mathcal{O}(\epsilon)\,. \tag{3.59}$$

Using $X^\epsilon = 1+\epsilon\log(X)+\mathcal{O}(\epsilon^2)$ and introducing the *chiral scale* Λ_χ to maintain the canonical dimensionality of the couplings, eqn. 3.59 becomes

$$\frac{-\chi_l}{(4\pi)^2}\underbrace{\left(-\frac{2}{\epsilon}+\gamma-1-\log 4\pi+\log\frac{\chi_l}{\Lambda_\chi^2}+\mathcal{O}(\epsilon)\right)}_{\mathrm{I}(\chi_l,\Lambda_\chi,\epsilon)}\,. \tag{3.60}$$

Transforming back to Minkowski space $p^2 \to -p^2$, the first term on the right of eqn. 3.53 becomes

$$\frac{-8i}{3f^2}\int \frac{d^dk}{(2\pi)^d}\frac{\left(p^2+\frac{5}{4}\chi_l\right)}{k^2+\chi_l} = \frac{8i\chi_l\left(-p^2+\frac{5}{4}\chi_l\right)}{3(4\pi)^2f^2}\mathrm{I}(\chi_l,\Lambda_\chi,\epsilon)\,. \tag{3.61}$$

Treating the second integral term of eqn. 3.53 as above and using

$$\Gamma(-2+\epsilon) = \frac{1}{\epsilon} - \frac{1}{2}\gamma + \frac{3}{4} + \mathcal{O}(\epsilon)\,, \tag{3.62}$$

gives

$$\int \frac{d^dk}{(2\pi)^d}\frac{k^2}{k^2+\chi_l} = \frac{\chi_l^2}{(4\pi)^2}I(\chi_l,\Lambda_\chi,\epsilon)\,. \tag{3.63}$$

Combining this with eqn. 3.61, the one-loop self-energy correction of eqn. 3.53 reduces to

$$-i\Sigma_{\mathcal{L}_2}(p^2) = \frac{i\chi_l}{3(4\pi)^2f^2}I(\chi_l,\Lambda_\chi,\epsilon)\left(\chi_l-4p^2\right)\,. \tag{3.64}$$

Here an overall symmetry factor of $\frac{1}{2}$ has been applied, which arises from the fact that for any choice of two legs A and B to form the loop, there are two identical assignments: $A \leftrightarrow B$ and $B \leftrightarrow A$, which have until now been overcounted.

Tree-level corrections from $\mathcal{L}_4$

Expanding U in eqn. 3.42 up to second order in ϕ, keeping only the two-point interactions of ϕ_3, and applying the rules expounded in the previous section, one finds a two-point vertex with the Feynman rule

$$\Big(\ \phi_3 \xrightarrow{\quad p \quad} \phi_3\ \Big)_{\mathcal{L}_4} = \frac{16i\chi_l}{f^2}\left[p^2\left(l_5+2l_4\right)-2\chi_l\left(2l_6+l_8\right)\right] = -i\Sigma_{\mathcal{L}_4}(p^2)\,, \tag{3.65}$$

which forms the $\mathcal{L}_4$ correction to the self-energy.

Calculation of the pion mass

The corrections to the self-energy can be considered as an additive renormalisation of the pole mass in the dressed propagator. This has the form

$$\frac{1}{k^2-m_{ll}^2}, \quad \text{where} \quad m_{ll}^2 = \chi_l - \Sigma(m_{ll}^2)\,. \tag{3.66}$$

Here $\Sigma(m_{ll}^2)$ is the sum over the corrections arising from 1-PI connected diagrams evaluated at $p^2 = m_{ll}^2$. In the previous two subsections, Σ has been calculated to order p^4. The solutions have the form

$$\Sigma(p^2) = A + Bp^2\,, \tag{3.67}$$

where

$$A = \frac{-\chi_l^2}{3(4\pi)^2 f^2} I(\chi_l, \Lambda_\chi, \epsilon) + \frac{32\chi_l^2}{f^2}\left(2l_6 + l_8\right) \tag{3.68}$$

and

$$B = \frac{4\chi_l}{3(4\pi)^2 f^2} I(\chi_l, \Lambda_\chi, \epsilon) - \frac{16\chi_l}{f^2}\left(l_5 + 2l_4\right) . \tag{3.69}$$

Thus

$$\begin{aligned}(m_{ll}^2)_{\mathcal{O}(p^4)} &= \chi_l(1+B) + A \\ &= \chi_l\Big(1 + \frac{16\chi_l}{f^2}(2l_8 - l_5) + \frac{32\chi_l}{f^2}(2l_6 - l_4) \\ &\quad + \frac{\chi_l}{(4\pi)^2 f^2} I(\chi_l, \Lambda_\chi, \epsilon)\Big) ,\end{aligned} \tag{3.70}$$

with

$$I(\chi_l, \Lambda_\chi, \epsilon) = \left(-\frac{2}{\epsilon} + \gamma - 1 - \log 4\pi + \log\frac{\chi_l}{\Lambda_\chi^2} + \mathcal{O}(\epsilon)\right) \tag{3.71}$$

as before. Defining renormalised LECs in the $\overline{\text{MS}}$-scheme as

$$l_i^r = l_i - \frac{\Gamma_i}{2(4\pi)^2}\left(-\frac{2}{\epsilon} + \gamma - 1 - \log 4\pi\right) , \tag{3.72}$$

where Γ_i are rational coefficients, the NLO pion mass obtains its standard form

$$(m_{ll}^2)_{\mathcal{O}(p^4)} = \chi_l\left\{1 + \frac{16\chi_l}{f^2}(2l_8^r - l_5^r) + \frac{32\chi_l}{f^2}(2l_6^r - l_4^r) + \frac{\chi_l}{(4\pi)^2 f^2}\log\frac{\chi_l}{\Lambda_\chi^2}\right\} . \tag{3.73}$$

The coefficients Γ_i for $i = \{4, 5, 6, 8\}$ can be calculated by considering three other processes at $\mathcal{O}(p^4)$ in the chiral expansion. They can be found in ref. [80]. For the remainder of this work, the $\mathcal{O}(p^4)$ subscript is dropped from NLO formulae, as is the superscript r denoting renormalised LECs.

For later use, the equivalent formula for the pseudoscalar decay constant f_{ll} is [1]

$$f_{ll} = f\left\{1 + \frac{16}{f^2}l_4\chi_l + \frac{8}{f^2}l_5\chi_l - \frac{2\chi_l}{(4\pi)^2 f^2}\log\frac{\chi_l}{\Lambda_\chi^2}\right\} . \tag{3.74}$$

3.2.4 Partially-quenched ChPT

Partial-quenching refers to the procedure of varying the valence quark masses independently of the sea quark masses. This is clearly unphysical as the resulting theory is not unitary. It also results in double-poles in the quark propagators [81]. Nevertheless, the *unitary points* at which the sea and valence masses are equal 'anchor' the partially-quenched theory to the physical theory. The partially-quenched theory can thus be used to quantitatively extract information about the physical theory. This is very useful in lattice simulations as it is relatively cheap to generate partially-quenched data.

A partially-quenched theory can be formed as follows. Consider extending single-

flavour QCD with an extra 'valence quark' field q_V of mass m_V and labelling the existing quark fields as 'sea quarks' q_S of mass m_S. Then

$$\begin{aligned} Z_{PQ} &= \int \mathcal{D}A\mathcal{D}\bar{q}_V\mathcal{D}q_V\mathcal{D}\bar{q}_S\mathcal{D}q_S \exp\left\{ i\int \mathcal{L}_{PQ}\right\}, \text{ and} \\ \mathcal{L}_{PQ} &= S_{\text{gauge}}(A) + \bar{q}_V(\not{D}+m_V)q_V + \bar{q}_S(\not{D}+m_S)q_S\,. \end{aligned} \tag{3.75}$$

Momentarily ignoring the gauge action, the Euclidean-space integral over the valence quark fields simply generates a factor of the determinant,

$$\int \mathcal{D}\bar{q}_V\mathcal{D}q_V \exp\left\{ -\int \bar{q}_V(\not{D}+m_V)q_V\right\} = \text{Det}(\not{D}+m_V)\,, \tag{3.76}$$

which can be cancelled using Morel's trick [82] of introducing a commuting spin-1/2 *ghost field* $\tilde{q}_V$ into the action as

$$\mathcal{L}_{PQ} \to \mathcal{L}_{PQ} + \tilde{q}_V^\dagger(\not{D}+m_V)\tilde{q}_V\,, \tag{3.77}$$

and using the property

$$\int \mathcal{D}\tilde{q}_V^\dagger\mathcal{D}\tilde{q}_V \exp\left\{ -\int \tilde{q}_V^\dagger(\not{D}+m_V)\tilde{q}_V\right\} = \frac{1}{\text{Det}(\not{D}+m_V)}\,. \tag{3.78}$$

The path integral Z_{PQ} (with the ghost fields included) reproduces that of QCD after integrating out the quark and ghost fields [83].

The symmetries of the partially-quenched Lagrangian are similar to those of QCD. Specifically, for the N flavour theory with N_V valence quarks it has an $SU(N_V+N|N_V)_L \times SU(N_V+N|N_V)_R \times U(1)_V$ *graded* chiral symmetry in the limit of massless fields, which mixes both the quark and ghost fields. The group generators contain both commuting and non-commuting components. Using this symmetry a *partially-quenched chiral effective theory* can be written down, with an effective Lagrangian that is almost identical in form to eqns. 3.41 and 3.42 [83]. The perturbative form is referred to as *partially-quenched chiral perturbation theory* (PQChPT).

In PQChPT, the two flavour NLO formula for the pion mass derived in section 3.2.3 has the form

$$\begin{aligned} m_{xy}^2 &= \frac{\chi_x+\chi_y}{2}\left\{ 1 + \frac{32}{f^2}\chi_l(2l_6-l_4) + \frac{8}{f^2}(\chi_x+\chi_y)(2l_8-l_5) \right. \\ &\quad \left. + \frac{1}{(4\pi)^2 f^2}\left[\frac{\chi_x-\chi_l}{\chi_x-\chi_y}\chi_x \log\frac{\chi_x}{\Lambda_\chi^2} + \frac{\chi_y-\chi_l}{\chi_y-\chi_x}\chi_y\log\frac{\chi_y}{\Lambda_\chi^2}\right]\right\}, \end{aligned} \tag{3.79}$$

where x and y are valence quarks and l is the light sea quark. This reduces to eqn. 3.73 in the degenerate limit. Again for later use, the formula for the pseudoscalar decay

constant f_{xy} is

$$\begin{aligned} f_{xy} = \; & f\left\{1+\frac{16}{f^2}l_4\chi_l+\frac{4}{f^2}l_5(\chi_x+\chi_y)\right. \\ & -\frac{1}{2(4\pi)^2f^2}\left[(\chi_x+\chi_l)\log\frac{\chi_x+\chi_l}{2\Lambda_\chi^2}+(\chi_y+\chi_l)\log\frac{\chi_y+\chi_l}{2\Lambda_\chi^2}\right] \\ & \left.+\frac{1}{4(4\pi)^2f^2}\left[\chi_x+\chi_y-2\chi_l+\frac{2\chi_x\chi_y-\chi_l(\chi_x+\chi_y)}{\chi_y-\chi_x}\log\frac{\chi_x}{\chi_y}\right]\right\}. \end{aligned} \tag{3.80}$$

3.2.5 Coupling to the kaon sector

The aim of this section is to partially reintroduce the kaons as *heavy* degrees of freedom into the $SU(2)$ ChPT Lagrangian, limiting the vertices to those with a single incoming and outgoing kaon line.

At leading order this can be achieved by including the kaons as a pair of massive degenerate (psuedo-)scalar fields

$$\mathcal{L}_{\pi K}^{(1)} = D_\mu K^\dagger D^\mu K - M^2 K^\dagger K, \quad \text{where} \quad K = \begin{pmatrix} K^+ \\ K^0 \end{pmatrix} \quad \text{and} \quad K^\dagger = \begin{pmatrix} \bar{K}^0, K^- \end{pmatrix}. \tag{3.81}$$

Here the covariant derivative provides the coupling to the pion sector through the vector current V_μ:

$$D_\mu = \partial_\mu + V_\mu, \quad \text{where} \quad V_\mu = \frac{1}{2}\left(\xi^\dagger\partial_\mu\xi + \xi\partial_\mu\xi^\dagger\right) \quad \text{and} \quad \xi(x) = \sqrt{U(x)}\,. \tag{3.82}$$

Unlike the pion masses, which are treated as $\mathcal{O}(p^1)$, the kaon mass is treated as $\mathcal{O}(p^0)$ in the power-counting scheme.

At the next chiral order there are terms coupling the kaon bilinear to two derivatives of the pion fields and to the quark mass matrix. Again the terms are chosen to respect the underlying symmetries, except where explicitly broken (e.g. mass terms). The NLO Lagrangian can be found in ref. [84].

In this thesis, the NLO forms for the kaon mass, the kaon decay constant and the neutral kaon mixing parameter are required. These are given below.

Kaon mass

As with the pion mass in section 3.2.3, the kaon mass at $\mathcal{O}(p^4)$ obtains loop corrections from the leading order Lagrangian and tree corrections from the NLO Lagrangian.

Expanding the covariant derivative in the pion fields $V_\mu = [\phi, \partial_\mu\phi]/2f^2$, the $KK\pi\pi$ vertex at leading order has the form $K\partial_\mu K\,[\phi, \partial_\mu\phi]$. As a result, the tadpole integral is odd in the pion's loop momentum and therefore vanishes. The result at $\mathcal{O}(p^4)$ contains

just the tree-level terms from the NLO Lagrangian [1],

$$m_{lh}^2 = m^{(K)\,2}\left\{1 + \frac{\lambda_1 + \lambda_2}{f^2}\chi_l\right\} . \tag{3.83}$$

A similar formula is obtained for the partially-quenched theory:

$$m_{xy}^2 = m^{(K)\,2}\left\{1 + \frac{\lambda_1}{f^2}\chi_l + \frac{\lambda_2}{f^2}\chi_x\right\} . \tag{3.84}$$

Notice these forms do not have an explicit dependence on the heavy sea and valence quark masses, denoted m_h and m_y respectively. The dependence enters implicitly through the values the low energy constants.

Kaon decay constant

Including a coupling to the axial current [1]

$$A_\mu = \frac{i}{2}\left(\xi^\dagger\partial_\mu\xi - \xi\partial_\mu\xi^\dagger\right) , \tag{3.85}$$

the kaon decay constant, defined in eqn. 3.33, can be calculated in the unitary and partially-quenched theory. One obtains

$$\begin{aligned} f_{lh} &= f^{(K)}\left\{1 + \frac{\lambda_3 + \lambda_4}{f^2}\chi_l - \frac{3}{4(4\pi f)^2}\chi_l \log\frac{\chi_l}{\Lambda_\chi^2}\right\} , \text{ and} \\ f_{xy} &= f^{(K)}\left\{1 + \frac{\lambda_3}{f^2}\chi_l + \frac{\lambda_4}{f^2}\chi_x - \frac{1}{(4\pi f)^2}\left[\frac{\chi_x + \chi_l}{2}\log\frac{\chi_x + \chi_l}{2\Lambda_\chi^2} + \frac{\chi_l - 2\chi_x}{4}\log\frac{\chi_x}{\Lambda_\chi^2}\right]\right\} , \end{aligned} \tag{3.86}$$

where again the LECs are implicitly dependent on m_h and m_y.

Neutral kaon mixing parameter

Following ref. [1], a $\Delta S = 2$ effective operator is introduced at leading order. This has the form

$$\mathcal{O}_{ab} = 2\beta(\xi K)_{\{a}(\xi K)_{b\}} , \tag{3.87}$$

which is symmetrised over the flavour indices a and b. Here β is a low energy constant. The neutral kaon mixing matrix element is then determined as $\langle\bar{K}^0|\mathcal{O}_{dd}|K^0\rangle$. Using eqn. 3.32, this evaluates to $\frac{8}{3}m_K^2 f_K^2 B_{PS}^{(K)}$ at tree-level, where $B_{PS}^{(K)}$ is the leading order value of B_K. Expanding the unitary and partially-quenched theories in the fields to

NLO gives

$$\begin{aligned} B_{lh} &= B_{PS}^{(K)} \left\{ 1 + \frac{b_1 + b_2}{f^2} \chi_l - \frac{\chi_l}{32\pi^2 f^2} \log \frac{\chi_l}{\Lambda_\chi^2} \right\}, \text{ and} \\ B_{xh} &= B_{PS}^{(K)} \left\{ 1 + \frac{b_1}{f^2} \chi_l + \frac{b_2}{f^2} \chi_x - \frac{\chi_l}{32\pi^2 f^2} \log \frac{\chi_x}{\Lambda_\chi^2} \right\}. \end{aligned} \tag{3.88}$$

Chapter 4

Lattice Methods

Lattice QCD is a formulation of quantum chromodynamics upon a discretised Euclidean space-time. In this realisation, the path integral is equivalent to a Boltzmann distribution with the discretised action as the Boltzmann weight. This system can be simulated using Monte Carlo statistical techniques. Lattice methods are at present the only systematically improvable means by which the low energy structure of QCD can be investigated.

This chapter introduces the Domain Wall Fermion (DWF) formulation of Lattice QCD and the techniques whereby Green's functions can be measured on the lattice. Under analytic continuation to Euclidean space, the formerly oscillatory behaviour of Minkowski-space Green's functions becomes exponential decay, allowing the lightest propagating states to be picked out at large Euclidean times. This allows for the determination of a number of physical quantities, including pseudoscalar masses and decay constants, and the neutral kaon mixing parameter B_K.

4.1 Discretising the action

4.1.1 Naive discretisation and the Wilson Action

In Euclidean space, the gamma matrices γ_E are Hermitian, and are related to the Minkowski gamma matrices γ as $\gamma_E^4 = \gamma_0$ and $\gamma_E^j = i\gamma^j \, \forall j \in \{1, 2, 3\}$. Under a Wick rotation $x^0 \to -ix_E^4$, the Minkowski-space free-fermion action,

$$S = \int d^4x \bar{\psi}(x)(\gamma^\mu \partial_\mu - m)\psi(x)\,, \tag{4.1}$$

becomes

$$S_E = -iS = \int d^4x_E \bar{\psi}(x_E)(\gamma_E^\mu \partial_{E\,\mu} + m)\psi(x_E)\,. \tag{4.2}$$

For the remainder of this work, the subscript E on Euclidean quantities is dropped unless the situation is ambiguous. The Euclidean action (formerly S_E) can be discretised by replacing the continuous integral over space-time with a sum over lattice sites and discretising the partial derivative. The simplest discretised derivative that

preserves the anti-Hermiticity of the $\partial\!\!\!/$ operator is

$$\partial_\mu \psi(x) \to \sum_y \frac{1}{2a} \left(\delta_{x+a\hat{\mu},y} - \delta_{x-a\hat{\mu},y}\right) \psi(y)\,, \tag{4.3}$$

where a is the lattice spacing and $\hat{\mu}$ is a unit vector in the μ direction. The discretised Euclidean free-fermion action is therefore

$$S = a^4 \sum_{x,y} \bar{\psi}(x) \mathcal{G}^{-1}(x,y) \psi(y) \quad \text{where} \quad \mathcal{G}^{-1}(x,y) = \tfrac{1}{2a} \textstyle\sum_\mu \left(\delta_{x+a\hat{\mu},y} - \delta_{x-a\hat{\mu},y}\right) + m\delta_{x,y} \tag{4.4}$$

is the inverse propagator in position space. In momentum space the action has the form

$$S = \int \frac{d^4p}{(2\pi)^4} \mathcal{G}^{-1}(p) \bar{\psi}(p) \psi(-p)\,, \quad \text{where} \quad \mathcal{G}(p) = \frac{-i \sum_\mu \frac{1}{a} \gamma^\mu \sin a p_\mu + m}{\frac{1}{a^2} \sum_\mu \sin^2 a p_\mu + m^2}\,, \tag{4.5}$$

and the momentum integral is performed over the Brillouin zone $-\pi/a$ to π/a. $\mathcal{G}(p)$ is the discretised propagator in momentum space. The poles of the propagator correspond to the on-shell physical states of the system. These occur when

$$-\frac{1}{a^2} \sin^2 a p_4 = m^2 + \frac{1}{a^2} \sum_i \sin^2 a p_i\,, \tag{4.6}$$

for $i \in \{1,2,3\}$. At a fixed momentum, the sine terms $\frac{1}{a^2} \sin^2 a p_\mu \to p_\mu^2$ as $a \to 0$, and the energy-momentum relation is restored to its (Euclidean) continuum form, $-E^2 = \vec{p}^2 + m^2$. However, due to the periodicity of the energy-momentum relation as $p_\mu \to p_\mu + \pi$, there are degenerate physical states known as *doublers* residing in the corners of the Brillouin zone. In an interacting theory these states can be pair produced and will therefore affect the dynamics.

The doublers can be decoupled from the theory by giving them a mass proportional to the inverse lattice spacing. The result is the Wilson action [85]:

$$\begin{aligned} S_W \quad = a^4 \sum_x \Bigg\{ \left(m + \frac{4r}{a}\right) \bar{\psi}(x)\psi(x) - \frac{1}{2a} \sum_\mu \Big(& \bar{\psi}(x + a\hat{\mu})[r + \gamma_\mu]\psi(x) \\ & + \bar{\psi}(x - a\hat{\mu})[r - \gamma_\mu]\psi(x) \Big) \Bigg\}\,, \end{aligned} \tag{4.7}$$

where r is the *Wilson parameter*. The terms proportional to r comprise the *Wilson term*. In the continuum limit this term becomes the dimension-5 operator $\frac{ar}{2} \bar{\psi}(x) \Box \psi(x)$ which is an irrelevant operator that vanishes linearly in a. Unfortunately the Wilson action does not possess the chiral symmetry at $m = 0$ that is essential for the description of the low energy dynamics of QCD. Before discussing improved actions that go some

way towards remedying this problem, it is expedient to introduce interactions into the lattice theory.

4.1.2 Interacting lattice theories

As discussed in section 1.1, QCD is associated with a local invariance under the $SU(3)_C$ gauge group. Under a gauge transformation $\psi(x) \to e^{i\theta^a(x)t^a}\psi(x)$, the partial derivative in the kinetic term of the Lagrangian generates an additional term $i\partial_\mu\theta^a t^a$, which is cancelled by a corresponding transformation to the gauge fields,

$$A^a_\mu \to A^a_\mu - \frac{1}{g}\partial_\mu\theta^a - f^{abc}\theta^b A^c_\mu \,. \tag{4.8}$$

In a sense the gauge fields communicate the gauge transformation across the infinitesimal separation of the partial derivative. They act as *parallel transporters*. In the discretised theory, the partial derivative (eqn. 4.3) is non-local, and thus the parallel transporters, or *gauge links*, between neighbouring sites must also be non-local. Their form can be determined by considering a two-point non-local term under a gauge transformation:

$$\bar\psi(x)\psi(x+a\hat\mu) \to \bar\psi(x)e^{-i\theta^a(x)t^a}e^{i\theta^a(x+a\hat\mu)t^a}\psi(x+a\hat\mu)\,. \tag{4.9}$$

This can be made gauge invariant by bridging the gap with a gauge link of the form

$$U_\mu(x, x+a\hat\mu) \equiv \mathcal{P}e^{ig\int_x^{x+a\hat\mu} dz_\mu A^b_\mu(z)t^b}\,, \tag{4.10}$$

where $\mathcal{P}$ indicates that the exponential is path-ordered, such that

$$\bar\psi(x)\psi(x+a\hat\mu) \to \bar\psi(x)U_\mu(x, x+a\hat\mu)\psi(x+a\hat\mu)\,, \tag{4.11}$$

with A^b_μ transforming according to eqn. 4.8. When a is small, the link reduces to a simpler form,

$$U_\mu(x) \equiv e^{igaA^b_\mu(x)t^b}\,, \tag{4.12}$$

which spans the gap between the neighbouring lattice sites at x and $x+\hat\mu$.

The gauge field action is formed from gauge-invariant path-ordered products of link variables known as *Wilson loops*. The simplest Wilson loop is the 1×1 *plaquette*,

$$U_{\mu\nu}(x) = U_\mu(x)U_\nu(x+a\hat\mu)U^\dagger_\mu(x+a\hat\nu)U^\dagger_\nu(x)\,, \tag{4.13}$$

from which the gauge action can be formed as

$$S_G = \beta \mathrm{tr} \sum_{\mu<\nu} \sum_x \left[1 - \frac{1}{2} \left(U_{\mu\nu}(x) + U^\dagger_{\mu\nu}(x) \right) \right] . \tag{4.14}$$

The plaquette can be rewritten as $U_{\mu\nu} = \exp\left\{ iga^2 \mathcal{F}^a_{\mu\nu} t^a \right\}$. In the limit $a \to 0$, the tensor $\mathcal{F}^a_{\mu\nu}$ reduces to the QCD field strength tensor $F^a_{\mu\nu}$ of eqn. 1.3. With this identity, the gauge action in the continuum limit assumes the usual form (eqn. 1.1), and the coupling β can be identified as $\beta = \frac{6}{g^2}$. Note the factor a^4 obtained by expanding the plaquette to second order becomes the Jacobian in the continuum limit $a^4 \sum_x \to \int d^4x$.

At non-zero lattice spacing, the lattice field strength tensor $\mathcal{F}_{\mu\nu}$ contains derivative terms in A_μ that are $\mathcal{O}(a^2)$. These correspond to irrelevant operators of the UV fixed point. In the plaquette action, these terms share the coupling β with the relevant $F^2_{\mu\nu}$ term. As a result, a simulation of one-flavour QCD using the plaquette action at finite lattice spacing corresponds to a point in coupling-space that lies off the (g, m) plane. The RG flow from this point converges asymptotically to the renormalised trajectory, which flows in the (g, m) plane in the vicinity of the UV fixed point and defines the continuum physics. At a finite scale $\mu < a^{-1}$, the simulation point in coupling-space is separated from the continuum flow by a small distance. For physics at the scale μ, this results in discrepancies from the continuum physics known as *lattice artefacts*. These include chiral symmetry breaking effects in domain wall fermions [86] (cf. next section). Of course if $\mu \ll a^{-1}$, the flow is very close to the renormalised trajectory and the lattice artefacts are small. As a result, having $a\Lambda_{QCD} \ll 1$ is a requirement for the good description of low-energy dynamics.

More complicated gauge invariant quantities can be formed by including Wilson Loops of other forms. The next simplest Wilson loop to the plaquette is the 1×2 *rectangle* $R_{\mu\nu}(x)$, which can be included in the gauge action as

$$S^{(2)}_G = \beta \mathrm{tr} \sum_x \left[(1 - 8c_1) \sum_{\mu<\nu} \frac{1}{2} \left(U_{\mu\nu}(x) + U^\dagger_{\mu\nu}(x) \right) + c_1 \sum_{\mu\neq\nu} \frac{1}{2} \left(R_{\mu\nu}(x) + R^\dagger_{\mu\nu}(x) \right) \right] , \tag{4.15}$$

where c_1 is a free coefficient that can be fixed by *renormalisation group improvement* (RGI), in which the coefficient is adjusted to bring the lattice action closer to renormalised trajectory in the directions of the irrelevant operators. The Iwasaki improved gauge action is defined with $c_1 = -0.331$ [87][88][89], which was obtained via a non-perturbative spin-blocking procedure. This improved action has been shown to allow sufficient gauge field topology sampling in Monte Carlo simulations while retaining good chiral properties, when used in conjunction with Domain Wall fermions [90]. As a result this action is used for the simulations analysed in chapters 6 and 8.

As a side-note, the expectation value of a Wilson Loop $W(\vec{r},t)$ of spatial side-length $\vec{r}$ and a large time extent t has the form

$$\langle W(\vec{r},t)\rangle = C(\vec{r})e^{-V(\vec{r})t}\,, \tag{4.16}$$

where $C(\vec{r})$ is some coefficient and $V(\vec{r})$ is the *static inter-quark potential*: the potential energy between a quark and anti-quark at a spatial separation $\vec{r}$. Due to confinement, it is expected that $V(\vec{r})$ will have a linear dependence on $\vec{r}$ at large separation, whereas at small separation the behaviour is expected to be the usual $1/|\vec{r}|$ dependence:

$$V(\vec{r}) = V_0 - \alpha/|\vec{r}| + \sigma|\vec{r}|\,. \tag{4.17}$$

In section 6.7 the static inter-quark potential is calculated on two sets of Domain Wall fermion ensembles, and it is shown that the behaviour is consistent with the above. From the potential, two scales, r_0 and r_1, can be defined as the separations at which the inter-quark force takes on certain values:

$$|\vec{r}|^2\frac{\partial V(\vec{r})}{\partial|\vec{r}|}\,\Big|_{|\vec{r}|=r_0} = 1.65 \quad \text{and} \quad |\vec{r}|^2\frac{\partial V(\vec{r})}{\partial|\vec{r}|}\,\Big|_{|\vec{r}|=r_1} = 1.00\,. \tag{4.18}$$

r_0 is referred to as the Sommer scale [91][93], and is commonly used in the determination of the lattice spacing. Assuming the potential has the form of eqn. 4.17, these scales can be determined as

$$r_0 = \sqrt{\frac{1.65-\alpha}{\sigma}}\,, \quad \text{and} \quad r_1 = \sqrt{\frac{1.00-\alpha}{\sigma}}\,, \tag{4.19}$$

where the coefficients are determined from a fit to the lattice data. This method is preferred by RBC&UKQCD. It is applied in section 6.7 to determine r_0 and r_1, and their continuum limits are determined in section 8.6. An alternative approach is to calculate the inter-quark force directly from the numerical derivative of the potential, from which r_0 and r_1 can be determined using eqn. 4.18 directly. Here the form of the derivative can be used to remove the leading lattice artefacts [91], but the higher order artefacts remain until a continuum extrapolation is performed. The remaining lattice artefacts result in a scatter of the data which must be smoothed over by locally interpolating the force. The scatter can be reduced by defining a 'corrected' potential [92] by combining a local interpolation of the force with a fit to the potential using the form given in eqn.4.19.

4.1.3 Domain Wall Fermions

One method of restoring the chiral symmetry is through the use of Domain Wall Fermions (DWF) [94][95], which are based on earlier work by Kaplan [96]. DWF is a formulation of lattice QCD in five dimensions, where the fifth dimension is labelled by an index s and has a finite extent L_s. The five dimensional fermion fields ψ are coupled to four dimensional gauge fields, represented by gauge links U in all five dimensions that are set to unity away from the boundaries. Five dimensional scalar fields ϕ with fermion indices, known as Pauli-Villars fields, are included in the action in order to cancel a bulk infinity arising as $L_s \to \infty$. The Domain Wall fermion action is

$$S = S_G(U) + S_F(\bar{\psi}, \psi, U) + S_{PV}(\phi^\dagger, \phi, U)\,. \tag{4.20}$$

The fermionic component of the action has the form

$$S_F = \sum_{i=1}^{3} \bar{\psi}_i \left[D^\dagger_{DWF}(M_5, m_i) D_{DWF}(M_5, m_i) \right]^{\frac{1}{2}} \psi_i\,, \tag{4.21}$$

where the Dirac matrix is

$$D^{DWF}_{x,s;y,s'}(M_5, m_f) = \delta_{s,s'} D^{\parallel}_{x,y}(M_5) + \delta_{x,y} D^{\perp}_{s,s'}(m_f) \tag{4.22}$$

and i is a flavour index. Here the discussion assumes three (or $2+1$) flavours. The component

$$D^{\parallel}_{x,y}(M_5) = \frac{1}{2} \sum_{\mu} \Big((1+\gamma_\mu) U_{x,\mu} \delta_{x+\hat{\mu},y} + (1-\gamma_\mu) U^\dagger_{y,\mu} \delta_{x-\hat{\mu},y} \Big) + (M_5 - 4)\delta_{x,y} \tag{4.23}$$

governs the behaviour in the usual four dimensions. Apart from the unconventional sign on the mass, this is the standard covariant derivative of massive Wilson fermions. This term possesses γ^5-*hermiticity*,

$$\gamma^5 D^{\parallel\,\dagger} \gamma^5 = D^{\parallel} \quad \Rightarrow \quad \gamma^5 \mathcal{G}^{\parallel\,\dagger}_{x,y} \gamma^5 = \mathcal{G}^{\parallel}_{y,x}\,, \tag{4.24}$$

which leads to the very useful property of the 4d propagator $\mathcal{G}^{\parallel}$ given on the right-hand side of the above. The component

$$D^{\perp}_{s,s'}(m_f) = \begin{cases} P_R \delta_{1,s'} - m_f P_L \delta_{L_s-1,s'} - \delta_{0,s'}, & s = 0 \\ P_R \delta_{s+1,s'} + P_L \delta_{s-1,s'} - \delta_{s,s'}, & 0 < s < L_s - 1 \\ -m_f P_R \delta_{0,s'} + P_L \delta_{L_s-2,s'} - \delta_{L_s-1,s'}, & s = L_s - 1 \end{cases} \tag{4.25}$$

governs the behaviour in the fifth dimension. Here m_f is a fermion mass, M_5 is the 'domain wall height', $P_{L/R} = \frac{1}{2}(1 \pm \gamma_5)$ are the chiral projection operators, and $U_{x,\mu} = U_\mu(x)$ are gauge links. In eqn. 4.21, the root of the square of the Dirac operator is used rather than the Dirac operator on its own for algorithmic convenience: the determinant of the Dirac matrix, which contains the fermionic contributions to the action, is unchanged by this replacement. The Pauli-Villars action is [97]

$$S_{PV} = \sum_{i=1}^{3} \phi_i^\dagger \left[D_{DWF}^\dagger(M_5, 1) D_{DWF}(M_5, 1) \right]^{\frac{1}{2}} \phi_i \,, \tag{4.26}$$

and in this thesis the gauge action is the Iwasaki improved action of eqn. 4.15.

For each quark flavour, the physical modes are a pair of left- and right-handed Weyl fermions that are bound to opposite 'walls' of the fifth dimension, $s = 0$ and $s = L_s - 1$. A triplet of four-dimensional Dirac spinors can be formed by combining the Weyl fermions as

$$q_x = P_R \psi_{x,0} + P_L \psi_{x,L_s-1} \quad \text{and} \quad \bar{q}_x = P_R \bar{\psi}_{x,L_s-1} + P_L \bar{\psi}_{x,0} \,. \tag{4.27}$$

The right and left handed modes are coupled directly via the quark masses m_i in eqn. 4.25. Additional mixing arises due to the propagation of chiral modes across the fifth dimension. Here the amplitudes of the propagators that span the fifth dimension are exponentially suppressed in L_s (apart from in the region of a near-zero mode of the Hamiltonian[90][98]) . Consequently, in the limit of $L_s \to \infty$, the massless theory possesses an exact $SU(3)_L \times SU(3)_R \times U(1)_V$ chiral symmetry. The equivalents of the axial and vector currents of eqn. 1.4 can be defined from the 5d conserved currents associated with the invariance of the DWF action under global $U(3)$ flavour transformations, that act upon the field triplet ψ in the fundamental representation. These are

$$j_\mu^a(x,s) = \frac{1}{2} \left[\bar{\psi}(x+\hat{\mu}, s)(1+\gamma_\mu) U_{x,\mu}^\dagger t^a \psi(x,s) - \bar{\psi}(x,s)(1-\gamma_\mu) U_{x,\mu} t^a \psi(x+\hat{\mu}, s) \right] . \tag{4.28}$$

There is a unique vector transformation that gives rise to a conserved 4d vector current

$$\mathcal{V}_\mu^a(x) = \sum_{s=0}^{L_s-1} j_\mu^a(x,s) \,, \tag{4.29}$$

but there are many ways to define the axial transformation that all reduce to the standard form in the continuum limit. One definition of the transformation is [95]

$$\delta_A^a \psi_{x,s} = +iQ(s) \lambda^a \psi_{x,s} \,, \quad \delta_A^a \bar{\psi}_{x,s} = -iQ(s) \bar{\psi}_{x,s} \lambda^a \,, \tag{4.30}$$

where $Q(s) = 1$ for $0 \leq x < L_s/2$ and $Q(s) = -1$ for $L_s/2 < x \leq L_s$. The associated four-dimensional axial current is

$$\mathcal{A}^a_\mu(x) = \sum_{s=0}^{L_s-1} \operatorname{sgn}\left(s - \frac{L_s - 1}{2}\right) j^a_\mu(x, s)\,. \tag{4.31}$$

In addition, local four-dimensional vector and axial currents can be defined as

$$A^a_\mu(x) = \bar{q}(x) t^a \gamma_\mu \gamma^5 q(x) \quad \text{and} \quad V^a_\mu(x) = \bar{q}(x) t^a \gamma_\mu q(x)\,, \tag{4.32}$$

which are related to $\mathcal{A}^a_\mu$ and $\mathcal{V}^a_\mu$ by multiplicative 'renormalisation factors',

$$Z_A A^a_\mu = \mathcal{A}^a_\mu\,, \quad \text{and} \quad Z_V V^a_\mu = \mathcal{V}^a_\mu\,. \tag{4.33}$$

With exact chiral symmetry the factors Z_A and Z_V are equal [99]. They are determined for two DWF simulations in section 6.2.

With finite L_s and quark masses, the chiral symmetry is broken and the now *partially-conserved axial current* (PCAC) $\mathcal{A}^a_\mu$ has a non-zero divergence [95],

$$\Delta_\mu \mathcal{A}^a_\mu(x) = 2 m_f J^a_5(x) + 2 J^a_{5q}(x)\,, \tag{4.34}$$

where

$$J^a_5(x) = -\bar{\psi}(x, L_s - 1) P_L t^a \psi(x, 0) + \bar{\psi}(x, 0) P_R t^a \psi(x, L_s - 1) = \bar{q}(x) \gamma^5 t^a q(x) \tag{4.35}$$

is the 4d pseudoscalar density, $\Delta_\mu f(x) = f(x) - f(x - \hat{\mu})$ is the left discretised derivative, and

$$J^a_{5q}(x) = -\bar{\psi}(x, L_s/2 - 1) P_L t^a \psi(x, L_s/2) + \bar{\psi}(x, L_s/2) P_R t^a \psi(x, L_s/2 - 1) \tag{4.36}$$

is the *midpoint* term. In continuum QCD, the divergence of the axial current has the same form, apart from the midpoint term which contains the finite-L_s contribution to the chiral symmetry breaking.

The effects of the chiral symmetry breaking can be understood via Symanzik's effective theory [48], which describes the effects of discretising continuum QCD in terms of an expansion in a series of irrelevant parameters of the Gaussian fixed point. In the effective Lagrangian, the leading chiral symmetry breaking appears as a dimension-3 operator, $m_{\text{res}}\,\bar{q}q$, where the coefficient is referred to as the *residual mass* [100]. The residual mass can be related to the midpoint term by the following relation [99][100],

$$J^a_{5q} = m_{\text{res}} J^a_5 - \frac{(Z_{\mathcal{A}} - 1)}{2} \Delta_\mu \mathcal{A}^a_\mu + \mathcal{O}(a)\,. \tag{4.37}$$

Inserting this into eqn. 4.34 gives

$$Z_{\mathcal{A}}\Delta_\mu \mathcal{A}^a_\mu(x) = 2(m_f + m_{\text{res}})J^a_5(x) + \mathcal{O}(a)\,. \tag{4.38}$$

This can be made equal to the continuum PCAC relation to $\mathcal{O}(a)$ by a multiplicative renormalisation of the PCAC current

$$\mathcal{A}^a_\mu \to Z_{\mathcal{A}}\mathcal{A}^a_\mu\,, \tag{4.39}$$

and an additive renormalisation of the bare quark masses

$$m_f \to m_f + m_{\text{res}}\,. \tag{4.40}$$

This removes the leading chiral symmetry breaking effects. Note that the renormalisation coefficient $Z_{\mathcal{A}}$ is not the same as the coefficient Z_A which relates the local axial current to the PCAC.

In the continuum, the PCAC current does not require renormalisation. It becomes necessary at finite L_s due to the propagation of right-handed modes via a left-handed current [99]. The standard argument [101][102][99] states that as the right-handed modes and the left-handed currents are bound to opposite boundaries of the fifth dimension, this mixing requires both the fermion and anti-fermion modes to propagate across the fifth dimension, and is thus suppressed by $e^{-2\alpha L_s} \sim m^2_{\text{res}}$ [99]. This implies that $Z_{\mathcal{A}} \approx 1$, hence the renormalisation of the PCAC is often ignored. In fact the argument above is incorrect [1]: the right-handed modes need only propagate to the midpoint in order to interact via a left-handed current, as the current is not in fact bound to the wall, but spans the entire volume of the fifth dimension between the midpoint and the left-handed boundary. As a result, the suppression is only $e^{-2\alpha L_s/2} \sim m_{\text{res}}$. The effects of this will be discussed shortly.

In practise, the residual mass cannot be measured exactly in numerical simulations. The typical solution is to measure a quantity m'_{res}, defined as

$$m'_{\text{res}} = \frac{\langle 0|J^a_{5q}|\pi\rangle}{\langle 0|J^a_5|\pi\rangle}\,. \tag{4.41}$$

This is useful for the following reason. Inserting this definition into to PCAC relation (eqn. 4.34) gives

$$m_f + m'_{\text{res}} = \frac{\langle 0|\Delta_\mu \mathcal{A}^a_\mu|\pi\rangle}{2\langle 0|J^a_5|\pi\rangle}\,. \tag{4.42}$$

The right-hand side of the above is proportional to m^2_π. Goldstone's theorem implies that this must be zero in the limit of zero quark mass, which is satisfied to all orders if

the quark masses are again redefined as

$$\tilde{m}_f = m_f + m'_{\text{res}} \,. \tag{4.43}$$

The *chiral limit* of Domain Wall fermions is therefore defined at $m_f = -m'_{\text{res}}$ rather than at $m_f = 0$. Another useful property of the definition of m'_{res} is that it includes the higher order terms in eqn. 4.37. The $\mathcal{O}(a)$ terms comprise all of the chiral symmetry breaking operators at this order in the Symanzik effective Lagrangian [99]. The theory is therefore automatically $\mathcal{O}(a)$ improved.

Inserting the definition of m'_{res} into eqn. 4.37 and using the PCAC relation gives

$$m'_{\text{res}} = \frac{1}{Z_{\mathcal{A}}}\Big(m_{\text{res}} - (Z_{\mathcal{A}} - 1)m_f\Big) + \mathcal{O}(a) \,. \tag{4.44}$$

As discussed above, the $Z_{\mathcal{A}} - 1$ term cannot be discounted. This term results in a leading order dependence of m'_{res} on the quark mass, and additional mass dependence arises in the higher order terms [99]. This behaviour has been observed in numerical simulations [103][86][104] (also see section 6.1). Unfortunately it is not possible to accurately determine $Z_{\mathcal{A}} - 1$ in current simulations due to contamination from the higher order terms [1]. It is therefore taken to be zero and a small systematic error is assigned to the axial current normalisation.

The mass dependence creates an ambiguity in the definition of m'_{res}. In this thesis, the value of m'_{res} at zero quark mass is used to renormalise all quark masses. For the remainder of this work, this quantity is referred to as m_{res}, leaving m'_{res} to specify the mass-dependent definition. The uncertainty in the definition of m'_{res} is considered as a possible source of error in chapter 8.

4.2 Simulating the theory

4.2.1 Ensemble generation

Under a Wick rotation into Euclidean space, the action picks up a coefficient of i (cf. eqn. 4.2) such that the (formerly oscillatory) discretised path integral takes on the form of a Boltzmann distribution:

$$\int \mathcal{D}\bar{\psi}\mathcal{D}\psi\mathcal{D}U \, \exp\{iS\} \rightarrow \int \mathcal{D}\bar{\psi}\mathcal{D}\psi\mathcal{D}U \, \exp\{-S_E\} \,. \tag{4.45}$$

Again, for the remainder of this section the subscript E on Euclidean quantities is dropped. The integral can be formally defined for a generic field ϕ as the product

$$\int \mathcal{D}\phi = \prod_x \int d\phi(x) \tag{4.46}$$

over lattice sites x. The Grassman-valued (anti-commuting) fermion fields are very difficult to treat on a computer. Typically these fields are formally integrated out, leaving the path integral as a function of the gauge links. The result has the generic form

$$Z = \prod_{x,\mu} \int dU_\mu \, \det D(U) \, \exp\left\{-S_G[U]\right\} \, , \tag{4.47}$$

where D is the Dirac matrix and S_G is the gauge action.

A Green's function of a general operator containing gauge fields and fermion propagators $\mathcal{G}(U) = D^{-1}(U)$, can be evaluated as

$$\langle \mathcal{O}\left(U, \mathcal{G}(U)\right)\rangle = \frac{1}{Z} \prod_{x,\mu} \int dU_\mu \, \mathcal{O}\left(U, \mathcal{G}(U)\right) \, \det D(U) \, \exp\left\{-S_G[U]\right\} \, . \tag{4.48}$$

This can be viewed as the sum over all possible configurations of the gauge fields. For a limited number N of *gauge configurations* $U_i = \{U_i(x)\} \, \forall \, x$, drawn according to the probability distribution

$$P(U_i) = \det D(U_i) \, \exp\left\{-S_G[U_i]\right\} \, , \tag{4.49}$$

an approximation to the Green's function can be obtained as

$$\langle \mathcal{O}\left(U, \mathcal{G}(U)\right)\rangle \approx \frac{1}{N} \sum_{i=1}^{N} \mathcal{O}\left(U_i, \mathcal{G}(U_i)\right) \, . \tag{4.50}$$

There are a variety of *Monte-Carlo* statistical algorithms for generating *ensembles* of gauge configurations according to eqn. 4.49. Details of these techniques are beyond the scope of this work, suffice to say that the ensembles used in later chapters were generated using the *Rational Hybrid Monte Carlo* (RHMC) algorithm [105].

4.2.2 Reweighting

Reweighting [106][107] is a technique whereby small post-simulation changes can be made to sea-quark masses. In chapter 6, the sea strange quark mass is reweighted over a range of values allowing an interpolation to the physical strange quark mass to be performed in chapter 8. An overview of the technique is given below.

After integrating the fermions out of the path integral, the dependence of a gauge

configuration upon the sea-quarks is encapsulated in the fermion determinant $\det D(U_i)$ of eqn. 4.49. Typically the determinant is rewritten as $\sqrt{\det D^\dagger D}$ for algorithmic convenience. Consider eqn. 4.50 with a single sea-quark flavour of mass m_2 and with the above modification to the determinant:

$$\langle O\rangle_2 = \frac{\int DU e^{-S_g}\sqrt{\det(D_2^\dagger D_2)}O[U]}{\int DU e^{-S_g}\sqrt{\det(D_2^\dagger D_2)}}\,. \tag{4.51}$$

Here the subscript on the Dirac matrix indexes the mass; $D_q = D[U, m_q]$. The Green's function $\langle O\rangle_2$ can be expressed in terms of Dirac matrices D_1 with a quark mass of m_1 as

$$\langle O\rangle_2 = \frac{\int DU e^{-S_g}\, w[U]\,\sqrt{\det(D_1^\dagger D_1)}O[U]}{\int DU e^{-S_g}\, w[U]\,\sqrt{\det(D_1^\dagger D_1)}}\,, \tag{4.52}$$

where

$$w[U] = \det\left(\frac{D_2^\dagger[U]D_2[U]}{D_1^\dagger[U]D_1[U]}\right)^{1/2} \equiv \det{}^{-1/2}(\Omega) \tag{4.53}$$

with $\Omega = D_2^{-1}D_1D_1^\dagger(D_2^\dagger)^{-1}$. $w[U]$ can be calculated as an expectation value over Gaussian distributed complex scalar fields ξ,

$$w[U] = \left(\frac{\int D\xi e^{-\xi^\dagger\sqrt{\Omega[U]}\xi}}{\int D\xi e^{-\xi^\dagger\xi}}\right) = \langle e^{-\xi^\dagger(\sqrt{\Omega[U]}-1)\xi}\rangle_\xi\,, \tag{4.54}$$

such that eqn. 4.52 becomes

$$\langle O\rangle_2 = \frac{\int DU D\xi e^{-S_g}\sqrt{\det(D_1^\dagger D_1)}e^{-\xi^\dagger(\sqrt{\Omega[U]}-1)\xi}e^{-\xi^\dagger\xi}O[U]}{\int DU D\xi e^{-S_g}\sqrt{\det(D_1^\dagger D_1)}e^{-\xi^\dagger(\sqrt{\Omega[U]}-1)\xi}e^{-\xi^\dagger\xi}}\,. \tag{4.55}$$

If the fields U and ξ are jointly importance sampled, the former from the distribution $e^{-S_g}\sqrt{\det(D_1^\dagger D_1)}$ and the latter from the Gaussian distribution $e^{-\xi^\dagger\xi}$, an estimate for $\langle O\rangle_2$ is obtained as

$$\langle O\rangle_2 \simeq \frac{\sum_{i=1..N}\, s_i O[U_i]}{\sum_{i=1..N}\, s_i} \tag{4.56}$$

where the *weight* $s_i[U]$ is given by

$$s_i[U_i] = \frac{1}{N_\xi}\sum_{j=1..N_\xi} e^{-\xi_j^\dagger(\sqrt{\Omega[U_i]}-1)\xi_j}\,. \tag{4.57}$$

s_i is obtained from the N_ξ samples of ξ for each gauge configuration U_i.

As the gauge fields U_i are importance sampled from a distribution depending solely

on m_1, the overlap of this set with the dominant configurations for the mass m_2 becomes less as the mass is changed. In practice this limits the range over which the reweighting can be performed.

4.2.3 Measuring Green's functions

From eqn. 4.50, a generic n-point Green's function (aka *correlation function*) $\langle \mathcal{O}(x_1, x_2, \ldots) \rangle$, for which the operator $\mathcal{O}$ contains time ordered products of quark fields and gauge links, is measured by replacing pairs of quark fields with propagators and averaging over an ensemble of gauge configurations. The standard procedure of replacing the quark fields with functional derivatives of source terms, used in chapters 2 and 3, can be simplified as follows. Using Wick's theorem [108], the time-ordered product of field variables can be rewritten in terms of *normal ordered* operators, in which all of the creation operators have been anti-commuted to the left:

$$\begin{aligned}\mathcal{T} \prod_{i=1}^{m} \prod_{j=1}^{n} \bar{\psi}(x_i)\psi(x_j) \quad = \quad & : \prod_{i=1}^{m} \prod_{j=1}^{n} \bar{\psi}(x_i)\psi(x_j) : \pm \sum_{\alpha,\beta} \overbrace{\psi(x_\alpha)\bar{\psi}}(x_\beta) : \prod_{i\neq\beta}^{} \prod_{j\neq\alpha}^{n} \bar{\psi}(x_i)\psi(x_j) : \\ & \pm \sum_{\alpha,\beta,\gamma,\delta} \overbrace{\psi(x_\alpha)\bar{\psi}}(x_\beta)\overbrace{\psi(x_\gamma)\bar{\psi}}(x_\delta) : \prod_{i\neq\beta,\delta}^{} \prod_{j\neq\alpha,\gamma}^{n} \bar{\psi}(x_i)\psi(x_j) : + \ldots ,\end{aligned} \tag{4.58}$$

where the sign of each term depends on how many times the fields were anti-commuted, $: \mathcal{O} :$ denotes the normal order of the operator $\mathcal{O}$, and

$$\overbrace{\psi(x)\bar{\psi}}(y) = \mathcal{G}(x \leftarrow y) \tag{4.59}$$

is the *Wick contraction* of the fields into the quark propagator $\mathcal{G}$. Here the replacement is made only to adjacent field operators of the same flavour. The arrow in the argument of the propagator is used to clarify the direction of propagation and the ordering of the indices. In this notation, the γ^5-hermiticity of the propagator (eqn. 4.24) is written

$$\mathcal{G}(\vec{x}, \tau \leftarrow \vec{y}, t) = \gamma^5 \mathcal{G}^\dagger(\vec{x}, \tau \rightarrow \vec{y}, t)\gamma^5 \,. \tag{4.60}$$

Here it is understood that the source indices of the conjugate propagator lie on the left and those of the unconjugated propagator on the right. This notation is used extensively in chapters 5 and 7, where the order of index contraction is important.

By definition, the normal ordered product annihilates the vacuum, therefore only completely contracted terms contribute to vacuum-vacuum Green's functions. As an example of a typical measurement, the momentum-space Green's function of

pseudoscalar bilinears (cf. table 1.1)

$$\mathcal{F}(\vec{p};t,\tau) = \sum_{\vec{x},\vec{y}} e^{-i\vec{p}\cdot(\vec{x}-\vec{y})} \langle \bar{u}(\vec{x},t)\gamma^5 s(\vec{x},t)\bar{s}(\vec{y},\tau)\gamma^5 u(\vec{y},\tau)\rangle \tag{4.61}$$

becomes

$$\mathcal{F}(\vec{p};t,\tau) = \sum_{\vec{x},\vec{y}} e^{-i\vec{p}\cdot(\vec{x}-\vec{y})} \overbrace{\bar{u}_i(\vec{x},t)\gamma^5_{ij} s_j(\vec{x},t)\bar{s}_k(\vec{y},\tau)\gamma^5_{kl} u_l(\vec{y},\tau)} \tag{4.62}$$

where the subscripts are combined spin-colour indices. Performing the Wick contractions gives

$$\begin{aligned}\mathcal{F}(\vec{p};t,\tau) &= \sum_{\vec{x},\vec{y}} e^{-i\vec{p}\cdot(\vec{x}-\vec{y})} [\mathcal{G}_u]_{li}(\vec{y},\tau \leftarrow \vec{x},t)\gamma^5_{ij}[\mathcal{G}_s]_{jk}(\vec{x},t \leftarrow \vec{y},\tau)\gamma^5_{kl} \\ &= \mathrm{tr} \sum_{\vec{x},\vec{y}} e^{-i\vec{p}\cdot(\vec{x}-\vec{y})} \mathcal{G}_u(\vec{y},\tau \leftarrow \vec{x},t)\gamma^5 \mathcal{G}_s(\vec{x},t \leftarrow \vec{y},\tau)\gamma^5 \,,\end{aligned} \tag{4.63}$$

where the trace is over spin and colour indices. Using the γ^5-hermiticity of the propagator (eqn. 4.60), $\mathcal{G}_u(\vec{y},\tau \leftarrow \vec{x},t)$ can be replaced by the conjugate propagator $\gamma^5\mathcal{G}_u^\dagger(\vec{y},\tau \rightarrow \vec{x},t)\gamma^5$ originating from $(\vec{y},\tau)$. This is exploited in chapters 5 and 6.

The pseudoscalar bilinear $\bar{s}\gamma^5 u$ in the example above has the same flavour and spin quantum numbers as the negatively charged kaon K^-, as well as a number of orbitally excited states $\{X_i\}$. As such the operator generates a state that is a linear combination of these

$$(\bar{s}\gamma^5 u)(\vec{p},t)|0\rangle = |\Psi(\vec{p},t)\rangle = a_0|K^-(\vec{p},t)\rangle + \sum_{i=1}^{\infty} a_i|X_i(\vec{p},t)\rangle \,. \tag{4.64}$$

Here

$$a_i = \langle X_i|\bar{s}(\vec{x},t)\gamma^5 u(\vec{x},t)|0\rangle \tag{4.65}$$

is a position independent amplitude.

Inserting eqn. 4.64 into the Green's function of eqn. 4.61, and applying the Euclidean time evolution operator $e^{-H(t-\tau)}$, where H is the Hamiltonian, gives

$$\mathcal{F}(\vec{p};t,\tau) = \langle\Psi(\vec{x},t)|e^{-H(t-\tau)}|\Psi(\vec{y},\tau)\rangle = |a_0|^2 e^{-E^K_{\vec{p}}(t-\tau)} + \sum_{i=1}^{\infty} |a_i|^2 e^{-E^i_{\vec{p}}(t-\tau)} \,, \tag{4.66}$$

where $E^i_{\vec{p}}$ is the energy of the state X_i of momentum $\vec{p}$. At $\vec{p}=0$, the kaon energy $E^K_{\vec{p}} \rightarrow m_K$. At large Euclidean time separations, the heavier excited states are exponentially suppressed and the lightest state, the kaon, dominates. The standard technique of extracting quantities such as m_K from the lattice follows from the above: simply numerically fit the time evolution of the corresponding zero-momentum Green's function to an exponential form (or sum of exponentials) at large lattice time

separations.

Using other interpolating operators with the same quantum numbers can increase the relative size of a chosen amplitude a_i with respect to that of the other intermediate states, increasing the signal-to-noise ratio of measurements. A more general, non-local pseudoscalar operator has the form

$$\mathcal{O}(\vec{p},\vec{q};\tau) = \sum_{\vec{x},\vec{y}} e^{i(\vec{p}\cdot\vec{x}+\vec{q}\cdot\vec{y})}\xi(\vec{x},\vec{y})\ \left(\bar{s}(\vec{x},\tau)\gamma^5\mathcal{P}[U](\vec{x},\vec{y};\tau)u(\vec{y},\tau)\right)\ . \tag{4.67}$$

Here the function $\xi(\vec{x},\vec{y})$ is dimensionless and real, and the path-ordered product of gauge links $\mathcal{P}[U](\vec{x},\vec{y};\tau)$ is required to maintain gauge invariance. The Green's function

$$\begin{aligned}\mathcal{F}(\vec{p}+\vec{q};t,\tau) &= \sum_{\vec{z}} e^{-i(\vec{p}+\vec{q})\cdot\vec{z}}\langle\bar{u}(\vec{z},t)\gamma^5 s(\vec{z},t)\mathcal{O}(\vec{p},\vec{q};\tau)\rangle \\ &= \mathrm{tr}\sum_{\vec{x},\vec{y},\vec{z}} e^{-i\vec{p}\cdot(\vec{z}-\vec{x})}e^{-i\vec{q}\cdot(\vec{z}-\vec{y})}\,\xi(\vec{x},\vec{y})\times \\ &\qquad \left(\gamma^5\mathcal{G}_u^\dagger(\vec{y},\tau\to\vec{z},t)\gamma^5\right)\gamma^5\mathcal{G}_s(\vec{z},t\leftarrow\vec{x},\tau)\mathcal{P}[U](\vec{x},\vec{y};\tau)\gamma^5\end{aligned} \tag{4.68}$$

varies with the time separation as a series of exponentials per eqn. 4.66, but now the amplitudes a_i are implicitly dependent on ξ. By varying the functional form of ξ, the relative sizes of the amplitudes can be changed to enhance a chosen intermediate state. One choice is

$$\xi(\vec{x},\vec{y}) = \begin{cases} 1 & \text{if } \vec{x},\vec{y}\in\mathcal{R}_{\mathrm{box}} \\ 0 & \text{otherwise}\,, \end{cases} \tag{4.69}$$

where the corresponding operator is referred to as a *box operator*. Here $\mathcal{R}_{\mathrm{box}}$ is a cubic region of space on the timeslice τ. Similar box interpolating operators are used in section 6.5 to improve measurements of ground-state baryon masses. If $\mathcal{R}_{\mathrm{box}}$ occupies the entire physical volume, the operator is referred to as a *wall operator*. These operators are used extensively in chapter 6 for measuring pseudoscalar quantities. In section 4.2.8 it will be shown that Green's functions containing these non-local operators can be generated using box and wall source propagators on gauge fixed configurations.

For the purpose of determining the optimal fitting range, it is useful to define a quantity known as the *effective mass*,

$$m_{\mathrm{eff}} = \log\left(\frac{\mathcal{F}(\vec{0};t,\tau)}{\mathcal{F}(\vec{0};t+1,\tau)}\right)\xrightarrow{t\to\infty} m_K\,. \tag{4.70}$$

Typical plots of the effective mass demonstrate an exponential fall followed by a plateau. The plateau indicates the region in which the time dependence (eqn. 4.66) is dominated by the leading exponential, and thus defines the range over which a fit to a single exponential should be performed. The fit range may be extended by including more

exponential terms in the fit form, but at the cost of a potential numerical instability arising from having too many fit parameters. Chapters 5 and 6 contain numerous examples of effective mass plots.

The time dependence of the series in eqn. 4.66 varies depending on the boundary conditions used in the simulation, and thus the form of eqn. 4.70 will also change. This is discussed in section 4.2.7.

4.2.4 Statistical techniques

The calculation and propagation of statistical errors through the fitting procedure can be accomplished in a number of ways. The standard techniques are the *bootstrap* and *jackknife* procedures, whereby a distribution of raw measurements $\{Y_i\,;\, i = 1 \ldots N\}$ is *resampled* to form a distribution of means $\{\bar{Y}_j\,;\, j = 1 \ldots \bar{N}\}$, from which an error on the mean can be calculated.

In the bootstrap procedure, the resampling is performed by averaging N randomly selected samples (with replacement) from $\{Y\}$. This is repeated $\bar{N}$ times to generate the distribution of mean values $\{\bar{Y}\}$:

$$\bar{Y}_j = \frac{1}{N}\sum_{k=1}^{N} \mathrm{rand}\{Y\} \quad \text{for} \quad j = 1 \ldots \bar{N}\,. \tag{4.71}$$

The upper and lower bounds of the error on the mean are calculated by sorting $\{\bar{Y}\}$ in ascending order and selecting the 16^{th} and 84^{th} percentiles respectively, which bound the 68% confidence region assuming a Gaussian distribution. For a good estimate, $\bar{N}$ needs to be large; typical values are $\mathcal{O}(500)$.

For the jackknife procedure, $\bar{Y}_j$ is calculated as

$$\bar{Y}_j = \frac{1}{N-1}\left[\left(\sum_{i=1}^{N} Y_i\right) - Y_j\right] \quad \text{for} \quad j = 1 \ldots \bar{N} = N\,, \tag{4.72}$$

which generates a resampled distribution of the same size as the distribution of raw measurements. The (assumed symmetric) error on the mean is then calculated as

$$\sigma^2 = \frac{N-1}{N}\sum_{j=1}^{N}\left(\bar{Y}_j - \langle\bar{Y}\rangle\right)^2\,, \tag{4.73}$$

where $\langle\bar{Y}\rangle$ is the average mean value.

The jackknife and bootstrap procedures are suitable for calculations involving correlated measurements on a single ensemble. Measurements on different ensembles are completely uncorrelated, thus results obtained from fits over multiple ensembles

should ideally maintain the contributions from each ensemble separately in order to avoid accidental cancellations. This can be achieved by forming a distribution $\{\bar{Y}\}$ comprising a set of sub-distributions of contributions from each ensemble:

$$\{\bar{Y}\} = \left(\{\bar{Y}^A\}, \{\bar{Y}^B\}, \ldots\right) . \tag{4.74}$$

Here the superscript $A, B \ldots$ labels the different ensembles. The error on the distribution is found by combining the errors on each sub-distribution in quadrature:

$$\sigma^2\{\bar{Y}\} = \sigma^2\{\bar{Y}^A\} + \sigma^2\{\bar{Y}^B\} + \ldots . \tag{4.75}$$

The individual sub-distributions can be resampled using either bootstrap or jackknife methods, hence $\{\bar{Y}\}$ is referred to as a *superjackboot* distribution. If only jackknife sub-distributions are involved, the distribution may be referred to as a *superjackknife*. The superjackknife technique is described clearly in refs. [109] and [110].

If a superjackboot distribution contains no contributions from a given ensemble, the elements of the corresponding sub-distribution are set equal to the central value of the distribution, such that the value is propagated correctly. As it has zero error, the sub-distribution does not contribute to the error on the distribution.

Aside from the benefit of keeping uncorrelated data sets separate, the use of superjackboot distributions allows for the combined analysis of sub-distributions of different sizes, which is particularly useful when they are jackknife resampled. As a result, superjackknife distributions are used extensively in the combined chiral-continuum extrapolation of Domain Wall QCD ensembles in chapter 8.

4.2.5 The fitting procedure

The procedure for fitting to a Green's function $\mathcal{F}$ is as follows:

1. For each gauge configuration ($U_i\,;\, i = 1 \ldots N_{\text{conf}}$), a measurement of the Green's function $\mathcal{F}_i[U_i]$ is performed.

2. Successive gauge configurations are generally correlated. Groups of correlated measurements are *binned* over (averaged), leaving a set of N_{binned} - ideally uncorrelated - measurements. The optimal bin size can be found by steadily increasing it until the error estimate stops changing.

3. Optionally, the covariance matrix is calculated from the binned data. If this is the case, the matrix is described as being *frozen*.

4. The binned distribution is resampled using the chosen procedure.

5. If an *unfrozen* covariance matrix is desired, it is calculated from the resampled distribution.

6. The fit is performed using the frozen or unfrozen covariance matrix.

The covariance matrix is the matrix of covariances between the elements of a set of measurements. For a fit to the time dependence of a Green's function, the covariances are measured between elements at different time separations t and t' from the source time τ:

$$C_{t,t'} = Z \sum_{i=1}^{N} \sum_{j=1}^{N} \Big(\mathcal{F}_i(t) - \langle F(t) \rangle \Big) \Big(\mathcal{F}_j(t') - \langle F(t') \rangle \Big) \,. \tag{4.76}$$

Here Z is a normalisation that depends on the resampling method used for the data:

$$Z = \begin{cases} \dfrac{1}{N(N-1)} & \text{(raw)} \\ \dfrac{(N-1)}{N} & \text{(jackknife)} \\ \dfrac{1}{N} & \text{(bootstrap)} \,. \end{cases} \tag{4.77}$$

The diagonal elements of the covariance matrix are the variances $C_{t,t} = \sigma^2[\mathcal{F}(t)] \equiv \sigma_t^2$. The covariance matrix is normalised by the variances in order to form an estimate of the *correlation matrix*, with elements

$$\tilde{C}_{t,t'} = \frac{C_{t,t'}}{\sigma_t \sigma_{t'}} \,. \tag{4.78}$$

A fit that incorporates the full correlation matrix is referred to as a *correlated fit*. Here the correlation matrix is inverted and used in the iterative update of the fit parameters by fitting algorithms such as the Marquardt-Levenberg procedure. If the estimate of the correlation matrix is poor due to a lack of data, the matrix inversion can render correlated fits unusable. The alternative is to use *uncorrelated fits*, for which the correlation matrix is replaced by the unit matrix. All of the fits in this thesis use frozen covariance matrices calculated from the binned data.

4.2.6 Gauge fixing

In some cases it is necessary to gauge fix an ensemble. This is achieved on a per-configuration basis by applying gauge transformations to all links,

$$U_\mu^g(x) = U_\mu(x) \to g(x) U_\mu(x) g^\dagger(x + \hat{\mu}) \,, \tag{4.79}$$

where $g(x)$ are $SU(3)$ matrices $g(x)$, in order to satisfy the gauge fixing condition.

The Coulomb gauge is defined by the condition

$$\partial_i A_i^c = 0 \tag{4.80}$$

for all colour indices c, where i runs over the spatial indices. Here the gauge fields A_i^c can be found at leading order in a by Taylor expanding the formula for the link variables (eqn. 4.12), giving

$$A_\mu^c = 2\mathrm{tr}\, T^c A_\mu = 2\mathrm{tr}\frac{1}{2iag} T^c \left[U_\mu(\vec{x},t) - U_\mu^\dagger(\vec{x},t)\right] . \tag{4.81}$$

The gauge fixing condition is met by the set of transformed links $\{U^g\}$ (eqn.4.79) that minimises the quantity [111][112]

$$F[g] = \sum_{\mu=1}^{3}\sum_{\vec{x},t}\frac{1}{3V}\mathrm{Re}\,\mathrm{tr}\,\left[1 - U_\mu^g(\vec{x},t)\right] . \tag{4.82}$$

The minimisation is achieved recursively, and can be applied to each timeslice independently as i runs only over spatial indices. The algorithm for fixing into Landau gauge

$$\partial_\mu A_\mu^c = 0 \tag{4.83}$$

also minimises $F[g]$, but with the summation applied over all four space-time directions [113].

4.2.7 Finite-volume effects and boundary conditions

Lattice simulations are performed on finite spatial volumes with a typical side length of $L \sim 2-3$ fm. This introduces an additional source of error on states whose Compton wavelength is of the order of the lattice size. The lightest state is the pion, which has the largest Compton wavelength, $1/m_\pi$. As a result, lattice simulations must satisfy the criteria $1/m_\pi \ll aL$ in order to successfully describe low-energy physics. In some situations, the finite volume effects can be corrected for, for example by using finite volume ChPT (cf. chapter 8), and in some cases this can even be useful, such as in the study of $\pi\pi$ states [114][115][116].

The finite volume introduces an additional freedom: that of choosing the boundary conditions. In fact one can often set the boundary conditions on the gauge fields and the fermion propagators independently while only introducing errors that vanish as $a \to 0$ [117]. Typically simulations are performed using periodic boundary conditions in all four directions for the gauge fields, and in the three spatial directions of the fermion fields, with anti-periodic boundary conditions applied in the Euclidean time

direction.

Another useful choice of boundary condition for the fermion states is the *twisted boundary condition* [117]

$$\psi(x + \vec{e}_i L) = e^{i\theta_i}\psi(x)\,, \tag{4.84}$$

where θ is a *twist-angle* vector and $\vec{e}_i$ is a unit vector in the i-direction. Fourier transforming

$$\int \frac{d^4k}{(2\pi)^4} e^{ik(x+\vec{e}_i L)}\psi(k) = \int \frac{d^4k}{(2\pi)^4} e^{ikx+i\theta_i}\psi(k) \tag{4.85}$$

implies $\exp\{ik_iL\} = \exp\{i\theta_i\}$ and thus $k_i = \frac{n_i 2\pi}{L} + \frac{\theta_i}{L}$ where n_i is an integer. This technique can be used to fix the momentum of the lowest-lying state to an arbitrary non-zero value.

The choice of boundary condition modifies the Euclidean time propagation of states. For example the exponential decay of zero-momentum pseudoscalar amplitudes (eg. eqn. 4.66) with antiperiodic boundary conditions becomes

$$\mathcal{F}(\vec{0}; t, \tau) = A\left(e^{-m_{\mathrm{PS}}(t-\tau)} + e^{-m_{\mathrm{PS}}(T-t+\tau)}\right) \tag{4.86}$$

at large $(t-\tau)$, where A is a constant, m_{PS} is the pseudoscalar mass and T is the lattice time extent. Here the additional component arises from around-the-world propagation of states over the boundary. The around-the-world contributions can be suppressed by taking linear combinations of states with periodic and antiperiodic fermionic boundary conditions. This is discussed in more detail in chapter 6.

4.2.8 Measuring the propagator

The propagator is the inverse of the Dirac matrix D. For a 4d lattice of spatial extent L and time extent T, the Dirac matrix contains $\left(L^3 \times T \times 4 \times 3\right)^2$ entries. Here the factors of 4 and 3 relate to the spin and colour indices respectively. On an ensemble of Domain Wall fermions, the number of lattice sites is multiplied by $L_s \sim 16$. Currently the complete inversion of this matrix cannot be performed in any reasonable timescale. The solution is to calculate only the subset of these elements originating from a small lattice *source* $\eta(\vec{x}, \tau)$. This is performed by numerically solving the matrix equation

$$\sum_{\vec{y},t} D(\vec{x}, \tau\ ;\ \vec{y}, t)\psi(\vec{y}, t) = \eta(\vec{x}, \tau) \tag{4.87}$$

for the *solution vector*

$$\psi(\vec{y}, t) = \sum_{\vec{x},\tau} \mathcal{G}(\vec{y}, t \leftarrow \vec{x}, \tau)\eta(\vec{x}, \tau)\,. \tag{4.88}$$

Equation 4.87 can be solved using, for example, the conjugate gradient algorithm. The source η is a complex-valued vector quantity with spin and colour indices. In the above, the contraction over spin and colour indices is assumed.

The simplest source is the *point source*, which consists of a unit spin and colour vectors on a single space-time point $(\vec{x}_0, t_0)$. The 12 possible spin and colour source vectors are typically combined into a matrix source $\tilde{\eta}$, where

$$\begin{array}{rl|l} \tilde{\eta}(\vec{x},t) & = \mathbb{I}_{4\times4} \otimes \mathbb{I}_{3\times3} & (\vec{x},t) = (\vec{x}_0,t_0) \\ & = 0 & \text{otherwise} \end{array} \tag{4.89}$$

and the solution is also matrix-valued. Here $\mathbb{I}_{N\times N}$ is the $N \times N$ unit matrix. Point source solution matrices, or *one-to-all propagators*, contain the subset of elements of the propagator from a single space-time point to all other points on the lattice, for all combinations of spin and colour indices at source and sink:

$$\psi(\vec{y},t) = \mathcal{G}(\vec{y},t \leftarrow \vec{x}_0,t_0)\,. \tag{4.90}$$

Calculating this requires 12 inversions of the Dirac matrix. From this one can form a bilinear function

$$\begin{aligned} \mathrm{tr} \sum_{\vec{x}} e^{-i\vec{p}\cdot(\vec{x}-\vec{x}_0)} \left(\gamma^5 \psi_u^\dagger(\vec{x},t)\gamma^5\right) \gamma^5 \psi_s(\vec{x},t)\gamma^5 = \\ \mathrm{tr} \sum_{\vec{x}} e^{-i\vec{p}\cdot(\vec{x}-\vec{x}_0)} \left(\gamma^5 \mathcal{G}_u^\dagger(\vec{x}_0,t_0 \rightarrow \vec{x},t)\gamma^5\right) \gamma^5 \mathcal{G}_s(\vec{x},t \leftarrow \vec{x}_0,t_0)\gamma^5 \end{aligned}\,, \tag{4.91}$$

which is a single element of the local pseudoscalar Green's function of eqn. 4.63.

Measurements of Green's functions using point sources are sensitive to statistical fluctuations in the gauge fields. In addition, propagators inverted upon a point source that overlaps a localised near-zero mode of the Dirac matrix produce large outlying measurements. These problems can be alleviated to an extent by summing over measurements using several point sources, but at a proportionally larger cost in computing time. The alternative is to use a source that *smears* the source location of the propagator over a large spatial volume. Below, three smeared source types are introduced: the *box*, *wall*, and *lattice volume* sources.

Box and wall sources are typically used for correlation functions at zero momentum. The box source occupies a cubic spatial volume $\mathcal{R}_{\mathrm{box}}$ on a single timeplane τ:

$$\begin{array}{rl|l} \tilde{\eta}(\vec{x},t) & = \mathbb{I}_{4\times4} \otimes \mathbb{I}_{3\times3} & t = \tau \text{ and } \vec{x} \in \mathcal{R}_{\mathrm{box}} \\ & = 0 & \text{otherwise}\,, \end{array} \tag{4.92}$$

giving a solution matrix of the form

$$\psi(\vec{y},t) = \sum_{\vec{x}\in\mathcal{R}_{\text{box}}} \mathcal{G}(\vec{y},t \leftarrow \vec{x},\tau)\,. \tag{4.93}$$

Up to the path-ordered product of gauge links required to maintain gauge invariance, the function

$$\begin{aligned} &\text{tr}\sum_{\vec{z}} \left(\gamma^5\psi_u^\dagger(\vec{z},t)\gamma^5\right)\gamma^5\psi_s(\vec{z},t)\gamma^5 \\ &\quad = \text{tr}\sum_{\vec{z}}\sum_{\vec{x},\vec{y}\in\mathcal{R}_{\text{box}}} \left(\gamma^5\mathcal{G}_u^\dagger(\vec{y},\tau\rightarrow\vec{z},t)\gamma^5\right)\gamma^5\mathcal{G}_s(\vec{z},t\leftarrow\vec{x},\tau)\gamma^5 \end{aligned} \tag{4.94}$$

is identical to the pseudoscalar Green's function $\mathcal{F}(\vec{0};t,\tau)$ of eqn. 4.68 with a box operator at zero momentum. If the configurations are gauge fixed, the gauge links are not required, and box momentum source propagators can be used without issue. A wall source is simply a box source for which $\mathcal{R}_{\text{box}}$ fills the entire spatial volume on the timeslice τ. Box and wall sources are used extensively in chapter 6 for the extraction of ground-state pseudoscalar and baryon masses.

Lattice volume sources are defined as

$$\tilde{\eta}(x;p) \quad = e^{ip\cdot x}\mathbb{I}_{4\times4}\otimes\mathbb{I}_{3\times3} \;\Big|\; \forall\, x\,, \tag{4.95}$$

where x and p are position and momentum four-vectors respectively. These allow non-zero quark four-momenta to be induced:

$$\sum_y e^{-ip\cdot y}\psi(y;p) = \sum_y e^{-ip\cdot y}\left(\sum_x e^{ip\cdot x}\mathcal{G}(y\leftarrow x)\right) = \mathcal{G}(p)\,. \tag{4.96}$$

These sources are used in chapter 7 for the determination of the off-shell vertex functions used to calculate non-perturbative renormalisation coefficients.

4.2.9 Lattice measurement of B_K

The neutral kaon mixing parameter B_K, defined in section 3.1.4, is a phenomenologically important quantity that can be calculated on the lattice at high precision. The unrenormalised lattice value is obtained using eqn. 3.32, with the quantity $f_K^2 m_K^2$ obtained from the decay of the neutral kaon via the zeroth component of the axial current A_0:

$$B_K = \frac{\langle\bar{K}^0|\mathcal{O}_{VV+AA}|K^0\rangle}{\frac{8}{3}\langle K^0|A_0|0\rangle\langle 0|A_0|\bar{K}^0\rangle}\,, \tag{4.97}$$

where

$$\mathcal{O}_{VV+AA} = (\bar{s}\gamma^\mu d)(\bar{s}\gamma^\mu d) + (\bar{s}\gamma^5\gamma^\mu d)(\bar{s}\gamma^5\gamma^\mu d)\,. \tag{4.98}$$

On the lattice, B_K is calculated on gauge fixed configurations by evaluating the following correlation function that describes the creation and annihilation of zero-momentum neutral kaons at times τ and t respectively, with the kaon mixing occuring at an intermediate time t':

$$\langle \bar{K}^0(t)|\mathcal{O}_{\Gamma\Gamma}(t')|K^0(\tau)\rangle = \sum_{\vec{z}_1,\vec{z}_2}\sum_{\vec{y}}\sum_{\vec{x}_1,\vec{x}_2}\langle 0|s(\vec{z}_1,t)\bar{d}(\vec{z}_2,t)\,\Big[\bar{s}\Gamma d\;\bar{s}\Gamma d\Big](\vec{y},t')\;s(\vec{x}_1,\tau)\bar{d}(\vec{x}_2,\tau)|0\rangle\,, \tag{4.99}$$

where $\Gamma = V - A$. The Green's function has four Wick contractions

$$\langle 0|s(\vec{z}_1,t)\bar{d}(\vec{z}_2,t)\,\Big[\bar{s}\Gamma d\;\bar{s}\Gamma d\Big](\vec{y},t')\;s(\vec{x}_1,\tau)\bar{d}(\vec{x}_2,\tau)|0\rangle \tag{4.100}$$

$$\langle 0|s(\vec{z}_1,t)\bar{d}(\vec{z}_2,t)\,\Big[\bar{s}\Gamma d\;\bar{s}\Gamma d\Big](\vec{y},t')\;s(\vec{x}_1,\tau)\bar{d}(\vec{x}_2,\tau)|0\rangle \tag{4.101}$$

$$\langle 0|s(\vec{z}_1,t)\bar{d}(\vec{z}_2,t)\,\Big[\bar{s}\Gamma d\;\bar{s}\Gamma d\Big](\vec{y},t')\;s(\vec{x}_1,\tau)\bar{d}(\vec{x}_2,\tau)|0\rangle \tag{4.102}$$

$$\langle 0|s(\vec{z}_1,t)\bar{d}(\vec{z}_2,t)\,\Big[\bar{s}\Gamma d\;\bar{s}\Gamma d\Big](\vec{y},t')\;s(\vec{x}_1,\tau)\bar{d}(\vec{x}_2,\tau)|0\rangle \tag{4.103}$$

The first and second contractions evaluate to

$$\mathrm{tr}\Big[\left(\gamma^5\mathcal{G}_s^\dagger(\vec{z}_2,t\to\vec{y},t')\gamma^5\right)\Gamma\mathcal{G}_d(\vec{y},t'\leftarrow\vec{z}_2,t)\Big]\times\mathrm{tr}\Big[\left(\gamma^5\mathcal{G}_s^\dagger(\vec{x}_1,\tau\to\vec{y},t')\gamma^5\right)\Gamma\mathcal{G}_d(\vec{y},t'\leftarrow\vec{x}_2,\tau)\Big] \tag{4.104}$$

and the third and fourth to

$$-\mathrm{tr}\Big[\left(\gamma^5\mathcal{G}_s^\dagger(\vec{z}_2,t\to\vec{y},t')\gamma^5\right)\Gamma\mathcal{G}_d(\vec{y},t'\leftarrow\vec{z}_2,t)\left(\gamma^5\mathcal{G}_s^\dagger(\vec{x}_1,\tau\to\vec{y},t')\gamma^5\right)\Gamma\mathcal{G}_d(\vec{y},t'\leftarrow\vec{x}_2,\tau)\Big]\,. \tag{4.105}$$

Here as usual the subscript on the propagators indicates the quark flavour. Non-local sources are required for this calculation due to the form of the kaon interpolating operators. The calculation is performed using non-local stochastic sources in section 5.2, and using wall source propagators in sections 5.2 and 6.6. In addition, the non-perturbative renormalisation coefficients of B_K are calculated in chapter 7 and the continuum limit is taken in chapter 8.

Chapter 5

Improved techniques for meson correlation functions

Meson correlation functions are fundamental to phenomenological applications of lattice QCD. Pseudoscalar states in particular are used to determine quark masses, the LECs of the Chiral Effective Lagrangian, and CKM relevant observables such as B_K and the K_{l3} form factor. This chapter details a study of the use of stochastic sources for the improved calculation of meson two- and three-point correlation functions.

Local meson interpolating operators $\mathcal{O}_{1,2}$ have the general form

$$\mathcal{O}_{1,2} = \bar{\psi}_1 \Gamma \psi_2 \,, \tag{5.1}$$

where Γ is a product of gamma matrices set to give the operator the correct quantum numbers (cf. table 1.1), and ψ_i are quark fields of flavour i. The local-local two-point meson correlator is defined as

$$C(t';\vec{p}) = \sum_{\vec{x},\vec{y}} e^{-i\vec{p}\cdot(\vec{y}-\vec{x})} \langle \mathcal{O}_{2,1}(\vec{y},t)\mathcal{O}_{1,2}(\vec{x},\tau)\rangle \,, \tag{5.2}$$

where $t' \equiv t - \tau$ is the time separation. Performing the Wick contraction as in section 4.2.3, and neglecting the disconnected contribution that appears when $\psi_1 = \psi_2$, gives

$$C(t';\vec{p}) = \sum_{\vec{x},\vec{y}} e^{-i\vec{p}\cdot(\vec{y}-\vec{x})} \times \ \mathrm{tr}\left(\gamma^5 \Gamma \mathcal{G}_1(\vec{y},t \leftarrow \vec{x},\tau)\Gamma\gamma^5 \mathcal{G}_2^\dagger(\vec{x},\tau \rightarrow \vec{y},t)\right) \,, \tag{5.3}$$

where the trace is over spin and colour indices and $\mathcal{G}_i$ is a quark propagator of flavour i.

This chapter is concerned with stochastic vector sources, for which the elements of the source are randomly drawn from a symmetric distribution $\mathcal{D}$

$$\{\eta^{(n)}(x)_{a\alpha} \in \mathcal{D} | n = 1 \ldots N_{\mathrm{hits}}\} \quad \text{for } x \in \mathcal{R} \tag{5.4}$$

on a region $\mathcal{R}$ of the lattice. Here a is a colour index and α a spin index. If $\mathcal{R}$ spans the entire four-volume, the sources are referred to as *volume stochastic sources*. A set of N_{hits} randomly generated *hits* of the volume stochastic source has the property that in the limit of $N_{\text{hits}} \to \infty$,

$$\langle \eta^{(n)}_{a\alpha}(x)\eta^{\dagger(n)}_{b\beta}(y)\rangle_n \equiv \frac{1}{N}\sum_{n=1}^{N_{\text{hits}}} \eta^{(n)}_{a\alpha}(x)\eta^{\dagger(n)}_{b\beta}(y) \to \delta_{x,y}\delta_{ab}\delta_{\alpha\beta}\,. \tag{5.5}$$

Volume stochastic sources have been used in the past in order to estimate the entire propagator matrix [118][119][120][121][122][123]. Here the solutions are referred to as *stochastic all-to-all propagators*. Dong and Liu [118] demonstrated that sources with $\mathbb{Z}(2)$ noise $\mathcal{D} = \mathbb{Z}(2) = \{+1, -1\}$ or generally $\mathcal{D} = \mathbb{Z}(N)$ for any N, deviate less from the orthonormality condition of eqn 5.5 for a fixed number of hits than those estimated with Gaussian or 'double-hump' Gaussian-like distributions. Foster and Michael [120] suggest that the optimal choice is the c-number distribution $\mathcal{D} = \mathbb{Z}(2) \otimes \mathbb{Z}(2)$, which contains random $\mathbb{Z}(2)$ numbers in both its real and imaginary parts, i.e.

$$\mathcal{D} = \left\{ \frac{1}{\sqrt{2}}(\pm 1 \pm i) \right\}. \tag{5.6}$$

Stochastic all-to-all propagators are typically very noisy, and thus are generally used only if the number of gauge configurations is limited and one must extract as much information as possible from each [121][122]. This chapter details an exploration into an alternate use of stochastic sources for the calculation of meson correlators at zero momentum, based upon the work of Foster and Michael [120] (appendix), a form of which is referred to as the *one-end trick* [123]. This method has been used by the ETM collaboration for the calculation of meson two-point [124][125][126] and three-point functions [127]. The aim of this analysis is to determine whether stochastic correlators can be calculated with better statistics at fixed cost than traditional point and wall source correlators, and to investigate the competitiveness of extensions of this method to a range of matrix elements compared to the respective traditional approaches.

The layout of the chapter is as follows. The method of the one-end trick is introduced in the context of the two-point correlation functions, based upon Foster and Michael's [120] description, followed by the details of the two stochastic source types chosen to overcome the highlighted issues. The stochastic two-point correlators are compared to point source correlators on the unit gauge in order to prove the correct behaviour of the stochastic correlators on a trivial gauge. Results for pseudoscalar and vector correlators, analysed on a $16^3 \times 32$ Domain Wall QCD ensemble, are then presented and discussed. The performance of the stochastic source technique in the computation of the neutral kaon bag parameter B_K is assessed. To this end, a

comparison is made of the evaluation of the relevant three-point functions with a single stochastic wall source fixed to Coulomb gauge and a single wall source. In addition, the single-wall approach is compared to the two-wall approach of Antonio et al. [128]. The chapter concludes with a discussion of the calculation of hadronic form factors using the stochastic method, as adopted by the ETM collaboration [127] and the RBC & UKQCD collaboration [7].

5.1 Stochastic methods for two-point correlation functions

Consider the meson two-point correlator of eqn. 5.3 at zero momentum, and insert a product of Kronecker delta functions:

$$C(t';\vec{0}) = \sum_{\vec{x},\vec{y},\vec{z}} (\gamma^5\Gamma)_{\alpha\beta}[\mathcal{G}_1]_{b\beta,c\kappa}(\vec{y},t \leftarrow \vec{x},\tau)\Big[\delta_{\kappa\lambda}\delta_{cd}\delta_{\vec{x},\vec{z}}\Big](\Gamma\gamma^5)_{\lambda\rho}[\mathcal{G}_2^\dagger]_{d\rho,b\alpha}(\vec{z},\tau \rightarrow \vec{y},t)\,. \tag{5.7}$$

Here Greek letters represent spin indices and Roman letters colour indices. Using stochastic-noise wall sources, for which the source-region $\mathcal{R}$ spans the timeslice τ,

$$\begin{array}{rl|l} \eta^{(n)}_{c\kappa}(\vec{x},t|\tau) & \in \mathcal{D} & t = \tau \\ & = 0 & t \neq \tau\,, \end{array} \tag{5.8}$$

where $\mathcal{D}$ is the noise distribution introduced in the previous section, the delta functions can be replaced by a hit average

$$\delta_{\kappa\lambda}\delta_{cd}\delta_{\vec{x},\vec{z}} = \langle \eta^{(n)}_{c\kappa}(\vec{x},\tau|\tau)\eta^{\dagger(n)}_{d\lambda}(\vec{z},\tau|\tau)\rangle_n\,, \tag{5.9}$$

using the orthonormality condition of eqn. 5.5. Inserting this into eqn. 5.7 gives

$$C(t';\vec{0}) = \sum_{\vec{y}} \Big\langle \Big(\gamma^5\Gamma\psi^{(n)}_1(\vec{y},t|\tau)\Big) \cdot \psi_2^{\Gamma\,\dagger(n)}(\vec{y},t|\tau)\Big\rangle_n\,. \tag{5.10}$$

The correlator is the scalar-product of two solution vectors,

$$\psi^{(n)}_1(\vec{y},t|\tau) \equiv \sum_{\vec{x}} \mathcal{G}_1(\vec{y},t \leftarrow \vec{x},\tau)\ \eta^{(n)}(\vec{x},\tau|\tau)\,,\ \text{and} \tag{5.11}$$

$$\psi_2^{\Gamma\,(n)}(\vec{y},t|\tau) \equiv \sum_{\vec{x}} \mathcal{G}_2(\vec{y},t \leftarrow \vec{x},\tau)(\Gamma\gamma^5)^\dagger\eta^{(n)}(\vec{x},\tau|\tau)\,, \tag{5.12}$$

contracted at the sink location. The source indices are contracted automatically by the stochastic average, completing the trace in the $N_{\text{hits}} \rightarrow \infty$ limit.

The advantages of the above method for the calculation of the entire meson spectrum are reduced by the necessity of calculating ψ^Γ for each of the 16 Γ matrices, requiring 16 inversions per stochastic hit. This can be reduced to 4 inversions per hit by calculating the spin structure explicitly. These are referred to as spin-explicit or *SEM* sources following ref. [129]. These sources are further discussed in section 5.1.2.

5.1.1 Pseudoscalar *Z2PSWall* source

In the pseudoscalar case, $\Gamma = \gamma^5$, and thus the solution vectors ψ_i and ψ_i^Γ are identical. The pseudoscalar meson correlator can therefore be calculated with only a single inversion of the Dirac matrix per hit and quark flavour. The source, eqn. 5.8, is referred to as a *Z2PSWall* source.

The spin and colour space components of the *Z2PSWall* source can be represented as a single 12-component column vector $\Xi^{(n)}(\vec{x})$, such that the source has the form

$$\eta^{(n)}(\vec{x}, t|\tau) = \{\delta_{t,\tau}\} \otimes \Xi^{(n)}(\vec{x})\,. \tag{5.13}$$

The elements of $\Xi^{(n)}(\vec{x})$ are stochastically sampled from the probability distribution $\mathcal{D}$,

$$\{\Xi_i^{(n)}(\vec{x}) \in \mathcal{D} | i = 1 \ldots 12\}\,, \tag{5.14}$$

and thus the vectors obey the orthonormality condition

$$M(\vec{x}, \vec{y}) \equiv \left\langle \Xi^{(n)}(\vec{x}) \otimes \Xi^{(n)\,\dagger}(\vec{y}) \right\rangle_n \to \delta_{\vec{x},\vec{y}}\, \mathbb{I}_{12\times 12}\,, \tag{5.15}$$

where $\otimes$ is the tensor direct product. The matrix M is Hermitian under the spin, colour and spatial conjugate

$$M_{ij}^\dagger(\vec{x}, \vec{y}) = M_{ji}^*(\vec{y}, \vec{x}) = M_{ij}(\vec{x}, \vec{y})\,, \tag{5.16}$$

and all diagonal elements (i.e. those with both $\vec{x} = \vec{y}$ and $i = j$) are unity. Subtracting the diagonal elements, define the stochastic noise matrix K as

$$K(\vec{x}, \vec{z}) = M(\vec{x}, \vec{z}) - \delta_{\vec{x},\vec{z}}\, \mathbb{I}_{12\times 12}\,. \tag{5.17}$$

The correlator eqn. 5.10 then splits into signal and noise components,

$$\begin{aligned} C(t') &\equiv \textstyle\sum_{\vec{y}} \langle \psi_1^{(n)}(\vec{y}, t|\tau) \psi_2^{\dagger(n)}(\vec{y}, t|\tau) \rangle_n \\ &= C_S(t') + \Delta C(t')\,, \end{aligned} \tag{5.18}$$

where

$$C_S(t') \equiv \sum_{\vec{x},\vec{y}} \mathrm{tr}\left(\mathcal{G}_1(\vec{y},t \leftarrow \vec{x},\tau)\mathcal{G}_2^\dagger(\vec{x},\tau \rightarrow \vec{y},t)\right) \tag{5.19}$$

is the gauge-invariant signal component and

$$\Delta C(t') = \sum_{\vec{x},\vec{y},\vec{z}} \mathrm{tr}\left(\mathcal{G}_1(\vec{y},t \leftarrow \vec{x},\tau)K(\vec{x},\vec{z})\mathcal{G}_2^\dagger(\vec{z},\tau \rightarrow \vec{y},t)\right) \tag{5.20}$$

is the noise component. Here the trace over sink indices has been reintroduced as this is now a product over matrices. For finite N_{hits}, the noise component contains a mixture of gauge-invariant and gauge-dependent pieces, as well as contributions from other meson correlators. This can be seen by decomposing $K(\vec{x},\vec{y}) \in \mathbb{C}^{144}$ onto the basis $\{\lambda_r \otimes \Gamma_i\}$, composed of the eight Gell-Mann matrices $\{\lambda_r \,|r = 1\ldots 8\}$, the 3×3 unit matrix $\lambda_0 = \mathbb{I}_{3\times 3}$, the 4×4 unit matrix $\Gamma_0 = \mathbb{I}_{4\times 4}$, and the fifteen tensor combinations of the gamma matrices $\{\Gamma_i \,|i = 1\ldots 15\}$. The components of this basis are orthogonal under the trace operation

$$\mathrm{tr}\,(\lambda_r \otimes \Gamma_i \;\; \lambda_s \otimes \Gamma_j) = \alpha_r \delta_{rs}\delta_{ij}\,, \tag{5.21}$$

where $\alpha_0 = 12\,,\ \alpha_r = 8\,|r \neq 0$. Under this decomposition,

$$K(\vec{x},\vec{y}) = \sum_{i,r} A_r^i(\vec{x},\vec{z})\ \lambda_r \otimes \Gamma_i\,, \tag{5.22}$$

with c-number coefficients $A_r^i(\vec{x},\vec{z})$. The noise component $\Delta C(t')$ becomes

$$\Delta C(t') = \sum_{i,r}\sum_{\vec{x},\vec{y},\vec{z}} A_r^i(\vec{x},\vec{z})\ \mathrm{tr}\left(\mathcal{G}_1(\vec{y},t \leftarrow \vec{x},\tau)\ \lambda_r \otimes \Gamma_i\ \mathcal{G}_2^\dagger(\vec{z},\tau \rightarrow \vec{y},t)\right)\,. \tag{5.23}$$

With reference to eqn. 5.3, it is clear that for all components bar the unit matrix contribution $\lambda_0 \otimes \Gamma_0$, the spin and colour matrices at the source location are different from those at the sink. These components are formed from the Green's function of two *different* interpolating operators: the pseudoscalar $\mathcal{O}(\lambda_0 \otimes \gamma^5)$ at the sink with the polluting 'unwanted operators' $\mathcal{O}(\lambda_r \otimes \Gamma_i\gamma^5)$ at the source. The contaminating noise is small in the case of the scalar, vector and tensor Dirac structures as the pseudoscalar is the lightest state. These contributions are eliminated in the ensemble average due to parity, and also in the $N_{\mathrm{hits}} \rightarrow \infty$ limit. The overlap with the axial state A_0 is eliminated in the hit limit and is empirically smaller in magnitude than the pseudoscalar signal. The effects of the gauge-dependent terms with $\vec{x} \neq \vec{z}$, which are referred to as *cross-terms*, and components with $\lambda_r \neq \mathbb{I}_{3\times 3}$ are discussed further in section 5.1.3.

The *Z2PSWall* source can be implemented within a software framework designed

for 12×12 matrix sources (cf. sec. 4.2.8) allowing for the reuse of existing propagator contraction code without further modification. This can be achieved by placing the stochastic source vector $\Xi^{(n)}(\vec{x})$ on the first column of an empty 12×12 matrix $\Phi(\vec{x}, t)$ on each lattice site of the source timeslice τ:

$$\begin{aligned} \Phi^{(n)}(\vec{x}, t) &= \left(\begin{array}{ccccc} : & 0 & 0 & 0 & \cdots \\ \Xi^{(n)}(\vec{x}) & 0 & 0 & 0 & \cdots \\ : & : & : & : & \cdots \end{array} \right) \Bigg| \begin{array}{l} t = \tau \\ \\ t \neq \tau \end{array} \\ &= 0 \end{aligned} \quad . \tag{5.24}$$

The solution $\psi'^{(n)}(\vec{y}, t|\tau)$ is matrix valued,

$$\psi'^{(n)}(\vec{y}, t|\tau)_{AC} \equiv \sum_{\vec{x}} \mathcal{G}_{AB}(\vec{y}, t\ ;\ \vec{x}, \tau) \Phi^{(n)}_{BC}(\vec{x}, \tau)\,, \tag{5.25}$$

but with all columns zero bar the first ($C = 0$). Here A, B, C are spin-colour indices. The inverter, of course, checks for a zero norm source vector before inversion. With this implementation, the direct product that forms the stochastic matrix M of equation (5.15) simplifies to the stochastic average of the matrix product

$$M(\vec{x}, \vec{y}) = \langle \Phi(\vec{x}) \Phi^{\dagger}(\vec{y}) \rangle_n\,, \tag{5.26}$$

such that the meson two-point function of equation (5.10) becomes simply a trace over a product of matrices

$$C(t'; \vec{0}) = \sum_{\vec{y}} \mathrm{tr}\ \langle \psi_1^{(n)}(\vec{y}, t|\tau) \psi_2^{(n)\,\dagger}(\vec{y}, t|\tau) \rangle_n\,, \tag{5.27}$$

which has the same form as the standard point source meson correlator contraction.

5.1.2 Spin-explicit *Z2SEMWall* sources

Spin-explicit *Z2SEMWall* sources, for which stochastic noise is used only on the colour indices, can be used to stochastically estimate the general meson two-point correlator of eqn. 5.10 with just four inversions of the Dirac matrix. These sources were used by Viehoff et al. [129] for the calculation of the matrix element of the axial vector current between proton states, and later by Boucaud et al. [124][126] for meson correlation functions, where they are referred to as 'linked sources'.

Similarly to the point source, the four spin vectors can be combined into a single 4×4 unit spin matrix. A different stochastic colour vector $\xi^{(n)}$ is used on every site of the timeslice such that the spatial and colour delta functions are retained in the hit average, while an explicit Kronecker delta is used for the spin components. The source

has the structure

$$\eta^{(n)}(\vec{x},t|\tau) = \{\delta_{t,\tau}\} \otimes \mathbb{I}_{4\times 4} \otimes \xi^{(n)}(\vec{x})\,, \tag{5.28}$$

where

$$\{\xi_a^{(n)}(\vec{x}) \in \mathcal{D} | a = 1 \ldots 3\} \tag{5.29}$$

obeys the orthonormality condition

$$M(\vec{x},\vec{y}) \equiv \left\langle \xi^{(n)}(\vec{x}) \otimes \xi^{(n)\,\dagger}(\vec{y}) \right\rangle_n \to \delta_{\vec{x},\vec{y}}\, \mathbb{I}_{3\times 3}\,. \tag{5.30}$$

For a finite number of hits, the matrix M can again be decomposed onto the basis of Gell-Mann matrices and the unit matrix λ_0. As before, it is expected that the gauge dependent terms will be suppressed by the ensemble average.

As with the *Z2PSWall* source, the *Z2SEMWall* can be placed within a 12×12 matrix, allowing for the reuse of existing measurement code:

$$\Phi(\vec{x},t) = \begin{pmatrix} 1 & 0 & 0 & 0 \\ 0 & 1 & 0 & 0 \\ 0 & 0 & 1 & 0 \\ 0 & 0 & 0 & 1 \end{pmatrix} \otimes \begin{pmatrix} : & 0 & 0 \\ \xi^{(n)}(\vec{x}) & 0 & 0 \\ : & 0 & 0 \end{pmatrix} \tag{5.31}$$

at $t = \tau$ and zero elsewhere.

5.1.3 Hit averaging and the ensemble average

The elements of the noise matrix K (eqn. 5.17) are either stochastically generated or zero. Therefore, provided the distribution $\mathcal{D}$ is symmetric about zero, the combined probability distribution of the gauge configurations U and the stochastic matrix K has the property

$$P[U,K] = P[U]P[K] = P[U]P[-K]\,. \tag{5.32}$$

Here the noise components of the correlator containing gauge-dependent terms are considered. Gauge invariance breaking terms are naturally suppressed by averaging over gauge-equivalent configurations within an ensemble. However the Monte Carlo sampling of a gauge orbit is typically quite slow as the ensemble size is increased due to autocorrelations between configurations. The stochastic method improves upon this by explicitly removing these terms through the symmetric fluctuations of K about zero.

If sufficiently many hits per configuration are sampled, then the cancellation will be near exact, while for a smaller number of hits this will take place stochastically as the distribution of gauge fields and sources is jointly sampled. For a large enough ensemble, the difference between having few hits and having many is likely to be small.

Lattice size	$16^3 \times 32$
Action	Domain Wall
Gauge Action	Iwasaki
Domain wall height	1.8
L_s	16
β	2.13
$\frac{1}{a}$ (GeV)	1.73(3)
Sea quark masses (latt. units)	$m_u = 0.01$, $m_s = 0.04$

Table 5.1: Ensemble properties.

5.1.4 Demonstration on the unit gauge

This section contains a preliminary investigation of the use of the *Z2PSWall* and *Z2SEMWall* sources for meson correlators. The intention is to demonstrate the convergence of the correlators to the true result as the number of hits is increased, and to compare the rate at which the statistical errors decrease. The analysis is performed on the unit gauge configuration of Domain Wall QCD, for which all gauge links are unity. Due to the translational invariance of this gauge field, the point source solution is exactly equal to the volume averaged propagator, hence the comparison is made to the point source solution. The noise distribution is chosen as $\mathcal{D} = \mathbb{Z}(2) \otimes \mathbb{Z}(2)$ following ref. [120].

The pseudoscalar two-point correlator, with a valence quark mass of 0.04 in lattice units, is calculated using different numbers of hits of both *Z2PSWall* and *Z2SEMWall* sources. For each choice of the number of hits N_{hits}, 80 measurements of the correlator are obtained, each an average over N_{hits} independent stochastic estimates. From these the standard error on the mean is estimated. In order to avoid having to generate new data for each N_{hits}, the stochastic estimates used for each of the 80 measurements are randomly drawn from a large pool, ensuring that for a given N_{hits} no data point is drawn more than once. This produces 80 independent measurements for each N_{hits} and minimises correlation between values of N_{hits}.

Figure 5.1 shows a plot of the means and standard errors of these distributions taken from the correlation function at $t = 16$. For the pseudoscalar two-point function, it appears that the *Z2PSWall* result converges more quickly than the *Z2SEMWall* result, while requiring only one quarter of the number of inversions. However it is found in the next section that the *Z2SEMWall* benefits from its exact spin structure in the full calculation.

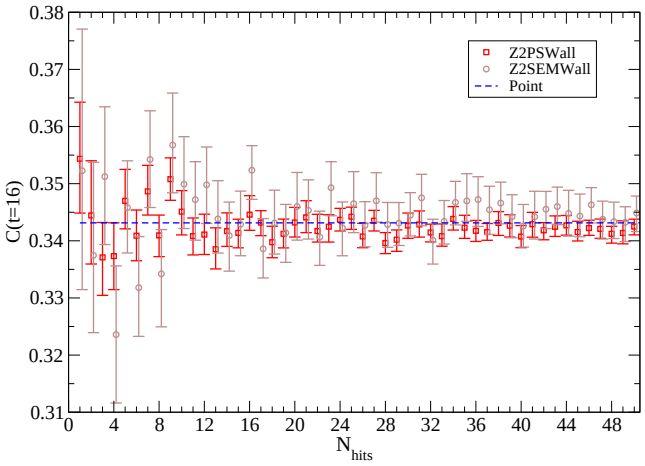

Figure 5.1: Demonstration of the dependence of the trivial gauge pseudoscalar meson correlator on the number of stochastic hits N_{hits} of *Z2PSWall* and *Z2SEMWall*. These are compared to the point source correlator, which is the exact solution for this gauge configuration. Errors are estimated from 80 separate measurements, each determined by averaging N_{hits} independent stochastic estimates. The data have been shifted slightly for clarity.

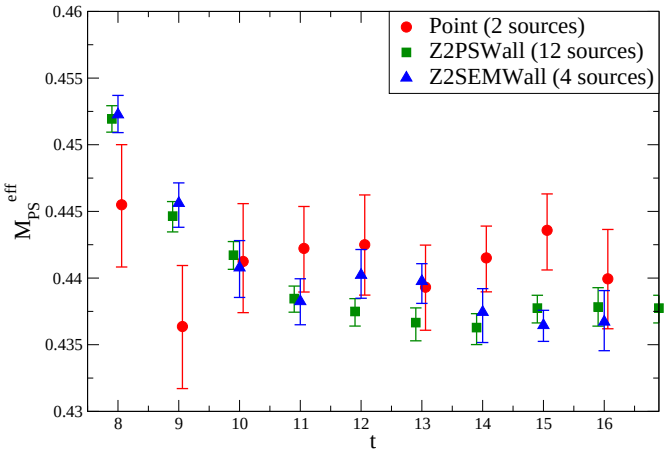

Figure 5.2: Pseudoscalar meson effective mass plot from averaged correlators with a bin size of 8 configurations. This is not a comparison at fixed cost. The points have been slightly shifted for clarity.

5.1.5 Two-point meson correlator results

This section contains a detailed comparison of pseudoscalar meson correlators calculated using stochastic sources and those measured with a point source. Measurements are performed on 392 configurations (separated by 5 molecular dynamics time-steps) of an RBC-UKQCD $16^3 \times 32$ 2+1 flavour Domain Wall QCD ensemble with properties detailed in table 5.1. Previous results on this ensemble are available for comparison [130]. *Z2PSWall* propagators are calculated from 12 different source timeplanes, each with a single stochastic hit per configuration. Three further hits are calculated from timeslice $\tau_{\text{src}} = 0$. In addition, *Z2SEMWall* propagators are calculated from 4 timeplanes and point source propagators from two source origins. The propagators are calculated using the conjugate gradient algorithm with a residual of 10^{-7} and a valence quark mass of 0.04 in lattice units. This large valence quark mass was chosen as it is cheaper to invert, allowing for better statistics for a given computational cost.

In order to take account of autocorrelations in molecular dynamics time, adjacent configurations are binned over 40 molecular dynamics time units (8 configurations). This bin size was chosen by increasing the size incrementally until the errors stopped increasing, and is consistent with the previous analysis in ref. [130].

Figure 5.2 contains an overlay of pseudoscalar effective mass plots for each source type. Here the *Z2PSWall* correlator is obtained by averaging over the 12 single-hit estimates measured from different source timeplanes. The additional hits on timeslice $\tau_{\text{src}} = 0$ are not included as this would bias the measurement towards a particular timeslice. Based on this figure, a constant fit range of $10 - 16$ is chosen for the point source correlators and $11 - 16$ for the *Z2PSWall* and *Z2SEMWall* correlators.

Table 5.2 contains the results for the pseudoscalar meson mass fits for the various sources over all 392 available configurations. Here the correlators have been averaged about the central timeslice (folded) for better statistics, using the forwards-backwards symmetry of the correlator. The fits are correlated and the error bars are obtained using the bootstrap procedure. For some choices of timeslice/origin, the correlation functions show deviations from the expected time-dependence, which manifests itself in a large value for χ^2/d.o.f. These effects however disappear after averaging the correlation functions over source positions.

The *Z2PSWall* masses are consistently lower than those of the point sources, differing by 5σ between the 12-source-averaged *Z2PSWall* correlator and the point source average. This discrepancy is likely to be caused by statistical fluctuations in the point source correlators as the 12-source-averaged *Z2PSWall* result of 0.4372(9) is in much better agreement with the mass obtained in the previous analysis of 0.438(3) [130] than the 2-point-source-averaged value of 0.4418(12). The central

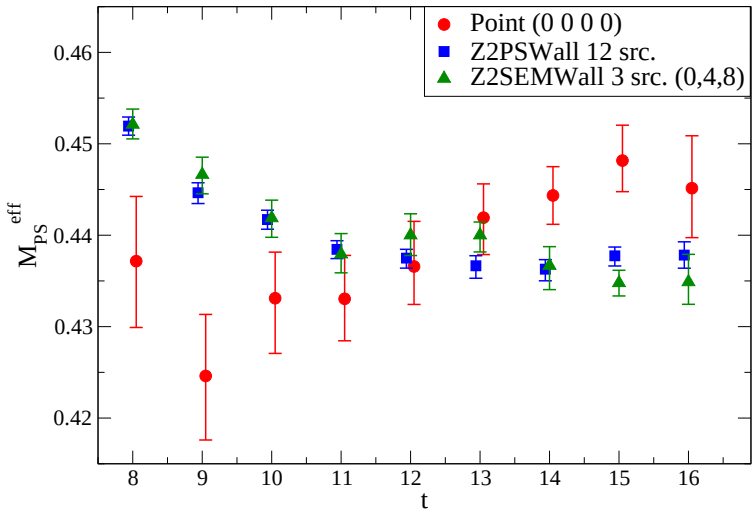

Figure 5.3: Pseudoscalar effective mass plots at a fixed cost of 4704 inversions of the Dirac matrix.

value and error estimates of the cited result were obtained by averaging over the pseudoscalar-pseudoscalar and axial-axial correlators for several point source smearings and locations, and the error was scaled by a factor of 1.5 to account for fluctuations in the gauge fields, and as such should not be compared unfavourably with the results of the present analysis.

At a fixed cost of 12 inversions per configuration (4704 inversions in total), it is evident that the 12-source-averaged *Z2PSWall* result shows at least a factor of two improvement in the statistical error over the point source result. The 3-source averaged *Z2SEMWall* results agree with the *Z2PSWall* result, and also show a consistent factor of 2 improvement in errors over the point source at the same cost.

The third- and second-to-last lines in the *Z2PSWall* section of table 5.2 allow for a fixed cost comparison between the use of four stochastic hits upon a single source timeslice and a single hit on four different timeslices. The 40% reduction in the statistical error suggests that a new three-volume sample of the gauge field should be preferentially chosen when forming a new stochastic source, separated in space-time and molecular dynamics time in order to maximise decorrelation between the samples.

Figure 5.3 contains a comparison of the effective masses at a fixed cost of 4704 inversions. The stochastic sources both give significantly better plateaus than that of a single point source. The plateaus for the stochastic sources appear to be very similar. This result displays a spectacular improvement for pseudoscalar masses at no

Point					
N_{src}	Cost	Origin(s)		Mass	χ^2/d.o.f.
1	4704	$x_1 \equiv (0,0,0,0)$		0.4413(+19)(-16)	0.543
1	4704	$x_2 \equiv (8,8,8,16)$		0.4416(+20)(-23)	2.046
2	9408	x_1 , x_2		0.4418(+12)(-12)	0.163
Z2PSWall					
N_{src}	Cost	N_τ	τ_{src}	N_{hits}/N_τ	Mass	χ^2/d.o.f.
1	392	1	0	1 (a)	0.4398(+19)(-16)	0.236
1	392	1	0	1 (b)	0.4375(+23)(-24)	0.300
1	392	1	0	1 (c)	0.4397(+24)(-24)	0.241
1	392	1	0	1 (d)	0.4405(+21)(-19)	0.481
1	392	1	2	1	0.4386(+19)(-21)	0.361
1	392	1	4	1	0.4345(+24)(-26)	0.216
1	392	1	6	1	0.4323(+19)(-21)	1.917
1	392	1	8	1	0.4356(+19)(-23)	0.286
1	392	1	10	1	0.4407(+20)(-23)	0.267
1	392	1	12	1	0.4394(+21)(-22)	0.120
1	392	1	14	1	0.4397(+21)(-20)	0.177
1	392	1	16	1	0.4354(+22)(-23)	0.069
1	392	1	18	1	0.4362(+21)(-20)	0.034
1	392	1	20	1	0.4334(+20)(-21)	0.222
1	392	1	22	1	0.4390(+24)(-27)	0.731
4	1568	4	0,4,6,8	1	0.4374(+10)(-11)	0.632
4	1568	1	0	4	0.4393(+16)(-16)	0.371
12	4704	12	0-22; even	1	0.4372(+8)(-9)	0.388

Z2SEMWall						
N_{src}	Cost	N_τ	τ_{src}	N_{hits}/N_τ	Mass	χ^2/d.o.f.
1	1568	1	0	1	0.4395(+15)(-14)	0.190
1	1568	1	4	1	0.4375(+25)(-24)	0.507
1	1568	1	8	1	0.4348(+16)(-18)	0.707
1	1568	1	12	1	0.4406(+17)(-16)	0.054
3	4704	3	0,4,8	1	0.4372(+9)(-11)	0.657
3	4704	3	0,4,12	1	0.4394(+11)(-12)	0.068
3	4704	3	0,8,12	1	0.4383(+9)(-10)	0.127
3	4704	3	4,8,12	1	0.4375(+11)(-12)	0.644
4	6272	4	0,4,8,12	1	0.4381(+9)(-10)	0.378

Table 5.2: Pseudoscalar meson masses obtained using the various sources, fitting to the range $10 - 16$ (point) and $11 - 16$ (stoch. sources), with a bin size of 8 configurations, over an ensemble of 392 configurations. Here N_{src} is the total number of sources used in the fit, with the equivalent cost in inversions of the Dirac matrix detailed in the next column. The third column of the stochastic source tables contains the number of source timeslices used N_τ; the fourth a list of these times τ_{src}; and the fifth the number of hits (stochastic samples) on those timeslices (N_{hits}/N_τ). The four independent hits of *Z2PSWall* are distinguished by a Roman letter.

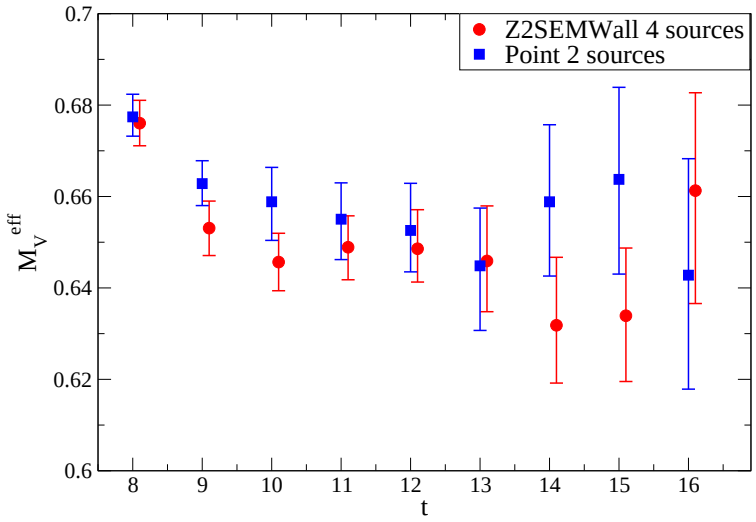

Figure 5.4: Vector meson effective mass plot from averaged *Z2SEMWall* and point source correlators with a bin size of 8 configurations. This is not a fixed cost comparison. This figure is used to select the fit ranges.

additional cost. It is also concluded that the difference in the quality of the stochastic source results at fixed cost is not large enough to warrant using *Z2PSWall* sources over the spin-explicit *Z2SEMWall* sources which can be used for a larger number of measurements.

In addition to the pseudoscalar correlators, the *Z2SEMWall* and point source propagators are used to measure the vector meson correlator, for which the interpolating operator is $\mathcal{O}_{1,2} = \bar{\psi}_1 \gamma^\mu \psi_2$. Figure 5.4 shows the vector meson effective mass for the 4 combined *Z2SEMWall* sources and the 2 point sources. This is not a fixed cost comparison. The correlators for the three spatial directions have been averaged together and folded about the central timeslice for better statistics. Based upon this plot a fit range of 9-16 is chosen for both source types.

Table 5.3 contains the fit results for the vector meson mass. At fixed cost, a reduction in error by ~ 2 over the point source result is observed. The plateau of the effective mass shown in figure 5.5 is noticeably better for the stochastic source.

5.2 Stochastic calculation of the B_K three-point function

The success of the stochastic method for meson two-point functions motivates the extention of the technique to include meson three-point functions. In this section,

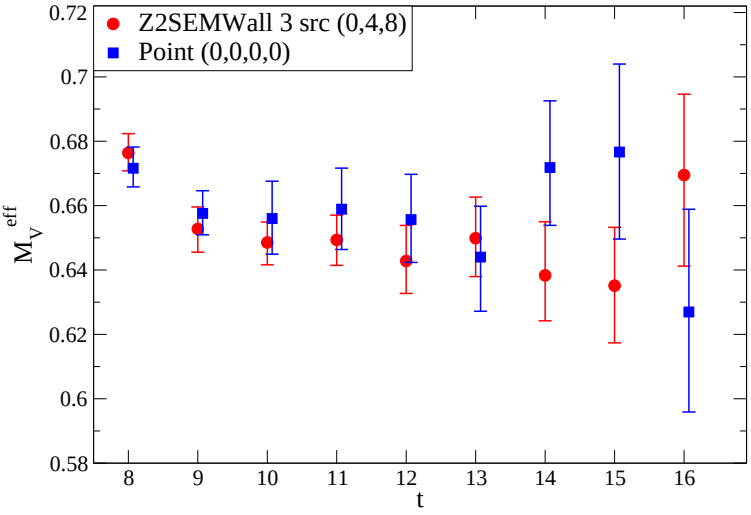

Figure 5.5: Vector meson effective mass plots at a fixed cost of 4704 inversions of the Dirac matrix.

Point						
N_{src}	Cost	Origin(s)			Mass	χ^2/d.o.f.
1	4704	$x_1 \equiv (0,0,0,0)$			0.656(+10)(-9)	0.404
1	4704	$x_2 \equiv (8,8,8,16)$			0.657(+8)(-9)	0.172
2	9408	x_1 , x_2			0.657(+7)(-7)	0.372
Z2SEMWall						
N_{src}	Cost	N_τ	τ_{src}	N_{hits}/N_τ	Mass	χ^2/d.o.f.
1	1568	1	0	1	0.642(+8)(-8)	0.207
1	1568	1	4	1	0.660(+10)(-11)	0.328
1	1568	1	8	1	0.642(+10)(-9)	0.407
1	1568	1	12	1	0.637(+9)(-9)	0.538
3	4704	3	0,4,8	1	0.649(+5)(-5)	0.153
3	4704	3	0,4,12	1	0.647(+5)(-6)	0.101
3	4704	3	0,8,12	1	0.641(+5)(-5)	0.377
3	4704	3	4,8,12	1	0.646(+6)(-6)	0.457
4	6272	4	0,4,8,12	1	0.646(+4)(-5)	0.179

Table 5.3: Vector meson masses obtained from point and stochastic source correlators, fitting to range $9-16$ with a bin size of 8 configurations. Here the conventions established in table 5.2 have been used.

stochastic methods are used for the calculation of the neutral kaon mixing parameter B_K.

The general strategy for measuring B_K on the lattice is discussed in section 4.2.9. RBC & UKQCD typically use propagators calculated from a pair of spatially separated wall sources on Coulomb gauge fixed configurations. These sources are referred to here as *GFWall* sources. They are usually calculated with both periodic (p) and antiperiodic (a) boundary conditions, using the $p + a$ combination to eliminate unwanted round-the-world contributions to the three-point function by doubling the periodicity of the meson's propagation. This method has been used to calculate B_K on this $16^3 \times 32$ ensemble [128], using *GFWall* sources on timeslices $t_1 = 5$ and $t_2 = 27$. In this section a variant of this method is investigated in which a single *GFWall* source at time τ is used, with the boundary conditions implemented on all time-directed gauge links $U_t(\tau - 1, \vec{x})$ between τ and the previous timeplane. Here the $p + a$ combination gives a forwards propagating solution, and $p - a$ a backwards propagating solution. The two Wick contractions of eqns. 4.104 and 4.105 are formed using these solutions by replacing the propagators originating on the source timeslice τ with the forwards propagating solutions, and the propagators originating on the sink timeplane t with the backwards propagating solutions. The product of AP and PA correlation functions in the denominator of eqn. 4.97 is formed from the correlation functions of the forwards- and backwards-flowing propagators respectively. This method has been used by Aubin et al. [131] for the removal of round-the-world pion propagation in the calculation of the pseudoscalar decay constant.

The Wick contractions are of a suitable form for calculation using both *Z2PSWall* and *Z2SEMWall* sources. However these sources are designed to suppress the cross-terms for which the propagator source locations differ on the source timeslice. These cross-terms are required for the non-local kaon interpolating operator of eqn. 4.97. Wall-like stochastic sources can be formed by choosing the same set of stochastic numbers on every site of the source timeslice for a given hit. Then $M(\vec{x}, \vec{y})$ becomes position independent, yet still retains the delta function in spin and colour space in the large hit limit. The resulting sources are referred to as *Z2PSGFWall* and *Z2SEMGFWall* sources. Other than the position independence of the stochastic noise, these sources are identical to the existing stochastic types. These sources should be used on gauge fixed configurations.

5.2.1 B_K results

B_K is calculated on the $16^3 \times 32$ ensemble detailed in section 5.1.5 using propagators of mass 0.04 in lattice units generated using *Z2PSGFWall* and *Z2SEMGFWall* stochastic sources as well as the standard *GFWall* source. The configurations are fixed to the

the Coulomb gauge prior to the generation of the propagators. For comparison, the matrix element is also calculated using *Z2PSWall* and *Z2SEMWall* source propagators without gauge fixing. Following the discussion in section 5.1.3 and the conclusions of the previous section, a single stochastic hit per configuration is used for all source types apart from the cheaper *Z2PSWall* and *Z2PSGFWall*. For the latter, the limited size of the ensemble forces an increase in the number of hits per configuration to four in order to compare to the *GFWall* results with reasonable statistics. For a fair comparison at a given cost, the configurations used for the *GFWall* correlators were separated as far as possible in molecular dynamics time, in order to reduce the effect of autocorrelations.

A spatial translation by a predetermined four-vector $\vec{d}$ is performed upon each gauge configuration. With every new configuration, $\vec{d}$ is incremented by an amount $\vec{\Delta}$, allowing the sources to be spread throughout the lattice volume without the need to alter the location of the timeplane upon which the boundary conditions are applied: the sources are always placed at $t = 0$ on the shifted configuration with the boundary conditions applied on the boundary between $t = T - 1$ and $t = 0$. It was intended that the n^{th} configuration be shifted $\vec{d}_n = \vec{d}_1 + (n-1)\vec{\Delta}$, where the periodicity of the lattice is implicit. While this rule was mostly followed in contiguous segments, due to restarting the code this rule was interrupted at several points in the chain. The actual source origins are widely distributed and for the most part follow the above rule, and thus this will not substantially affect the conclusions. The subsequent production running for phenomenological calculations detailed in chapter 6 follows the above rule strictly.

Source Type	#conf.	Fit range	Fit value	χ^2/d.o.f.	Scaled fit
Z2PSWall	384	7-22	0.6338(75)	1.882	0.6338(160)
		9-24	0.6736(88)	1.039	0.6736(188)
		7-25	0.6374(83)	1.185	0.6374(177)
		9-24	0.6479(68)	1.162	0.6479(145)
Z2PSGFWall	384	7-24	0.6155(79)	0.721	0.6155(198)
		9-23	0.6595(81)	1.092	0.6595(203)
		10-23	0.6492(94)	0.857	0.6492(235)
		8-22	0.6250(85)	1.108	0.6250(213)
Z2SEMWall	96	9-24	0.6752(56)	0.753	0.6752(173)
Z2SEMGFWall	96	10-24	0.6685(43)	1.874	0.6685(67)

Table 5.4: Results for B_K on the $16^3 \times 32$ ensemble for the various source types, calculated at a fixed cost of 384 inversions. The number of configurations is given in the second column. Four independent hits over the same set of configurations were calculated for the *Z2PS* types; here the results of independent fits to each of these sets is quoted, in order to demonstrate the fluctuations in the correlators resulting from the choice of different random numbers. These data are inconsistent and thus the errors are scaled by a PDG scale factor, with the results given in the last column. PDG scale factors are calculated for the *Z2SEM* types by splitting the available data into two sets and performing separate fits as discussed below.

Source Type	Fit range	Fit value	χ^2/d.o.f.	Scaled fit
Z2SEMWall	9-23	0.6626(39)	1.010	0.6626(121)
	8-23	0.6815(49)	1.193	0.6815(152)
Z2SEMGFWall	8-24	0.6665(48)	0.801	0.6665(75)
	7 25	0.6572(38)	1.138	0.6572(59)
GFWall	7-25	0.6590(28)	1.278	
	8-25	0.6579(24)	1.081	

Table 5.5: B_K fits over 2 sets of 192 configurations with a separation of 10 configurations. The two sets are staggered by 5 configurations such that there is no overlap, thus approximating 2 hits on the same configurations.

Source Type	#conf.	Fit range	Fit value	χ^2/d.o.f.	Scaled fit
Z2PSWall	4×384	8-24	0.6548(51)	0.261	0.6548(109)
Z2PSGFWall	4×384	8-25	0.6365(50)	0.676	0.6365(125)
Z2SEMWall	384	7-23	0.6728(30)	0.755	0.6728(93)
Z2SEMGFWall	384	7-24	0.6653(28)	0.913	0.6653(43)
GFWall	128	9-23	0.6554(32)	2.000	

Table 5.6: Results for B_K on the $16^3 \times 32$ ensemble for the various source types. These data are calculated at a fixed cost of 1536 inversions, where the *Z2PS* types were evaluated for 4 hits over the same 384 configurations. The value quoted in Antonio et al. [128] is 0.659(3).

Table 5.4 shows the results for the stochastic types calculated at a fixed cost of 384 inversions. The fit ranges are chosen based upon the plateau range of the PA correlators in the denominator of eqn. 4.97, and the errors were estimated using the jackknife procedure. The data were binned over a minimum of 40 molecular dynamics time units as before. The *GFWall* results have been omitted from this table due to the lack of statistics at this number of inversions (32 configurations). The fits to each of the 4 hits of *Z2PSWall* and *Z2PSGFWall* are inconsistent, with a combined χ^2/d.o.f. of 4.569 and 6.274 respectively. No improvement in consistency was found by increasing the bin size. Due to the large statistics on these correlation functions and the spatial translation of the gauge fields between adjacent configurations, it is unlikely that the discrepancy arises due to gauge field fluctuations. Instead it is likely an indication that the amplitude of the four-quark operator is more strongly effected by the unwanted operators arising due to the stochastic noise. As a result a scale factor is applied to the *Z2PS* error bars in order to account for this unlikely, high χ^2/d.o.f.. Defining the scale factor as the $\sqrt{\chi^2/\text{d.o.f.}}$ ensures that the results agree with a combined χ^2/d.o.f. of unity. This strategy is employed by the Particle Data Group (PDG) to combine experimental results that disagree due to underestimated errors, and is henceforth referred to as a PDG scale factor. Of course this method can hide all manner of sins, and thus should only be used when the source of the discrepancy is known. In this case it is used to apply a systematic error associated with the unwanted operator contributions. The scaled results are given in the far right column.

The scaling factors for the other stochastic source types are obtained by comparing fits to two independent sets of 192 configurations with a separation of 10 and a bin size of 40 MD time units (4 configurations). The sets are staggered by 5 time units such that, due to correlations between nearby configurations, this method approximates two hits on the same 192 configurations without the need for further computation. The results of this analysis are presented in table 5.5. A combined χ^2/d.o.f. is determined for each pair of fits, giving an estimated of the PDG scale factor as above. It is clear that the *GFWall* results agree very well within errors, with a χ^2/d.o.f. of 0.091, and therefore need no scaling. This is expected if the discrepancies arise due to unwanted operator pollution. The agreement of the *Z2SEM*-type correlators is poorer, with a χ^2/d.o.f. of 9.591 for the *Z2SEMWall* results and 2.436 for the *Z2SEMGFWall*. These results are scaled by the PDG scale factor and the results included in tables 5.4 and 5.5.

In table 5.6, the *GFWall* source matrix elements are compared to the stochastic source results, with and without PDG scaling factors, at a fixed cost of 1536 inversions. This corresponds to 128 configurations with *GFWall* sources. After rescaling, all of the fits agree with the value $B_K = 0.659(3)$ of ref. [128]. It is concluded that the stochastic

Source Configuration	Fit range	Fit value	χ^2/d.o.f.
1 wall, $t = 0$	7-25	0.6591(28)	1.353
2 walls, $t_1 = 5$, $t_2 = 27$	9-23	0.6634(26)	0.779

Table 5.7: Fits to the B_K three-point function using *GFWall* sources at fixed cost, comparing the single-wall source method to the traditional two-wall source method.

approach shows no advantage over the traditional method for the calculation of the B_K matrix element, although the *Z2SEMGFWall* correlators, which have the same structure as the *GFWall* correlators in the large N_{hits} limit, give comparable results at the same cost.

5.2.2 Comparison of the two-wall and single-wall approach to B_K

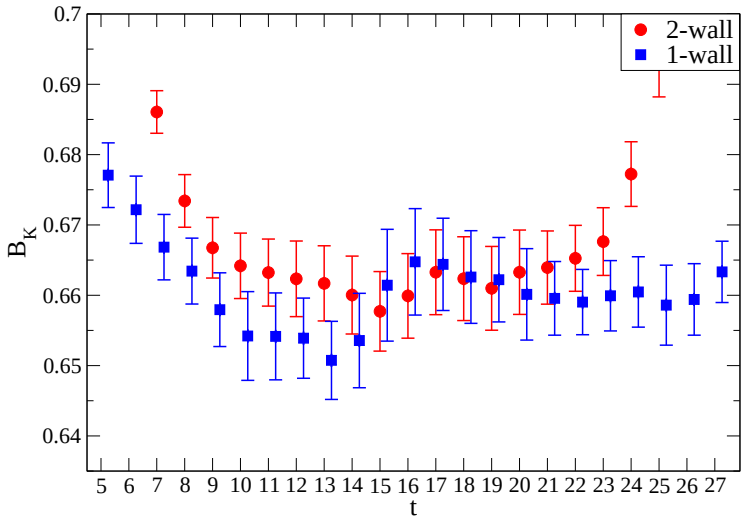

Figure 5.6: A comparison of the plateau of B_K calculated using the single-wall and two-wall approaches at a fixed cost in inversions. The two-wall sources reside on timeslices 5 and 27.

Comparing the results of the previous section to those in ref. [128], a comparison of the single-wall approach to the calculation of B_K with the traditional two-wall method can be made. Recall that the single-wall approach uses a single gauge-fixed wall source on the lattice time boundary, from which the $p+a$ and $p-a$ combinations of boundary conditions allow forwards and backwards propagating states to be formed. The two-wall approach uses two temporally-separated gauge-fixed wall sources, from which the $p+a$ combination of boundary conditions is calculated from each wall to eliminate the

leading round-the-world contributions. The single-wall approach therefore costs half as much as the two-wall approach. The results are compared at fixed cost, using 196 configurations of single-wall data and 98 configurations of two-wall data. The sets of configurations overlap and are of a similar length, having configuration separations of 10 and 20 molecular dynamics time units respectively. Both data-sets are analysed with a bin size of 40 MD time units. The gauge fields of the single-wall calculation are shifted between configurations in order to reduce the effects of autocorrelations, whereas the two wall sources were fixed at $t = 5$ and 27. The results are given in table 5.7, and the plateaux are compared in figure 5.6. From these results it is concluded that the single-wall method gives equivalent results at fixed cost. However, this method affords the sampling of more timeslices and configurations than the two-wall approach for the same cost. As a result this strategy is adopted for the analysis of B_K on the $32^3 \times 64$ $\beta = 2.25$ ensembles detailed in section 6.6.

5.3 Stochastic calculation of three-point hadronic form factors

The $\bar{K}^0 \to \pi^+ l \nu_l$ form factor K_{l3} and the pion electromagnetic form factor are phenomenologically interesting parameters calculated from relatively simple meson three-point functions and the meson two-point correlators discussed in section 5.1. In the notation of ref. [132], the three-point functions have the form

$$\begin{aligned} C_{P_i P_f}(t_i, t, t_f, \vec{p}_i, \vec{p}_f) &= \sum_{\vec{x}_f, \vec{x}} e^{i\vec{p}_f \cdot (\vec{x}_f - \vec{x})} e^{i\vec{p}_i \cdot \vec{x}} \langle\, O_f(t_f, \vec{x}_f)\, V_\mu(t, \vec{x})\, O_i^\dagger(t_i, \vec{0})\,\rangle \\ &= \frac{Z_i\, Z_f}{4 E_i E_f} \langle\, P_f(\vec{p}_f)\,|\, V_\mu(0)\,|\, P_i(\vec{p}_i)\,\rangle \\ &\times \left\{ \theta(t_f - t)\, e^{-E_i(t - t_i) - E_f(t_f - t)} \;-\; \theta(t - t_f)\, e^{-E_i(T + t_i - t) - E_f(t - t_f)} \right\}, \end{aligned} \tag{5.33}$$

where pseudoscalar ($i, f \in \{\pi, K\}$) initial states P_i and final states P_f, with energies E_i and E_f respectively, are created using the interpolating operators $\mathcal{O}_{i,f} = \bar{\psi}_1 \gamma^5 \psi_2$ with fermions of the appropriate flavour. Here V_μ is the vector current operator and $Z_f = Z_i^* = \langle\, 0\,|\, O_f(0, \vec{0})\,|\, P_f\,\rangle$. The source and sink timeplanes t_i and t_f are typically fixed, with a large time separation to remove the round-the-world contribution.

After Wick contraction, the three-point function has the form

$$\mathrm{tr}\left(\mathcal{G}(\vec{0}, t_i \leftarrow \vec{x}_f, t_f) \gamma^5 \mathcal{G}(\vec{x}_f, t_f \leftarrow \vec{x}, t) \gamma^\mu \mathcal{G}(\vec{x}, t \leftarrow \vec{0}, t_i) \gamma^5 \right). \tag{5.34}$$

These propagators can be determined using a standard point source on the site $(\vec{0}, t_i)$ for the propagator $\mathcal{G}(\vec{x}, t \leftarrow \vec{0}, t_i)$ and a sequential propagator [133]

$$\mathcal{G}(\vec{0}, t_i \leftarrow \vec{p}_f, t_f \leftarrow \vec{x}, t) = \sum_{\vec{x}_f} \gamma_5 \left(\mathcal{G}(\vec{x}, t \leftarrow \vec{x}_f, t_f) \gamma^5 \mathcal{G}(\vec{x}_f, t_f \leftarrow \vec{0}, t_i)\, e^{-i\vec{p}_f \cdot \vec{x}_f} \right)^\dagger \gamma_5 \tag{5.35}$$

for the product $\mathcal{G}(\vec{0}, t_i \leftarrow \vec{x}_f, t_f)\gamma^5 \mathcal{G}(\vec{x}_f, t_f \leftarrow \vec{x}, t)$, including a Fourier transform over $\vec{x}_f$ to momentum $\vec{p}_f$ at the sink timeplane t_f. The Fourier transform of the trace is then performed over the vertex location $\vec{x}$, with the phase factor $e^{i(\vec{p}_i - \vec{p}_f)\cdot\vec{x}}$.

At zero spatial momentum $\vec{p}_i$ at t_i, a stochastic wall source can be used in place of the traditional point source, giving an estimate of the spatial volume average. The stochastic averaging to Kronecker deltas will occur on the source timeplane, with the second leg of the sequential propagator inverted on the stochastic solution vector. Note that although the stochastic sources explicitly project to zero source momentum, partially twisted boundary conditions [132][134] can be used in conjunction with this method to apply a residual momentum $\vec{p}_i$. Here the twisted boundary conditions (cf. section 4.2.7) are applied only in the valence sector.

The propagator contraction at the source location in eqn. 5.34 is performed without an intervening spin matrix, thus both *Z2PSWall* sources, as well as the more general *Z2SEMWall* sources, can be used for this calculation. This method has been adopted by the RBC & UKQCD collaboration [7] for the calculation of meson form factors. In the above, the authors compare the point source and stochastic approaches at a fixed statistical accuracy, concluding that the stochastic approach is vastly superior to the point source, offering similar statistical errors for less than ten percent of the computational cost. A similar approach is also used by the ETM collaboration [127].

5.4 Summary and conclusions

This chapter details an investigation into the use of stochastic wall sources for the improved calculation of meson two- and three-point functions using the one-end trick [120][123]. It is important to emphasise that this method is a different application of stochastic sources to that of approximating the all-to-all propagator for the calculation of disconnected correlation functions: the one-end trick uses the properties of the stochastic sources to offer a volume averaging of the standard connected correlation function alongside an overall reduction in computational cost.

Section 5.1.1 describes in detail the structure of two $\mathbb{Z}(2) \otimes \mathbb{Z}(2)$ stochastic wall source types, namely the *Z2PSWall* and *Z2SEMWall*, where the former is random in spin and colour space and the latter only in colour space. The form of the noise introduced into various measurements is discussed.

The viability of these source types for the calculation of meson two-point functions on the unit gauge and on a $16^3 \times 32$ Domain Wall QCD ensemble is demonstrated in sections 5.1.4 and 5.1.5. It is shown that both stochastic source types give errors on the pseudoscalar meson mass that are smaller by a factor of two or more than those of the conventional point source approach at the same cost. In addition to the reduced error, there is a substantial improvement in the quality of the plateaux (fig. 5.3), inspiring greater confidence in the results.

In principle the wall source techniques offer better sampling of low probability tails of the QCD functional distribution, for example physically significant contributions from rare, low eigenvalue modes of the Dirac matrix. Such modes are likely to produce outliers when sampled by a point source. The relative improvement of wall sources over point sources will likely increase with increasing lattice volume and decreasing quark mass, a feature in common with the low mode averaging approach [135][136].

The *Z2SEMWall* is also shown to be viable for other meson correlators, showing improved statistical error over the point source for the vector meson mass. It is therefore concluded that meson spectrum measurements such as masses and decay constants can be calculated with improved precision and confidence using the stochastic method.

In section 5.2 it is shown that stochastic sources are viable for the calculation of the neutral kaon mixing parameter, B_K. Here two additional stochastic source types are included in the analysis that stochastically estimate the Coulomb gauge fixed wall source (*GFWall*), each treating the spin-colour trace differently. These are referred to as *Z2PSGFWall* and *Z2SEMGFWall* sources. However, it is found that the more complex structure of these three-point functions is less well treated by stochastic methods. Multiple measurements using stochastic sources on the same configurations show disagreements in their central values outside of the jackknife error bars, forcing the application a PDG scale factor of $\sqrt{\chi^2/\text{d.o.f.}}$ to the error bars of the stochastic results. It is concluded that for three-point matrix elements of $\mathcal{O}_{VV+AA}$, the stochastic method offers no corresponding substantial gain over the traditional *GFWall* method.

It is also found that the use of a single *GFWall* source calculated with periodic and antiperiodic boundary conditions, from which the forwards $(p + a)$ and backwards $(p - a)$ propagating components can be calculated, offers comparable cost-effectiveness to the two-wall methods, but may allow more time origins or more configurations to be used when measurement cost is the limiting factor. As a result this technique is adopted for the high-precision measurements of B_K on the $32^3 \times 64$ ensemble sets in section 6.6.

Finally, in section 5.3 a method of stochastically estimating hadronic form factors is discussed. This method has been adopted by RBC&UKQCD for a calculation of the K_{l3} form factor [7], with the conclusion that a significant reduction in computational

cost can be achieved for the same statistical error using the stochastic method coupled with partially twisted boundary conditions.

The relative difference in gain between the K_{l3} form factor and B_K can be explained as follows. The standard *GFWall* method for the calculation of B_K already provides an exact three-volume average of the operator insertion point, and thus the only benefit of the stochastic wall method is in the reduced cost of the spin-colour tracing in the pseudoscalar interpolating operators. The results suggest that this is empirically ineffective.

In contrast, the requirement of non-zero momentum for K_{l3} results in a comparison of a localised source to a three-volume average, and there is much more scope for the stochastic volume average to gain. In this calculation, of course, momentum is injected using partially twisted boundary conditions, and thus the cost of requiring multiple inversions for different momenta must be included. It is certainly possible that, similar to B_K, a gauge fixed wall source in combination with partially twisted boundary conditions could result in an even greater improvement than the stochastic wall, by similarly providing an non-approximate volume average at similar cost.

Chapter 6

Lattice results for light hadronic quantities

This chapter details the analysis of two 2+1 flavour Domain Wall fermion ensemble sets at $\beta = 2.13$ and $\beta = 2.25$, and with lattice sizes of $24^3 \times 64$ and $32^3 \times 64$ respectively. Both ensemble sets have a fifth dimension of length $L_s = 16$, and use the Iwasaki gauge action. In this thesis the $32^3 \times 64$ ensemble set is labelled **A** and the $24^3 \times 64$ ensemble set **B**. The **B** ensembles were previously analysed in ref. [1], but since then have been doubled in statistics. This new analysis is performed on the expanded data sets. Details of the ensembles can be found in table 6.1. Note that for the **A** ensembles, configuration numbers are incremented every 2 molecular dynamics time units, hence adjacent configurations are separated by 20 MD time units.

All fits in this chapter are uncorrelated and use a frozen diagonal covariance matrix, although in practise the use of frozen or un-frozen covariance matrices has little effect on the result. Data on both ensemble sets are binned over 80 molecular dynamics time units, corresponding to 4 adjacent configurations on the **A** ensembles and 2 on the **B** ensembles, and are resampled using the jackknife procedure.

Both simulations are performed at a single heavy (strange-like) sea-quark mass of 0.03 and 0.04 in lattice units for the **A** and **B** ensemble sets respectively. To allow for later interpolation to the physical strange mass (determined in chapter 8), both simulations make use of reweighting in the sea strange quark sector. For the **A** ensembles, weights have been produced spanning the range between the simulated mass 0.03 and the mass 0.025. The **B** ensembles are reweighted over the range lying between the simulated mass of 0.04 and the mass 0.03. The weights were generated in sequential mass-steps, where the step-size Δm, alongside the number of stochastic samples of the determinant ratio N_ξ, contributes to the reweighting error. The **A** ensembles have $N_\xi = 4$ and mass increments of $\Delta m = 0.0005$, whereas the **B** ensembles use a smaller $N_\xi = 2$ compensated for by a smaller step size of $\Delta m = 0.00025$. Examples of effective mass plots at differing strange sea-quark masses can be found in each section of this chapter.

Propagators are generated from spatial wall sources on configurations fixed to

Lattice	m_h	m_l	traj.(# meas.)
A $(32^3 \times 64)$	0.03	0.004	260-3250 (300)
	0.03	0.006	500-3610 (312)
	0.03	0.008	260-2770 (252)
B $(24^3 \times 64)$	0.04	0.005	900-8940 (202)
	0.04	0.01	1460-8540 (178)

Table 6.1: Ensemble details. Here traj. refers to the Monte Carlo trajectories used in the measurements. The bracketed # meas. refers to the number of measurements, separated by 40 molecular dynamics time units (40 trajectories) for the B ensembles, and 20 MD time units (10 trajectories) for the A ensembles. To reduce the effects of auto-correlations the data are block-averaged over 80 MD time units, and the blocked measurements are used for the purposes of statistical analysis.

Coulomb gauge. From these, wall-local (LW) correlation functions are measured by contracting the propagators at the sink location to form the appropriate interpolating operator. Wall-wall (WW) correlation functions are also measured, for which the sink operator is formed from propagators that have been spatially summed over the sink timeslice prior to contraction. This is performed for each timeslice. In addition, Coulomb gauge fixed box-source propagators are used to generate box-local (LB) baryon correlation functions. In this thesis, only the Omega baryon $|sss\rangle$ is relevant, as it is used to obtain the lattice spacings in chapter 8. Here the two-letter descriptions of the correlation functions, for example LW for wall-local and LB for box-local correlators, give the source type on the right and the sink type on the left, following the ordering of the operators in the correlation function.

On the **A** ensembles, the wall-source propagators are generated from a single source on timeslice $\tau = 0$ with both periodic p and antiperiodic a boundary conditions, from which forwards $f = p + a$ and backwards $b = p - a$ propagating states are formed. On the **B** ensembles, propagators are calculated from two wall-sources at $\tau = 5$ and 57, again with both periodic and antiperiodic boundary conditions. Here the correlators containing p and a propagators are averaged together, removing the unwanted round-the-world contributions and increasing statistics. The single-wall and two-wall approaches were compared for the B_K matrix element in section 5.2.2, with the conclusion that although comparable results are obtained, the single-wall approach benefits from the sampling of more independent gauge configurations for the same computational cost. The latter approach was taken to optimise the measurement of B_K on the **A** ensembles. Following the procedure outlined in the previous chapter, the position of the wall source on the **A** configurations is varied between configurations to reduce correlations by applying a shift of $\delta = 16$ in the time-direction to the gauge fields on each subsequent configuration.

The box-source propagators are generated on both ensemble sets using anti-periodic

boundary conditions and sources on the $\tau = 0$ and $\tau = 32$ timeplanes. The sources have physical volumes of 16^3 and 20^3 on the **A** and **B** ensembles respectively.

The layout of this chapter is as follows. The residual mass $m_{\rm res}$ and the axial renormalisation Z_A are determined for both lattices. Here $m_{\rm res}$ is needed to extrapolate Z_A to the chiral limit, the result of which is used in the determination of the pseudoscalar decay constants. The pseudoscalar masses are then obtained by simultaneously fitting to five wall-local and wall-wall correlation functions containing combinations of pseudoscalar and axial-vector interpolating operators. The amplitudes of the correlation functions are then combined with Z_A in order to determine the pseudoscalar decay constants. The B_K matrix element is then measured using wall-local correlation functions and the Omega baryon masses are obtained from the box-local baryon correlation functions. Finally the Sommer scale r_0 and the related scale r_1 are determined.

In each section, effective mass plots are shown for the lightest ensemble in each set, both at the simulated strange sea-quark mass and at the closest reweighted value to the physical strange sea-quark mass. Tables of the data at the simulated and physical strange quark mass are presented. For quantities with only light valence quark masses, the latter are obtained by linearly interpolating over the reweighted data. For quantities with heavy valence quarks, the heavy sea-quark mass is first reweighted until it is equal to the heavy valence-quark mass, then the interpolation to the physical strange quark mass is performed over the now unitary data.

The physical strange quark mass is determined in chapter 8 using three different ansätze for the chiral extrapolation. The ChPT-fv and ChPT ansätze derive from NLO $SU(2)$ ChPT with and without finite volume corrections respectively, and the analytic ansatz uses planar fit forms. Here only the result obtained using the analytic ansatz is used. However as the determinations differ by only $\sim 0.3\%$ (table 8.7), the dependence of the data at the physical strange quark mass on the chiral ansatz is very small.

Concerning the nomenclature used in this chapter and also chapter 8, the simulated partially-quenched valence quark masses are labelled m_x and m_y, and the simulated light and heavy sea-quark masses are labelled m_l and m_h respectively. A generic valence quark mass is labelled m_v. The physical strange quark mass is either explicitly labelled m_s, or is referred to as the physical m_h ($m_h^{\rm phys}$). Similarly the physical averaged up/down quark mass is labelled $m_{u/d}$ or is referred to as the physical m_l ($m_l^{\rm phys}$).

6.1 The residual mass $m_{\rm res}$

The residual mass, $m_{\rm res}$, is the additive correction to the lattice bare quark masses resulting from the residual chiral symmetry breaking of Domain Wall fermions.

Following the discussion in section 4.1.3, m_{res} is obtained by taking the unitary massless limit of the quantity m'_{res}, defined in eqn. 4.41. In terms of lattice correlation functions, m'_{res} is obtained as a function of the partially-quenched valence and sea quark masses, m_x and m_l, by measuring the ratio

$$R(t) = \frac{\sum_{\vec{x}} \langle J^a_{5q}(\vec{x}, t)\pi^a(0)\rangle}{\sum_{\vec{x}} \langle J^a_5(\vec{x}, t)\pi^a(0)\rangle} \tag{6.1}$$

in the limit of large lattice times, calculated using valence quarks of mass m_x on an ensemble with light sea-quark mass m_l. Both the 4d pseudoscalar density $\langle J^a_5\pi^a\rangle$ and the midpoint term $\langle J^a_{5q}\pi^a\rangle$ are calculated during the evaluation of the wall source propagators. Here the form of the source is unimportant as the effect on the pion amplitudes at the source location of the correlators is cancelled in the ratio, and only the large t dependence is of interest.

The calculation proceeds as follows. The ratio $R(t)$ is formed on each ensemble from propagators with antiperiodic boundary conditions and the full range of dynamical masses. Using the time-symmetry of the correlators, the data are averaged about $t = 32$. The asymptotic time dependence is determined by fitting the ratio to a constant, $m'_{\text{res}}(m_x, m_l)$, at large lattice times. Figure 6.1 contains plots of $R(t)$ with unitary masses as a function of lattice time, on the lightest ensembles of the **A** and **B** ensemble sets respectively. Using such plots, the fit ranges are chosen as 4–30 and 10–32. The resulting values of $m'_{\text{res}}(m_x, m_l)$ for the full range of valence and sea quark masses are given in tables 6.2 and 6.3 at the simulated strange quark mass and in tables 6.4 and 6.5 at the physical strange quark mass. m_{res} is obtained by taking the linear chiral limit of the unitary data, $m'_{\text{res}}(m_l, m_l)$. The chiral fits to m'_{res} are shown in figure 6.2, and the resulting values of m_{res} are given in table 6.1. The strange sea-quark mass dependence of m_{res} in the massless ($m_l = 0$) limit is shown in figure 6.3.

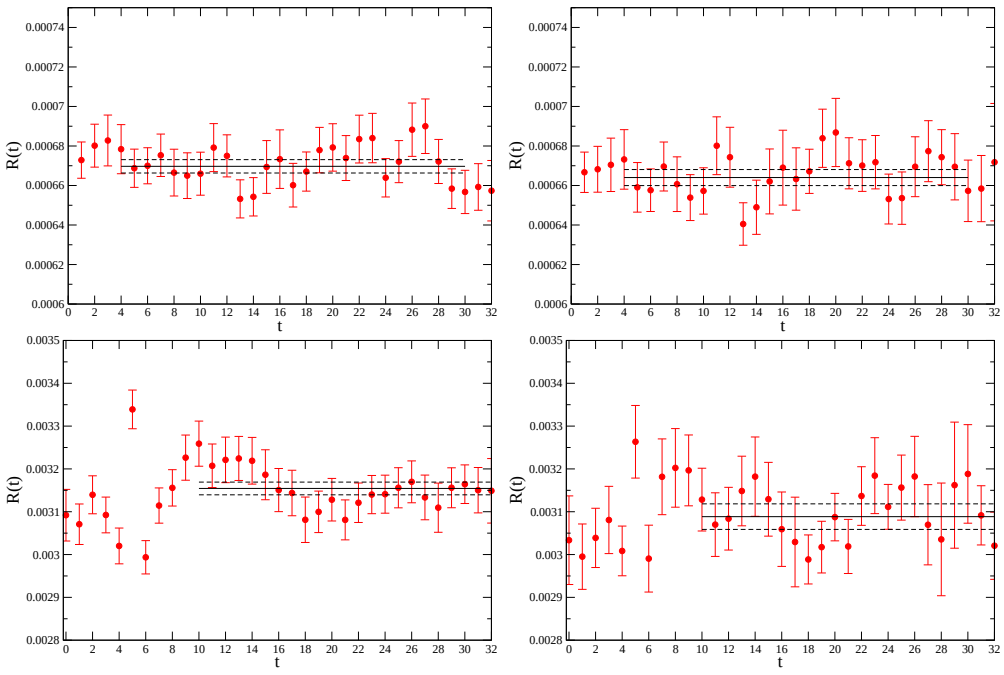

Figure 6.1: Fits of the ratio $R(t)$ on both ensemble sets. The upper plots show the fits, over the range 4–30, of the ratio calculated with $m_x = m_l = 0.004$ on the **A** ensemble set at the simulated strange mass $m_h = 0.03$ (top-left), and at the closest reweighted strange quark mass $m_h = 0.027$ to the physical value (top-right). The lower plots show the fits, over the range 10–32, of the ratio calculated with $m_x = m_l = 0.005$ on the **B** ensemble set at the simulated strange mass $m_h = 0.04$ (bottom-left), and at the closest reweighted strange quark mass $m_h = 0.0345$ to the physical value (bottom-right).

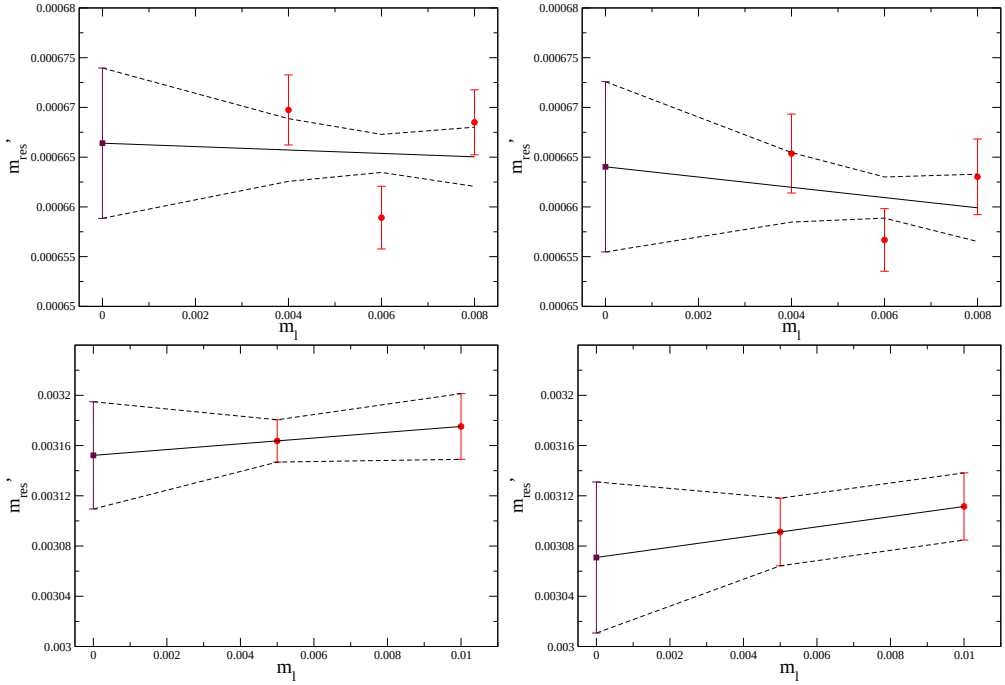

Figure 6.2: The chiral extrapolation of m'_{res} (circles) on both ensemble sets. The upper plots show the extrapolation over the **A** ensembles at the simulated strange quark mass $m_h = 0.03$ (top-left) and at the closest reweighted strange mass $m_h = 0.027$ to the physical value (top-right). The lower plots show the extrapolation over the **B** ensembles at the simulated strange mass $m_h = 0.04$ (bottom-left) and at the closest reweighted strange quark mass $m_h = 0.0345$ to the physical value (bottom-right). The extrapolated value of m_{res} (square) is also shown.

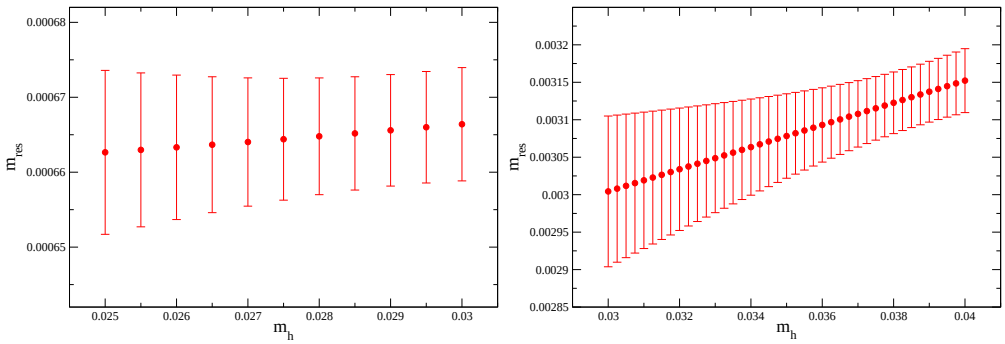

Figure 6.3: Strange sea quark mass dependence of m_{res} on the **A** ensemble set (left) and the **B** ensemble set (right).

m_x	m_l		
	0.004	0.006	0.008
0.002	0.000676(4)	0.000669(3)	0.000682(4)
0.004	0.000670(3)	0.000665(3)	0.000679(4)
0.006	0.000662(3)	0.000659(3)	0.000674(4)
0.008	0.000655(3)	0.000652(3)	0.000668(3)
0.025	0.000609(2)	0.000609(2)	0.000622(3)
0.03	0.000599(2)	0.000600(2)	0.000612(2)

Table 6.2: $m'_{\rm res}$ on the **A** ensemble set at the simulated strange quark mass, $m_h = 0.03$.

m_x	m_l	
	0.005	0.01
0.001	0.00319(2)	0.00329(3)
0.005	0.00315(2)	0.00326(3)
0.01	0.00308(1)	0.00319(2)
0.02	0.00294(1)	0.00304(2)
0.03	0.00282(1)	0.00292(2)
0.04	0.00273(1)	0.00282(2)

Table 6.3: $m'_{\rm res}$ on the **B** ensemble set at the simulated strange quark mass, $m_h = 0.04$.

m_x	m_l		
	0.004	0.006	0.008
0.002	0.000671(4)	0.000667(4)	0.000678(5)
0.004	0.000666(4)	0.000663(3)	0.000675(4)
0.006	0.000658(4)	0.000657(3)	0.000669(4)
0.008	0.000651(4)	0.000650(3)	0.000663(4)
0.025	0.000606(3)	0.000606(2)	0.000618(3)
0.03	0.000596(3)	0.000596(2)	0.000608(3)

Table 6.4: $m'_{\rm res}$ on the **A** ensemble set at the physical strange quark mass.

m_x	m_l	
	0.005	0.001
0.001	0.00314(3)	0.00322(3)
0.005	0.00309(3)	0.00319(3)
0.01	0.00302(3)	0.00312(3)
0.02	0.00289(3)	0.00298(3)
0.03	0.00277(2)	0.00286(2)
0.04	0.00268(2)	0.00276(2)

Table 6.5: $m'_{\rm res}$ on the **B** ensemble set at the physical strange quark mass.

m_h	$m_{\text{res}}^{\mathbf{A}}$	$m_{\text{res}}^{\mathbf{B}}$
m_h^{sim}	0.000666(8)	0.00315(4)
m_h^{phys}	0.000664(8)	0.00307(6)

Table 6.6: m_{res}, defined as the limit of m'_{res} at zero quark mass, on the **A** and **B** ensemble sets, at the simulated and physical strange sea-quark masses.

6.2 The axial current renormalisation coefficient Z_A

The axial current renormalisation coefficient Z_A relates the PCAC $\mathcal{A}_\mu^a$ of eqn. 4.31 to the local 4d axial current A_μ^a of eqn. 4.32 via the relation given in eqn. 4.33. It is obtained by fitting to the improved form [86][100]

$$Z_A = \frac{1}{t_{\max} - t_{\min}} \sum_{t=t_{\min}}^{t_{\max}} \frac{1}{2} \left\{ \frac{C(t+\frac{1}{2}) - C(t-\frac{1}{2})}{2L(t)} + \frac{2C(t+\frac{1}{2})}{L(t)+L(t+1)} \right\}, \tag{6.2}$$

where $t_{\min}$ and $t_{\max}$ bound the fit range,

$$C(t+\tfrac{1}{2}) = \sum_{\vec{x}} \langle \mathcal{A}_\mu^a(\vec{x},t)\pi^a(\vec{0},0)\rangle \quad \text{and} \quad L(t) = \sum_{\vec{x}} \langle A_\mu^a(\vec{x},t)\pi^a(\vec{0},0)\rangle \,. \tag{6.3}$$

The $\frac{1}{2}$ in the arguments is necessary because the PCAC current is not defined on the site x, but on the link between x and $x+\hat{\mu}$ (cf. eqn 4.28). Both terms on the right-hand side of eqn. 6.2 estimate Z_A without $\mathcal{O}(a)$ errors, and the combination was chosen to minimise those at $\mathcal{O}(a^2)$ following ref. [100].

In a similar way to m_{res}, the wall-local correlators are averaged about the midpoint and fit to eqn. 6.2 over a sensible plateau. The quantities are then extrapolated to the full chiral limit $m_l = -m_{\text{res}}$. The fits, shown in figure 6.4, are also performed over the ranges 4–30 and 10–32 for the **A** and **B** ensemble sets respectively, giving the results in tables 6.2 and 6.2. The chiral extrapolations are shown in figure 6.5, and the results are included in the tables above. The dependence of Z_A on the strange sea-quark mass in the chiral limit is shown in figure 6.6.

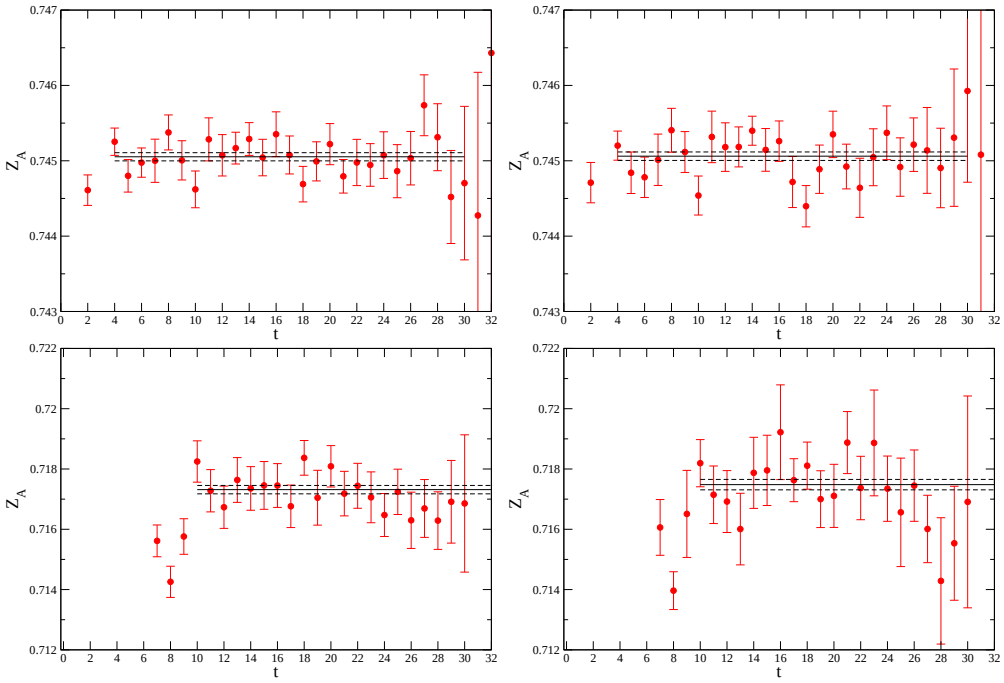

Figure 6.4: Fits to the quantity Z_A on both ensemble sets. The upper plots show the fits, over the range 4–30, of the quantity calculated with $m_x = m_l = 0.004$ on the **A** ensemble set at the simulated strange quark mass $m_h = 0.03$ (top-left), and at the closest reweighted strange quark mass $m_h = 0.027$ to the physical value (top-right). The lower plots show the fits, over the range 10–32, of the quantity calculated with $m_x = m_l = 0.005$ on the **B** ensemble set at the simulated strange quark mass $m_h = 0.04$ (bottom-left), and at the closest reweighted strange quark mass $m_h = 0.0345$ to the physical value (bottom-right).

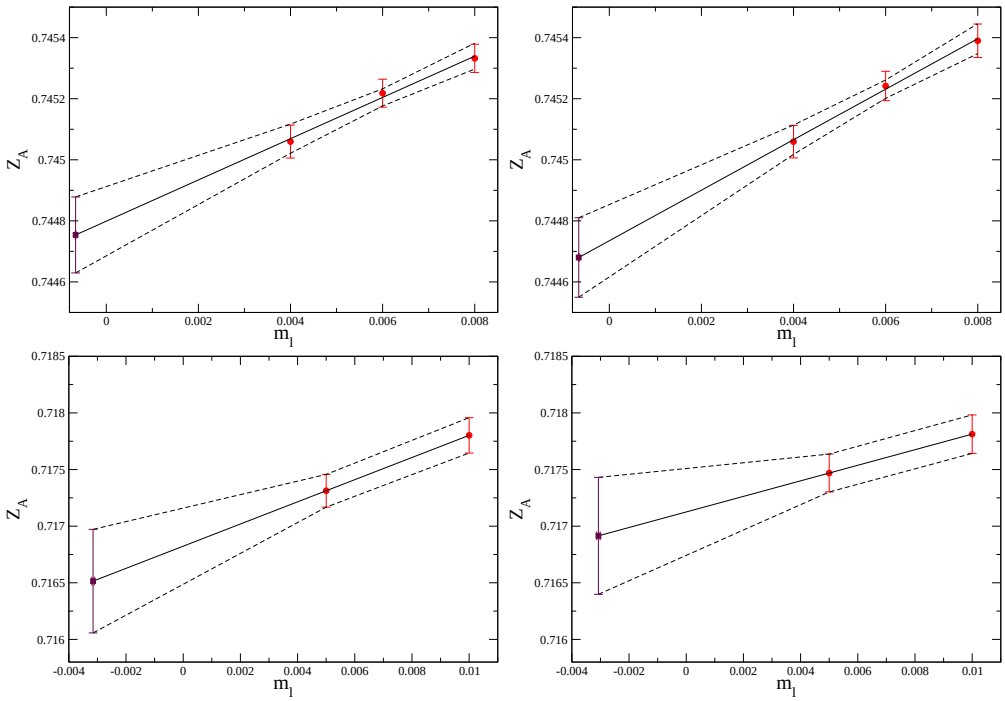

Figure 6.5: The chiral extrapolation of Z_A (circles) on both ensemble sets. The upper plots show the extrapolation over the **A** ensembles at the simulated strange quark mass $m_h = 0.03$ (top-left), and at the closest reweighted strange quark mass $m_h = 0.027$ to the physical value (top-right). The lower plots show the extrapolation over the **B** ensembles at the simulated strange quark mass $m_h = 0.04$ (bottom-left), and at the closest reweighted strange quark mass $m_h = 0.0345$ to the physical value (bottom-right). The value of Z_A in the chiral limit (square) is also shown.

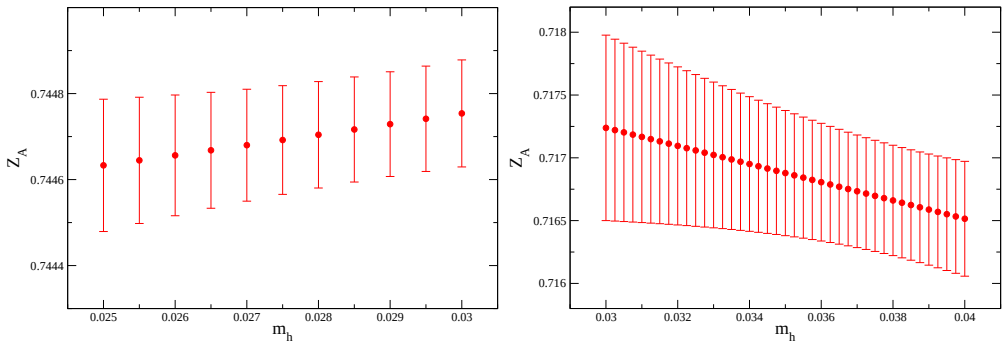

Figure 6.6: The strange sea quark mass dependence of Z_A on the **A** ensemble set (left) and the **B** ensemble set (right).

m_h	$Z_A(chiral)$	$Z_A(m_l = 0.004)$	$Z_A(m_l = 0.006)$	$Z_A(m_l = 0.008)$
$m_h^{\rm sim} = 0.03$	0.74475(12)	0.74505(5)	0.74522(5)	0.74533(5)
$m_h^{\rm phys}$	0.74468(13)	0.74506(5)	0.74524(5)	0.74539(6)

Table 6.7: Z_A on the **A** ensemble set, at the simulated and physical strange sea-quark masses.

m_h	$Z_A(chiral)$	$Z_A(m_l = 0.005)$	$Z_A(m_l = 0.01)$
$m_h^{\rm sim} = 0.04$	0.7165(5)	0.7173(1)	0.7178(2)
$m_h^{\rm phys}$	0.7169(5)	0.7175(2)	0.7178(2)

Table 6.8: Z_A on the **B** ensemble set, at the simulated and physical strange sea-quark masses.

6.3 Pseudoscalar masses

Following refs. [1] and [137], the pseudoscalar masses and correlator amplitudes are obtained by simultaneously fitting to the following five correlation functions:

$$\langle A^L(t)|P^W(0)\rangle, \quad \langle A^L(t)|A^W(0)\rangle, \quad \langle P^L(t)|P^W(0)\rangle, \quad \langle A^W(t)|P^W(0)\rangle, \quad \langle P^W(t)|P^W(0)\rangle\,. \tag{6.4}$$

Here the superscript indicates the source (right) or sink (left) meson source type, P stands for the pseudoscalar interpolating operator and A the interpolating operator of the fourth Euclidean component of the local axial current A_4. The amplitudes of the correlators are labelled

$$\mathcal{N}_{AP}^{LW}, \quad \mathcal{N}_{AA}^{LW}, \quad \mathcal{N}_{PP}^{LW}, \quad \mathcal{N}_{AP}^{WW}, \quad \text{and} \quad \mathcal{N}_{PP}^{WW} \tag{6.5}$$

respectively.

On the **A** ensembles, correlation functions obtained using the forwards (f) and backwards (b) propagators are averaged for better statistics. This requires a time-reflection $Y(t) \to Y(T-t)$ of the correlation functions of the backwards propagating states. The AP correlators pick up a minus sign under time-reflection which is cancelled by a further reflection about the t-axis $Y(t) \to -Y(t)$.

As previously mentioned, the correlation functions on the **B** ensembles are obtained from two wall sources at $\tau = 5$ and 57, averaging over states containing p and a propagators. These are combined together for better statistics by first translating both correlators in time such that the sources lie on the origin $t = 0$. The $\tau = 57$ correlators are then time-reflected as above and the two correlators are averaged.

The PP and AA correlation functions are fit to the 'cosh' form

$$Y(t; m_x, m_y) = \mathcal{N}_{xy}\Big\{ \exp\Big(- m_{xy}t\Big) + \exp\Big(- m_{xy}(2T - t)\Big)\Big\} \tag{6.6}$$

and the AP correlators are fit to the 'sinh' form

$$Y(t; m_x, m_y) = \mathcal{N}_{xy}\Big\{ \exp\Big(- m_{xy}t\Big) - \exp\Big(- m_{xy}(2T - t)\Big)\Big\}, \tag{6.7}$$

where x and y index the valence quark masses, m_{xy} is the pseudoscalar mass and the minus sign on the backwards propagating component of eqn. 6.7 appears as discussed above. Here the backwards propagating state from the boundary at $t = T$ is cancelled by the $p + a$ combination of boundary conditions, leaving only the doubly-suppressed states propagating from the boundary at $t = 2T$. At large t, the amplitudes are simply the product of the overlaps of the source and sink interpolating operators with the pion intermediate state, normalised in the usual relativistic fashion:

$$\mathcal{N}^{s_1 s_2}_{\mathcal{O}_1\mathcal{O}_2} = \frac{\langle 0|\mathcal{O}_1^{s_1}|\pi\rangle\langle\pi|\mathcal{O}_2^{s_2}|0\rangle}{2m_{xy}V}, \tag{6.8}$$

where V is the spatial volume.

Figures 6.7 and 6.8 each contain plots of the unitary effective pion mass m_{ll} for the five correlators on the $m_l = 0.004$ ensemble of set **A** , at the simulated and physical strange quark masses respectively. Figures 6.9 and 6.10 show the same for the $m_x = 0.004$, $m_y = 0.03$ kaon, in which only the strange sea quark mass has been adjusted. These plots are overlaid by the mass obtained from a simultaneous fit to the five correlators over the range $t = 12$–52 on both ensemble sets. The fitted masses at the simulated strange quark mass, for all combinations of valence quark masses on each ensemble, are given in table 6.9. Tables 6.10 and 6.11 contain the pion and kaon masses at the (unitary) physical strange quark mass. Here the cut separating 'light' from 'heavy' valence quarks has been set at $m_v = 0.008$. As mentioned in the introduction to this chapter, the kaon masses are obtained by first reweighting the kaonic pseudoscalars ($m_y = 0.03$ and 0.025) such that $m_h = m_x$, then linearly interpolating in the now-unitary heavy quark mass at fixed m_x to the physical strange quark mass.

Figures 6.11–6.14 show the equivalent plots to those above for the $m_l = 0.005$ ensemble of set **B** . Here the apparent oscillatory behaviour evident for example in figure 6.11 is likely due to statistical fluctuations in the gauge fields that are correlated in time. On the **B** ensembles, the simultaneous fits are performed over the range $t = 10 - 50$. The strange sea quark mass dependence of the fitted masses on both ensemble sets is shown in figure 6.15. Table 6.12 contains the pseudoscalar meson masses at the simulated strange sea quark mass, and tables 6.13 and 6.14 contain the pion and kaon masses at the physical strange sea quark mass. Here, following ref. [1],

the cut on the maximum light quark mass on the **B** ensembles is chosen at $m_v = 0.01$, and the states with $m_x = 0.02$ are deemed too light to be kaons.

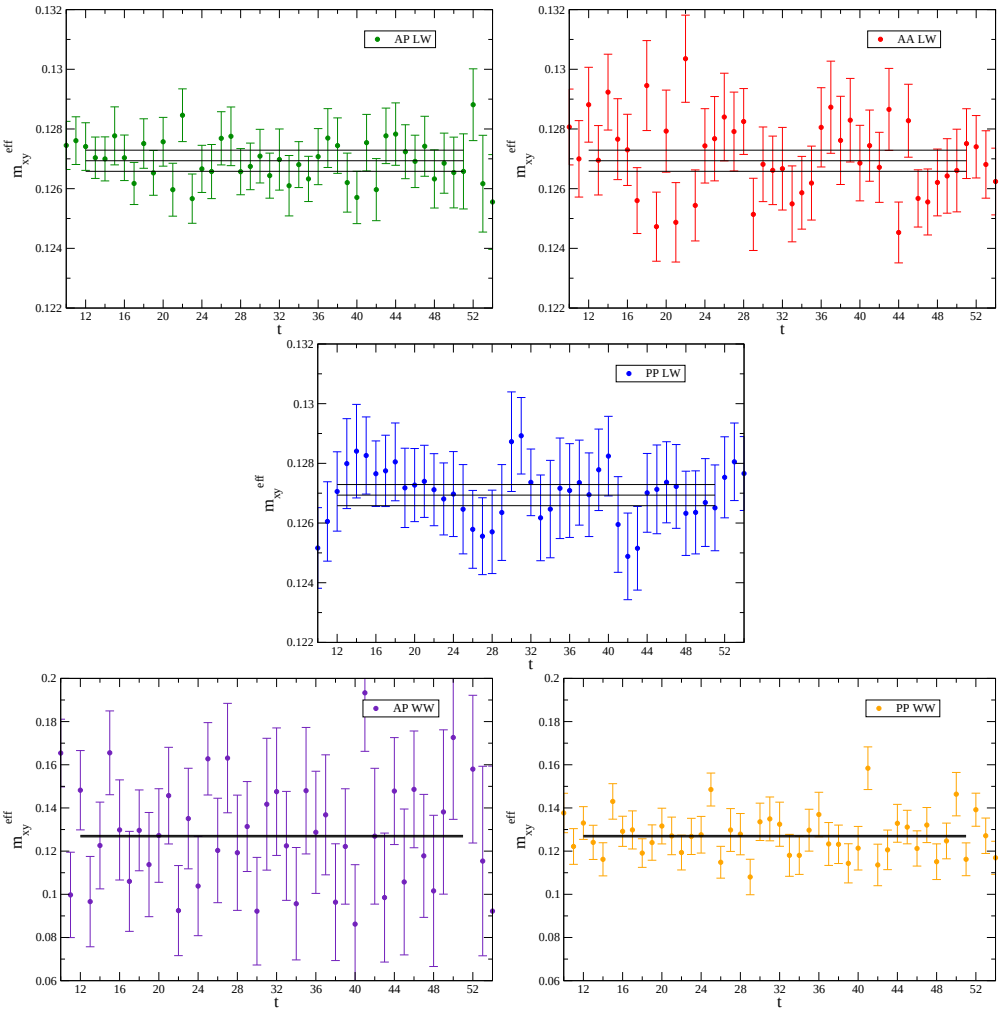

Figure 6.7: Effective mass plots of the light-light AP (top-left), AA (top-right) and PP (centre) wall-local pion correlators, and the light-light AP (bottom-left) and PP (bottom-right) wall-wall pion correlators, on the **A** ensemble set with $m_x = m_y = m_l = 0.004$ and m_h at the simulated strange quark mass, $m_h = 0.03$. These are overlaid by the result of a simultaneous fit to the five correlators over the range 12–52. The wall-wall correlators are shown on a different scale to the wall-local correlators as they are considerably noisier.

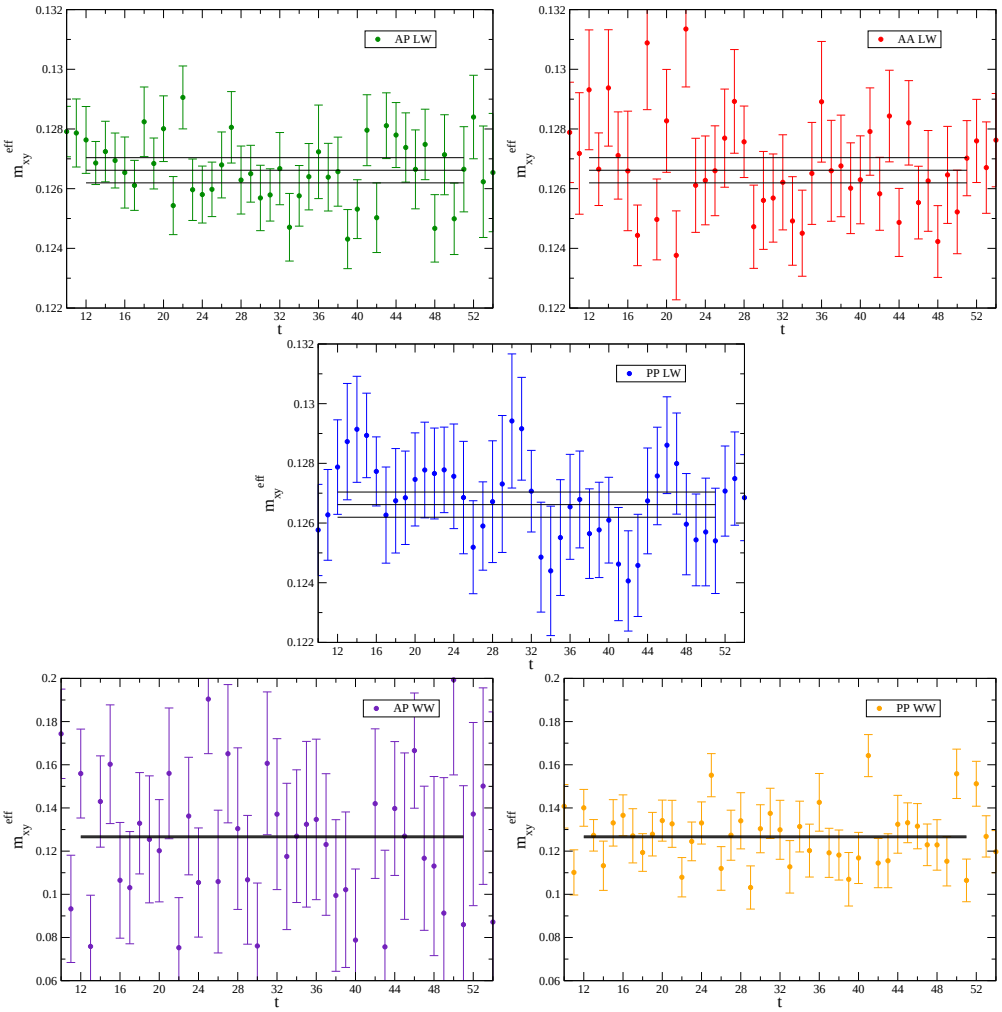

Figure 6.8: Effective mass plots of the light-light AP (top-left), AA (top-right) and PP (centre) wall-local pion correlators, and the light-light AP (bottom-left) and PP (bottom-right) wall-wall pion correlators, on the **A** ensemble set with $m_x = m_y = m_l = 0.004$ and m_h at the closest reweighted strange mass $m_h = 0.027$ to the physical value. These are overlaid by the result of a simultaneous fit to the five correlators over the range 12–52. The wall-wall correlators are shown on a different scale to the wall-local correlators as they are considerably noisier.

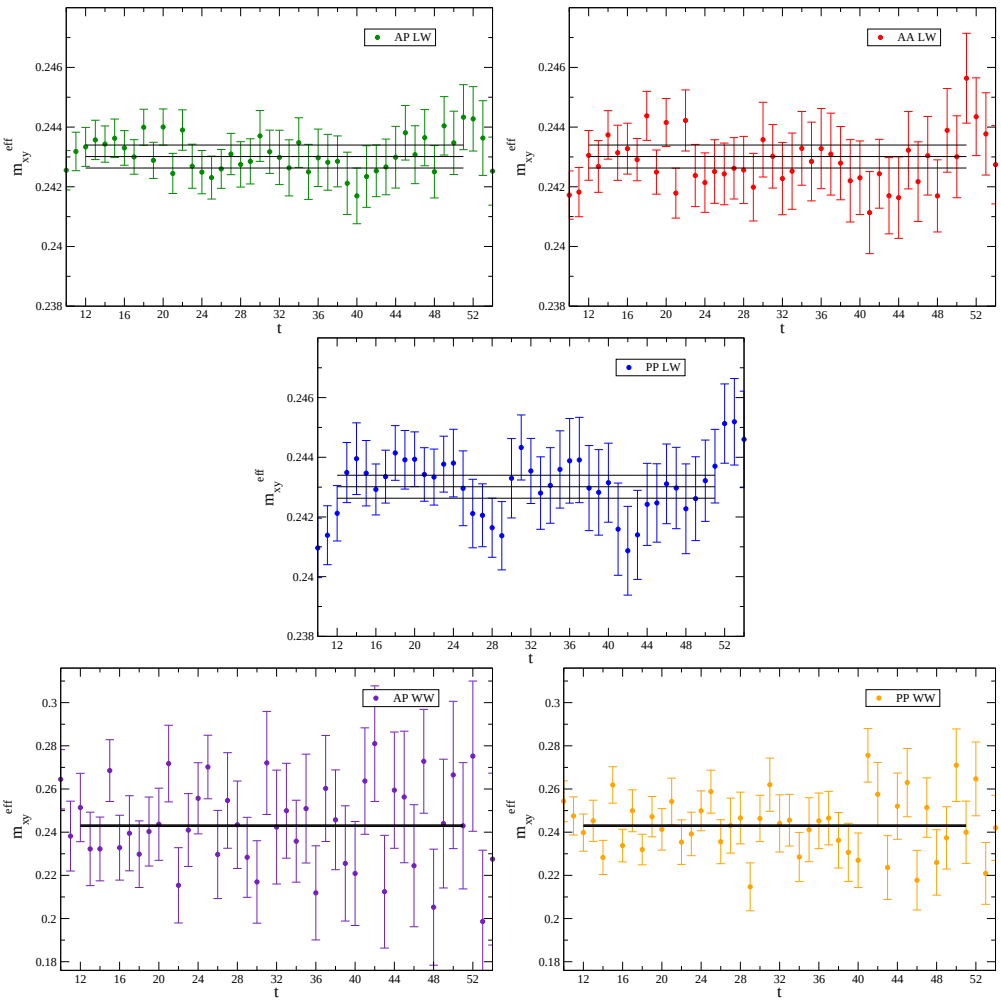

Figure 6.9: Effective mass plots of the heavy-light AP (top-left), AA (top-right) and PP (centre) wall-local kaon correlators, and the heavy-light AP (bottom-left) and PP (bottom-right) wall-wall kaon correlators, on the **A** ensemble set with $m_x = m_l = 0.004$ and m_y and m_h at the simulated strange quark mass $m_y = m_h = 0.03$. These are overlaid by the result of a simultaneous fit to the five correlators over the range 12–52. The wall-wall correlators are shown on a different scale to the wall-local correlators as they are considerably noisier.

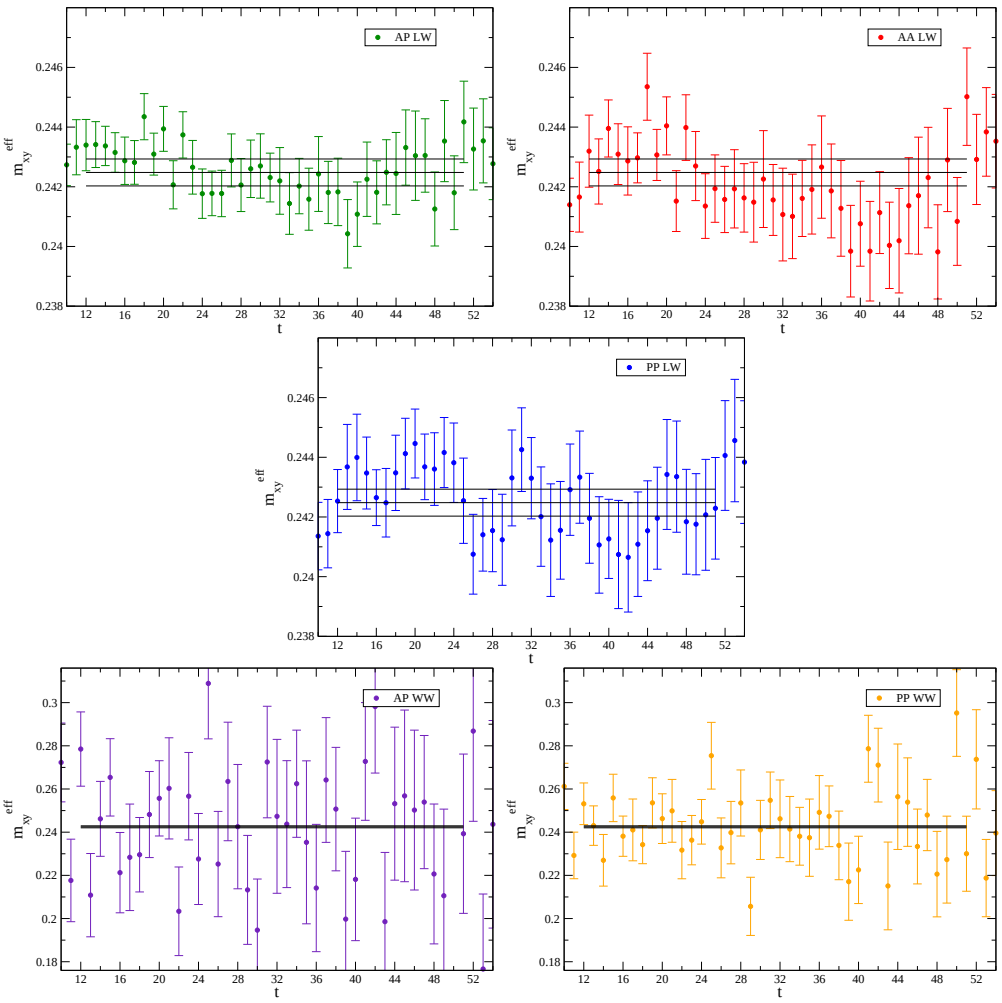

Figure 6.10: Effective mass plots of the heavy-light AP (top-left), AA (top-right) and PP (centre) wall-local kaon correlators, and the heavy-light AP (bottom-left) and PP (bottom-right) wall-wall kaon correlators, on the **A** ensemble set with $m_x = m_l = 0.004$, $m_y = 0.03$ and m_h at the closest reweighted strange mass $m_h = 0.027$ to the physical value. These are overlaid by the result of a simultaneous fit to the five correlators over the range 12–52. The wall-wall correlators are shown on a different scale to the wall-local correlators as they are considerably noisier.

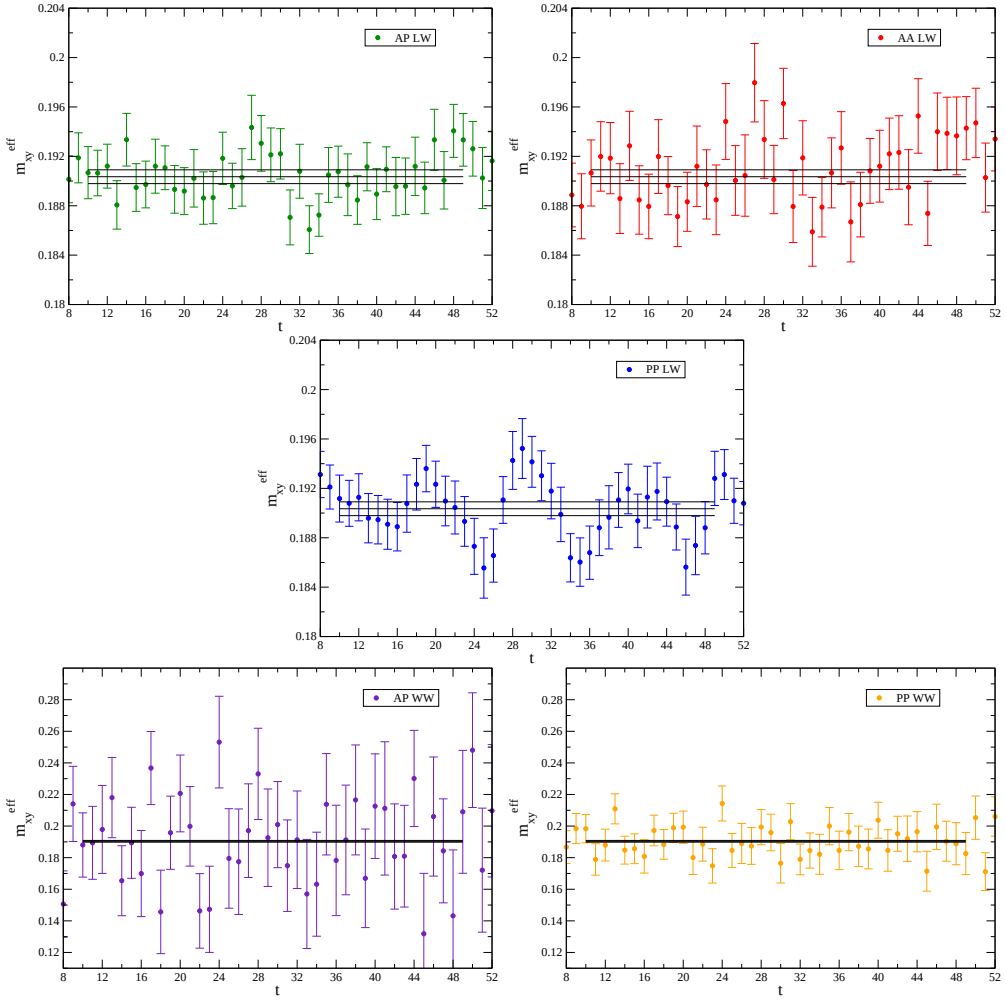

Figure 6.11: Effective mass plots of the light-light AP (top-left), AA (top-right) and PP (centre) wall-local pion correlators, and the light-light AP (bottom-left) and PP (bottom-right) wall-wall pion correlators, on the **B** ensemble set with $m_x = m_y = m_l = 0.005$ and m_h at the simulated strange quark mass, $m_h = 0.04$. These are overlaid by the result of a simultaneous fit to the five correlators over the range 10–50. The wall-wall correlators are shown on a different scale to the wall-local correlators as they are considerably noisier.

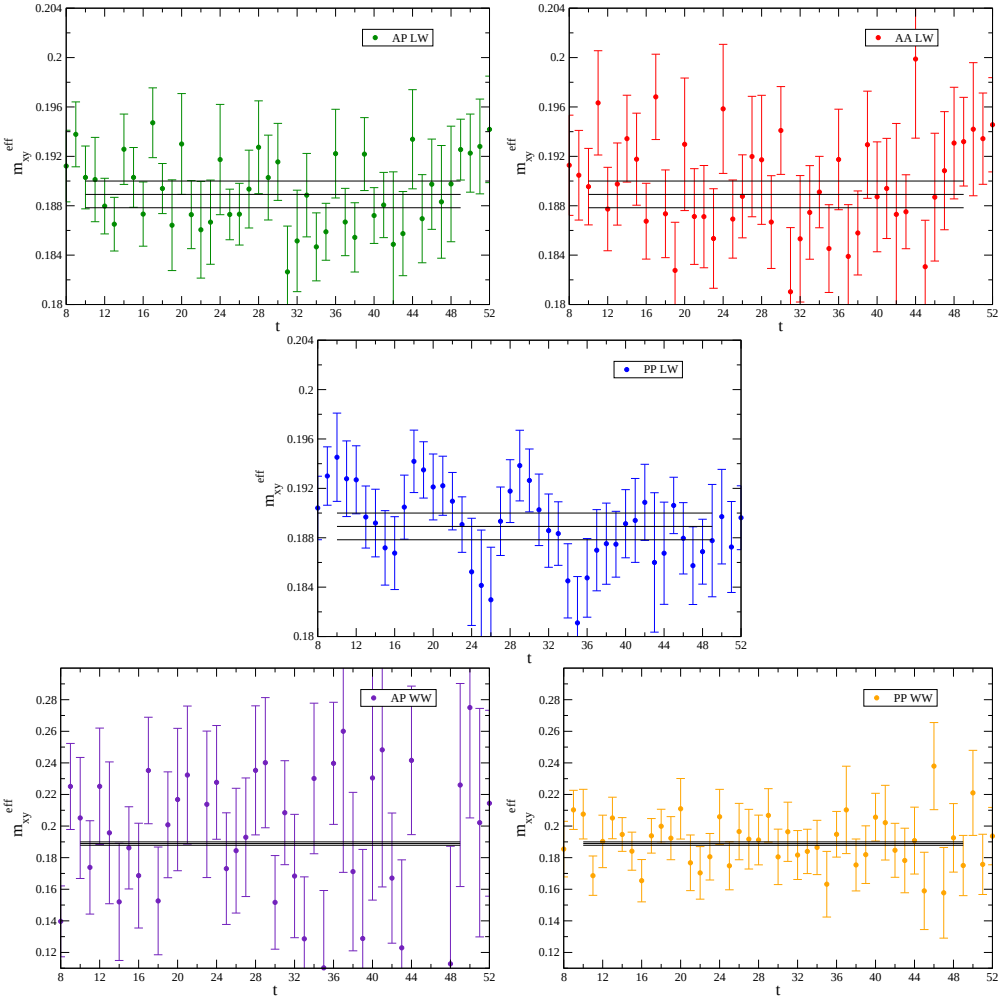

Figure 6.12: Effective mass plots of the light-light AP (top-left), AA (top-right) and PP (centre) wall-local pion correlators, and the light-light AP (bottom-left) and PP (bottom-right) wall-wall pion correlators, on the **B** ensemble set with $m_x = m_y = m_l = 0.005$ and m_h at the closest reweighted strange mass $m_h = 0.0345$ to the physical value. These are overlaid by the result of a simultaneous fit to the five correlators over the range 10–50. The wall-wall correlators are shown on a different scale to the wall-local correlators as they are considerably noisier.

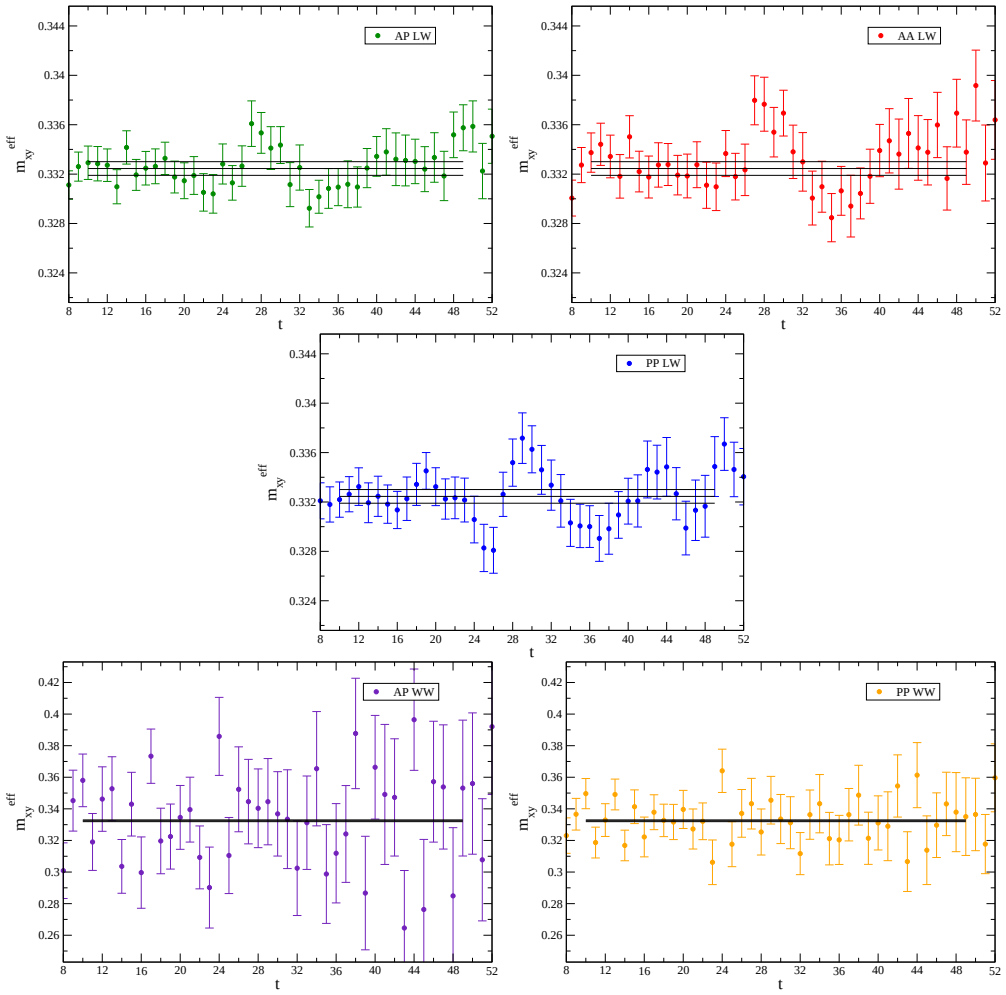

Figure 6.13: Effective mass plots of the heavy-light AP (top-left), AA (top-right) and PP (centre) wall-local kaon correlators, and the heavy-light AP (bottom-left) and PP (bottom-right) wall-wall kaon correlators, on the **B** ensemble set with $m_x = m_l = 0.005$ and m_y and m_h at the simulated strange quark mass, $m_y = m_h = 0.04$. These are overlaid by the result of a simultaneous fit to the five correlators over the range 10–50. The wall-wall correlators are shown on a different scale to the wall-local correlators as they are considerably noisier.

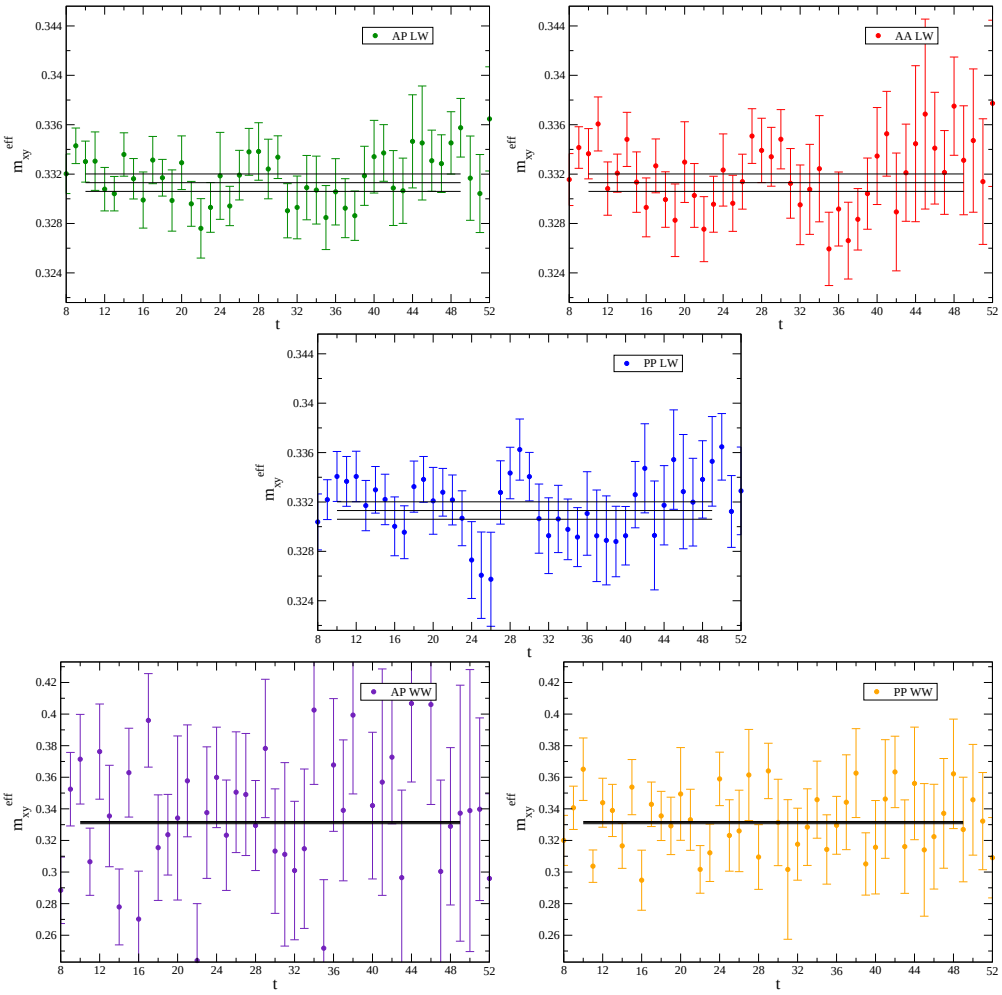

Figure 6.14: Effective mass plots of the heavy-light AP (top-left), AA (top-right) and PP (centre) wall-local kaon correlators, and the heavy-light AP (bottom-left) and PP (bottom-right) wall-wall kaon correlators, on the **B** ensemble set with $m_x = m_l = 0.005$, $m_y = 0.04$ and m_h at the closest reweighted strange mass $m_h = 0.0345$ to the physical value. These are overlaid by the result of a simultaneous fit to the five correlators over the range 10–50. The wall-wall correlators are shown on a different scale to the wall-local correlators as they are considerably noisier.

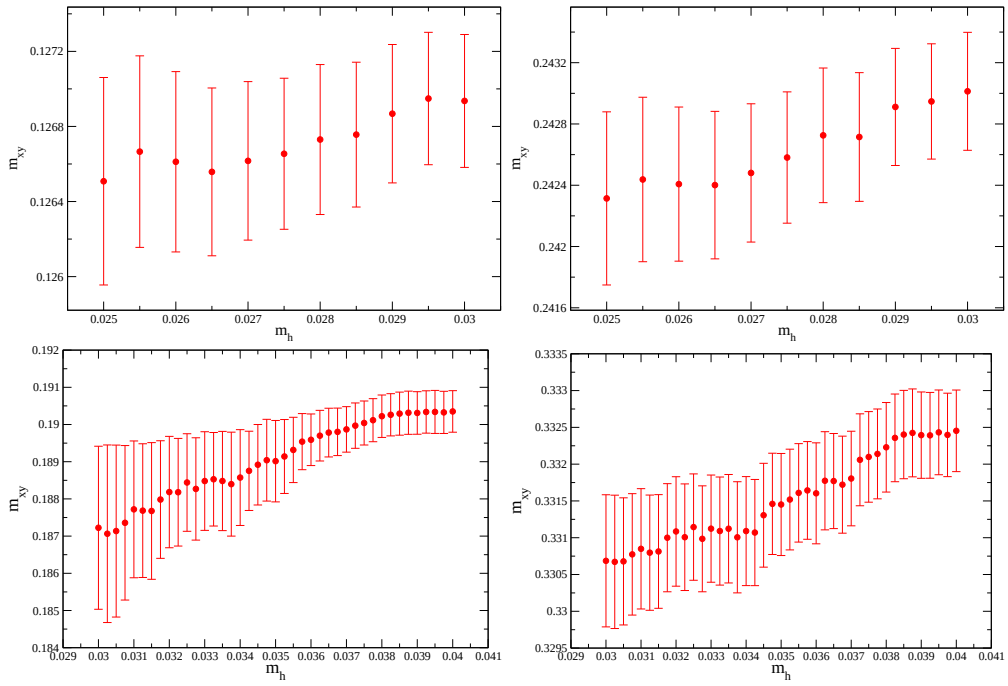

Figure 6.15: Strange sea quark mass dependence of the pion and kaon masses on both ensemble sets. The upper plots are of the pion mass with $m_x = m_y = m_l = 0.004$ (top-left) and the kaon mass with $m_x = m_l = 0.004$ and $m_y = 0.03$ (top-right), on the **A** ensembles. The lower plots are of the pion mass with $m_x = m_y = m_l = 0.005$ (bottom-left) and the kaon mass with $m_x = m_l = 0.005$ and $m_y = 0.04$ (bottom-right), on the **B** ensembles.

m_x	m_y	$m_{xy}(0.004)$	$m_{xy}(0.006)$	$m_{xy}(0.008)$	$f_{xy}(0.004)$	$f_{xy}(0.006)$	$f_{xy}(0.008)$
0.03	0.03	0.3212(3)	0.3216(2)	0.3224(3)	0.0807(3)	0.0810(2)	0.0815(2)
0.025	0.03	0.3073(3)	0.3078(2)	0.3086(3)	0.0791(3)	0.0795(2)	0.0800(2)
0.008	0.03	0.2561(3)	0.2565(2)	0.2579(4)	0.0728(3)	0.0734(3)	0.0743(3)
0.006	0.03	0.2496(3)	0.2500(3)	0.2516(4)	0.0720(3)	0.0726(3)	0.0736(3)
0.004	0.03	0.2430(4)	0.2434(3)	0.2452(5)	0.0712(3)	0.0718(3)	0.0730(3)
0.002	0.03	0.2363(5)	0.2367(3)	0.2388(6)	0.0705(3)	0.0714(3)	0.0728(4)
0.025	0.025	0.2930(3)	0.2934(2)	0.2943(3)	0.0776(3)	0.0780(2)	0.0786(2)
0.008	0.025	0.2392(3)	0.2396(2)	0.2410(4)	0.0714(3)	0.0720(3)	0.0729(3)
0.006	0.025	0.2323(3)	0.2327(3)	0.2342(4)	0.0706(3)	0.0712(3)	0.0722(3)
0.004	0.025	0.2252(4)	0.2256(3)	0.2273(5)	0.0698(3)	0.0704(3)	0.0716(3)
0.002	0.025	0.2180(4)	0.2184(3)	0.2203(5)	0.0691(3)	0.0699(3)	0.0713(3)
0.008	0.008	0.1708(3)	0.1714(2)	0.1727(4)	0.0654(3)	0.0661(3)	0.0671(3)
0.006	0.008	0.1610(3)	0.1616(3)	0.1629(4)	0.0646(3)	0.0653(3)	0.0663(3)
0.004	0.008	0.1506(3)	0.1513(3)	0.1526(4)	0.0637(3)	0.0645(3)	0.0656(3)
0.002	0.008	0.1395(4)	0.1403(3)	0.1417(4)	0.0629(3)	0.0638(3)	0.0651(3)
0.006	0.006	0.1505(3)	0.1512(3)	0.1525(4)	0.0637(2)	0.0645(3)	0.0655(3)
0.004	0.006	0.1393(3)	0.1400(3)	0.1413(4)	0.0628(2)	0.0636(3)	0.0647(3)
0.002	0.006	0.1271(4)	0.1280(3)	0.1293(4)	0.0620(2)	0.0629(3)	0.0641(3)
0.004	0.004	0.1269(4)	0.1278(3)	0.1291(4)	0.0619(2)	0.0627(3)	0.0639(3)
0.002	0.004	0.1133(4)	0.1144(3)	0.1156(4)	0.0610(2)	0.0619(3)	0.0632(3)
0.002	0.002	0.0976(4)	0.0989(4)	0.1001(5)	0.0599(3)	0.0608(3)	0.0622(4)

Table 6.9: Pseudoscalar masses $m_{xy}(m_l)$ and decay constants $f_{xy}(m_l)$ on ensemble set **A** at the simulated strange quark mass ($m_h = 0.03$).

m_x	m_y	$m_{xy}(0.004)$	$m_{xy}(0.006)$	$m_{xy}(0.008)$	$f_{xy}(0.004)$	$f_{xy}(0.006)$	$f_{xy}(0.008)$
0.008	0.008	0.1706(4)	0.1711(3)	0.1725(5)	0.0649(3)	0.0657(3)	0.0666(4)
0.006	0.008	0.1607(4)	0.1613(3)	0.1628(5)	0.0640(3)	0.0649(3)	0.0659(4)
0.004	0.008	0.1503(4)	0.1510(3)	0.1526(5)	0.0631(3)	0.0640(3)	0.0651(4)
0.002	0.008	0.1391(4)	0.1401(4)	0.1417(5)	0.0624(3)	0.0634(4)	0.0645(4)
0.006	0.006	0.1502(4)	0.1509(3)	0.1524(5)	0.0632(3)	0.0640(3)	0.0650(4)
0.004	0.006	0.1390(4)	0.1398(3)	0.1413(5)	0.0623(3)	0.0632(3)	0.0642(4)
0.002	0.006	0.1268(4)	0.1278(4)	0.1295(5)	0.0614(4)	0.0624(4)	0.0636(4)
0.004	0.004	0.1267(4)	0.1276(3)	0.1292(5)	0.0613(3)	0.0622(3)	0.0634(4)
0.002	0.004	0.1131(4)	0.1142(4)	0.1158(5)	0.0604(4)	0.0613(4)	0.0626(4)
0.002	0.002	0.0974(4)	0.0987(4)	0.1004(5)	0.0594(4)	0.0602(4)	0.0615(5)

Table 6.10: Pion masses $m_{xy}(m_l)$ and decay constants $f_{xy}(m_l)$ computed on ensemble set **A** at the physical strange quark mass.

m_x	$m_{xh}(0.004)$	$m_{xh}(0.006)$	$m_{xh}(0.008)$	$f_{xh}(0.004)$	$f_{xh}(0.006)$	$f_{xh}(0.008)$
0.008	0.246(2)	0.246(2)	0.248(3)	0.0715(4)	0.0722(4)	0.0731(5)
0.006	0.239(2)	0.240(3)	0.241(3)	0.0707(4)	0.0714(5)	0.0723(5)
0.004	0.232(2)	0.233(3)	0.234(3)	0.0698(4)	0.0707(5)	0.0717(5)
0.002	0.225(3)	0.226(3)	0.228(3)	0.0691(4)	0.0702(5)	0.0714(6)

Table 6.11: Kaon masses $m_{xh}(m_l)$ and decay constants $f_{xy}(m_l)$ on ensemble set **A** at the physical strange quark mass.

m_x	m_y	$m_{xy}(0.005)$	$m_{xy}(0.01)$	$f_{xy}(0.005)$	$f_{xy}(0.01)$
0.04	0.04	0.4317(4)	0.4344(4)	0.1085(4)	0.1109(4)
0.03	0.04	0.4051(4)	0.4080(4)	0.1056(4)	0.1081(4)
0.02	0.04	0.3772(5)	0.3802(4)	0.1023(4)	0.1050(4)
0.01	0.04	0.3478(5)	0.3509(5)	0.0987(4)	0.1017(4)
0.005	0.04	0.3325(6)	0.3358(5)	0.0968(4)	0.1002(5)
0.001	0.04	0.3199(7)	0.3233(7)	0.0956(5)	0.0995(6)
0.03	0.03	0.3771(4)	0.3800(4)	0.1027(4)	0.1053(4)
0.02	0.03	0.3472(5)	0.3502(4)	0.0994(4)	0.1022(4)
0.01	0.03	0.3152(5)	0.3184(4)	0.0958(4)	0.0989(4)
0.005	0.03	0.2983(5)	0.3016(5)	0.0940(4)	0.0974(5)
0.001	0.03	0.2843(6)	0.2877(6)	0.0927(4)	0.0966(5)
0.02	0.02	0.3149(5)	0.3179(4)	0.0962(4)	0.0991(4)
0.01	0.02	0.2794(5)	0.2826(5)	0.0926(4)	0.0958(4)
0.005	0.02	0.2603(5)	0.2636(5)	0.0908(4)	0.0942(4)
0.001	0.02	0.2440(6)	0.2475(6)	0.0894(4)	0.0934(5)
0.01	0.01	0.2389(5)	0.2422(5)	0.0891(4)	0.0924(4)
0.005	0.01	0.2161(5)	0.2195(5)	0.0871(4)	0.0907(4)
0.001	0.01	0.1960(6)	0.1997(6)	0.0857(4)	0.0897(4)
0.005	0.005	0.1904(6)	0.1940(6)	0.0851(4)	0.0889(4)
0.001	0.005	0.1669(6)	0.1709(6)	0.0836(4)	0.0876(4)
0.001	0.001	0.1391(6)	0.1434(7)	0.0818(5)	0.0858(5)

Table 6.12: Pseudoscalar masses $m_{xy}(m_l)$ and decay constants $f_{xy}(m_l)$ on ensemble set **B** at the simulated strange quark mass ($m_h = 0.04$).

m_x	m_y	$m_{xy}(0.005)$	$m_{xy}(0.01)$	$f_{xy}(0.005)$	$f_{xy}(0.01)$
0.01	0.01	0.2377(8)	0.2419(7)	0.0885(4)	0.0919(5)
0.005	0.01	0.2148(9)	0.2192(7)	0.0865(5)	0.0901(5)
0.001	0.01	0.1947(11)	0.1993(8)	0.0850(5)	0.0889(6)
0.005	0.005	0.1890(10)	0.1936(8)	0.0845(5)	0.0881(5)
0.001	0.005	0.1655(12)	0.1703(8)	0.0830(5)	0.0867(6)
0.001	0.001	0.1376(13)	0.1427(9)	0.0813(6)	0.0849(6)

Table 6.13: Pion masses $m_{xy}(m_l)$ and decay constants $f_{xy}(m_l)$ on ensemble set **B** at the physical strange quark mass.

m_x	$m_{xh}(0.005)$	$m_{xh}(0.01)$	$f_{xh}(0.005)$	$f_{xh}(0.01)$
0.01	0.329(4)	0.333(4)	0.0966(6)	0.0998(8)
0.005	0.312(4)	0.317(4)	0.0947(7)	0.0983(8)
0.001	0.299(4)	0.303(4)	0.0933(7)	0.0975(9)

Table 6.14: Kaon masses $m_{xh}(m_l)$ and decay constants $f_{xh}(m_l)$ on ensemble set **B** at the physical strange quark mass.

6.4 Pseudoscalar decay constants

The pseudoscalar decay constants can be obtained from eqn. 3.33, using the fourth Euclidean component of the (PCAC) axial-current at zero-momentum:

$$f_{xy} = \frac{|\langle 0|\mathcal{A}_4|P_{xy}\rangle|}{m_{xy}} = Z_A \frac{|\langle 0|A_4|P_{xy}\rangle|}{m_{xy}} \tag{6.9}$$

This can be rewritten in terms of the amplitudes of eqn. 6.5 using the definition in eqn. 6.8, giving [137]

$$f_{xy} = Z_A \sqrt{\frac{2}{m_{xy}} \frac{\mathcal{N}_{AP}^{LW\,2}}{\mathcal{N}_{PP}^{WW}}}\,. \tag{6.10}$$

Here the wall-wall PP amplitude is included to cancel the extraneous wall source amplitudes $\langle \pi|P^W|0\rangle$ in the numerator. Although there are additional methods of obtaining the decay constants, for example using the axial Ward identity [137][100], the method above was determined as optimal during the previous analysis of the **B** ensemble set (ref. [1]) due to the precision to which the local axial current renormalisation is known.

Figure 6.16 shows the 'effective amplitude' of the AP^{LW} and PP^{WW} pion correlators with $m_x = m_y = m_l = 0.004$ on the **A** ensembles, at the simulated and physical strange sea-quark masses, and figure 6.17 shows the same for the kaon correlators with $m_x = m_l = 0.004$ and $m_y = 0.03$. The effective amplitude is obtained by dividing the correlation function on each timeplane by the time dependence implied by the effective mass. For example, the effective amplitude of the AP^{LW} correlator is determined as

$$\mathcal{N}_{AP\,\mathrm{eff}}^{LW}(t) = \frac{Y(t)}{\exp\Big(-m_{\mathrm{eff}}t\Big) - \exp\Big(-m_{\mathrm{eff}}(2T-t)\Big)}\,, \tag{6.11}$$

where $Y(t)$ is the simulated value and $m_{\mathrm{eff}} = m_{\mathrm{eff}}(t)$.

Table 6.15 contains the values of the amplitudes on the **A** ensembles at the simulated strange sea quark mass, and tables 6.16 and 6.17 contain the amplitudes at the physical

strange quark mass. Here the heavy quark interpolation is performed as in section 6.3. These amplitudes are combined according to eqn. 6.10 and the resulting values of f_{xy} are given in table 6.9 at the simulated strange quark mass and in tables 6.10 and 6.11 at the unitary physical strange mass. The strange sea-quark dependence of the correlators and the resulting decay constants are shown in figures 6.18 and 6.19 respectively.

The figures and plots for the **B** ensembles are included in the same order as for the **A** ensembles. Figures 6.20 and 6.21 contain the effective amplitudes of the $m_x = m_y = m_l = 0.005$ pionic and $m_x = m_l = 0.005$ and $m_y = 0.04$ kaonic correlators respectively. Tables 6.18–6.20 contain the values of the amplitudes at the simulated and physical strange quark masses, and tables 6.12–6.14 contain the resulting values of f_{xy}. Finally, the strange sea-quark dependence of the correlators and decay constants on the **B** ensembles are shown in figures 6.22 and 6.23 respectively.

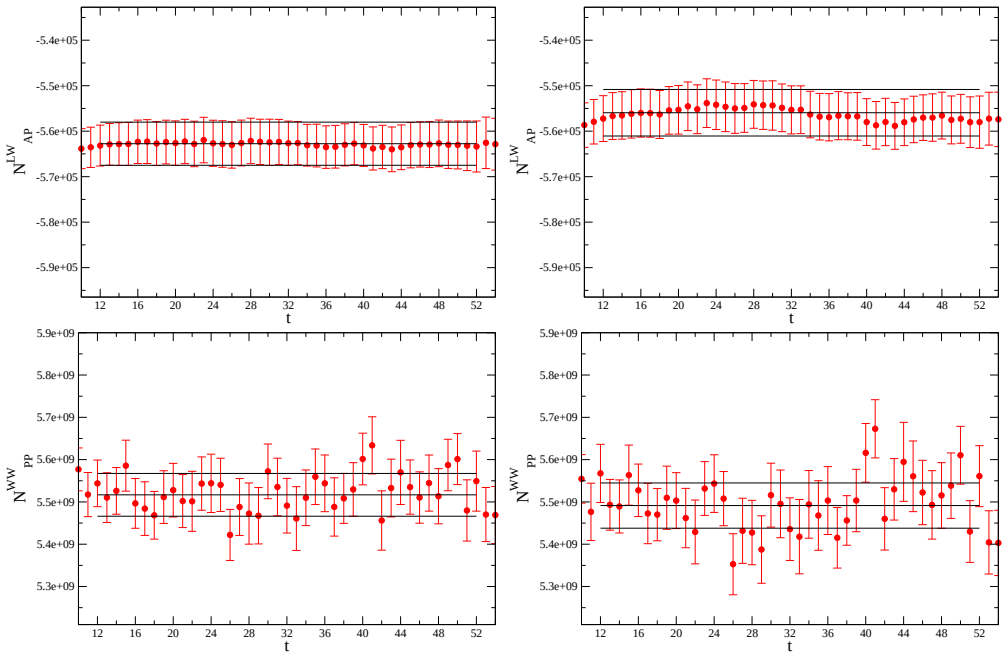

Figure 6.16: Effective amplitude plots of the light-light AP wall-local (AP^{LW}) and PP wall-wall (PP^{WW}) correlators used in the calculation of the pion decay constant with $m_x = m_y = m_l = 0.004$ on the **A** ensembles. The top row contains the AP^{LW} amplitude at the simulated strange quark mass $m_h = 0.03$ (top-left) and at the closest reweighted strange quark mass $m_h = 0.027$ to the physical value (top-right). These are overlaid by the result of a simultaneous fit to the five pseudoscalar correlators over the range 12–52. The bottom row is the same for the PP^{WW} amplitudes.

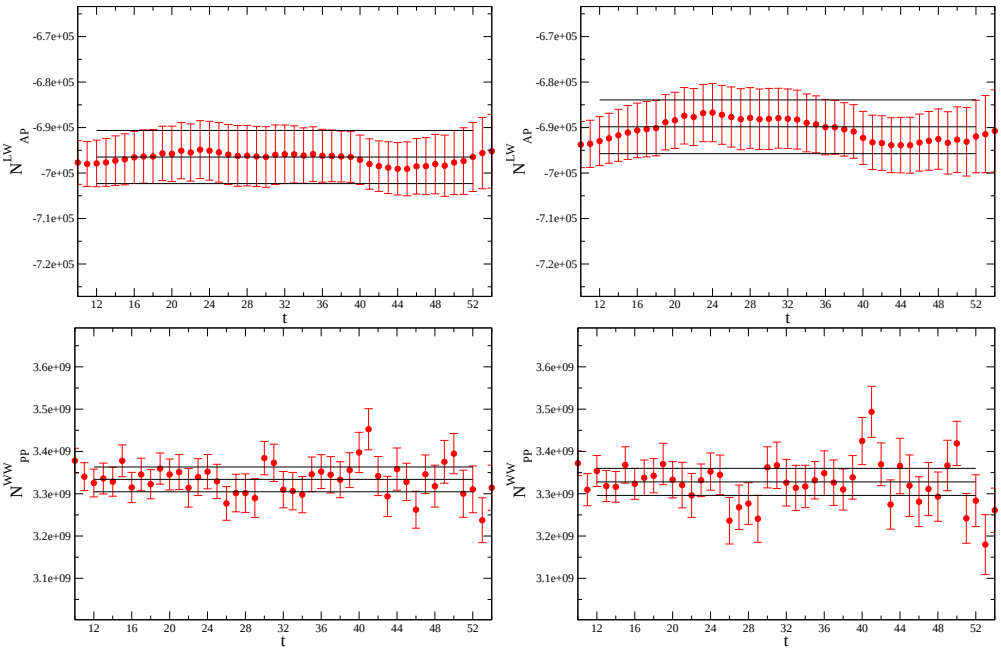

Figure 6.17: Effective amplitude plots of the heavy-light AP wall-local (AP^{LW}) and PP wall-wall (PP^{WW}) correlators used in the calculation of the kaon decay constant with $m_x = m_l = 0.004$ and $m_y = 0.03$ on the **A** ensembles. The top row contains the AP^{LW} amplitude at the simulated strange quark mass $m_h = 0.03$ (top-left) and at the closest reweighted strange quark mass $m_h = 0.027$ to the physical value (top-right). These are overlaid by the result of a simultaneous fit to the five pseudoscalar correlators over the range 12–52. The bottom row is the same for the PP^{WW} amplitudes.

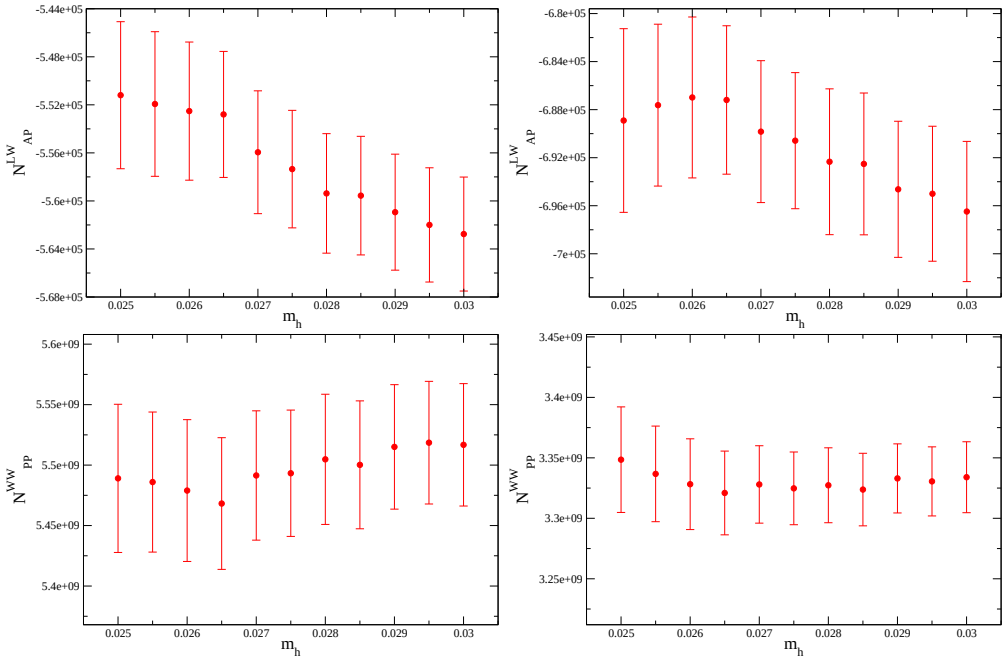

Figure 6.18: Examples of the strange sea quark mass dependence of the light-light and heavy-light AP wall-local (AP^{LW}) and PP wall-wall (PP^{WW}) amplitudes used to obtain the pion and kaon decay constants on the **A** ensembles. The top row contains the AP^{LW} with $m_x = m_y = m_l = 0.004$ (top-left) and $m_x = m_l = 0.004$ and $m_y = 0.03$ (top-right). The bottom row is the same for the PP^{WW} amplitudes.

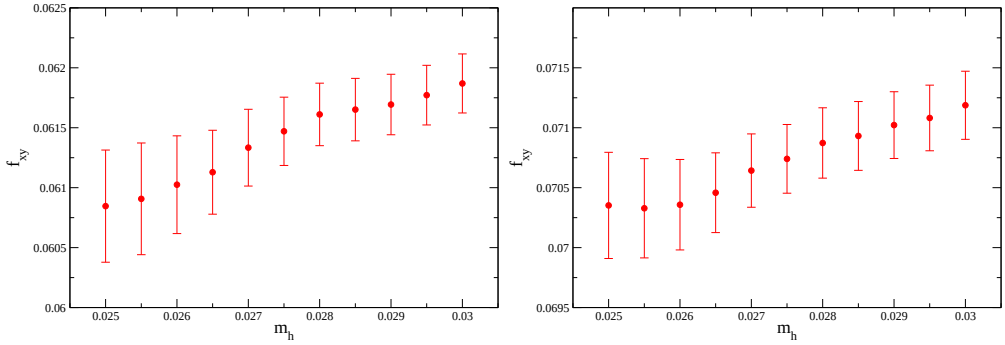

Figure 6.19: Examples of the strange sea quark mass dependence of the light-light and heavy-light pseudoscalar decay constants on the **A** ensembles. The left plot shows the dependence of the decay constant with $m_x = m_y = m_l = 0.004$, and the right with $m_x = m_l = 0.004$ and $m_y = 0.03$.

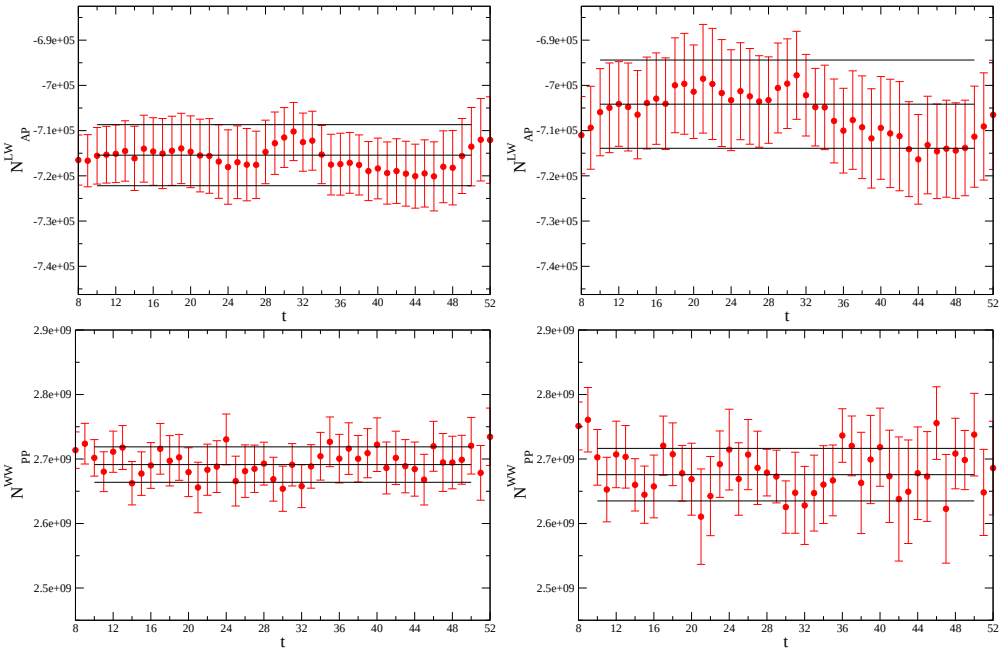

Figure 6.20: Effective amplitude plots of the light-light AP wall-local (AP^{LW}) and PP wall-wall (PP^{WW}) correlators used in the calculation of the pion decay constant with $m_x = m_y = m_l = 0.005$ on the **B** ensembles. The top row contains the AP^{LW} amplitude at the simulated strange quark mass $m_h = 0.04$ (top-left) and at the closest reweighted strange quark mass $m_h = 0.0345$ to the physical value (top-right). These are overlaid by the result of a simultaneous fit to the five pseudoscalar correlators over the range 10–50. The bottom row is the same for the PP^{WW} amplitudes.

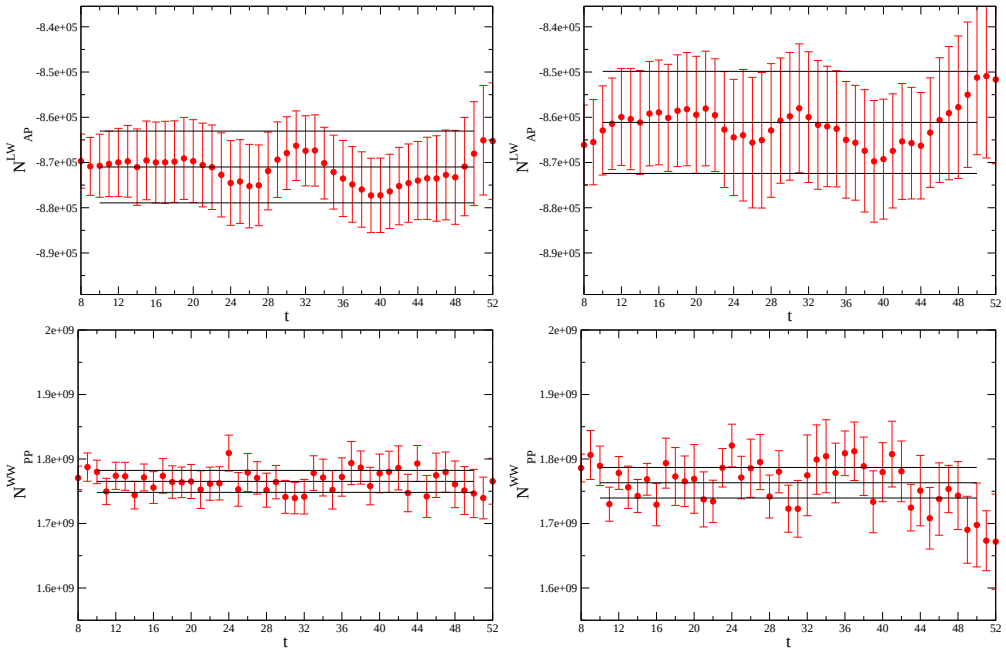

Figure 6.21: Effective amplitude plots of the heavy-light AP wall-local (AP^{LW}) and PP wall-wall (PP^{WW}) correlators used in the calculation of the kaon decay constant with $m_x = m_l = 0.005$ and $m_y = 0.04$ on the **B** ensembles. The top row contains the AP^{LW} amplitude at the simulated strange quark mass $m_h = 0.04$ (top-left) and at the closest reweighted strange quark mass $m_h = 0.0345$ to the physical value (top-right). These are overlaid by the result of a simultaneous fit to the five pseudoscalar correlators over the range 10–50. The bottom row is the same for the PP^{WW} amplitudes.

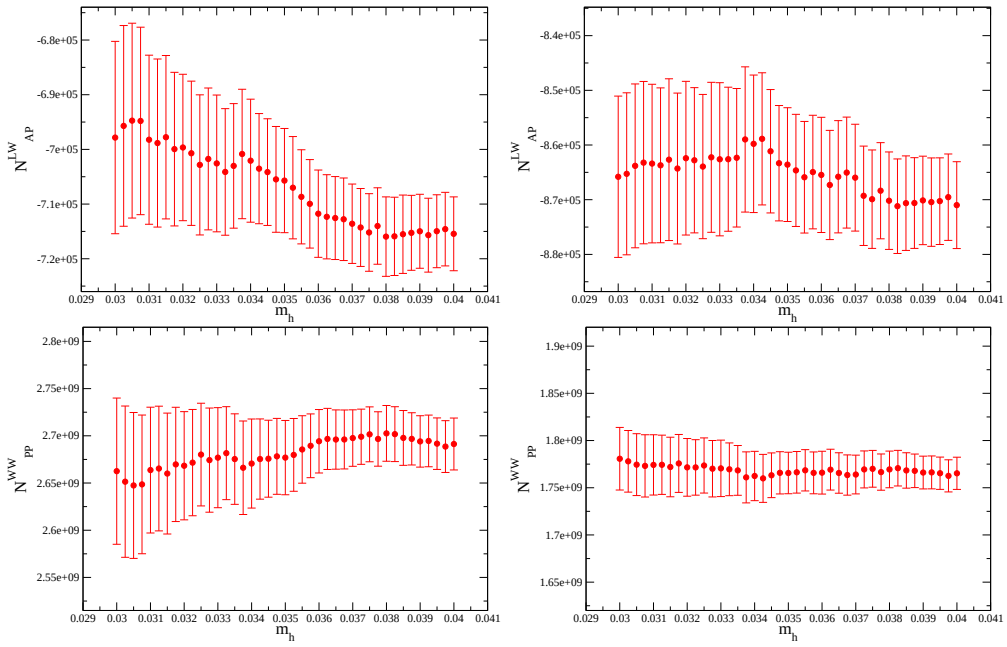

Figure 6.22: Examples of the strange sea quark mass dependence of the light-light and heavy-light AP wall-local (AP^{LW}) and PP wall-wall (PP^{WW}) amplitudes used to obtain the pion and kaon decay constants on the **B** ensembles. The top row contains the AP^{LW} with $m_x = m_y = m_l = 0.005$ (top-left) and $m_x = m_l = 0.005$ and $m_y = 0.04$ (top-right). The bottom row is the same for the PP^{WW} amplitudes.

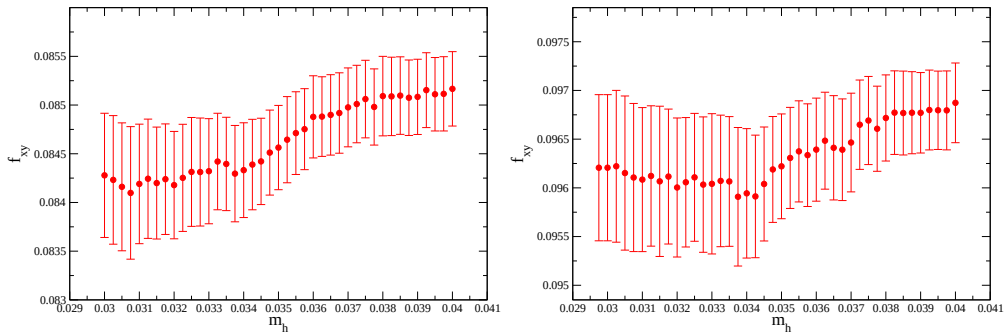

Figure 6.23: Examples of the strange sea quark mass dependence of the light-light and heavy-light pseudoscalar decay constants on the **B** ensembles. The left plot shows the dependence of the decay constant with $m_x = m_y = m_l = 0.005$ and the right with $m_x = m_l = 0.005$ and $m_y = 0.04$.

		$\mathcal{N}^{LW}_{APxy}(m_l)$			$\mathcal{N}^{WW}_{PPxy}(m_l)(\times 10^4)$		
m_x	m_y	$m_l = 0.004$	$m_l = 0.006$	$m_l = 0.008$	$m_l = 0.004$	$m_l = 0.006$	$m_l = 0.008$
0.03	0.03	6.47(4)	6.46(4)	6.50(4)	2.22(1)	2.20(1)	2.19(1)
0.025	0.03	6.27(4)	6.27(4)	6.31(4)	2.27(2)	2.24(1)	2.24(1)
0.008	0.03	5.51(4)	5.53(4)	5.64(4)	2.47(2)	2.45(2)	2.48(2)
0.006	0.03	5.41(4)	5.43(4)	5.57(4)	2.51(2)	2.48(2)	2.52(2)
0.004	0.03	5.31(4)	5.35(4)	5.51(4)	2.54(2)	2.52(2)	2.58(2)
0.002	0.03	5.25(5)	5.31(5)	5.52(6)	2.60(3)	2.59(2)	2.67(3)
0.025	0.025	6.08(4)	6.08(4)	6.13(4)	2.33(2)	2.30(1)	2.30(1)
0.008	0.025	5.33(4)	5.35(4)	5.47(4)	2.58(2)	2.56(2)	2.59(2)
0.006	0.025	5.23(4)	5.26(4)	5.39(4)	2.63(2)	2.61(2)	2.65(2)
0.004	0.025	5.14(4)	5.18(4)	5.34(4)	2.68(2)	2.66(2)	2.71(2)
0.002	0.025	5.08(5)	5.14(4)	5.34(5)	2.75(3)	2.75(2)	2.82(3)
0.008	0.008	4.64(4)	4.70(3)	4.82(4)	3.27(3)	3.27(2)	3.32(3)
0.006	0.008	4.55(4)	4.62(3)	4.75(4)	3.43(3)	3.43(3)	3.49(3)
0.004	0.008	4.47(4)	4.55(4)	4.69(4)	3.62(3)	3.65(3)	3.71(3)
0.002	0.008	4.40(4)	4.51(4)	4.68(5)	3.90(4)	3.95(4)	4.04(4)
0.006	0.006	4.47(4)	4.54(3)	4.68(4)	3.62(3)	3.64(3)	3.70(3)
0.004	0.006	4.38(4)	4.47(4)	4.61(4)	3.87(3)	3.91(3)	3.99(4)
0.002	0.006	4.31(4)	4.44(4)	4.60(5)	4.23(4)	4.31(4)	4.41(5)
0.004	0.004	4.29(4)	4.40(4)	4.55(4)	4.21(4)	4.27(4)	4.36(4)
0.002	0.004	4.23(4)	4.36(4)	4.53(5)	4.71(5)	4.83(5)	4.94(6)
0.002	0.002	4.16(4)	4.32(5)	4.51(5)	5.48(6)	5.68(7)	5.83(8)

Table 6.15: The correlation function amplitudes at the simulated strange sea quark mass $m_h = 0.03$ used to calculate f_{xy} on the **A** ensembles.

		$\mathcal{N}^{LW}_{APxy}(m_l)$			$\mathcal{N}^{WW}_{PPxy}(m_l)(\times 10^4)$		
m_x	m_y	$m_l = 0.004$	$m_l = 0.006$	$m_l = 0.008$	$m_l = 0.004$	$m_l = 0.006$	$m_l = 0.008$
0.008	0.008	4.60(4)	4.66(4)	4.80(5)	3.27(3)	3.27(3)	3.33(3)
0.006	0.008	4.51(4)	4.58(5)	4.72(5)	3.42(3)	3.43(4)	3.51(3)
0.004	0.008	4.42(4)	4.51(5)	4.66(5)	3.61(3)	3.64(4)	3.73(4)
0.002	0.008	4.35(4)	4.47(5)	4.65(5)	3.88(4)	3.94(5)	4.07(5)
0.006	0.006	4.42(4)	4.50(5)	4.65(5)	3.61(3)	3.63(4)	3.72(4)
0.004	0.006	4.33(4)	4.43(5)	4.59(5)	3.86(4)	3.90(4)	4.01(4)
0.002	0.006	4.26(4)	4.39(5)	4.58(5)	4.21(4)	4.30(6)	4.44(6)
0.004	0.004	4.24(4)	4.35(5)	4.53(5)	4.19(4)	4.25(5)	4.38(5)
0.002	0.004	4.17(4)	4.31(5)	4.51(6)	4.69(5)	4.80(7)	4.97(7)
0.002	0.002	4.11(4)	4.27(6)	4.48(6)	5.45(6)	5.65(9)	5.87(9)

Table 6.16: The correlation function amplitudes at the physical strange sea-quark mass used to calculate light-light f_{xy} on the **A** ensembles.

	$\mathcal{N}^{LW}_{APxh}(m_l)$			$\mathcal{N}^{WW}_{PPxh}(m_l)(\times 10^4)$		
m_x	$m_l = 0.004$	$m_l = 0.006$	$m_l = 0.008$	$m_l = 0.004$	$m_l = 0.006$	$m_l = 0.008$
0.008	5.37(5)	5.40(6)	5.52(6)	2.54(3)	2.52(3)	2.56(3)
0.006	5.27(5)	5.31(6)	5.44(6)	2.58(3)	2.56(3)	2.61(3)
0.004	5.17(5)	5.23(6)	5.38(7)	2.62(3)	2.61(3)	2.67(3)
0.002	5.08(6)	5.19(7)	5.38(8)	2.67(4)	2.69(4)	2.77(4)

Table 6.17: The correlation function amplitudes at the physical strange sea-quark mass used to calculate heavy-light f_{xh} on the **A** ensembles.

		$\mathcal{N}^{LW}_{APxy}(m_l)$		$\mathcal{N}^{WW}_{PPxy}(m_l)(\times 10^4)$	
m_x	m_y	$m_l = 0.005$	$m_l = 0.01$	$m_l = 0.005$	$m_l = 0.01$
0.04	0.04	7.32(6)	7.54(6)	1.08(1)	1.09(1)
0.03	0.04	7.01(6)	7.24(6)	1.12(1)	1.13(1)
0.02	0.04	6.68(6)	6.93(6)	1.16(1)	1.18(1)
0.01	0.04	6.32(5)	6.62(6)	1.21(1)	1.24(1)
0.005	0.04	6.15(6)	6.49(7)	1.25(1)	1.28(2)
0.001	0.04	6.05(7)	6.46(9)	1.29(2)	1.34(2)
0.03	0.03	6.71(6)	6.95(5)	1.16(1)	1.18(1)
0.02	0.03	6.38(5)	6.64(5)	1.22(1)	1.24(1)
0.01	0.03	6.03(5)	6.33(6)	1.29(1)	1.32(1)
0.005	0.03	5.86(5)	6.20(6)	1.34(1)	1.38(2)
0.001	0.03	5.76(6)	6.16(8)	1.39(2)	1.45(2)
0.02	0.02	6.06(5)	6.33(5)	1.29(1)	1.32(1)
0.01	0.02	5.72(5)	6.02(6)	1.40(1)	1.43(1)
0.005	0.02	5.55(5)	5.89(6)	1.47(1)	1.52(2)
0.001	0.02	5.45(6)	5.85(7)	1.56(2)	1.63(2)
0.01	0.01	5.38(5)	5.71(6)	1.57(1)	1.62(2)
0.005	0.01	5.22(5)	5.58(6)	1.70(2)	1.77(2)
0.001	0.01	5.12(5)	5.55(6)	1.87(2)	1.97(3)
0.005	0.005	5.05(5)	5.45(6)	1.90(2)	1.99(3)
0.001	0.005	4.96(5)	5.41(6)	2.16(2)	2.29(3)
0.001	0.001	4.86(5)	5.35(7)	2.60(3)	2.79(4)

Table 6.18: The correlation function amplitudes at the simulated strange sea quark mass $m_h = 0.04$ used to calculate f_{xy} on the **B** ensembles.

		$\mathcal{N}^{LW}_{APxy}(m_l)$		$\mathcal{N}^{WW}_{PPxy}(m_l)(\times 10^4)$	
m_x	m_y	$m_l = 0.005$	$m_l = 0.01$	$m_l = 0.005$	$m_l = 0.01$
0.01	0.01	5.33(7)	5.71(7)	1.57(2)	1.64(2)
0.005	0.01	5.15(7)	5.57(7)	1.70(2)	1.79(3)
0.001	0.01	5.05(8)	5.52(8)	1.86(3)	1.99(3)
0.005	0.005	4.99(7)	5.42(7)	1.89(3)	2.01(3)
0.001	0.005	4.89(8)	5.37(8)	2.15(4)	2.31(4)
0.001	0.001	4.79(8)	5.30(9)	2.60(5)	2.81(6)

Table 6.19: The correlation function amplitudes at the physical strange sea quark mass used to calculate light-light f_{xy} on the **B** ensembles.

	$\mathcal{N}^{LW}_{APxh}(m_l)$		$\mathcal{N}^{WW}_{PPxh}(m_l)(\times 10^4)$	
m_x	$m_l = 0.005$	$m_l = 0.01$	$m_l = 0.005$	$m_l = 0.01$
0.01	6.11(8)	6.47(9)	1.26(2)	1.30(2)
0.005	5.94(8)	6.34(10)	1.30(2)	1.36(2)
0.001	5.83(9)	6.29(12)	1.35(3)	1.42(3)

Table 6.20: The correlation function amplitudes at the physical strange sea quark mass used to calculate heavy-light f_{xh} on the **B** ensembles.

6.5 Omega baryon masses

The interpolating operator for the Ω^- baryon is [1]

$$\chi_\mu = \epsilon_{abc} \left[s_a^T C \gamma_\mu s_b \right] s_c \,, \tag{6.12}$$

where Roman subscripts are colour indices and C is the charge conjugation operator of eqn. 1.17. Although this operator transforms with positive parity, it also couples to the heavier, negative-parity partner of the Omega [139]. The upper spin-components of two-point matrix correlation function can be decomposed into a forwards-propagating positive-parity Omega state and a backwards-propagating negative-parity state, and the converse applies to the lower spin-components [140]. The upper spin components are projected out of the matrix correlation function by taking the trace with the parity projection operator $\frac{1}{2}(1+\gamma_4) = \begin{pmatrix} I & 0 \\ 0 & 0 \end{pmatrix}$. For increased statistics, the lower spin-components are also calculated by taking the trace with $\frac{1}{2}(1-\gamma_4)$. By performing a double-reflection, $Y(t) \to -Y(T-t)$, to the correlation function of the lower spin-components, it can be averaged with the corresponding result for the upper spin-components. In general the heavier negative-parity state decays away sufficiently quickly to allow for the Omega mass (m_{yyy}) to be extracted using a simple exponential

fit to the averaged correlator:

$$Y(t; m_y) = \mathcal{N} \exp\{-m_{yyy} t\} \ . \tag{6.13}$$

For this calculation, the correlation functions of the upper and lower spin-components are first measured on each configuration using the two box-source propagators, and are then averaged over all three spatial directions of the interpolating operator. The correlation functions generated using the source at $t = 32$ are shifted in time and averaged with those generated using the source at $t = 0$ in the same way as the pseudoscalar correlation functions were in section 6.3.

Figure 6.24 contains plots of the effective Omega baryon mass at the simulated and physical strange sea-quark masses, on the $m_l = 0.004$ ensemble of set **A** and the $m_l = 0.005$ ensemble of set **B** . As with the kaons in section 6.3, these plots show only the effect of reweighting the strange sea-quark mass to the physical value: the valence quark masses remain fixed. The fits are performed to the ranges $t = 7$–13 and 5–11 for the **A** and **B** ensemble sets respectively, giving the results listed in tables 6.21 and 6.22. These tables also contain the Omega mass at the unitary physical strange quark mass.

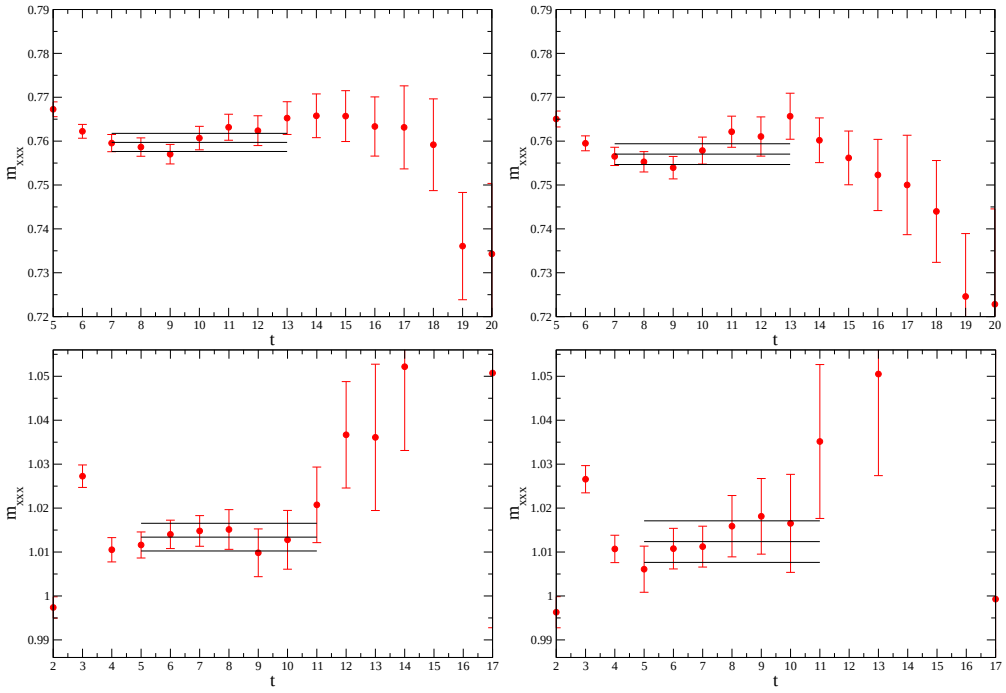

Figure 6.24: Effective mass plots of the box-local Omega baryon correlators on both ensemble sets. The upper plots show the $m_x = m_y = 0.03$, $m_l = 0.004$ effective mass on the **A** ensembles at the simulated strange quark mass $m_h = 0.03$ (top-left) and at the closest reweighted strange quark mass $m_h = 0.027$ to the physical value (top-right). These are overlaid by the results of a fit to the range 7–13. The lower plots show the $m_x = m_y = 0.04$, $m_l = 0.005$ effective mass on the **B** ensembles at the simulated strange quark mass $m_h = 0.04$ (bottom-left) and at the closest reweighted strange quark mass $m_h = 0.0345$ to the physical value (bottom-right). These are overlaid by the results of a fit to the range 5–11.

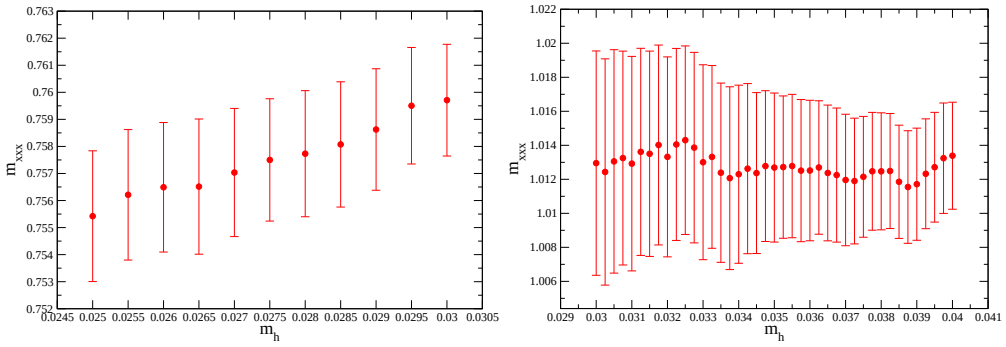

Figure 6.25: Strange sea quark mass dependence of the Omega baryon mass with $m_x = m_y = 0.03$ and $m_l = 0.004$ on the **A** ensembles (left) and with $m_x = m_y = 0.04$ and $m_l = 0.005$ on the **B** ensembles (right).

m_y	m_h	$m_\Omega(0.004)$	$m_\Omega(0.006)$	$m_\Omega(0.008)$
0.03	0.03	0.760(2)	0.765(2)	0.766(3)
0.025	0.03	0.733(2)	0.739(2)	0.740(3)
m_h^{phys}	m_h^{phys}	0.742(6)	0.747(5)	0.752(4)

Table 6.21: Omega baryon masses on ensemble set **A** , at the simulated strange quark mass (first two rows) and at the physical strange quark mass (third row).

m_y	m_h	$m_\Omega(0.005)$	$m_\Omega(0.01)$
0.04	0.04	1.013(3)	1.028(4)
0.03	0.04	0.963(4)	0.978(4)
m_h^{phys}	m_h^{phys}	0.986(9)	0.999(7)

Table 6.22: Omega baryon masses on ensemble set **B** , at the simulated strange quark mass (first two rows) and at the physical strange quark mass (third row).

6.6 Neutral kaon mixing parameter B_K

On the **A** ensembles, the neutral kaon mixing parameter is calculated using the single-wall method described in section 5.2, in which the matrix element of eqn. 4.97 is formed by contracting the forwards- and backwards-flowing wall source propagators at the interaction timeslice. For the **B** ensembles, the matrix elements were formed by contracting the $p + a$ propagators from the two walls at $\tau = 5$ and 59.

Figure 6.26 contains plots of the light-light matrix elements with $m_x = m_y = m_l = 0.004$ on the **A** ensembles, and $m_x = m_y = m_l = 0.005$ on the **B** ensembles, at the simulated and physical strange sea-quark mass. These are overlaid with fits to the chosen range $t = 12$–52 on both ensemble sets. Figure 6.27 contains similar plots for the heavy-light matrix elements with $m_x = m_l = 0.004$ and $m_y = 0.03$ on the **A** ensembles and with $m_x = m_l = 0.005$ and $m_y = 0.04$ on the **B** ensembles. The values of B_K at the simulated strange quark mass are given in tables 6.23 and 6.25 for the **A** and **B** ensemble sets respectively. The heavy-light matrix elements at the physical strange quark mass, which are used in the continuum extrapolation in section 8.7, are given in tables 6.24 and 6.26. The strange sea-quark dependence of the fitted values of the light-light and heavy-light matrix elements above is shown in figure 6.28.

Note that all values of B_K quoted in this section are not renormalised. The non-perturbative renormalisation coefficients that convert these values to the $\overline{\text{MS}}$-scheme are determined in chapter 7, and are used in chapter 8 during the determination of the continuum value of B_K.

m_x	m_y	$B_{xy}(m_l = 0.004)$	$B_{xy}(m_l = 0.006)$	$B_{xy}(m_l = 0.008)$
0.03	0.03	0.629(1)	0.631(1)	0.630(1)
0.025	0.03	0.620(1)	0.621(1)	0.621(1)
0.008	0.03	0.586(2)	0.588(2)	0.588(2)
0.006	0.03	0.582(2)	0.584(2)	0.584(2)
0.004	0.03	0.579(2)	0.580(3)	0.580(3)
0.002	0.03	0.577(5)	0.577(4)	0.578(5)
0.025	0.025	0.610(1)	0.612(2)	0.611(1)
0.008	0.025	0.573(2)	0.575(2)	0.574(2)
0.006	0.025	0.568(2)	0.570(2)	0.569(2)
0.004	0.025	0.563(2)	0.566(2)	0.565(3)
0.002	0.025	0.560(4)	0.563(4)	0.563(4)
0.008	0.008	0.514(2)	0.518(2)	0.514(2)
0.006	0.008	0.505(2)	0.510(2)	0.506(2)
0.004	0.008	0.495(2)	0.501(2)	0.497(3)
0.002	0.008	0.485(3)	0.494(3)	0.490(3)
0.006	0.006	0.495(2)	0.500(2)	0.496(2)
0.004	0.006	0.484(2)	0.491(3)	0.486(3)
0.002	0.006	0.473(3)	0.481(3)	0.478(4)
0.004	0.004	0.472(3)	0.479(3)	0.475(3)
0.002	0.004	0.458(3)	0.466(4)	0.465(4)
0.002	0.002	0.441(4)	0.447(4)	0.450(5)

Table 6.23: B_K matrix element values at the simulated strange sea quark mass on the **A** ensembles.

m_x	$B_{xh}(m_l = 0.004)$	$B_{xh}(m_l = 0.006)$	$B_{xh}(m_l = 0.008)$
0.008	0.580(3)	0.580(3)	0.582(3)
0.006	0.575(3)	0.576(3)	0.578(3)
0.004	0.571(3)	0.571(4)	0.575(4)
0.002	0.567(5)	0.567(5)	0.574(6)

Table 6.24: Heavy-light B_K matrix element values at the physical strange quark mass on the **A** ensembles.

m_x	m_y	$B_{xy}(m_l = 0.005)$	$B_{xy}(m_l = 0.01)$
0.04	0.04	0.657(1)	0.656(1)
0.03	0.04	0.644(1)	0.643(1)
0.02	0.04	0.630(2)	0.629(1)
0.01	0.04	0.615(2)	0.615(2)
0.005	0.04	0.608(3)	0.608(2)
0.001	0.04	0.602(5)	0.607(5)
0.03	0.03	0.629(1)	0.628(1)
0.02	0.03	0.612(2)	0.612(1)
0.01	0.03	0.595(2)	0.594(2)
0.005	0.03	0.586(2)	0.586(2)
0.001	0.03	0.579(4)	0.584(4)
0.02	0.02	0.593(2)	0.592(2)
0.01	0.02	0.571(2)	0.571(2)
0.005	0.02	0.560(2)	0.560(2)
0.001	0.02	0.551(4)	0.555(3)
0.01	0.01	0.543(2)	0.544(2)
0.005	0.01	0.527(3)	0.528(2)
0.001	0.01	0.513(4)	0.516(3)
0.005	0.005	0.508(3)	0.509(2)
0.001	0.005	0.489(4)	0.490(3)
0.001	0.001	0.465(6)	0.463(4)

Table 6.25: B_K matrix element values at the simulated strange sea quark mass on the **B** ensembles.

m_x	$B_{xh}(m_l = 0.005)$	$B_{xh}(m_l = 0.01)$
0.02	0.618(3)	0.618(3)
0.01	0.603(3)	0.602(3)
0.005	0.595(4)	0.594(4)
0.001	0.588(6)	0.589(6)

Table 6.26: Heavy-light B_K^{lat} matrix element values at the physical strange quark mass on the **B** ensembles.

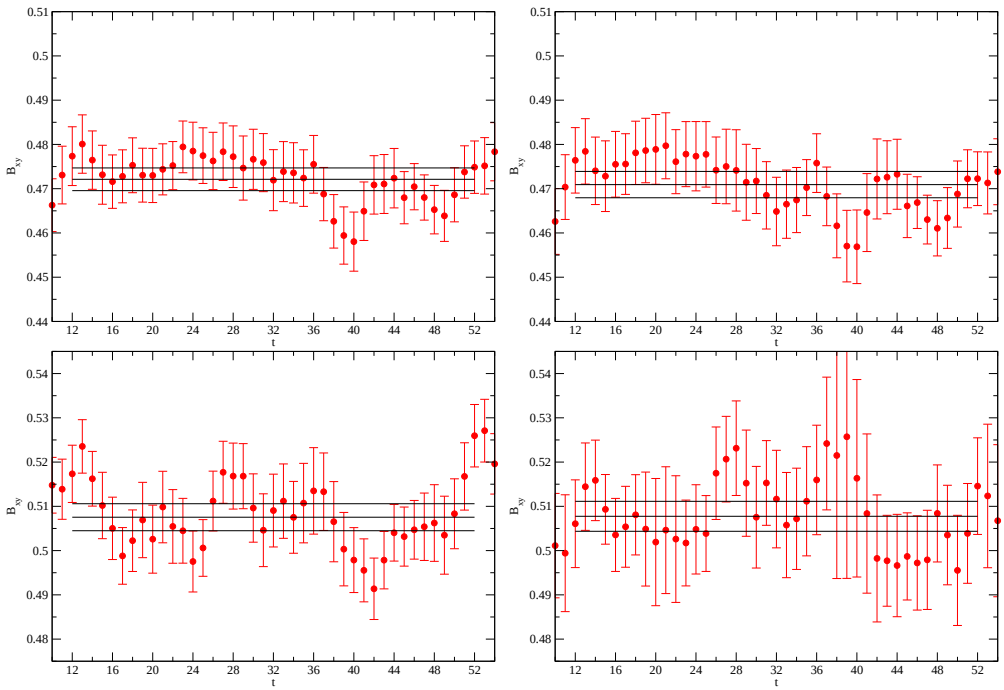

Figure 6.26: Light-light B_K matrix elements on both ensemble sets. The upper plots show the $m_x = m_y = m_l = 0.004$ matrix element on the **A** ensembles at the simulated strange quark mass $m_h = 0.03$ (top-left) and at the closest reweighted strange quark mass $m_h = 0.027$ to the physical value (top-right). These are overlaid by the results of a fit to the range $12 - 52$. The lower plots show the $m_x = m_y = m_l = 0.005$ matrix element on the **B** ensembles at the simulated strange quark mass $m_h = 0.04$ (bottom-left) and at the closest reweighted strange quark mass $m_h = 0.0345$ to the physical value (top-right). These are overlaid by the results of a fit to the range $12 - 52$.

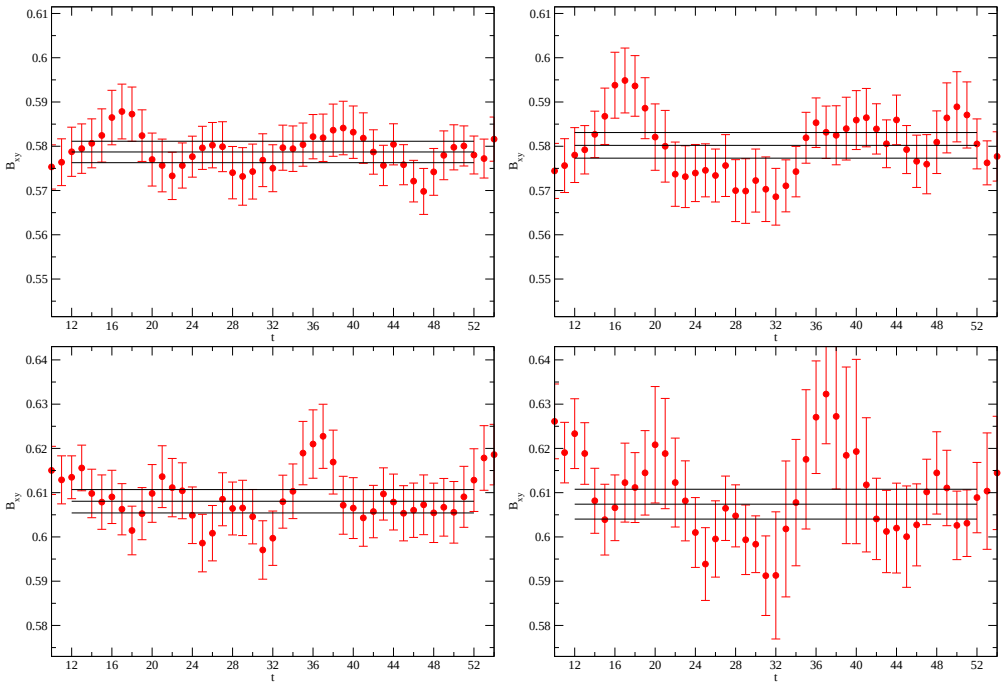

Figure 6.27: Heavy-light B_K matrix elements on both ensemble sets. The upper plots show the $m_x = m_l = 0.004$, $m_y = 0.03$ matrix element on the **A** ensembles at the simulated strange quark mass $m_h = 0.03$ (top-left) and at the closest reweighted strange quark mass $m_h = 0.027$ to the physical value (top-right). These are overlaid by the results of a fit to the range $12 - 52$. The lower plots show the $m_x = m_l = 0.005$, $m_y = 0.04$ matrix element on the **B** ensembles at the simulated strange quark mass $m_h = 0.04$ (bottom-left) and at the closest reweighted strange quark mass $m_h = 0.0345$ to the physical value (top-right). These are overlaid by the results of a fit to the range $12 - 52$.

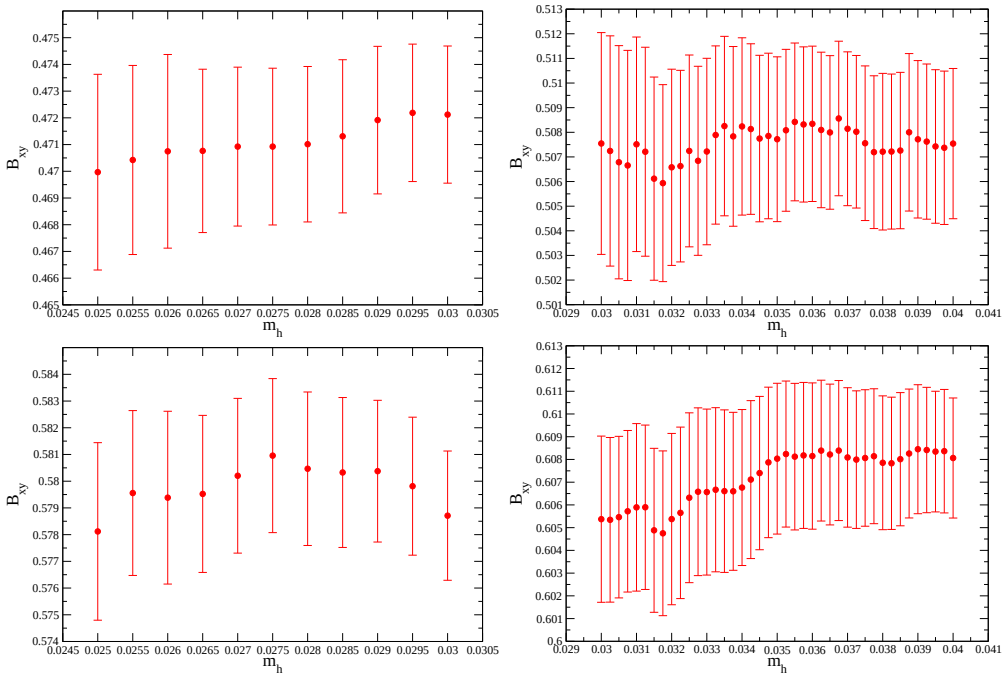

Figure 6.28: Strange sea quark mass dependence of the fitted light-light and heavy-light B_K matrix element amplitudes on both ensemble sets. The upper plots show the dependence of the light-light matrix element amplitudes with $m_x = m_y = m_l = 0.004$ on the **A** ensemble set (top-left) and with $m_x = m_y = m_l = 0.005$ on the **B** ensemble set (top-right). The lower plots show the dependence of the heavy-light matrix element amplitudes with $m_x = m_l = 0.004$ and $m_y = 0.03$ on the **A** ensemble set (top-left) and with $m_x = m_l = 0.005$ and $m_y = 0.04$ on the **B** ensemble set (bottom-right).

6.7 The scales r_0 and r_1

As discussed in section 4.1.2, the scales r_0 and r_1 are calculated from the dependence of the static inter-quark potential on the spatial extent of the Wilson loops. The potential is computed on the **A** and **B** ensembles using the technique described in ref. [138], in which the gauge configurations are fixed to the Coulomb gauge and the potential is calculated from all products of temporal Wilson lines at a given spatial separation. Due to the gauge fixing this is equivalent to computing Wilson loops $W(r,t)$ for all paths that join the Wilson lines on each timeplane. The spatial separations are varied over a range of 1–14 in units of the lattice spacing, and the time separation of the timeplanes upon which the amplitudes are measured is varied from 0 to 8. Beyond these ranges the data become too noisy to provide a signal. The data are fit to the exponential form of eqn. 4.16 in order to obtain the static inter-quark potential $V(r)$ as a function of the spatial separation of the Wilson lines. The potential is fit as a function of the separation to the form eqn. 4.17. The parameters of this fit form are then used to determine the scales r_0 and r_1 according to eqn. 4.19.

Figure 6.29 displays examples of the effective static inter-quark potential obtained with Wilson lines of spatial separation $r = 2.45$ and $r = 10$, on the $m_l = 0.004$ ensemble of set **A** at the simulated and physical strange sea-quark mass. These are overlaid by the results of a fit to the range $t = 4$–8. The separations above define the bounds on the range $r = 2.45$–10 over which the static inter-quark potential is fit. These fits are shown in figure 6.30. The resulting values of r_0, r_1 and the ratio of r_1 to r_0 are given in table 6.27 at the simulated strange sea quark mass and table 6.28 at the physical mass. The strange sea-quark mass dependence of these three quantities is shown in figure 6.31.

The data on the **B** ensembles are presented in the same order to the above. Figures 6.32 and 6.33 show examples of the effective potential on the $m_l = 0.005$ ensemble of set **B** and the fit to the static inter-quark respectively. Here the data are fit to the range $t = 3$–7 and the static inter-quark potential to $r = 2.45$–8. The values of r_0, r_1 and r_1/r_0 are given in tables 6.29 and 6.30 at the simulated and physical strange quark masses respectively. Their strange sea-quark mass dependence is shown in figure 6.34.

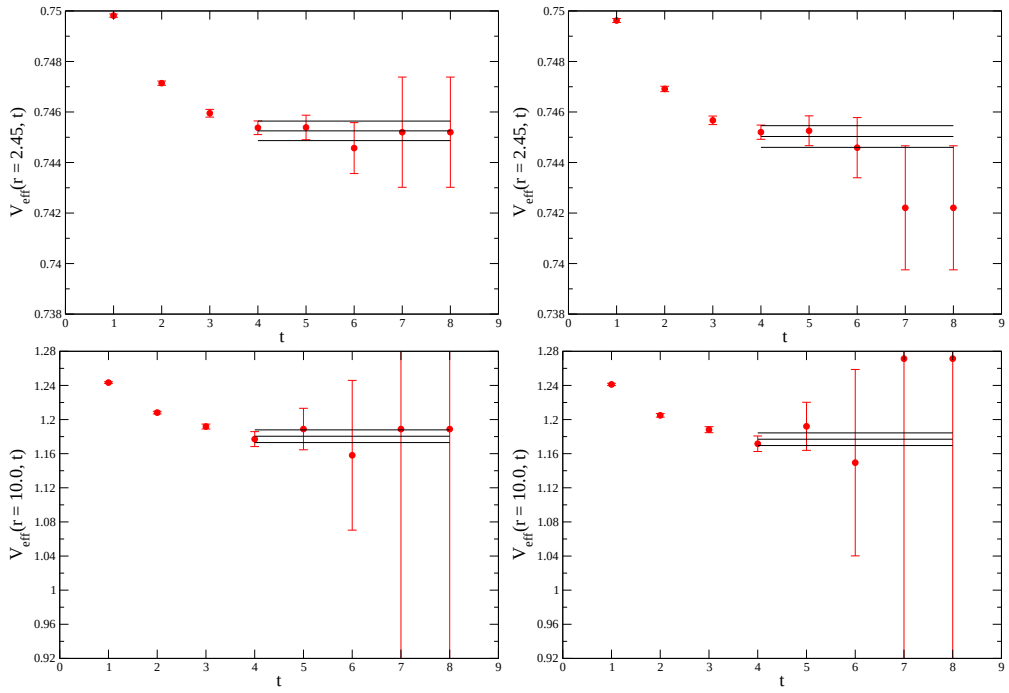

Figure 6.29: Plots of the effective static inter-quark potential obtained from the data on the $m_l = 0.004$ **A** ensemble at the values of spatial separation r bounding the range $2.45 - 10$ over which the fit to the static inter-quark potential is performed. The upper panels show the fit, over the range $t = 4$–8, to the time dependence of $W(r = 2.45, t)$ at the simulated strange quark mass $m_h = 0.03$ (top-left) and at the closest reweighted strange quark mass $m_h = 0.027$ to the physical value (top-right). The lower panels show the fit, over the same range $t = 4$–8, to the time dependence of $W(r = 10.00, t)$ at the simulated strange quark mass $m_h = 0.03$ (bottom-left) and at the closest reweighted strange quark mass $m_h = 0.027$ to the physical value (bottom-right).

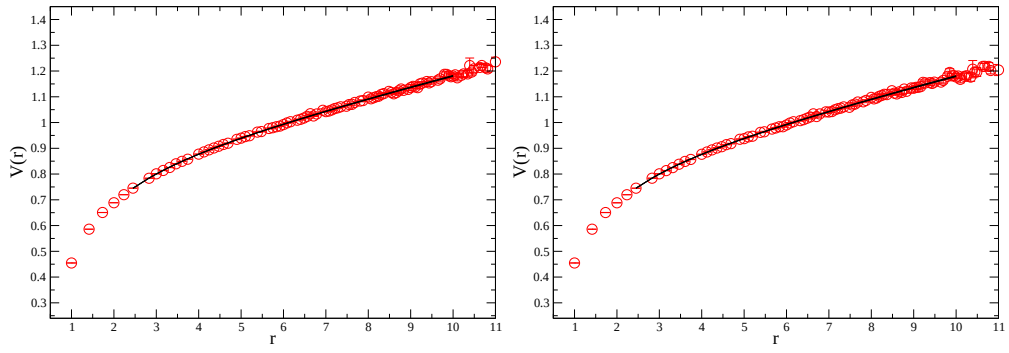

Figure 6.30: Plots of the static inter-quark potential as a function of the spatial separation of the Wilson lines on the $m_l = 0.004$ **A** ensemble at the simulated strange quark mass $m_h = 0.03$ (left) and at the closest reweighted strange quark mass $m_h = 0.027$ to the physical value (right). These are overlaid by the results of fits to the range $2.45 - 10$.

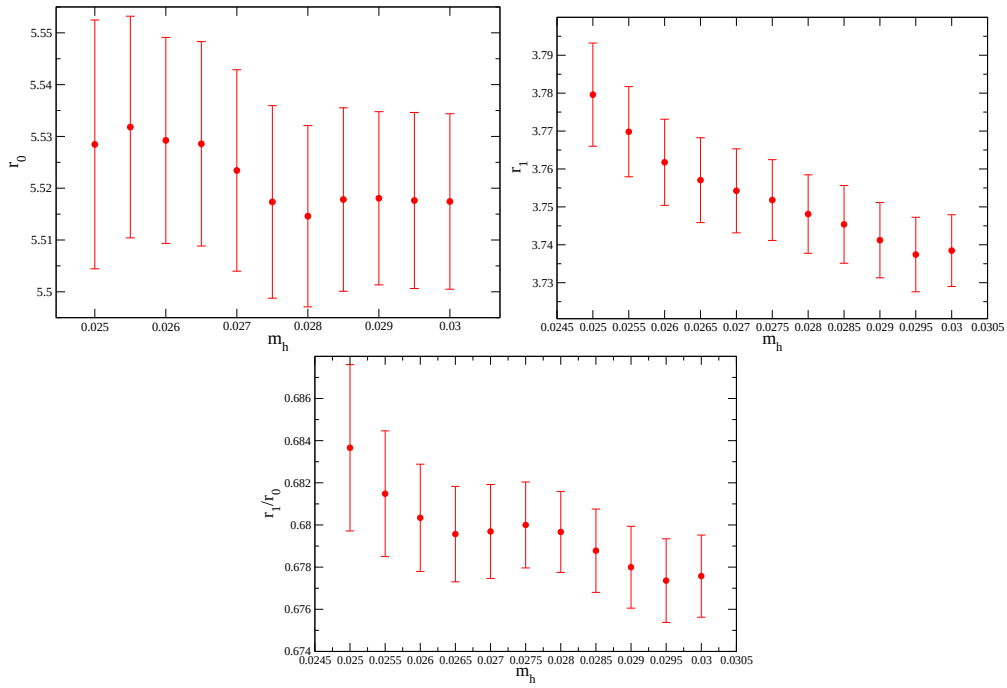

Figure 6.31: The strange sea-quark mass dependence of r_0 (top-left), r_1 (top-right) and the ratio r_1/r_0 (bottom) on the $m_l = 0.004$ **A** ensemble.

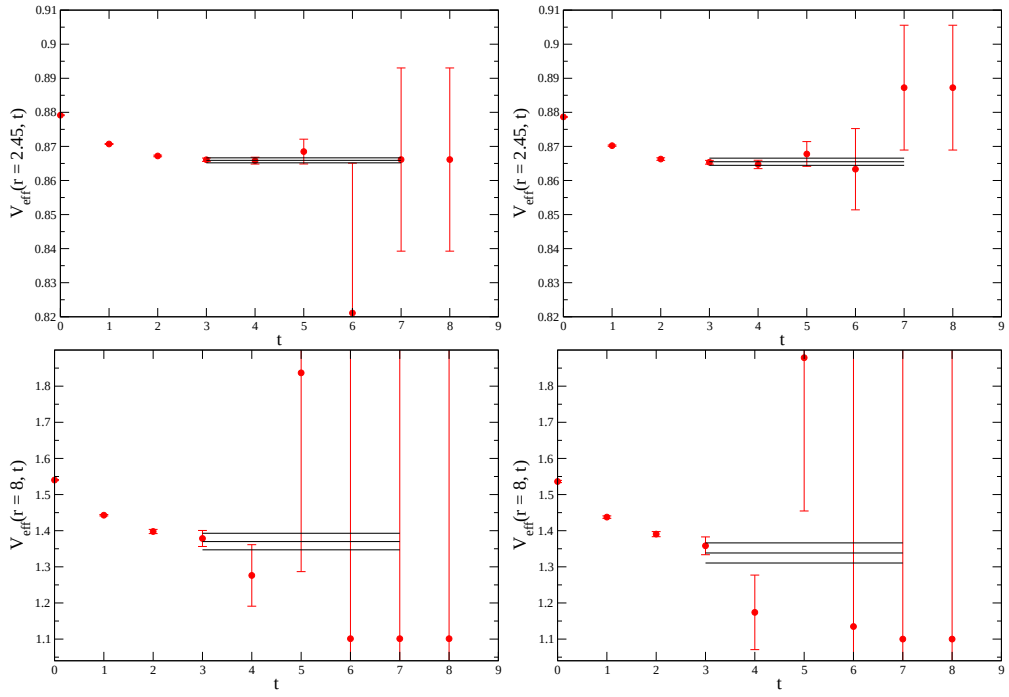

Figure 6.32: Plots of the effective static inter-quark potential obtained from the data on the $m_l = 0.005$ **B** ensemble at the values of spatial separation r bounding the range $2.45 - 8$ over which the fit to the static inter-quark potential is performed. The upper panels show the fit, over the range $t = 3$–7, to the time dependence of $W(r = 2.45, t)$ at the simulated strange quark mass $m_h = 0.04$ (top-left) and at the closest reweighted strange quark mass $m_h = 0.0345$ to the physical value (top-right). The lower panels show the fit, over the same range $t = 3$–7, to the time dependence of $W(r = 8.00, t)$ at the simulated strange quark mass $m_h = 0.04$ (bottom-left) and at the closest reweighted strange quark mass $m_h = 0.0345$ to the physical value (bottom-right).

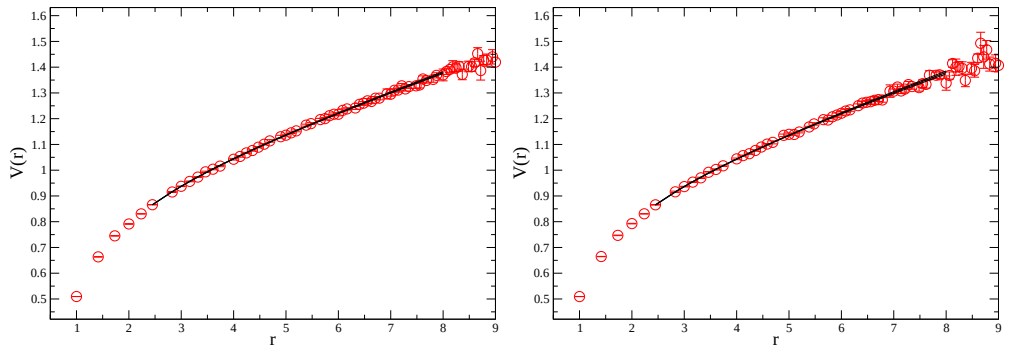

Figure 6.33: Plots of the static inter-quark potential as a function of the spatial separation of the Wilson lines on the $m_l = 0.005$ **B** ensemble at the simulated strange quark mass $m_h = 0.04$ (left) and at the closest reweighted strange quark mass $m_h = 0.0345$ to the physical value (right). These are overlaid by the results of fits to the range $2.45 - 8$.

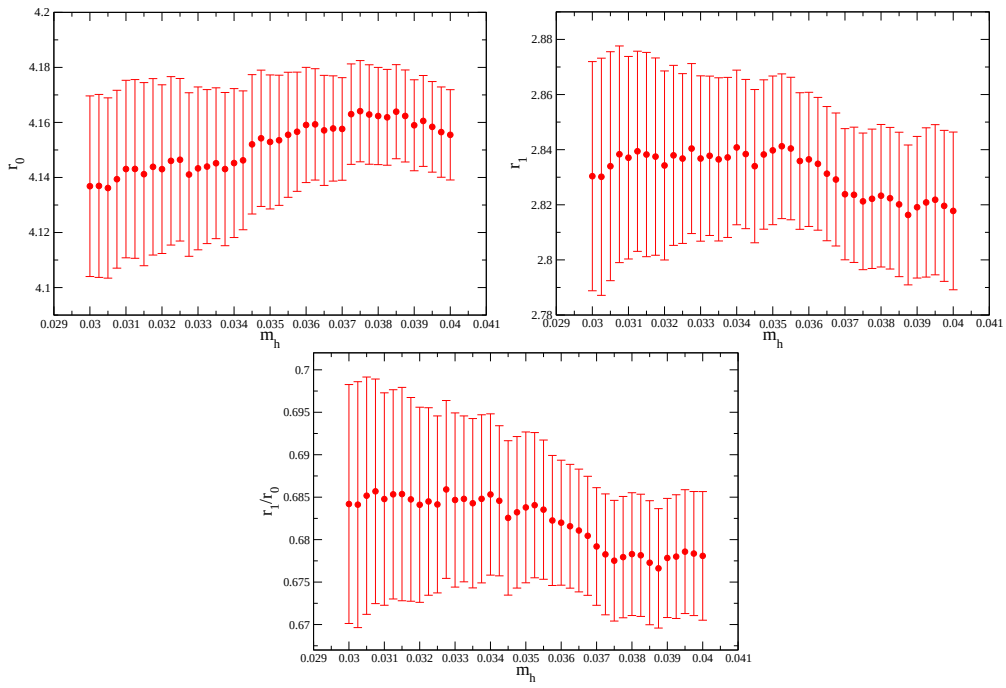

Figure 6.34: The strange sea-quark mass dependence of r_0 (top-left), r_1 (top-right) and the ratio r_1/r_0 (bottom) on the $m_l = 0.005$ **B** ensemble.

Q	$Q(m_l = 0.004)$	$Q(m_l = 0.006)$	$Q(m_l = 0.008)$
r_0	5.52(2)	5.50(2)	5.53(2)
r_1	3.738(9)	3.718(8)	3.707(9)
r_1/r_0	0.678(2)	0.676(2)	0.670(2)

Table 6.27: Quantities $Q \in \{r_0, r_1, r_1/r_0\}$ at the simulated strange quark mass on the **A** ensembles.

Q	$Q(m_l = 0.004)$	$Q(m_l = 0.006)$	$Q(m_l = 0.008)$
r_0	5.52(2)	5.52(2)	5.56(2)
r_1	3.756(12)	3.729(9)	3.724(10)
r_1/r_0	0.680(2)	0.675(2)	0.670(2)

Table 6.28: Quantities $Q \in \{r_0, r_1, r_1/r_0\}$ at the physical strange quark mass on the **A** ensembles.

Q	$Q(m_l = 0.005)$	$Q(m_l = 0.01)$
r_0	4.16(2)	4.10(2)
r_1	2.82(3)	2.70(2)
r_1/r_0	0.678(8)	0.657(6)

Table 6.29: Quantities $Q \in \{r_0, r_1, r_1/r_0\}$ at the simulated strange quark mass on the **B** ensembles.

Q	$Q(m_l = 0.005)$	$Q(m_l = 0.01)$
r_0	4.15(2)	4.12(3)
r_1	2.83(3)	2.72(4)
r_1/r_0	0.683(9)	0.661(11)

Table 6.30: Quantities $Q \in \{r_0, r_1, r_1/r_0\}$ at the physical strange quark mass on the **B** ensembles.

Chapter 7

Non-perturbative renormalisation of lattice quantities

Unphysical quantities such as the quark masses and the neutral kaon mixing parameter require renormalisation before the lattice cutoff can be removed. Usually these quantities are combined with high-energy perturbative calculations in order to extract physical quantities. For example, B_K is combined with perturbative Wilson coefficients and other parameters in order to obtain the physical quantity ϵ_K (section 3.1.4). This combination must be performed using quantities defined in a consistent renormalisation scheme. The perturbative calculations are typically performed in the $\overline{\text{MS}}$-scheme using dimensional regularisation. As this scheme is defined in a non-integer number of dimensions, it is not possible to calculate the renormalisation coefficients directly from the lattice. One approach is to use lattice perturbation theory, which is justified providing the lattice spacing and renormalisation scale are sufficiently far from the non-perturbative regime, $\mu \gg \Lambda_{\text{QCD}}$. However, such calculations suffer from ambiguities in the choice of the expansion parameter: calculations using the naive α_s in the 'tadpole-improved' scheme and the $\overline{\text{MS}}$ scheme can differ significantly [141]. In order to avoid these ambiguities, the renormalisation can be achieved non-perturbatively through a two stage process:

1. The non-perturbative quantity is renormalised into an intermediate scheme amenable to lattice calculation, and evolved to a scale in the perturbative regime.

2. A perturbative conversion factor is applied to move this into the $\overline{\text{MS}}$ scheme at the appropriate scale.

This chapter details the calculation of the renormalisation coefficients of several unphysical quantities, including B_K and the quark masses, using a set of intermediate schemes that generalise the *Rome-Southampton regularisation-invariant momentum scheme* (RI/MOM) [142]. In particular, the chapter details the first calculation of these quantities using lattice volume source propagators and non-exceptional momentum configurations to vastly reduce the statistical and systematic errors over the traditional

approach. Note, the prefix 'RI' will often be dropped from the scheme labels where convenient.

The layout is as follows. The point-source RI/MOM scheme determination of the mass and field renormalisation coefficients, as well as those for the bilinear and four-point $\Delta S = 2$ vertices, is discussed, followed by their generalisation to non-exceptional 'symmetric' kinematics using volume sources. A demonstration of the volume source technique is performed on a $16^3 \times 32$ Domain Wall fermion lattice, along with a small demonstration of the use of non-exceptional kinematics to reduce the effects of the dynamical chiral symmetry breaking at large momenta. Finally, the volume source technique with non-exceptional kinematics is applied on the $32^3 \times 64$ (**A**) and $24^3 \times 64$ (**B**) ensemble sets detailed in the previous chapter in order to generate the renormalisation coefficients for the quark masses and B_K. These are used in chapter 8.

7.1 The RI/MOM scheme with point sources

The RI/MOM technique defines a renormalisation condition for operator insertions that can easily be implemented in the framework of a lattice simulation, and also in calculations using any other regularisation. The renormalisation condition defines the renormalisation coefficient of any operator as the factor required to make the chiral limit of the amputated operator with a momentum transfer of p^2 in the Landau gauge equal to its tree-level value at the scale $\mu^2 = p^2$. This condition is easy to implement in both the lattice regularisation and also in dimensional regularisation using perturbation theory at any order.

In order to allow for the chiral limit to be taken unambiguously, the operator insertions are calculated using only unitary light-quark propagators. Where a flavour index is specified in this chapter, it is only for the sake of clarity: the simulation makes no distinction between valence quark flavours other than through the Wick contractions. The value of the strange sea-quark mass cannot be taken to the chiral limit on the ensembles used in these analyses. This introduces a small systematic error that must be taken into account. Further discussion of this error can be found in section 7.4.

The traditional implementation of the RI/MOM scheme is performed using point source propagators [141]. Here the vertices are formed from momentum-space propagators

$$\mathcal{G}(p, x_0) = \sum_x e^{-ip\cdot(x-x_0)} \mathcal{G}(x \leftarrow x_0) \tag{7.1}$$

on Landau-gauge fixed configurations, where the sum is over all four Euclidean directions. The momenta are

$$p_\mu = \frac{2\pi}{L_\mu} n_\mu \,, \tag{7.2}$$

where $L_\mu \in (L, L, L, T)$ for an $L^3 \times T$ lattice, and n are integer-component four-vectors. The benefit of using point sources for this calculation is that once the propagator has been generated, any momentum can be applied with virtually zero additional computational cost. This is not the case for lattice volume sources, as will be discussed in section 7.3. The values of the momenta that can be applied in both cases are limited only by the discretisation effects present when the scale approaches the momentum discretisation scale, π/a. Of course for a sensible perturbative matching the scale must also be much larger than Λ_{QCD}. These conditions define a *scaling window* $\Lambda_{\text{QCD}} \ll \mu \ll \pi/a$ in which the procedure can be performed. In practise it is difficult to satisfy these conditions as the lattice spatial extent L is typically only of the order of $20 - 30$. Instead the components of the momentum in any given direction are minimised, spreading the momentum across multiple directions. Although this seems to be empirically sound, it is not ideal. There remains a percent scale scatter in the data due to the lattice not being invariant under $O(4)$ rotations. This is discussed in section 7.5. Ideally one would take the continuum limit in a way that removes this issue, but this requires the direction of the lattice momenta to be fixed such that the same observable is considered at each value of the lattice spacing - this can be achieved using twisted boundary conditions [143], but the technique is beyond the scope of this work.

Above, and for the remainder of this chapter, dimensionful quantities such as the momentum p and mass m are given in lattice units for convenience. Only when discretisation errors are discussed is the lattice spacing shown explicitly.

7.1.1 Mass and field renormalisation

The mass and field renormalisation coefficients in the RI/MOM scheme are defined as

$$q_r(x) = Z_q^{\frac{1}{2}} q_0(x) \quad \text{and} \quad \tilde{m}_r = Z_m \tilde{m}_0 \,, \tag{7.3}$$

where a subscript r indicates a renormalised quantity, a subscript 0 indicates a bare lattice quantity, and $\tilde{m}_0 = m_f + m_{\text{res}}$, where m_f is the bare simulated quark mass. As mentioned previously, only unitary masses are used. The field renormalisation relates the bare propagator to the renormalised propagator:

$$\mathcal{G}_r(p, x_0; \tilde{m}_r) = Z_q \mathcal{G}_0(p, x_0; \tilde{m}_0) \,. \tag{7.4}$$

The bare QCD propagator can be written in terms of the self-energy $\Sigma(p)$ in a similar way to eqn. 3.66:

$$\mathcal{G}_0(p) = \frac{-1}{\not{p} - m_0 - \Sigma(p)} \,, \tag{7.5}$$

using the conventions of ref. [144]. At non-zero mass the self-energy term can have two possible γ-matrix structures: 1 and $\not{p}$. At $m_0 = 0$, the unit matrix structure cannot appear due to helicity conservation [145], hence this structure must appear with a coefficient of m_0. The bare propagator can therefore be written as

$$\mathcal{G}_0(p) = \frac{-1}{\not{p}\Big(1 - \Sigma_V(p^2)\Big) - m_0\Big(1 + \Sigma_S(p^2)\Big)}\,, \tag{7.6}$$

or in terms of renormalised quantities,

$$\mathcal{G}_r(p) = \frac{-Z_q}{\not{p}\Big(1 - \Sigma_V(p^2)\Big) - \dfrac{m_r}{Z_m}\Big(1 + \Sigma_S(p^2)\Big)}\,. \tag{7.7}$$

The field renormalisation can be isolated by taking the chiral limit of the inverse propagator and differentiating with respect to $\not{p}$:

$$\lim_{m_r \to 0} \frac{\partial}{\partial \not{p}} \mathcal{G}_r^{-1}(p) = -\frac{1 - \Sigma_V(p^2)}{Z_q}\,. \tag{7.8}$$

The RI/MOM scheme defines Z_q by fixing the above to its tree-level value, for which $\Sigma_V = 0$. For Domain Wall lattice point source propagators, the renormalisation condition is

$$\lim_{m_r \to 0} \frac{-1}{12} \mathrm{tr} \left\langle \mathcal{G}_r(p, x_0; \tilde{m}_r) \right\rangle^{-1}_{p^2 = \mu^2} = 1\,, \tag{7.9}$$

where the factor of 12 arises from the trace of the 12×12 unit spin-colour matrix.

With Z_q determined, the mass renormalisation can be calculated using the fact that $\not{p}$ is traceless:

$$\mathrm{tr}\, \mathcal{G}_r^{-1}(p) = \frac{12 m_r}{Z_m Z_q}\Big(1 + \Sigma_S(p^2)\Big)\,. \tag{7.10}$$

At tree-level this is equal to just $12m_r$. Z_m is then defined for Domain wall point source propagators by the RI/MOM condition through the following relation,

$$\lim_{m_r \to 0} \frac{1}{12 m_r} \mathrm{tr} \left\langle \mathcal{G}_r(p, x_0; \tilde{m}_r) \right\rangle^{-1}_{p^2 = \mu^2} = 1\,. \tag{7.11}$$

7.1.2 Bilinear vertices

Flavour non-singlet bilinear composite-operator insertions of the form $\bar{u}\Gamma d$ also require renormalisation. The renormalised quantities are related to their bare counterparts through the following relation,

$$\left[\bar{u}\Gamma d\right]_r(\mu) = Z_\Gamma(\mu)\left[\bar{u}\Gamma d\right]_0\,. \tag{7.12}$$

The renormalisation coefficient is calculated as follows. First, the vertex

$$\mathcal{F}_{\Gamma,0}(p) = \mathcal{G}(p,x_0)\Gamma\left(\gamma^5\mathcal{G}(p,x_0)^\dagger\gamma^5\right) \tag{7.13}$$

is formed at the source location of the unrenormalised point-source propagator on each gauge configuration. The vertex is then amputated by contracting it with the ensemble-average of the inverse propagators:

$$\Pi_{\Gamma,0}(p) = \Big\langle\mathcal{G}(p,x_0)\Big\rangle^{-1}\Big\langle\mathcal{F}_{\Gamma,0}(p)\Big\rangle\left(\gamma^5\Big\langle\mathcal{G}^\dagger(p,x_0)\Big\rangle^{-1}\gamma^5\right). \tag{7.14}$$

Apart from for $\Gamma = 1$, the fifteen independent tensor combinations of gamma-matrices that can be chosen for Γ are traceless, hence the amputated vertex must be projected onto the unit matrix with a *projection operator* $\mathcal{P}_\Gamma$ that satisfies

$$\mathrm{tr}\left(\Pi_{\Gamma,0}\mathcal{P}_\Gamma\right) = 1\,. \tag{7.15}$$

The simplest choice, which defines the original RI/MOM scheme for bilinears, is $\mathcal{P}_\Gamma = \Gamma$. The renormalisation conditions are defined separately for each spin-parity eigenstate combination of vertices; scalar (S), pseudoscalar (P), vector (V), axial-vector (A) and tensor (T). Dropping the subscript 0 on $\Pi_{\Gamma,0}$ for clarity, define

$$\begin{aligned}
\Lambda_S(p) &= \frac{1}{12}\mathrm{tr}\left(\Pi_1(p)1\right), & \Lambda_P(p) &= \frac{1}{12}\mathrm{tr}\left(\Pi_{\gamma^5}(p)\gamma^5\right), \\
\Lambda_V(p) &= \frac{1}{48}\mathrm{tr}\left(\sum_\mu \Pi_{\gamma^\mu}(p)\gamma^\mu\right), & \Lambda_A(p) &= \frac{1}{48}\mathrm{tr}\left(\sum_\mu \Pi_{\gamma^\mu\gamma^5}(p)\gamma^5\gamma^\mu\right), \\
& & \Lambda_T(p) &= \frac{1}{72}\mathrm{tr}\left(\sum_{\mu<\nu} \Pi_{\sigma_{\mu\nu}}(p)\sigma_{\nu\mu}\right).
\end{aligned} \tag{7.16}$$

The renormalisation conditions for the bilinear operators are then

$$\Lambda_i^r = \frac{Z_i}{Z_q}\Lambda_i = 1\,, \tag{7.17}$$

applied in the chiral limit $\tilde{m}_0 \to 0$, where $i \in (S,P,V,A,T)$.

The local axial-vector bilinear renormalisation coefficient Z_A is the same as the coefficient relating the PCAC to the local axial-current introduced in section 4.1.3. As this coefficient can be calculated precisely using hadronic matrix elements (cf. section 6.2), the renormalisation condition on the axial-current provides an alternative evaluation of the field renormalisation Z_q which is much simpler to implement than eqns. 7.9 and 7.11.

At large $(ap)^2$ the propagator scales as [141]

$$\frac{1}{12}\mathrm{tr}\left\langle \mathcal{G}(p;\tilde{m}_0)\right\rangle^{-1} = \frac{a^3\langle\bar{q}q\rangle}{a^2p^2}C_1Z_q + Z_mZ_qa\tilde{m}_0 + \mathcal{O}\left(a^2p^2\right) . \tag{7.18}$$

Combining this with the continuum vector Ward-Takahashi identity [141][103]

$$\Lambda_S = \frac{1}{12}\mathrm{tr}\left(\frac{\partial\left\langle \mathcal{G}(p;\tilde{m}_0)\right\rangle^{-1}}{\partial\tilde{m}_0}\right) , \tag{7.19}$$

implies

$$Z_m = \frac{1}{Z_S} . \tag{7.20}$$

As a result, using the value of Z_q determined from Λ_A, the mass renormalisation Z_m can be calculated from Λ_S. This is the method preferred by the authors of ref. [141].

7.1.3 Renormalisation of B_K

The renormalisation of the $\Delta S = 2$ four-quark operator

$$\mathcal{O}_{VV+AA} = \left(\bar{s}\gamma^\mu(1-\gamma^5)d\right)\left(\bar{s}\gamma_\mu(1-\gamma^5)d\right) \tag{7.21}$$

proceeds in much the same fashion as for the bilinears, providing chiral symmetry is intact. If the chiral symmetry is broken, $\mathcal{O}_{VV+AA}$ mixes under renormalisation with other $\Delta S = 2$ operators,

$$\begin{aligned}
\mathcal{O}_{VV-AA} &= \left(\bar{s}\gamma^\mu(1-\gamma^5)d\right)\left(\bar{s}\gamma_\mu(1+\gamma^5)d\right) , \\
\mathcal{O}_{SS+PP} &= \left(\bar{s}(1-\gamma^5)d\right)\left(\bar{s}(1-\gamma^5)d\right) , \\
\mathcal{O}_{SS-PP} &= \left(\bar{s}(1-\gamma^5)d\right)\left(\bar{s}(1+\gamma^5)d\right) , \text{ and} \\
\mathcal{O}_{TT} &= (\bar{s}\sigma^{\mu\nu}d)(\bar{s}\sigma_{\mu\nu}d) ,
\end{aligned} \tag{7.22}$$

which are labelled by the Dirac structure of the even-parity components. Here the odd-parity components do not contribute to neutral kaon mixing and have been ignored. In ref. [141], it was shown that the operator mixing is very small for Domain Wall fermions, and is thus neglected in these analyses.

The procedure for generating an amputated four-quark vertex of spin-structure $\Gamma\Gamma \in \{VV, AA\}$ is as follows. A rank-four tensor

$$[\mathcal{F}_{\Gamma\Gamma,0}(p)]_{ijkl} = \left[\mathcal{G}_s(p,x_0)\Gamma\left(\gamma^5\mathcal{G}_d^\dagger(p,x_0)\gamma^5\right)\right]_{ij} \times \left[\mathcal{G}_s(p,x_0)\Gamma\left(\gamma^5\mathcal{G}_d^\dagger(p,x_0)\gamma^5\right)\right]_{kl} \tag{7.23}$$

is formed on each gauge configuration. Here i, j, k, l are joint spin-colour indices. This

is then amputated by contracting each leg with the corresponding ensemble-averaged inverse-propagator:

$$\begin{aligned}\left[\Pi_{\Gamma\Gamma,0}(p)\right]_{mnop} &= \Big\langle \mathcal{G}_s(p,x_0)\Big\rangle^{-1}_{mi}\Big\langle \mathcal{G}_s(p,x_0)\Big\rangle^{-1}_{nk}\Big\langle \mathcal{F}_{\Gamma,0}(p)\Big\rangle_{ijkl} \\ &\quad\times\left(\gamma^5\Big\langle \mathcal{G}_d^\dagger(p,x_0)\Big\rangle^{-1}\gamma^5\right)_{jo}\left(\gamma^5\Big\langle \mathcal{G}_d^\dagger(p,x_0)\Big\rangle^{-1}\gamma^5\right)_{lp}.\end{aligned} \tag{7.24}$$

Here Einstein's summation convention is used in the sum over spin-colour indices. The $VV+AA$ amputated vertex is formed by the addition of separate VV and AA vertices:

$$\Pi_{VV+AA,0}(p) = \Pi_{VV,0}(p) + \Pi_{AA,0}(p)\,. \tag{7.25}$$

The projected vertices are formed by contracting the legs according to the forms of the Wick contractions given in eqns. 4.104 and 4.105:

$$\Lambda_{VV+AA} = \mathcal{P}_{ijkl}(\gamma^\mu)\left(\left[\Pi_{VV+AA,0}(p)\right]_{ijkl} - \left[\Pi_{VV+AA,0}(p)\right]_{iklj}\right), \tag{7.26}$$

where the projection operator is defined as

$$\mathcal{P}_{ijkl}(\gamma^\mu) = \frac{1}{3072}\Big((\gamma^\mu)_{ji}(\gamma_\mu)_{lk} + (\gamma^5\gamma^\mu)_{ji}(\gamma^5\gamma_\mu)_{lk}\Big)\,. \tag{7.27}$$

Here the coefficient is the magnitude of the tree-level vertex, and the γ-matrices should be interpreted as spin-colour matrices that are unit-diagonal on the colour indices. The renormalisation condition is then simply

$$\frac{1}{Z_q^2} Z_{VV+AA}\Lambda_{VV+AA} = 1\,, \tag{7.28}$$

which is applied in the chiral limit as before.

B_K is defined as the ratio (eqn. 4.97) of the $VV+AA$ matrix element to the square of the $\langle K^0|A|0\rangle$ correlation function. As such its renormalisation coefficient is determined as

$$Z_{B_K}^{RI/MOM} = \frac{Z_{VV+AA}}{Z_A^2}\,. \tag{7.29}$$

This can be obtained conveniently through the combination of the $VV+AA$ vertex and the axial-vector bilinear vertex

$$Z_{B_K}^{RI/MOM} = \Lambda_{VV+AA}^{-1}\Lambda_A^2 \tag{7.30}$$

in the chiral limit.

7.2 Exceptional and non-exceptional kinematics

In the previous section, bilinear vertices are formed by contracting Fourier-transformed point-source propagators of the same momentum. Here the incoming propagator carries the momentum to the vertex and the outgoing propagator carries it away, such that there is no net momentum transfer to any external field that is coupled to the vertex. These are referred to as *exceptional kinematics* [141].

In ref. [141], it was shown that the vector and axial-vector amputated vertices, Λ_V and Λ_A (as well as Λ_S and Λ_P), differed substantially apart from at very large momenta when calculated with exceptional kinematics. This is also demonstrated in section 7.3.3. Differences between these vertices can only arise through the breaking of the chiral symmetry, which allows the $(8,1)$ and $(1,8)$ representations of the $SU(3)_L \times SU(3)_R$ symmetry of 2+1 flavour DWF at infinite L_s to mix, such that the vertices receive different contributions of the form m^2/p^2 and $m\langle\bar{q}q\rangle/p^4$. It was argued that explicit, finite L_s chiral symmetry breaking effects are $\mathcal{O}(m_{\text{res}}^2)$, and are thus far too small to account for the size of the mixing observed. The differences must therefore arise due to the dynamical chiral symmetry breaking of QCD. However, the differences between the amputated vertices were observed far above the dynamical symmetry breaking scale, and it was shown that the scale dependence is too weak to be accounted for by the spontaneous breaking in a naive way. It was postulated that these differences arise from the choice of kinematics: at zero momentum transfer, there are bilinear graphs of the form

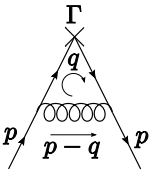

, (7.31)

for which there is a subgraph containing the vertex that carries only the loop momentum q. For graphs of this form, the interaction at the vertex is occuring at the scale of the loop momentum rather than that of the incoming momentum. When the loop momenta are soft, the vertex interaction occurs within the regime in which chiral symmetry is spontaneously broken, even if the momentum of the external propagators is large. This occurs with a suppression of $\sim 1/p^2$ arising from the single hard gluon propagator.

The suppression can be enhanced through the use of *non-exceptional* kinematics, in which the incoming and outgoing propagators have different momenta p_1 and p_2. The scale of the interaction is fixed by the momentum transfer q^2 if

$$p_1^2 = p_2^2 = (p_1 - p_2)^2 = q^2\,. \tag{7.32}$$

These are referred to as *symmetric* kinematics. Generalised versions of RI/MOM-

scheme using symmetric kinematics are referred to as RI/SMOM-schemes [144].

7.3 RI/MOM and RI/SMOM with lattice volume sources

Point source propagators allow for the calculation of the renormalisation coefficients at a large number of momentum scales with little additional computational cost. However, as described in section 4.2.8, measurements using these propagators are highly susceptible to gauge-field noise. In this section, the point-source techniques outlined in section 7.1 are generalised for use with lattice volume sources and symmetric kinematic configurations. The momentum of a volume-source propagator is fixed due to the necessity of including the phase factor in the sum over the spatial location of the source (cf. eqn. 4.96), therefore the use of these sources trades the ease of access to additional momenta for a lattice volume average over the source position.

An investigation of the viability of volume sources and non-exceptional kinematics is performed on a $16^3 \times 32$ Domain Wall ensemble, demonstrating a very large improvement in statistical errors and a large reduction in the size of chiral symmetry breaking effects. These techniques are applied in section 7.4 in order to obtain to renormalisation coefficients for quantities on the **A** and **B** ensembles.

7.3.1 Bilinear vertices

In section 7.1.2, point source propagators are contracted at the source location to form bilinear vertices. As there is only a single source location, the contraction of the momentum-space propagator (a 12×12 matrix on each configuration) can be performed during the analysis procedure rather than on the parallel machine during the simulation. This is not the case for volume source propagators: the inversion of the Dirac matrix upon a volume source involves a sum over the source location, and the Fourier transform sums over the sink location. As a result the vertex

$$\mathcal{F}_\Gamma(p_1,p_2) = \sum_y e^{-i(p_1-p_2)\cdot y}\psi(y;p_1)\Gamma\left(\gamma^5\psi(y;p_2)^\dagger\gamma^5\right) \tag{7.33}$$

must be formed on the parallel machine. Here $\psi(y;\vec{p})$ is the volume-source propagator defined in eqn. 4.96. Note, the phase factor at the vertex location cancels between the forwards- and backwards-flowing propagators when using exceptional kinematics. The Fourier-transformed vertex, $\mathcal{F}_\Gamma(p)$, is also a 12×12 matrix. This must be saved, for every Γ, alongside the Fourier-transformed propagator. From this point the analysis procedure is no different than before: the vertex is amputated according to eqn. 7.14, this time using the Fourier-transformed volume-source propagators, and the renormalisation condition of eqn. 7.15 is imposed.

With symmetric kinematics, an additional renormalisation scheme for the vector and axial-vector vertices, referred to as RI/SMOM$_{\not{q}}$, can be defined [144] by modifying the projection operator to include factors of $\hat{\not{q}} = \gamma^\mu \hat{q}_\mu$, where $\hat{q}_\mu = \sin q_\mu$ is the discretised momentum transfer:

$$\mathcal{P}_V(\text{SMOM}_{\not{q}}) = \hat{\not{q}}\hat{q}_\mu/\hat{q}^2\,, \tag{7.34}$$

$$\mathcal{P}_A(\text{SMOM}_{\not{q}}) = \hat{\not{q}}\gamma^5\hat{q}_\mu/\hat{q}^2. \tag{7.35}$$

Note, this scheme is referred to as the RI/SMOM scheme in ref. [144]. The variant containing the standard RI/MOM projection operators is referred to as the RI/SMOM$_{\gamma^\mu}$ scheme:

$$\mathcal{P}_V(\text{SMOM}_{\gamma^\mu}) = \gamma^\mu\,, \tag{7.36}$$

$$\mathcal{P}_A(\text{SMOM}_{\gamma^\mu}) = \gamma^5\gamma^\mu. \tag{7.37}$$

Note that the use of the discretised momentum $\hat{q}_\mu$ differs from the definitions in ref. [144], in which the continuum momentum q is used.

7.3.2 Renormalisation of $\Delta S = 2$ four-quark operators

Similarly to the bilinears, the average of the four-quark vertex over all insertion points,

$$[\mathcal{F}_\Gamma(p_1,p_2)]_{ijkl} = \sum_y e^{-2i(p_1-p_2)\cdot y}\Big[\left(\gamma^5\psi_s^\dagger(p_1,y)\gamma^5\right)\Gamma\psi_d(p_2,y)\Big]_{ij} \tag{7.38}$$

$$\times\Big[\left(\gamma^5\psi_s^\dagger(p_1,y)\gamma^5\right)\Gamma\psi_d(p_2,y)\Big]_{kl}\,, \tag{7.39}$$

which is the volume source equivalent of eqn. 7.23 with non-exceptional kinematics, must be performed on the parallel machine. Note the γ^5-hermiticity is applied to the s-quark propagators here as the vertex is formed at the propagator's sink location. The Fourier-transformed vertex is a rank-4 tensor containing 12^4 elements, which must be saved for each Γ. The formation of the amputated vertex

$$\begin{aligned}[\Pi_\Gamma(p_1,p_2)]_{ijkl} = &\left(\gamma^5\left\langle\mathcal{G}_s^\dagger(p_1)\right\rangle^{-1}\gamma^5\right)_{mi}\left(\gamma^5\left\langle\mathcal{G}_s^\dagger(p_1)\right\rangle^{-1}\gamma^5\right)_{nk}\\ &\times\left\langle\mathcal{F}_\Gamma(p_1,p_2)\right\rangle_{ijkl}\left\langle\mathcal{G}_d(p_2)\right\rangle^{-1}_{jo}\left\langle\mathcal{G}_d(p_2)\right\rangle^{-1}_{lp}\end{aligned} \tag{7.40}$$

requires careful attention to be paid to the spin-colour indices.

With symmetric kinematics, there are two choices of projection operator. The first is the same as the RI/MOM projector $\mathcal{P}(\gamma^\mu)$ defined in eqn. 7.27, while the second

includes factors of $\hat{\not{q}}$:

$$\mathcal{P}_{ijkl}(\not{q}) = \frac{1}{768q^2}\Big((\hat{\not{q}})_{ji}(\hat{\not{q}})_{lk} + (\gamma^5\hat{\not{q}})_{ji}(\gamma^5\hat{\not{q}})_{lk}\Big)\,. \tag{7.41}$$

Alongside the choice of projection operator, there is the choice of the renormalisation scheme for Z_q: RI/SMOM$_{\not{q}}$ or RI/SMOM$_{\gamma^\mu}$. As a result there are four independent SMOM renormalisation schemes for the four-quark operators. These are listed in table 7.3.2. When calculating Z_{B_K} using eqn. 7.30, the axial vertex must be renormalised in the same scheme as Z_q.

Scheme	$VV+AA$ projector	Z_q scheme
RI/MOM	$\mathcal{P}(\gamma^\mu)$	RI/MOM
SMOM$(\gamma^\mu, \not{q})$	$\mathcal{P}(\gamma^\mu)$	SMOM$_{\not{q}}$
SMOM(γ^μ, γ^μ)	$\mathcal{P}(\gamma^\mu)$	SMOM$_{\gamma^\mu}$
SMOM$(\not{q}, \not{q})$	$\mathcal{P}(\not{q})$	SMOM$_{\not{q}}$
SMOM$(\not{q}, \gamma^\mu)$	$\mathcal{P}(\not{q})$	SMOM$_{\gamma^\mu}$

Table 7.1: The five NPR-schemes used in the renormalisation of the $VV+AA$ four-quark operator.

7.3.3 Demonstration of RI/MOM with volume sources

This section contains a demonstration of non-perturbative renormalisation using the RI/MOM scheme with volume-source propagators, performed on three ensembles with $m_l = 0.03$, 0.02 and 0.01 in lattice units, of a $16^3 \times 32$, $\beta = 2.13$ Domain Wall fermion ensemble set with $L_s = 16$, and $a^{-1} \sim 1.73$ GeV. Data are generated on ten configurations per ensemble, each separated by 300 molecular dynamics time units.

These ensembles were used for the demonstration of stochastic source techniques in chapter 5. Non-perturbative RI/MOM renormalisation coefficients for the bilinear operators and the B_K four-quark operator were calculated on these ensembles using point source propagators in ref. [141].

The analysis is performed with exceptional kinematics at five different scales, using unitary-mass volume-source propagators. The chosen momenta are listed in table 7.2. The values of the bare bilinear vertices on each ensemble are given in tables 7.3, 7.4 and 7.5. Here the errors are analysed using the jackknife procedure. The differences between the vector and axial-vector amplitudes due to the exceptional kinematics are clearly visible in these three tables, and are plotted in figure 7.1 for the $m_l = 0.03$ ensemble.

In order to ensure that the jackknife errors are not being underestimated due to the small number of configurations, the analysis of the $m_l = 0.01$ ensemble is repeated

with an extra 9 configurations (totalling 19). The values of the bare vertices are listed in table 7.6. These values are consistent with those measured on 10 configurations (table 7.3), and show the expected reduction in errors.

The values of the bare vertices listed in the tables are all consistent with those calculated in ref. [141], and have substantially smaller errors. The values in the cited paper were calculated using four point sources over 75 gauge configurations, i.e. 6 times the computational cost of the volume source analysis, as measured in inversions of the Dirac matrix. Figure 7.1 also shows a comparison of the average of the bare vector and axial-vector vertices between the two analyses, showing clearly the marked reduction in errors.

The four-quark $\Delta S = 2$ vertex is also analysed using the volume-source propagators. Due to the exceptional kinematics, the estimates of Z_A/Z_q obtained from Λ_A and Λ_V differ. Following ref. [141], the average of Λ_A and Λ_V is used in place of Λ_A in eqn. 7.30, such that the renormalisation coefficient for B_K is obtained in the chiral limit through the following relation,

$$Z_{B_K}^{RI/MOM} = \frac{(\Lambda_A + \Lambda_V)^2}{4\Lambda_{VV+AA}}\,. \tag{7.42}$$

$Z_{B_K}^{RI/MOM}$ is calculated with the five momenta given previously, on 10 gauge configurations of each of the three ensembles. The values of the coefficient on each ensemble are listed in table 7.7, and a comparison between the point and volume source approaches on the $m_l = 0.03$ ensemble is shown in figure 7.2. Again there is a clear advantage to using volume sources over point sources.

Following the procedure outlined in ref. [141], the chiral limit is taken and a scheme change factor $w^{-1}[p^2]$ (eqn. 3.38) is applied to convert to the RGI scheme. This quantity retains a small scale dependence due to lattice artefacts. The artefacts are removed by fitting to the linear form

$$Z_{B_K}^{RGI}(a^2p^2) = A + B(ap)^2\,, \tag{7.43}$$

and setting $B = 0$. The RGI-scheme coefficient is then converted into the $\overline{\text{MS}}$-scheme. This procedure relies on the perturbative truncation errors being small compared to the lattice artefacts and the chiral symmetry breaking effects. In section 7.6 it becomes possible to take the continuum limit, removing the bulk of the lattice artefacts without the need for an extrapolation to $(ap)^2 = 0$. Non-exceptional kinematics are also used to remove the chiral symmetry breaking errors. As a result the truncation of the perturbative series becomes the dominant systematic error and this technique is no longer appropriate.

The chiral fits and the extrapolation of $Z_{B_K}^{RGI}$ are shown in figures 7.2 and 7.3

n_x	n_y	n_z	n_t	$(ap)^2$
1	2	1	2	1.079
1	2	1	3	1.272
1	2	1	4	1.542
2	2	2	1	1.889
2	1	2	4	2.005

Table 7.2: Chosen momenta for the demonstration of volume source NPR with exceptional kinematics. Here the value of $(ap)^2$ is determined as $(ap)^2 = \sum_\mu (2\pi n_\mu / L_\mu)^2$ where $L_\mu = 16 \,|\, \mu \in \{x, y, z\}$ and $L_t = 32$.

$(ap)^2$	Λ_A	Λ_V	Λ_P	Λ_S	Λ_T
1.079	1.1102(18)	1.1330(23)	3.027(39)	1.709(27)	0.9891(12)
1.272	1.1159(15)	1.1360(18)	2.758(41)	1.635(17)	1.0023(11)
1.542	1.1214(14)	1.1341(13)	2.445(40)	1.607(16)	1.0168(11)
1.889	1.1320(7)	1.1412(9)	2.220(22)	1.571(9)	1.0349(8)
2.005	1.1319(9)	1.1406(13)	2.173(22)	1.541(12)	1.0394(8)

Table 7.3: Bare bilinear vertex amplitudes on the $m_l = 0.01$ ensemble with 10 configurations.

respectively. After converting to the $\overline{\text{MS}}$ scheme, the following result is obtained:

$$Z_{BK}^{\overline{\text{MS}}}(2\text{GeV}) = 0.9208(18)\,, \tag{7.44}$$

where the error is statistical only. Comparing to the point source result of ref. [141],

$$Z_{BK}^{\overline{\text{MS}}}(2\text{GeV}) = 0.9276(52)\,, \tag{7.45}$$

where again the error is statistical only, it is clear that the volume source approach offers a significant improvement.

$(ap)^2$	Λ_A	Λ_V	Λ_P	Λ_S	Λ_T
1.079	1.1102(18)	1.1355(22)	2.562(26)	1.679(14)	0.9896(9)
1.272	1.1149(11)	1.1365(16)	2.358(19)	1.630(17)	1.0039(9)
1.542	1.1197(8)	1.1364(15)	2.163(14)	1.590(13)	1.0177(10)
1.889	1.1298(6)	1.1406(8)	1.982(7)	1.563(8)	1.0345(4)
2.005	1.1315(7)	1.1417(9)	1.945(9)	1.541(4)	1.0400(4)

Table 7.4: Bare bilinear vertex amplitudes on the $m_l = 0.02$ ensemble with 10 configurations.

$(ap)^2$	Λ_A	Λ_V	Λ_P	Λ_S	Λ_T
1.079	1.1030(13)	1.1345(9)	2.304(18)	1.651(13)	0.9886(9)
1.272	1.1109(9)	1.1340(11)	2.137(14)	1.622(9)	1.0020(7)
1.542	1.1182(9)	1.1342(10)	1.981(9)	1.588(5)	1.0157(5)
1.889	1.1276(7)	1.1410(7)	1.866(8)	1.545(4)	1.0343(5)
2.005	1.1302(8)	1.1430(7)	1.828(9)	1.528(5)	1.0397(8)

Table 7.5: Bare bilinear vertex amplitudes on the $m_l = 0.03$ ensemble with 10 configurations.

$(ap)^2$	Λ_A	Λ_V	Λ_P	Λ_S	Λ_T
1.079	1.1121(14)	1.1327(13)	2.999(41)	1.668(33)	0.9884(8)
1.272	1.1164(11)	1.1347(12)	2.720(33)	1.627(21)	1.0017(7)
1.542	1.1224(9)	1.1334(9)	2.421(24)	1.604(13)	1.0166(7)
1.889	1.1299(7)	1.1392(8)	2.208(16)	1.560(9)	1.0340(5)
2.005	1.1323(6)	1.1408(7)	2.167(13)	1.528(11)	1.0398(5)

Table 7.6: Bare bilinear vertex amplitudes on the $m_l = 0.01$ ensemble with 19 configurations.

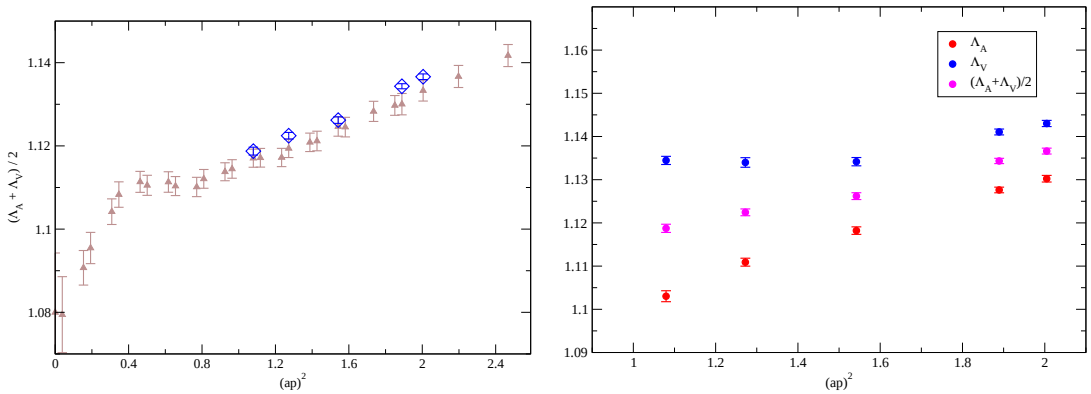

Figure 7.1:
Left: A comparison of $\frac{1}{2}(\Lambda_A + \Lambda_V)$ calculated on the 0.03 ensemble using a volume-source propagators (blue diamonds) on 10 gauge configurations, and four point-source propagators (grey triangles) on 75 gauge configurations.
Right: Bare vector and axial-vector vertex amplitudes calculated using volume-source propagators on the 0.03 ensemble.

$(ap)^2$	$m_l = 0.01$ (10 cfg)	$m_l = 0.01$ (19 cfg)	$m_l = 0.02$ (10 cfg)	$m_l = 0.03$ (10cfg)
1.079	0.9181(10)	0.9173(6)	0.9164(10)	0.9164(5)
1.272	0.9120(6)	0.9123(6)	0.9111(8)	0.9113(4)
1.542	0.9074(6)	0.9071(4	0.9064(7)	0.9061(4)
1.889	0.9020(4)	0.9023(2)	0.9015(3)	0.9014(3)
2.005	0.9005(4)	0.9005(3)	0.8998(3)	0.8995(4)

Table 7.7: $Z_B^{RI/MOM}$ on the three ensembles. Here the number of gauge configurations

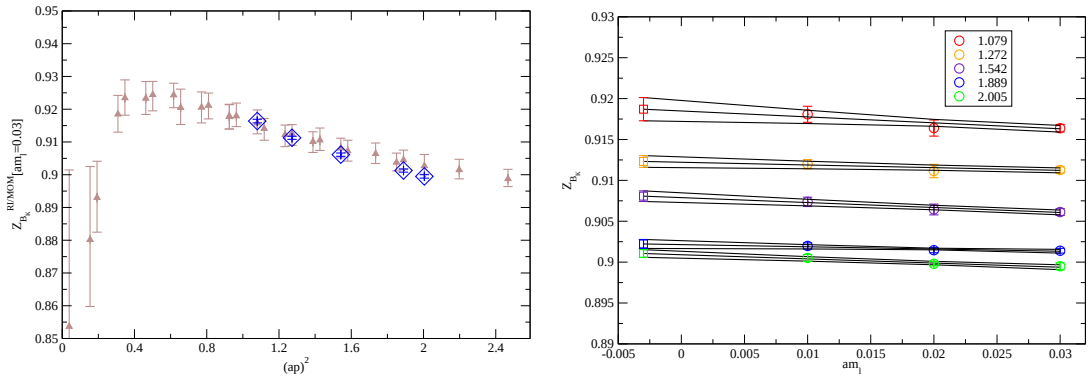

Figure 7.2:
Left: A comparison of Z_{B_K} in the RI/MOM scheme, calculated on the 0.03 ensemble using volume-source propagators (blue diamonds) on 10 gauge configurations, and four point-source propagators (grey triangles) on 75 gauge configurations. This figure clearly shows the improvement in statistical errors from the use of volume source propagators over point source propagators, even at $1/30^{\text{th}}$ of the computational cost.
Right: The chiral extrapolation of $Z_{B_K}(am_l)$ calculated in the RI/MOM scheme using volume-source propagators on 10 gauge configurations of each ensemble. Here the legends correspond to the value of $(ap)^2$ for each point. The data points are represented by circles, and the extrapolated points are represented by squares.

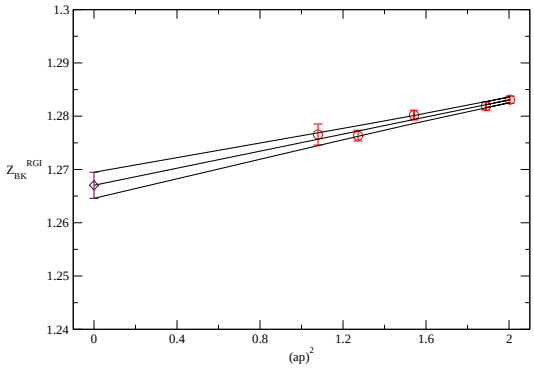

Figure 7.3: The fit of $Z_{B_K}^{RGI}$ to the form $A + B(ap)^2$, which is used here to remove lattice artefacts. The data are represented by red squares and the extrapolated point at $(ap)^2 = 0$ by a maroon diamond.

Vertex	p_1	p_2	p_1 & p_2
Λ_A	1.1188(7)	1.1188(6)	1.0548(3)
Λ_V	1.1359(7)	1.1373(8)	1.0581(3)
Λ_S	1.590(8)	1.585(8)	1.220(1)
Λ_P	1.982(11)	1.995(12)	1.238(1)

Table 7.8: A comparison between bare bilinear vertices calculated using exceptional and non-exceptional momentum configurations on the $16^3 \times 32$ $m_l = 0.03$ ensemble. Here $p_1 = (1, 1, 2, 4)$, $p_2 = (2, 1, 2, -2)$. Both momenta are at $(ap)^2 = 1.542$.

7.3.4 Demonstration of RI/SMOM$_{\gamma^\mu}$ with volume sources

A small demonstration of the suppression of chiral symmetry breaking effects at high momenta through the use of symmetric non-exceptional momentum configurations is performed by generating two additional volume-source propagators with $p_1 = (1, 1, 2, 4)$ and $p_2 = (2, 1, 2, -2)$, both with $(ap)^2 = 1.542$ and satisfying eqn. 7.32, on 10 configurations of the $16^3 \times 32$ $m_l = 0.03$ ensemble detailed in the previous section. The bare bilinear vertices Λ_i, for $i \in \{V, A, S, P\}$, are calculated using the non-exceptional momentum configuration with $p_{in} = p_1$ and $p_{out} = p_2$, and also from the two exceptional configurations with $p_{in} = p_{out} = p_1$ and $p_{in} = p_{out} = p_2$. The bare vertices with exceptional momenta are calculated in the RI/MOM scheme and those with non-exceptional momenta in the RI/SMOM$_{\gamma^\mu}$ scheme. Their values are given in table 7.8. The significant reduction in the differences between Λ_A and Λ_V, and between Λ_S and Λ_P, can be clearly seen. Further examples of this improvement can be found in the next section.

7.4 NPR on the A and B ensembles.

A	n_1	n_2	**B**	n_1	n_2
	(4,2,2,0)	(4,0,-2,4)		(0,4,4,0)	(4,0,4,0)
	(4,4,3,2)	(4,3,-1,-8)		(1,2,2,8)	(-2,-1,2,8)
	(4,-5,0,-6)	(4,0,-5,-6)		(1,4,2,8)	(2,-1,4,8)
	(-4,-1,-4,2)	(-4,-4,1,2)		(2,2,4,0)	(4,-2,2,0)
	(3,2,2,2)	(3,2,-1,-4)		(2,3,2,8)	(3,-2,2,8)
				(-3,1,1,8)	(1,1,3,8)

Table 7.9: Symmetric momentum configurations used in the evaluation of the amputated vertices on the **A** and **B** ensemble sets. The Fourier-components are given in Euclidean ordering (x, y, z, t) and the lattice momenta are related by $(ap_i)_\mu = 2\pi(n_i)_\mu / L_\mu$ where $L_\mu = 32 \,|\, \mu \in \{x, y, z\}$ and $L_t = 64$ on the **A** ensembles and $L_\mu = 24 \,|\, \mu \in \{x, y, z\}$ and $L_t = 64$ on the **B** ensembles. Exceptional momentum configurations are also generated by forming the vertex from a single propagator.

The RI/MOM point-source analysis on the $16^3 \times 32$ DWF ensembles [141], discussed in section 7.3.3, suffered from sizeable errors due to the enhancement of chiral symmetry breaking effects at high momenta by the exceptional kinematics, and also due to the truncation of the perturbative series that is used to match the RI/MOM-scheme data to the $\overline{\text{MS}}$ scheme. A pilot study of the use of the symmetric momentum schemes for bilinear operators was performed [146] using point source propagators on the same configurations, demonstrating the reduction in systematic errors expected from the discussion in sections 7.3.4 and 7.2.

This section presents an analysis of the renormalisation coefficients of the quark mass, vector and axial-vector bilinears and B_K, using volume source propagators with both exceptional and non-exceptional kinematics. As shown in section 7.3.3, the use of volume-source propagators all but eliminates the statistical error, allowing for a better determination of the various systematic error sources, as well as reducing the overall error. The propagators are generated on 20 gauge configurations of the three lightest ensembles of the **A** ($m_l = 0.004$, 0.006, 0.008) and **B** ($m_l = 0.005$, 0.01, 0.02) ensemble sets, and the momenta are given in table 7.9. The momentum ranges of the ensemble sets are chosen to overlap in the region $3.5\,\text{GeV}^2 < p^2 < 7.0\,\text{GeV}^2$, and there are additional larger momenta up to $p^2 < 11.0\,\text{GeV}^2$ on the finer **A** ensembles. The momenta are chosen in order to sample a range of scales while minimising $\sum_\mu (ap_\mu)^4$, a quantity which is expected to be proportional to the size of the $O(4)$ symmetry-breaking discretisation error mentioned previously and discussed in greater detail below. The renormalisation coefficients are calculated using several (S)MOM renormalisation schemes in order to allow for a better judgement of the truncation error. The lattice spacing is taken from the continuum analysis in chapter 8, given in eqn. 8.34. The analyses are performed using only the central value, and the effects of the error on the lattice spacing are accounted for by an additional systematic error.

7.5 Quark mass renormalisation

The quark mass renormalisation coefficient is calculated using bilinear operators, as described in section 7.1.2, using volume sources and symmetric momentum configurations. Both the RI/SMOM$_{\not{q}}$ and RI/SMOM$_{\gamma^\mu}$ schemes are used. In order to allow for the presence of chiral symmetry breaking effects, the renormalisation coefficients are calculated using the averages of the V and A, and the S and P vertices

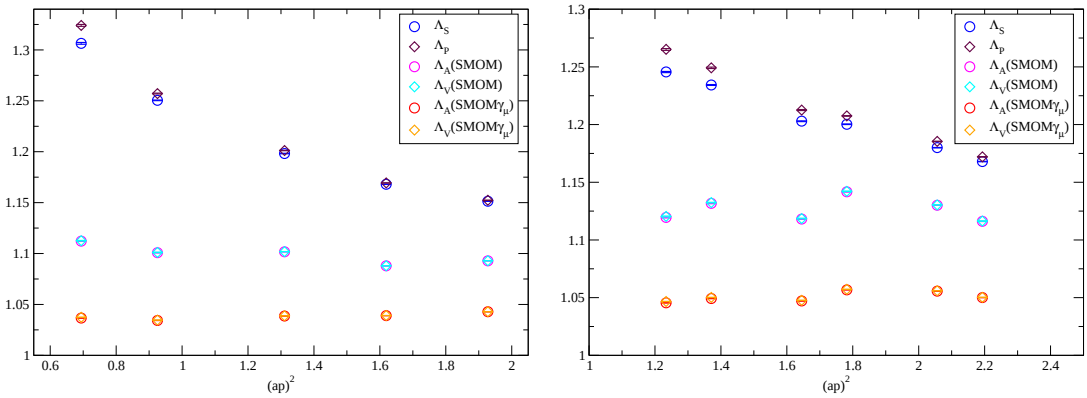

Figure 7.4: Amputated bilinear vertices with non-exceptional kinematics as a function of $(ap)^2$ on the **A** ensembles (left) and the **B** ensembles (right).

respectively:

$$\frac{Z_q}{Z_A} = \frac{1}{2}(\Lambda_V + \Lambda_A)\,, \tag{7.46}$$

$$Z_q Z_m = \frac{1}{2}(\Lambda_S + \Lambda_P)\,, \tag{7.47}$$

from which Z_m is calculated as

$$Z_m = \frac{1}{Z_A}\frac{\Lambda_S + \Lambda_P}{\Lambda_A + \Lambda_V}\,. \tag{7.48}$$

This is particularly important for the scalar and pseudoscalar vertices, which differ at the $1-2\%$ level at low momenta even with the non-exceptional kinematics, due to the residual effects of the dynamical chiral symmetry breaking. This can be seen in figure 7.4. The vector and axial-vector vertices on the other hand appear highly consistent. The values of the amputated vertices are listed in tables 7.10 through 7.15.

The chiral extrapolations of Z_m on each ensemble are presented in figure 7.5. They have a very benign mass dependence, and thus the systematic error resulting from the strange quark mass not being taken to the chiral limit is minimal (see below). The coefficients are converted into the $\overline{\text{MS}}$-scheme at 2 GeV for each value of the momentum transfer using the following formula,

$$Z_m^{\overline{\text{MS}}}(2\,\text{GeV}) = C_{S\to\overline{\text{MS}}}[2\,\text{GeV}, p]\, Z_m^{\overline{\text{MS}}}(p)\,, \tag{7.49}$$

where the conversion factors $C_{S\to\overline{\text{MS}}}[\mu', \mu]$ for the lattice scheme S are obtained from the ratio

$$C_{S\to\overline{\text{MS}}}[\mu', \mu] = \frac{w^S[\mu]}{w^{\overline{\text{MS}}}[\mu']} \tag{7.50}$$

$(ap)^2$	$A(SMOM_{\gamma_\mu})$	$V(SMOM_{\gamma_\mu})$	$A(SMOM_{\not{q}})$	$V(SMOM_{\not{q}})$
0.69396	1.0366(1)	1.0374(1)	1.1121(3)	1.1126(3)
0.92528	1.0342(1)	1.0346(1)	1.1008(3)	1.1011(3)
1.3108	1.0386(1)	1.0388(1)	1.1017(1)	1.1019(1)
1.6192	1.0390(1)	1.0391(1)	1.0879(1)	1.0880(1)
1.9277	1.0428(0)	1.0429(0)	1.0928(1)	1.0929(1)

$(ap)^2$	P	S	T
0.69396	1.3240(9)	1.3065(9)	0.9632(1)
0.92528	1.2571(4)	1.2505(3)	0.9734(1)
1.3108	1.2012(2)	1.1982(2)	0.9917(1)
1.6192	1.1694(1)	1.1680(1)	1.0004(1)
1.9277	1.1523(1)	1.1513(1)	1.0097(1)

Table 7.10: Bare bilinear vertex amplitudes on the $m_l = 0.004$ ensemble of set **A** .

$(ap)^2$	$A(SMOM_{\gamma_\mu})$	$V(SMOM_{\gamma_\mu})$	$A(SMOM_{\not{q}})$	$V(SMOM_{\not{q}})$
0.69396	1.0363(2)	1.0376(2)	1.1120(5)	1.1127(6)
0.92528	1.0341(1)	1.0346(1)	1.1007(2)	1.1011(2)
1.3108	1.0386(1)	1.0388(1)	1.1016(2)	1.1018(2)
1.6192	1.0390(1)	1.0392(1)	1.0881(1)	1.0882(1)
1.9277	1.0427(1)	1.0428(1)	1.0927(1)	1.0927(1)

$(ap)^2$	P	S	T
0.69396	1.3242(9)	1.3043(7)	0.9633(2)
0.92528	1.2585(3)	1.2497(2)	0.9734(1)
1.3108	1.2013(2)	1.1980(2)	0.9918(1)
1.6192	1.1694(2)	1.1677(1)	1.0005(1)
1.9277	1.1523(1)	1.1513(1)	1.0095(1)

Table 7.11: Bare bilinear vertex amplitudes on the $m_l = 0.006$ ensemble of set **A** .

$(ap)^2$	$A(SMOM_{\gamma_\mu})$	$V(SMOM_{\gamma_\mu})$	$A(SMOM_{\not{q}})$	$V(SMOM_{\not{q}})$
0.69396	1.0362(1)	1.0378(1)	1.1123(4)	1.1132(4)
0.92528	1.0339(1)	1.0347(1)	1.1011(3)	1.1015(3)
1.3108	1.0385(1)	1.0388(1)	1.1016(1)	1.1018(1)
1.6192	1.0389(1)	1.0391(1)	1.0881(2)	1.0882(2)
1.9277	1.0428(1)	1.0429(1)	1.0928(1)	1.0929(1)

$(ap)^2$	P	S	T
0.69396	1.3253(6)	1.3045(6)	0.9630(2)
0.92528	1.2591(3)	1.2498(3)	0.9733(1)
1.3108	1.2017(1)	1.1983(2)	0.9916(1)
1.6192	1.1697(1)	1.1679(1)	1.0003(1)
1.9277	1.1526(1)	1.1515(1)	1.0096(1)

Table 7.12: Bare bilinear vertex amplitudes on the $m_l = 0.008$ ensemble of set **A** .

$(ap)^2$	$A(SMOM_{\gamma_\mu})$	$V(SMOM_{\gamma_\mu})$	$A(SMOM_{\not{q}})$	$V(SMOM_{\not{q}})$
1.2337	1.0455(2)	1.0467(2)	1.1195(4)	1.1204(4)
1.3708	1.0492(2)	1.0502(1)	1.1317(3)	1.1324(3)
1.6449	1.0471(1)	1.0477(1)	1.1181(3)	1.1186(3)
1.7820	1.0568(1)	1.0572(1)	1.1417(3)	1.1422(3)
2.0562	1.0556(1)	1.0560(1)	1.1301(1)	1.1304(2)
2.1932	1.0501(1)	1.0503(1)	1.1161(2)	1.1164(2)

$(ap)^2$	P	S	T
1.2337	1.2652(8)	1.2456(5)	0.9878(2)
1.3708	1.2492(6)	1.2343(4)	0.9950(1)
1.6449	1.2126(4)	1.2030(3)	1.0004(1)
1.7820	1.2075(3)	1.2002(3)	1.0128(1)
2.0562	1.1854(2)	1.1800(2)	1.0171(1)
2.1932	1.1720(2)	1.1679(2)	1.0137(1)

Table 7.13: Bare bilinear vertex amplitudes on the $m_l = 0.005$ ensemble of set **B** .

$(ap)^2$	$A(SMOM_{\gamma_\mu})$	$V(SMOM_{\gamma_\mu})$	$A(SMOM_{\not{q}})$	$V(SMOM_{\not{q}})$
1.2337	1.0453(2)	1.0471(1)	1.1197(4)	1.1211(4)
1.3708	1.0491(1)	1.0506(1)	1.1318(4)	1.1329(5)
1.6449	1.0470(1)	1.0479(1)	1.1182(2)	1.1190(2)
1.7820	1.0568(1)	1.0576(1)	1.1418(2)	1.1426(2)
2.0562	1.0558(1)	1.0563(1)	1.1305(2)	1.1310(2)
2.1932	1.0502(1)	1.0506(1)	1.1164(2)	1.1168(2)

$(ap)^2$	P	S	T
1.2337	1.2670(5)	1.2454(4)	0.9877(1)
1.3708	1.2504(4)	1.2340(5)	0.9951(2)
1.6449	1.2134(3)	1.2030(3)	1.0004(1)
1.7820	1.2083(3)	1.2000(3)	1.0129(1)
2.0562	1.1857(2)	1.1801(2)	1.0173(1)
2.1932	1.1726(2)	1.1681(2)	1.0139(1)

Table 7.14: Bare bilinear vertex amplitudes on the $m_l = 0.01$ ensemble of set **B** .

$(ap)^2$	$A(SMOM_{\gamma_\mu})$	$V(SMOM_{\gamma_\mu})$	$A(SMOM_{\not{q}})$	$V(SMOM_{\not{q}})$
1.2337	1.0451(1)	1.0486(2)	1.1206(4)	1.1233(4)
1.3708	1.0491(1)	1.0519(1)	1.1333(2)	1.1356(2)
1.6449	1.0471(1)	1.0489(1)	1.1197(2)	1.1212(3)
1.7820	1.0567(1)	1.0583(1)	1.1432(3)	1.1447(3)
2.0562	1.0558(1)	1.0569(1)	1.1318(2)	1.1329(2)
2.1932	1.0504(1)	1.0513(1)	1.1178(2)	1.1186(2)

$(ap)^2$	P	S	T
1.2337	1.2716(5)	1.2434(5)	0.9882(2)
1.3708	1.2542(4)	1.2323(3)	0.9955(2)
1.6449	1.2163(3)	1.2033(3)	1.0008(1)
1.7820	1.2112(2)	1.1997(2)	1.0130(1)
2.0562	1.1876(2)	1.1800(1)	1.0174(1)
2.1932	1.1745(1)	1.1686(1)	1.0141(1)

Table 7.15: Bare bilinear vertex amplitudes on the $m_l = 0.02$ ensemble of set **B** .

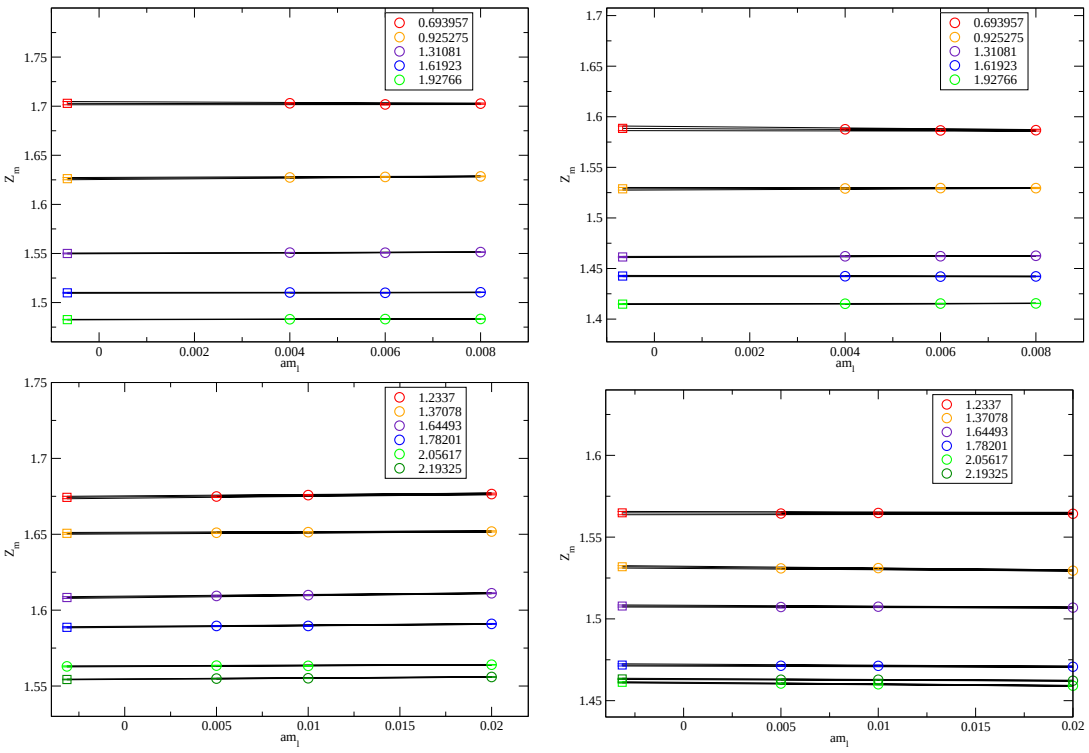

Figure 7.5: The chiral extrapolation of Z_m calculated in the RI/SMOM$_{\gamma^\mu}$ and RI/SMOM$_{\not{q}}$ schemes on both ensembles sets. The upper panels show the extrapolation over the **A** ensembles in the RI/SMOM$_{\gamma^\mu}$ (top-left) and the RI/SMOM$_{\not{q}}$ (top-right) scheme, and the lower panels show the same for the **B** ensembles. The legends give the values of $(ap)^2$. Circular points represent the data and square points the extrapolated values.

of the RGI scheme change factors $w[\mu]$ obtained from the higher-order generalisation [147] of eqn. 3.36. The conversion factors in the $\overline{\text{MS}}$-scheme are determined using the two-loop anomalous dimensions [148][149][150][151], and in the RI/SMOM$_{\gamma^\mu}$ and RI/SMOM$_{\not{q}}$ schemes using the one-loop anomalous dimensions [144]. Recent two-loop calculations of the anomalous dimensions in the SMOM schemes have become available [152][153] but are not used for this work. The $\overline{\text{MS}}$ β-function at four-loops [154] is used for all three schemes, as the scheme dependence enters only at three-loops, and thus the resulting discrepancy when used for the SMOM schemes is much smaller than the truncation errors associated with the one-loop anomalous dimensions.

Figure 7.6 shows the mass renormalisation coefficient in both SMOM schemes as a function of p^2, and also the result of the conversion of each data point to $\overline{\text{MS}}$ at 2 GeV through the procedure above. In principle, the data in the $\overline{\text{MS}}$-scheme obtained from both intermediate schemes should agree at all values of the momentum transfer. The fact that it does not is a result of the following systematic effects:

1. The truncation of the perturbative expansion.
2. Discretisation errors.
3. Chiral symmetry breaking.

Due to the non-exceptional kinematics, the dominant systematic errors are associated with the discretisation and the truncation of the perturbative series. In ref. [143], a study of Z_m in the RI/SMOM$_{\not{q}}$ and RI/SMOM$_{\gamma_\mu}$ schemes was performed using a novel technique to remove the scatter of the data seen in figure 7.6 (see below). The results showed that the values of $Z_m(\overline{\text{MS}}, 2\,\text{GeV})$ differ by $\sim 3.7\%$ over the range $1.73 < p < 2.5$ GeV in the RI/SMOM$_{\not{q}}$ scheme, and 1.3% in the RI/SMOM$_{\gamma_\mu}$ scheme, due to the truncation of the perturbative series. This appears to be reflected by the slope of the data in figure 7.6. In light of this observation it is clear that the procedure of extrapolating the renormalisation coefficient in the RGI scheme to $(ap)^2 = 0$ in order to remove the discretisation effects, as used in ref. [141] and section 7.3.3, is not appropriate as this approach assumes that the discretisation errors are much larger than the truncation errors. Instead the data are converted straight to $\overline{\text{MS}}$ and the removal of discretisation effects is left to the continuum extrapolation of the quark masses in section 8.5.2. A representative data point with minimal truncation errors is selected as the final value. This point is chosen at a value of $(ap)^2$ that is large enough to minimise the size of α_s while staying within the scaling window. The renormalisation coefficient at $p^2 = (2\,\text{GeV})^2$ is chosen for this purpose. The value is obtained by interpolating over the $\overline{\text{MS}}$ data with a linear fit form. Within the current errors, no curvature is observed over the range of data, therefore the fit is performed over all data points. This fit is also shown in figure 7.6.

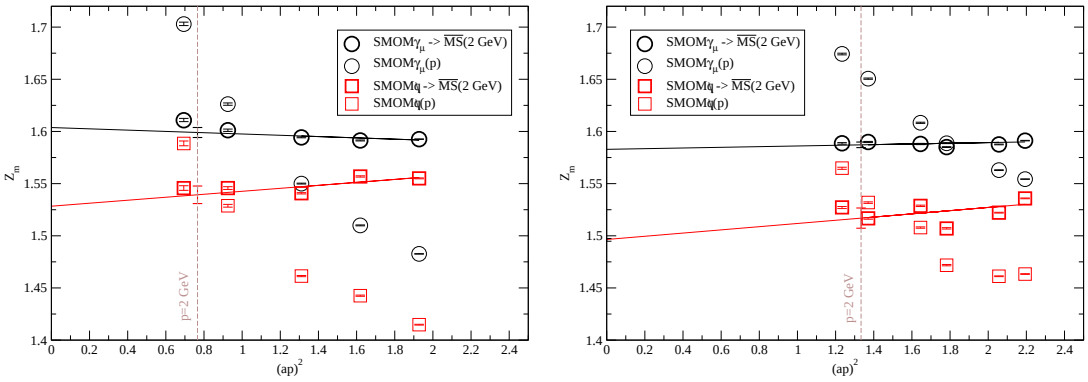

Figure 7.6: Z_m in the RI/SMOM$_{\not{q}}$ and RI/SMOM$_{\gamma^\mu}$ schemes as a function of p^2, and each point converted to the $\overline{\text{MS}}$-scheme at 2 GeV on the **A** and **B** ensembles respectively. The interpolated point at $p^2 = (2\,\text{GeV})^2$ is also shown.

The scatter of the data points around the lines in figure 7.6 occurs due to the breaking of the $O(4)$ rotational symmetry under discretisation, which results in momenta of the same size but in different directions having different $\mathcal{O}(a^2)$ discretisation errors. These effects can be removed by picking a single direction and using twisted boundary conditions to impose the momenta. A pilot study of this approach [143] has been performed on the $16^3 \times 32$ ensembles, demonstrating a significant improvement. For the purposes of this analysis, the scatter is accounted for by inflating the error on the interpolated point by a PDG scale factor of the $\sqrt{\chi^2/\text{d.o.f.}}$ taken from the linear fit used for the interpolation. The inflated error is referred to as the 'stat+spread' error.

The remaining systematic errors arise from the truncation of the perturbative series, the spontaneous chiral symmetry breaking and due to the fact that the strange sea-quark mass has not been taken to the chiral limit. The latter two are referred to as the SSB and m_s errors respectively. An estimate of the SSB error can be obtained from the difference of the scalar and pseudoscalar vertices, $\Lambda_S - \Lambda_P$, at 2 GeV, for which values of 0.5% and 0.6% are obtained on the **A** and **B** ensembles respectively. The m_s error is estimated from the slope of $\Lambda_S + \Lambda_P$ with respect to the light-quark mass, giving 0.1% and 0.2%. The difference $\Lambda_A - \Lambda_V$ was used to estimate the SSB errors on the RI/MOM scheme in ref. [141], but this is essentially zero for the SMOM schemes.

Estimating the truncation error is more difficult. It was noted above that the truncation of the perturbative series is responsible for the residual slope of $Z_m^{\overline{\text{MS}}}$ with respect to $(ap)^2$. As the slope is polluted by discretisation errors, it cannot be used to determine the absolute magnitude of the truncation error, but it can be used to gauge a relative weight of one scheme against the other. This *slope* error is taken to be the difference between the interpolated value of Z_m at $p^2 = (2\,\text{GeV})^2$ and the extrapolated value at $p^2 = (0\,\text{GeV})^2$. The values can be found in table 7.16. Once the continuum

(a) **A** ensembles

scheme	SMOM_{γ^μ}	$\text{SMOM}_{\not{q}}$
$Z_m^{\overline{\text{MS}}}(2\,\text{GeV})$	1.599	1.539
stat+spread	0.005	0.008
trunc	0.075	0.072
SSB	0.008	0.008
m_s	0.002	0.002
a	0.005	0.005
slope	0.005	0.011

(b) **B** ensembles

scheme	SMOM_{γ^μ}	$\text{SMOM}_{\not{q}}$
$Z_m^{\overline{\text{MS}}}(2\,\text{GeV})$	1.587	1.517
stat+spread	0.003	0.010
trunc	0.074	0.071
SSB	0.009	0.009
m_s	0.003	0.003
a	0.006	0.007
slope	0.004	0.020

Table 7.16: The renormalisation coefficient Z_m in the $\overline{\text{MS}}$ scheme at 2 GeV on the **A** and **B** ensembles, along with a breakdown of the systematic errors.

limit has been taken, these 'errors' are then applied to the renormalisation coefficients, and a fit to a constant is performed over the two schemes. The $\sqrt{\chi^2/\text{d.o.f.}}$ of this fit is used to define a PDG scaling factor to inflate the total errors, and an estimate of the truncation error can be determined from the size of the total error relative to the other errors. This analysis is performed in section 8.5.2, and give results that range from 0.6% to 1.5% over the lattices and schemes. The reliability of this estimate is difficult to judge as it has been obtained from only two renormalisation schemes. A more conservative estimate of 4.7% can be obtained from the relative magnitude of the 1-loop correction to the SMOM_{γ^μ} matching coefficients in ref. [144] - this estimate is used for the final result, and is henceforth referred to as the 'trunc' error to distinguish it from the 'slope' error.

An additional statistical error arises from the 1.27% and 1.44% errors on the inverse lattice spacing of the **A** and **B** ensembles respectively. This is included by estimating the slope of $Z_m^{\overline{\text{MS}}}$ with respect to the lattice spacings from a finite difference. The resulting value is denoted as 'a' in the error budget.

The results, including a full error breakdown, are given in table 7.16, and a summary is given below. On the **A** ensembles,

$$\begin{aligned} Z_m^{\mathbf{A}}\,(\overline{\text{MS}}\,2\,\text{GeV}, \text{SMOM}_{\gamma_\mu}) &= 1.599(5)_{\text{stat+spread}}(75)_{\text{sys}}\,, \\ Z_m^{\mathbf{A}}\,(\overline{\text{MS}}\,2\,\text{GeV}, \text{SMOM}_{\not{q}}) &= 1.539(8)_{\text{stat+spread}}(72)_{\text{sys}}\,, \end{aligned} \tag{7.51}$$

and on the **B** ensembles,

$$\begin{aligned} Z_m^{\mathbf{B}}\,(\overline{\text{MS}}\,2\,\text{GeV}, \text{SMOM}_{\gamma_\mu}) &= 1.587(3)_{\text{stat+spread}}(75)_{\text{sys}}\,, \\ Z_m^{\mathbf{B}}\,(\overline{\text{MS}}\,2\,\text{GeV}, \text{SMOM}_{\not{q}}) &= 1.517(10)_{\text{stat+spread}}(72)_{\text{sys}}\,. \end{aligned} \tag{7.52}$$

Here the systematic 'sys' error contains the a,m_s, SSB and truncation errors. Unlike the spread error, these are very strongly correlated between the two ensemble sets.

Therefore, when the renormalisation factors are extrapolated to the continuum limit in section 8.5.2, these errors should not be treated as independent on each ensemble set. Instead the errors are applied to the continuum renormalisation factors, where their continuum magnitudes are estimated from those on the finest ensemble set, **A** . Here the a errors are correlated between the ensembles because the ratio of lattice spacings is fixed prior to their determination (cf. section 8.4).

7.6 B_K NPR

The renormalisation coefficient for B_K is also calculated at the momenta given in table 7.9, in the four SMOM schemes listed in table 7.3.2. Due to the magnitude of the other sources of systematic error (described below), the renormalisation coefficients determined in the original RI/MOM scheme remain competitive with the SMOM schemes and are therefore also included in the analysis. The one-loop matching factors between the SMOM schemes and $\overline{\text{MS}}$ with naive dimensional reduction (referred to as the NDR scheme), and also the 2-loop anomalous running of these schemes, were calculated in ref. [5]. As in section 7.3.3, the average of the vector and axial-vector amplitudes $\frac{1}{2}(\Lambda_A + \Lambda_V)$ is used to determine Z_q/Z_A in order to minimise the effects of the chiral symmetry breaking, and the difference between using this and Λ_A on its own is included as a systematic error, labelled $V - A$.

The values of Z_{B_K} in the various schemes at finite quark mass are given in tables 7.17–7.22, and the chiral extrapolations are shown in figures 7.7 and 7.8. Figure 7.9 shows the momentum dependence of the five renormalisation schemes.

Following the procedure used in the previous section, the lattice-scheme data at each value of p^2 are converted to NDR at 2 GeV, and a central value is taken from a linear interpolation of these data to $p^2 = (2\,\text{GeV})^2$.

As before, a 'slope error' is determined for each intermediate scheme from the difference of $Z_{B_K}^{NDR}$ at $p^2 = (2\,\text{GeV})^2$ and $p^2 = (0\,\text{GeV})^2$, which is used to obtain the truncation error in the continuum limit. As five independent schemes are used for this analysis, the weighted combination of renormalisation coefficients in the continuum limit can be expected to yield a much more reliable estimate of the truncation error than for the quark mass renormalisation, where only two schemes were used. Notice that the separation between the NDR data obtained using the five intermediate schemes at momenta in the region of 3 GeV is considerably smaller than at 2 GeV, which lends further weight to the idea that the uncertainty arising from the truncation of the perturbative series is the dominant error in the analysis. This suggests that quoting the NDR results at a higher scale such as 3 GeV, or simply to quote the result only in the RGI scheme, may make sense, but it is likely that some effort will be

required to encourage the phenomenology and lattice communities to accept results in an unconventional form, therefore this is deferred to future work [143].

As mentioned above, an estimate of the chiral symmetry breaking error (SSB) is established as the difference in the result after repeating the analysis using Λ_A, rather than $\frac{1}{2}(\Lambda_A + \Lambda_V)$, in the determination of Z_{B_K} in the lattice schemes. The spread error associated with the $O(4)$ rotational symmetry breaking, and the m_s error resulting from the finite strange sea quark mass are determined as in section 7.5. As can be seen in figures 7.7 and 7.8, the mass dependence is benign, and as a result the m_s error is very small.

The values of Z_{B_K} in the NDR scheme at 2 GeV, determined from each of the five intermediate schemes, along with a breakdown of the systematic errors, are given in tables 7.23 and 7.24 for the **A** and **B** ensembles respectively. These are used in the continuum extrapolation of B_K in section 8.7.4.

$(ap)^2$	RI/MOM	SMOM($\gamma_\mu, \not{q}$)	SMOM(γ_μ, γ_μ)	SMOM($\not{q}, \not{q}$)	SMOM($\not{q}, \gamma_\mu$)
0.69395656	0.94421(26)	1.10268(45)	0.95835(19)	1.01326(16)	0.88064(35)
0.92527541	0.93707(15)	1.07899(38)	0.95255(11)	0.99954(10)	0.88237(30)
1.31080683	0.92756(9)	1.06187(18)	0.94377(5)	0.986319(51)	0.87661(14)
1.61923197	0.92115(8)	1.02991(16)	0.93940(7)	0.972245(48)	0.88680(15)
1.92765711	0.91696(6)	1.02759(15)	0.93570(4)	0.968620(56)	0.88201(12)

Table 7.17: $Z_{B_K}^{RI/MOM}$ on the $m_l = 0.004$ ensemble of set **A** .

$(ap)^2$	RI/MOM	SMOM($\gamma_\mu, \not{q}$)	SMOM(γ_μ, γ_μ)	SMOM($\not{q}, \not{q}$)	SMOM($\not{q}, \gamma_\mu$)
0.69395656	0.94442(20)	1.10289(66)	0.95853(16)	1.01350(27)	0.88082(45)
0.92527541	0.93737(13)	1.07920(32)	0.95258(11)	0.99952(9)	0.88227(23)
1.31080683	0.92773(9)	1.06176(20)	0.94383(8)	0.98627(5)	0.87671(20)
1.61923197	0.92114(7)	1.03015(16)	0.93946(5)	0.97234(5)	0.88674(13)
1.92765711	0.91708(7)	1.02760(14)	0.93579(6)	0.96869(5)	0.88213(14)

Table 7.18: $Z_{B_K}^{RI/MOM}$ on the $m_l = 0.006$ ensemble of set **A** .

$(ap)^2$	RI/MOM	SMOM($\gamma_\mu, \not{q}$)	SMOM(γ_μ, γ_μ)	SMOM($\not{q}, \not{q}$)	SMOM($\not{q}, \gamma_\mu$)
0.69395656	0.94435(17)	1.10316(47)	0.95811(14)	1.01333(13)	0.88010(42)
0.92527541	0.93709(12)	1.07966(36)	0.95233(10)	0.99953(9)	0.88169(31)
1.31080683	0.92743(7)	1.06171(26)	0.94365(7)	0.98619(6)	0.87651(19)
1.61923197	0.92109(4)	1.03037(15)	0.93934(4)	0.97233(4)	0.88645(15)
1.92765711	0.91694(6)	1.02747(9)	0.93564(6)	0.96856(4)	0.88200(9)

Table 7.19: $Z_{B_K}^{RI/MOM}$ on the $m_l = 0.008$ ensemble of set **A** .

$(ap)^2$	RI/MOM	SMOM($\gamma_\mu, \not{q}$)	SMOM(γ_μ, γ_μ)	SMOM($\not{q}, \not{q}$)	SMOM($\not{q}, \gamma_\mu$)
1.23370055	0.91593(17)	1.06959(56)	0.93315(15)	0.98552(23)	0.85981(35)
1.37077839	0.91341(12)	1.08166(29)	0.93002(10)	0.98675(12)	0.84841(21)
1.64493407	0.90855(14)	1.05751(38)	0.92761(9)	0.97633(12)	0.85640(28)
1.78201191	0.90526(11)	1.07711(24)	0.92280(8)	0.97894(9)	0.83870(18)
2.05616758	0.90207(9)	1.05563(24)	0.92117(7)	0.97026(9)	0.84667(15)
2.19324542	0.90029(10)	1.04105(21)	0.92141(9)	0.96563(6)	0.85465(21)

Table 7.20: $Z_{B_K}^{RI/MOM}$ on the $m_l = 0.005$ ensemble of set **B** .

$(ap)^2$	RI/MOM	SMOM($\gamma_\mu, \not{q}$)	SMOM(γ_μ, γ_μ)	SMOM($\not{q}, \not{q}$)	SMOM($\not{q}, \gamma_\mu$)
1.23370055	0.91593(14)	1.07001(41)	0.93293(13)	0.98556(13)	0.85930(30)
1.37077839	0.91317(14)	1.08174(44)	0.92987(13)	0.98675(12)	0.84822(42)
1.64493407	0.90845(11)	1.05775(26)	0.92744(11)	0.97632(8)	0.85604(21)
1.78201191	0.90519(13)	1.07688(28)	0.92257(10)	0.97881(10)	0.83855(19)
2.05616758	0.90183(11)	1.05584(21)	0.92093(8)	0.97022(7)	0.84625(19)
2.19324542	0.90002(9)	1.04107(18)	0.92121(8)	0.96553(6)	0.85437(16)

Table 7.21: $Z_{B_K}^{RI/MOM}$ on the $m_l = 0.01$ ensemble of set **B** .

$(ap)^2$	RI/MOM	SMOM($\gamma_\mu, \not{q}$)	SMOM(γ_μ, γ_μ)	SMOM($\not{q}, \not{q}$)	SMOM($\not{q}, \gamma_\mu$)
1.23370055	0.91517(17)	1.07060(50)	0.93210(13)	0.98555(16)	0.85805(36)
1.37077839	0.91251(15)	1.08333(25)	0.92885(13)	0.98690(8)	0.84618(23)
1.64493407	0.90796(15)	1.05928(25)	0.92666(13)	0.97645(9)	0.85420(26)
1.78201191	0.90480(11)	1.07889(32)	0.92198(11)	0.97920(9)	0.83679(25)
2.05616758	0.90141(10)	1.05736(19)	0.92025(11)	0.97046(5)	0.84463(24)
2.19324542	0.89948(14)	1.04232(18)	0.92048(11)	0.96559(5)	0.85272(21)

Table 7.22: $Z_{B_K}^{RI/MOM}$ on the $m_l = 0.02$ ensemble of set **B** .

scheme	MOM	SMOM $(\gamma_\mu, \not{q})$	SMOM (γ_μ, γ_μ)	SMOM $(\not{q}, \not{q})$	SMOM $(\not{q}, \gamma_\mu)$
$Z_{B_K}^{\overline{\text{NDR}}}(2\,\text{GeV})$	0.96283	1.03487	0.96358	0.99919	0.92698
stat+spread	0.00124	0.00818	0.00105	0.00261	0.00536
slope	0.00330	0.01256	0.00826	0.00136	0.01905
SSB	0.00805	0.00004	0.00019	0.00005	0.00043
m_s	0.00054	0.00161	0.00093	0.00010	0.00187
a	0.00088	0.00183	0.00085	0.00122	0.00031

Table 7.23: The renormalisation coefficient of B_K in the NDR scheme at 2 GeV on the **A** ensembles, along with a breakdown of the systematic errors.

scheme	MOM	SMOM $(\gamma_\mu, \not{q})$	SMOM (γ_μ, γ_μ)	SMOM $(\not{q}, \not{q})$	SMOM $(\not{q}, \gamma_\mu)$
$Z_{B_K}^{\overline{\text{NDR}}}(2\,\text{GeV})$	0.93226	1.01909	0.93592	0.97644	0.89350
stat+spread	0.00040	0.00870	0.00125	0.00191	0.00780
slope	0.00620	0.00117	0.01389	0.00397	0.01961
SSB	0.00729	0.00010	0.00021	0.00004	0.00006
m_s	0.00086	0.00239	0.00138	0.00035	0.00309
a	0.00081	0.00156	0.00070	0.00109	0.00028

Table 7.24: The renormalisation coefficient of B_K in the NDR scheme at 2 GeV on the **B** ensembles, along with a breakdown of the systematic errors.

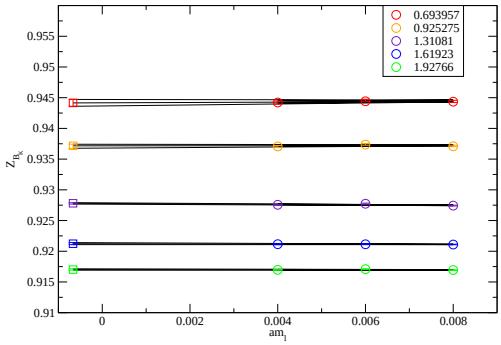

(a) RI/MOM

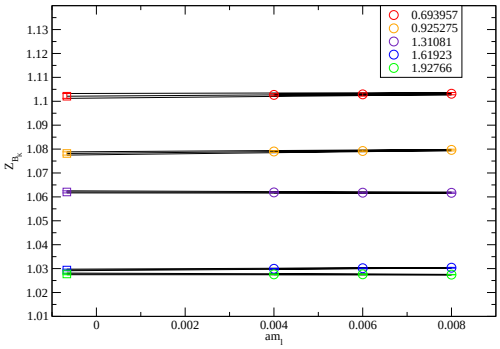

(b) SMOM($\gamma_\mu, \not{q}$)

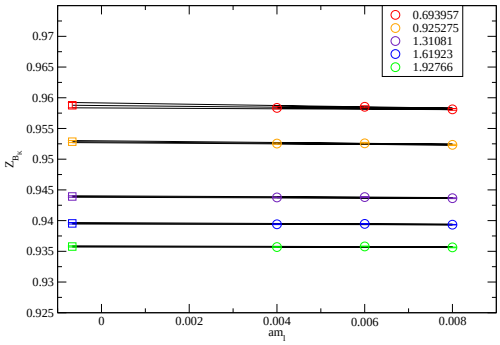

(c) SMOM(γ_μ, γ_μ)

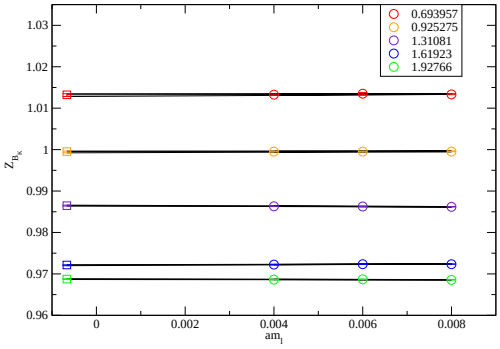

(d) SMOM($\not{q}, \not{q}$)

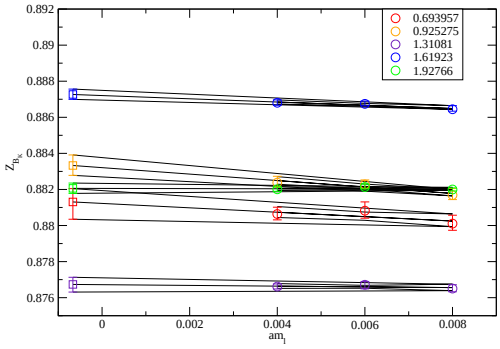

(e) SMOM($\not{q}, \gamma_\mu$)

Figure 7.7: The chiral extrapolation of Z_{B_K} on ensembles set **A** for all five schemes. The legends give the values of $(ap)^2$. Circular points represent the data and square points the extrapolated values.

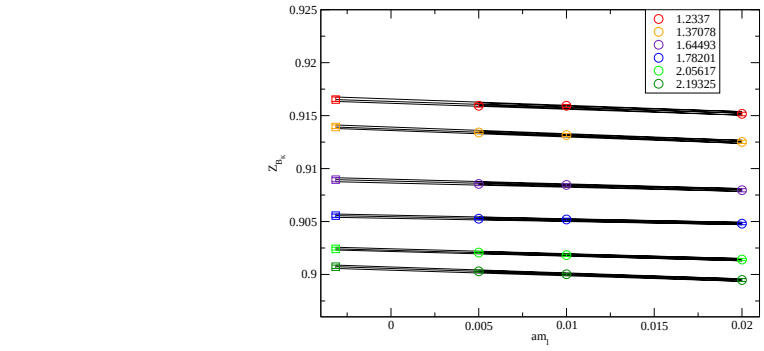

(a) RI/MOM

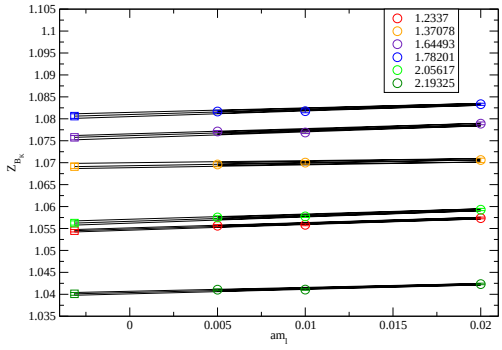

(b) SMOM($\gamma_\mu, \not{q}$)

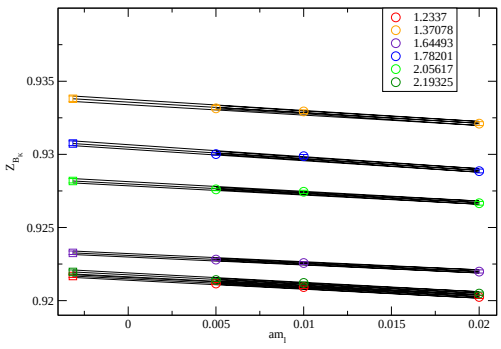

(c) SMOM(γ_μ, γ_μ)

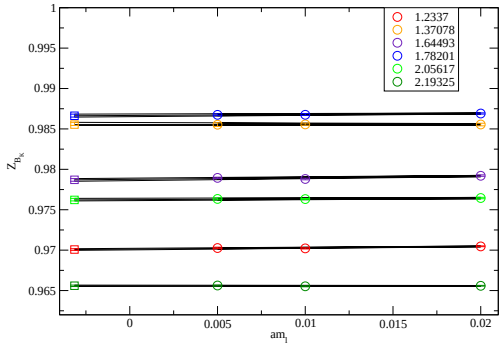

(d) SMOM($\not{q}, \not{q}$)

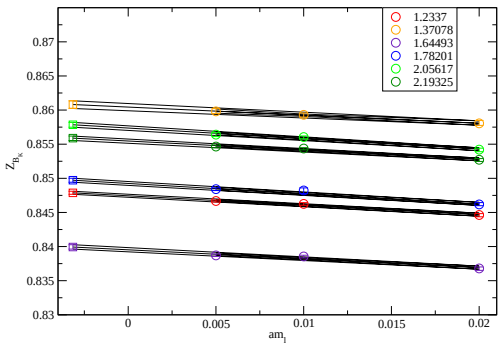

(e) SMOM($\not{q}, \gamma_\mu$)

Figure 7.8: The chiral extrapolation of Z_{B_K} on ensembles set **B** for all five schemes. The legends give the values of $(ap)^2$. Circular points represent the data and square points the extrapolated values.

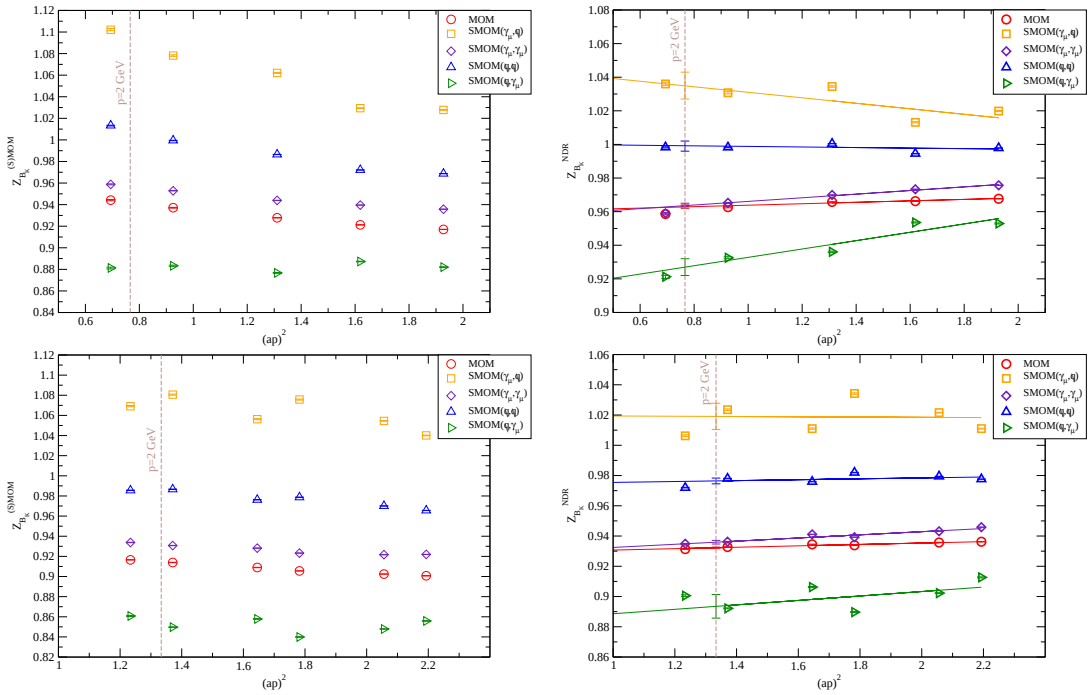

Figure 7.9: Z_{B_K} in the five schemes as a function of p^2, and each point converted to the $\overline{\text{MS}}$-scheme at 2 GeV on the **A** and **B** ensembles respectively. The interpolated point at $p^2 = (2\,\text{GeV})^2$ is also shown. The upper panels show the data on the **A** ensembles in the (S)MOM schemes (upper-left) and the NDR scheme (upper-right). The lower panels show the same for the **B** ensembles.

Chapter 8

Continuum results from lattice QCD

In chapter 6, separate analyses of lattice data at two bare couplings, $\beta = 2.25$ (the **A** ensembles) and $\beta = 2.13$ (the **B** ensembles) were presented. The lattice action of these simulations is accurate to $\mathcal{O}(a^2)$, thus physical predictions could in principle be obtained after setting the scale using a physical quantity, for example the Omega baryon mass. Such an analysis was performed for the **B** ensembles (with a smaller dataset) in refs. [1] and [128]. However, even with improved actions, discretisation effects remain a dominant systematic error on predictions made from a lattice simulation at a single lattice spacing. For example, assuming discretisation errors on the order of $(a\Lambda_{\mathrm{QCD}})^2$ and using $a^{-1} \sim 1.73$ GeV and $\Lambda_{\mathrm{QCD}} \sim 350$ MeV, the magnitude of the error on the **B** ensembles is expected to be around 4% [1].

This chapter presents an analysis of the continuum limit of QCD obtained from a combined extrapolation of the **A** and **B** ensemble sets. The analysis is performed by matching the two ensemble sets at an unphysical quark mass within the range of simulated data. From this, the ratios of lattice spacings and equivalent quark masses are obtained without experimental input, allowing the mass and lattice spacing dependence of the data to be fitted simultaneously and extrapolated to the chiral/continuum limit. Both $SU(2)$ ChPT and analytic fit forms are used in the extrapolation in order to allow an estimate of the systematic error associated with the extrapolation to be obtained. All stages of the analysis make use of the superjackknife procedure in order to allow the uncorrelated errors between each ensemble set to be kept separate.

As usual, quark masses with m_{res} included are labelled with a tilde, for example $\tilde{m}_q = m_q + m_{\mathrm{res}}$, where m_q is the bare lattice mass. Where masses are presented in physical units, the figure is accompanied by a unit (e.g. GeV). Also, for the sake of clarity, in discussions involving quantities in lattice and physical units, the lattice quantities may be given with an explicit coefficient of the lattice spacing, e.g. $a\tilde{m}_q$.

The layout of the chapter is as follows. The scaling trajectory, along which the continuum limit is taken, is defined. The procedure for taking the simultaneous chiral/continuum limit of both ensemble sets is then discussed, and the chiral ansätze are introduced. Results are then presented for the chiral/continuum fits applied to m_π,

f_π, m_K, f_K and m_Ω. Predictions for the physical decay constants and quark masses are presented, and the systematic errors are discussed. The chiral/continuum fit procedure is then applied to r_0, r_1 and B_K, and continuum predictions are presented, along with an in-depth discussion of the systematic errors. Finally the main results of the chapter are summarised, and a discussion of possible future avenues of investigation is given.

This is the first continuum limit analysis performed using a lattice action with good chiral symmetry. The most important results of this chapter are the average up/down quark mass, the strange quark mass and the neutral kaon mixing parameter B_K, which are presented in the $\overline{\text{MS}}$ scheme using the non-perturbative renormalisation coefficients obtained in the previous chapter.

8.1 The ideal scaling trajectory

Before discussing the practical implementation of the analysis, it is expedient to discuss the approach to the continuum limit in more general terms. In section 2.4, the concept of a scaling curve or trajectory was introduced as a one-dimensional curve of points $(m_{u/d}(\beta), m_s(\beta), \beta)$ in the infinite dimensional coupling-space that converge asymptotically under renormalisation group transformations to a particular renormalised trajectory, upon which a continuum theory is defined.

A 2+1 flavour lattice simulation can be tuned to a scaling curve by varying the input quark masses $m_{u/d}$ and m_s at fixed β, until the simulated values of two dimensionless ratios of quantities, $R_l = N_l/\mathcal{D}$ and $R_h = N_h/\mathcal{D}$ (for the light and heavy quarks respectively), match the values obtained on the renormalised trajectory. Defining the shared denominator $\mathcal{D}$ to be scale independent, the lattice spacings at each β can be determined via the ratio $(a\mathcal{D})/\mathcal{D}^{\text{phys}}$. Ideally this procedure is then repeated at a series of different values of β, allowing the continuum limit to be taken by extrapolation.

The scaling curve defined by this tuning procedure is not unique. The convergence of the renormalisation group flow from the simulation scale to the renormalised trajectory only occurs in the infrared limit. At finite hadronic scales the flow and the renormalised trajectory are separated by a distance $\sim (a\Lambda_{\text{QCD}})^2$ in parameter-space. The tuning procedure forces the scaling curve to intersect the renormalised trajectory in a non-trivial way, which then alters the scaling behaviour of other quantities. As a result the choices of R_l and R_h define different scaling curves to the continuum, all of which have low-energy Green's functions that are equivalent to $\mathcal{O}(a^2)$. The continuum limit is of course free of discretisation errors, thus the scaling curve can be chosen for convenience.

For this analysis, the ratios $R_l = m_\pi/m_\Omega$ and $R_h = m_K/m_\Omega$ are chosen, with the Omega baryon mass used to set the scale. These choices are equivalent to those used in ref. [1], in which m_π, m_K and m_Ω were used to set the light and heavy quark masses

and the lattice scale respectively.

In practise, there are a number of difficulties in the implementation of the idealised tuning procedure described above. The first is that the available set of lattice simulations all have unphysically large up/down quark masses. Therefore the idealised matching procedure requires a chiral extrapolation on each ensemble set, which introduces potentially large systematic errors in the continuum extrapolation that are difficult to control (cf. section 8.5). The second is that each lattice quantity has a statistical error (typically $\mathcal{O}(1\%)$) which limits the precision to which the simulations can be tuned to the scaling curve. The resolution of the first of these problems is the topic of the next section, and section 8.4 contains a discussion of the second.

8.2 Matching at unphysical masses

8.2.1 The fixed trajectory approach (I)

In order to avoid the need to perform a chiral extrapolation of each ensemble set independently, the two ensemble sets are matched to a scaling curve along which the values of m_π/m_Ω and m_K/m_Ω are fixed to values within the range of the simulated data, as opposed to their physical values. Once tuned to this curve, the continuum limit can be taken without extrapolating outside the range of simulated quark masses. Of course in order to make physical predictions, the extrapolated data must be tuned to a scaling curve of the physical renormalised trajectory, which inevitably requires a chiral extrapolation to be performed. However, the approach detailed in this section, referred to as the *fixed trajectory* approach [3], does make it significantly easier to isolate and estimate the associated systematic error (cf. section 8.5).

For the remainder of this chapter, dimensionless values of the pion, kaon and Omega masses at unphysical quark masses are labelled m_{ll}, m_{lh} and m_{hhh} respectively. Here l represents the light sea quark and h the heavy. Partially-quenched values of the pion and kaon masses are labelled m_{xy} and m_{xh}, where x and y represent light valence quark masses.

The values of $R_l = m_{ll}/m_{hhh}$ and $R_h = m_{lh}/m_{hhh}$ that define the *match point* can be chosen to correspond to a simulated point on one of the ensemble sets, labelled $\mathbf{M}$. Although the final physical predictions do not depend upon the choice of match point, certain choices are favoured due to the quality of the data at the match point and the range over which the data must be interpolated/extrapolated on the other ensembles to perform the matching. The ideal data point has as small a statistical error as possible, and lies within the range of simulated data on all of the ensembles, such that only a small interpolation is required. In practise, the errors on the mass ratios at the match point can be reduced by fitting to all partially-quenched simulated data on the ensemble

set **M**, and interpolating to the matching point along the unitary curve.

In order to perform the interpolations, an ansatz is needed for the light and heavy quark mass dependence of m_{xy}, m_{xh} and m_{hhh} within the range of simulated data. Examination of the data (figs. 8.2, 8.9 and 8.27 respectively) reveals a strong linearity across the range of simulated data, hence a linear ansatz is used in the light and heavy quark sectors. Prior to fitting, the m_{xh} and m_{hhh} data are linearly interpolated over the reweighted values such that the heavy sea-quark mass is equal to that of the heavy valence quark(s). Interpolations of m_{xy}, m_{xh} and m_{hhh} in the heavy quark mass are then performed, at fixed light quark masses, by linearly interpolating the (now unitary) data. Fits over the light quark mass dependence are performed at fixed heavy quark mass. These fits are performed over the full set of partially-quenched data. The ansätze for the light quark mass dependence are

$$m_{xy}^2 = c_0 + c_l\, m_l + c_v(m_x + m_y)\,, \tag{8.1}$$

$$m_{xh}^2 = d_0 + d_l\, m_l + d_v\, m_x\,, \text{ and} \tag{8.2}$$

$$m_{hhh} = e_0 + e_l\, m_l\,. \tag{8.3}$$

The first stage of the procedure is to perform partially-quenched linear fits over ensemble set **M** to the simulated pion, kaon and Omega masses. As previously mentioned, in order to improve the statistical errors, the values of $R_l^{\mathbf{M}}$ and $R_h^{\mathbf{M}}$, where the superscript denotes the ensemble, are determined from these fits rather than directly from the simulated data. After the ratios at the match point have been determined, the matching procedure is as follows:

1. An independent partially-quenched linear fit over each of the ensemble sets $\mathbf{e} \neq \mathbf{M}$ is performed to the simulated pion, kaon and Omega masses using the forms above. These fits are performed independently for each unitary heavy quark mass.

2. The pair of quark masses $(m_l^{\text{match}}, m_h^{\text{match}})^{\mathbf{e}}$ that corresponds to the match point is estimated for each ensemble set $\mathbf{e} \neq \mathbf{M}$.

3. For each value of the unitary heavy quark mass, the three hadronic masses are interpolated in the light-quark sector to the estimated $m_l^{\text{match},\,\mathbf{e}}$.

4. Each quantity is then linearly interpolated in the heavy-quark mass to the estimated value of $m_h^{\text{match},\,\mathbf{e}}$.

5. The ratios $R_l^{\mathbf{e}} = \dfrac{m_{ll}^{\text{match},\,\mathbf{e}}}{m_{hhh}^{\text{match},\,\mathbf{e}}}$ and $R_h^{\mathbf{e}} = \dfrac{m_{lh}^{\text{match},\,\mathbf{e}}}{m_{hhh}^{\text{match},\,\mathbf{e}}}$ are formed from the quantities at the match point.

6. By comparing $R_l^{\text{match},\,\mathbf{e}}$ to the corresponding value $R_l^{\text{match},\,\mathbf{M}}$ at the match point and using the measured slopes of $m_{ll}^{\mathbf{e}}$ and $m_{hhh}^{\mathbf{e}}$ with respect to $m_l^{\mathbf{e}}$, an updated estimate of $m_l^{\text{match},\,\mathbf{e}}$ is obtained.

7. Similarly, by comparing the ratio $R_h^{\text{match},\,\mathbf{e}}$ to $R_h^{\text{match},\,\mathbf{M}}$, an updated estimate of $m_h^{\text{match},\,\mathbf{e}}$ is obtained.

8. With these updated estimates of the quark masses $(m_l^{\text{match}}, m_h^{\text{match}})^{\mathbf{e}}$, the procedure loops back to step 3 and is iterated until the process convergences.

This procedure produces a set of bare quark masses $(m_l^{\text{match}}, m_h^{\text{match}})^{\mathbf{e}}$ which are equivalent in physical units to the masses $(m_l^{\text{match}}, m_h^{\text{match}})^{\mathbf{M}}$. Comparing the Omega baryon masses at these values of the quark masses allows for a determination of the ratio of lattice spacings between the ensemble set **e** and ensemble set **A** :

$$R_a^{\mathbf{e}} = \frac{a^{\mathbf{A}}}{a^{\mathbf{e}}} = \frac{m_{hhh}^{\text{match},\,\mathbf{A}}}{m_{hhh}^{\text{match},\,\mathbf{e}}} \,. \tag{8.4}$$

Here ensemble set **A** has been chosen as the *primary ensemble* against which the other quantities are defined. In addition, the ratios of the light and heavy quark masses between ensemble sets **e** and **A** can be calculated using $R_a^{\mathbf{e}}$ and the quark masses at the match point:

$$Z_f^{\mathbf{e}} = \frac{1}{R_a^{\mathbf{e}}} \frac{\widetilde{m}_f^{\text{match},\,\mathbf{A}}}{\widetilde{m}_f^{\text{match},\,\mathbf{e}}} \quad \text{for} \quad f = l \text{ or } h. \tag{8.5}$$

For the remainder of this chapter, the superscripts **e** on $Z_f^{\mathbf{e}}$ and $R_a^{\mathbf{e}}$ are dropped in the discussion of the application of this procedure to the two ensemble sets analysed in the previous chapter.

Table 8.1 contains the values of Z_f and R_a obtained by performing the matching at a range of match points on both ensemble sets. The similarity in the values of Z_l and Z_h can be explained as follows. For a general ensemble **e** at finite lattice spacing (briefly returning to the more explicit notation), the light and heavy quark masses are related to those in the continuum by effects of $\mathcal{O}(a^2)$

$$\frac{\tilde{m}_l^{\mathbf{e}}}{\tilde{m}_h^{\mathbf{e}}} = \lim_{a^{\mathbf{e}} \to 0} \left(\frac{\tilde{m}_l}{\tilde{m}_h} \right) \left(1 + c_m a^{\mathbf{e}\,\mathbf{2}} \right) \,, \tag{8.6}$$

where the coefficient c_m vanishes as $m_l \to m_h$. This implies that the ratios $Z_l^{\mathbf{e}}$ and $Z_h^{\mathbf{e}}$ can be expected to be very similar in magnitude:

$$Z_h^{\mathbf{e}} = Z_l^{\mathbf{e}} \left(1 + c_m \left[(a^{\mathbf{A}})^2 - (a^{\mathbf{e}})^2 \right] \right) \,. \tag{8.7}$$

With more than two ensemble sets, this relationship could be used to improve the

matching analysis by providing an additional constraint on the values of Z_l and Z_h between the ensemble sets.

In a similar way to eqn. 8.6, the quark masses on the ensemble **e** at the match point of two *different* trajectories, defined by the choices of the values of $R_l = m_{ll}/m_{hhh}$ and $R_h = m_{lh}/m_{hhh}$, can be related as

$$\frac{\tilde{m}_f^{\text{match},\,\mathbf{e}}(R_l, R_h)}{\tilde{m}_f^{\text{match},\,\mathbf{e}}(R'_l, R'_h)} = \lim_{a^{\mathbf{e}}\to 0}\left(\frac{\tilde{m}_f^{\text{match}}}{\tilde{m}_f'^{\text{match}}}\right)\left(1 + d_{m,f}a^{\mathbf{e}\,\mathbf{2}}\right) , \tag{8.8}$$

where primed and unprimed quantities are defined on the different trajectories. Taking the ratio of this result for the ensemble set **e** and the primary ensemble set **A** gives

$$\frac{Z_f^{\mathbf{e}}}{Z_f^{\mathbf{e}\prime}} = \left(1 + d_{m,f}\left[(a^{\mathbf{A}})^2 - (a^{\mathbf{e}})^2\right]\right) . \tag{8.9}$$

If the difference $\tilde{m}_f^{\text{match},\,\mathbf{e}}(R_l, R_h) - \tilde{m}_f^{\text{match},\,\mathbf{e}}(R'_l, R'_h)$ is small then the coefficient $d_{m,f}$ is also small, and the lattice spacing dependent terms on the right-hand side of eqn. 8.9 can be neglected. As a result, the values of Z_l and Z_h can be used to relate quark masses between the ensemble set **B** and the primary ensemble set **A**, providing those masses are not too far from the match point. This is used extensively in section 8.4. All of the results for Z_f and R_a agree very well between the various match points, suggesting that the coefficients $d_{m,f}$ are indeed small and can be neglected.

As discussed above, the ideal match point is reached without requiring an extrapolation outside of the range of the data. For the results given on the fourth and fifth lines of table 8.1, for which the **A** ensemble set is tuned to match points on the **B** ensemble set, a small extrapolation above the simulated strange quark mass on the **A** ensembles is required. The result on the fifth line also requires a 13% extrapolation in the light quark mass beyond the range of simulated data on the **A** ensembles. These points also have the largest errors, apart from the result on the first line in which the **B** ensembles are tuned to match the $m_l = 0.004$ match point on the **A** ensembles. Matching at this point requires a significant ($\sim 40\%$) extrapolation in the light-quark mass below the lightest unitary simulated point on the **B** ensembles, which is likely the source of the larger error. As a result, the final values of Z_f and R_a are taken from the second line, for which the **B** ensembles are tuned to match the $m_l = 0.006$ match point on the **A** ensembles. These values are $Z_l = 0.981(9)$, $Z_h = 0.974(7)$ and $R_a = 0.758(5)$.

M	$(m_l^{\text{match}})^{\mathbf{M}}$	$(m_h^{\text{match}})^{\mathbf{M}}$	$(m_l^{\text{match}})^{\mathbf{e}}$	$(m_h^{\text{match}})^{\mathbf{e}}$	Z_l	Z_h	R_a
A	0.004	0.03	0.00313(13)	0.03812(80)	0.980(15)	0.976(11)	0.7617(72)
A	0.006	0.03	0.00583(12)	0.03839(51)	0.981(9)	0.974(7)	0.7583(46)
A	0.008	0.03	0.00860(19)	0.03869(64)	0.979(10)	0.972(8)	0.7545(58)
B	0.005	0.04	0.00545(11)	0.03148(51)	0.985(12)	0.978(9)	0.7620(57)
B	0.01	0.04	0.00897(18)	0.03074(57)	0.974(11)	0.968(9)	0.7517(70)

Table 8.1: Values of the quark mass ratios Z_l and Z_h and the lattice spacing ratio R_a determined by matching at five points over both ensemble sets. The ensemble $\mathbf{e} \neq \mathbf{M}$.

8.2.2 Alternate approaches to the matching (II and III)

As mentioned in the previous section, the lack of dependence of Z_l and Z_h upon the match point allows quark masses on nearby scaling curves to be matched between the two ensemble sets without the need to redo the matching analysis. This allows fits to the quark mass dependence of both ensemble sets to be performed simultaneously. If the fits are performed to dimensionless ratios of physical quantities, then the quark masses can be expressed in lattice units, and only the products $Z_l R_a$ and $Z_h R_a$ are required:

$$(a\tilde{m}_f)^{\mathbf{A}} = Z_f R_a (a\tilde{m}_f)^{\mathbf{B}} \ . \tag{8.10}$$

Here $m_f^{\mathbf{A}}$ is the light/heavy quark mass on the **A** ensembles that corresponds to $m_f^{\mathbf{B}}$ on the **B** ensembles.

Exploiting the relation above, two additional methods are implemented with the aim of constraining the quark mass dependence of the three quantities m_{xy}, m_{xh} and m_{hhh} between the ensemble sets in order to improve the statistics in the matching procedure. Here the complication lies with the fact that the fits must be performed to dimensionless ratios of quantities, as the lattice spacings are unknown. The two methods differ in the approach to this problem.

The first alternative approach, labelled II, is as follows. As before, all data for quantities with a heavy valence quark are reweighted such that the valence and sea quark masses are equal. Independent fits of the Omega masses on each of the two ensembles are performed using the following fit form:

$$m_{hhh} = b_0 + b_l m_l + b_h m_h \, . \tag{8.11}$$

Unlike in the analysis of the previous section, the unitary heavy quark mass dependence is included in the fit here for convenience - of course the result would be the same if the heavy quark interpolation was performed separately. Using a guess for $Z_l R_a$ and $Z_h R_a$, the Omega masses are interpolated in the light and heavy quark directions to the chosen match point on both ensembles. The Omega masses at the match point

are labelled m_{hhh}^{match} as before. These are used to make the quantities dimensionless. Simultaneous fits over the simulated partially-quenched data on both ensemble sets are then performed to the forms

$$\begin{aligned}(m_{xy}/m_{hhh}^{\text{match}})^2 &= c_0 + c_l(a\tilde{m}_l) + c_v(a\tilde{m}_x + a\tilde{m}_y) + c_h(a\tilde{m}_h)\,, \text{ and} \\ (m_{xh}/m_{hhh}^{\text{match}})^2 &= d_0 + d_l(a\tilde{m}_l) + d_v(a\tilde{m}_x) + d_h(a\tilde{m}_h)\end{aligned} \tag{8.12}$$

for the data on the **A** ensembles and

$$\begin{aligned}(m_{xy}/m_{hhh}^{\text{match}})^2 &= c_0 + c_l Z_l R_a(a\tilde{m}_l) + c_v Z_l R_a(a\tilde{m}_x + a\tilde{m}_y) + c_h Z_h R_a(a\tilde{m}_h)\,, \text{ and} \\ (m_{xh}/m_{hhh}^{\text{match}})^2 &= d_0 + d_l Z_l R_a(a\tilde{m}_l) + d_v Z_l R_a(a\tilde{m}_x) + d_h Z_h R_a(a\tilde{m}_h)\end{aligned} \tag{8.13}$$

for that on the **B** ensembles. Here the fit coefficients (c_0, c_l, c_v, c_h) and (d_0, d_l, d_v, d_h) are constrained to be equal between the ensembles. $Z_l R_a$ and $Z_h R_a$ are also determined from the fit. These are then used to update the values of the Omega masses at the match point, and the process is iterated until convergence. The ratio of the Omega masses between the ensembles at the converged match point gives the value of R_a as before, which can then be used to determine Z_l and Z_h.

The iterative procedure can be avoided using a second alternative procedure (III). Once again quantities with heavy valence quarks are reweighted until the heavy quark mass is unitary. On each ensemble the ratios $m_{xy}(m_l, m_h)/m_{hhh}(m_l, m_h)$ and $m_{xh}(m_l, m_h)/m_{hhh}(m_l, m_h)$ are formed from the simulated data. These are simultaneously fit assuming a linear ansatz:

$$\begin{aligned}(m_{xy}/m_{hhh})^2 &= e_0 + e_l(a\tilde{m}_l) + e_v(a\tilde{m}_x + a\tilde{m}_y) + e_h(a\tilde{m}_h)\,, \text{ and} \\ (m_{xh}/m_{hhh})^2 &= f_0 + f_l(a\tilde{m}_l) + f_v(a\tilde{m}_x) + f_h(a\tilde{m}_h)\end{aligned} \tag{8.14}$$

for the ratios on the **A** ensembles and

$$\begin{aligned}(m_{xy}/m_{hhh})^2 &= e_0 + e_l Z_l R_a(a\tilde{m}_l) + e_v Z_l R_a(a\tilde{m}_x + a\tilde{m}_y) + e_h Z_h R_a(a\tilde{m}_h)\,, \text{ and} \\ (m_{xh}/m_{hhh})^2 &= f_0 + f_l Z_l R_a(a\tilde{m}_l) + f_v Z_l R_a(a\tilde{m}_x) + f_h Z_h R_a(a\tilde{m}_h)\,,\end{aligned} \tag{8.15}$$

where the shared fit coefficients are constrained to be equal as above. Again $Z_l R_a$ and $Z_h R_a$ are determined from the fit. This procedure still requires an independent fit over the simulated Omega masses on both ensemble sets in order to determine R_a, which is performed as in procedure II.

In section 8.4, a combined fit is performed over both ensemble sets with the data expressed in physical units, which is then used to take the continuum limit. From the discussion above it is clear that this global fit procedure could be performed to dimensionless data, which would require only the values of $Z_l R_a$ and $Z_h R_a$ (cf. eqns. 8.13 and 8.15). The lattice scale could then be assigned after the fit is performed.

Procedure	Z_l	Z_h	R_a
I	0.981(9)	0.974(7)	0.7583(46)
II	0.989(10)	0.978(7)	0.7594(47)
III	0.975(9)	0.962(5)	0.7558(41)

Table 8.2: Values of Z_l, Z_h and R_a obtained by matching the two ensemble sets at the unphysical quark masses $m_l^{\mathbf{A}} = 0.006$ and $m_h^{\mathbf{A}} = 0.03$ using the three procedures described in sections 8.2.1 and 8.2.2. Here procedure I is the fixed trajectory approach described in the former, and procedures II and III are the pseudo-generic scaling approaches described in the latter.

This method still requires an iterative procedure as the explicit values of the lattice spacings are required to determine the scaling coefficients of the other data (f_{xy},f_{xh} etc.). However at no point does this require a value for R_a to be fixed. In procedures II and III, the specification of a match point is needed only to determine R_a, and the fits implicitly take advantage of the weak mass dependence of Z_l and Z_h. If the match point is not specified, the scaling trajectory is fixed in an uncontrolled way that relies on this weak dependence and the relative statistical precision of the individual data points. This is known as a *generic scaling* approach [3]. Procedures II and III might be referred to as *pseudo-generic scaling* approaches.

Table 8.2 contains the results of the pseudo-generic scaling approaches applied at the match point $m_l^{\mathbf{A}} = 0.006$, $m_h^{\mathbf{A}} = 0.03$ chosen in section 8.2.1. The values agree well between the different approaches, but the gain from including data from both lattices in the fit is only small for approach III and non-existent in approach II. It is concluded that the gain from using approach III over the fixed scaling approach (I) is not significant enough to justify the loss of the ability to exactly define the scaling trajectory.

8.2.3 Scaling analysis

Once the values of Z_l, Z_h and R_a are known, an analysis of the scaling of the data at unphysical masses between the ensemble sets can be performed by interpolating other quantities to any match point on each ensemble set and comparing the results. This match point need not be that used in the determination of Z_l, Z_h and R_a, but it is illustrative to examine this point first. The procedure for comparing a lattice quantity Q, given here for a general number of ensemble sets, is similar to that in section 8.2.1: First a partially-quenched linear fit over ensemble set $\mathbf{M}$ to the quantity Q at the simulated strange quark mass is performed. If $Q = m_{xy}$, m_{xh} or m_{hhh}, the fit forms are those given in eqns. 8.1–8.3. The fit forms for the other quantities that were

calculated in chapter 6 are as follows:

$$\begin{aligned} f_{xy} &= f_0 + f_l\, m_l + f_v(m_x + m_y)\,, \\ f_{xh} &= g_0 + g_l\, m_l + g_v\, m_x\,, \text{ and} \\ r_0 &= h_0 + h_l\, m_l\,. \end{aligned} \tag{8.16}$$

The remainder of the procedure is given below.

1. The values of $m_h^{\text{match},\,\mathbf{e}}$ and $m_l^{\text{match},\,\mathbf{e}}$ corresponding to the match point are calculated using $R_a^{\mathbf{e}}$ and $Z_f^{\mathbf{e}}$.
2. The simulated values of Q are linearly interpolated to $m_h^{\text{match},\,\mathbf{e}}$.
3. An independent partially-quenched linear fit to this data is performed over each of the ensemble sets $\mathbf{e} \neq \mathbf{M}$ using the forms above.
4. Q is interpolated to $m_l^{\text{match},\,\mathbf{e}}$.
5. The ratio $R_Q \equiv (R_a^{\mathbf{e}})^{\eta}(aQ)^{\text{match},\,\mathbf{M}}/(aQ)^{\text{match},\,\mathbf{e}}$ is calculated, for which the deviation from unity gives an estimate of the size of the scaling errors at the match point.

The power η to which R_a is raised is as follows:

$$\eta = \left\{ \begin{array}{c|l} 1 & Q = r_0/a \\ -1 & Q \in \{am_{xy}, am_{xh}, af_{xy}, af_{xh}, am_{hhh}\} \end{array} \right. . \tag{8.17}$$

Table 8.2.3 contains the values of R_Q calculated between ensemble sets **A** and **B** at the match point $m_l^{\mathbf{A}} = 0.006$, $m_h^{\mathbf{A}} = 0.03$ that was used to define the scaling trajectory in section 8.2.1. As before the ensemble set labels have been dropped where there is no ambiguity. This analysis provides independent verification that m_{xy}, m_{xh} and m_{hhh} do indeed scale perfectly at the match point (up to tiny errors resulting from approximations in the procedure) as required. The quantities f_{xy}, f_{xh} and r_0 all appear to be scaling well, demonstrating differences due to discretisation effects that are $\lesssim 1\%$. As a^2 is changed by a factor of 2 between the ensemble sets, overall discretisation errors can be expected to be $\sim 1\%$ on the **A** ensembles and $\sim 2\%$ on the **B** ensembles. These estimates are substantially smaller than the 4% that was estimated for the **B** ensembles in ref. [1].

The analysis can be extended by considering the scaling of the quantities above at quark masses away from the match point at which Z_l, Z_h and R_a are defined. Figure 8.1 contains plots of the ratio R_Q as a function of the light quark mass on the **A** ensembles. Data on the **A** ensembles are available within the range $m_l^{\mathbf{A}} = 0.004$–0.008, and on the **B** ensemble set between $m_l^{\mathbf{A}} \sim 0.0054$–$0.0091$. Within this region, the separation of the

Q	m_{xy}	f_{xy}	m_{xh}	f_{xh}	m_{hhh}	r_0
R_Q	1.0001(1)	0.9872(56)	1.0000(0)	0.9887(50)	1.0000(0)	1.0075(72)

Table 8.3: A comparison of various quantities between the two ensemble sets at the match point $m_l^{\mathbf{A}} = 0.006$, $m_h^{\mathbf{A}} = 0.03$ from which the values of Z_l, Z_h and R_a were determined in section 8.2.1. $R_Q = 1$ indicates perfect scaling. m_{xy}, m_{xh} and m_{hhh} are chosen to scale perfectly in order to define the scaling trajectory. Here the tiny error on m_{xy} arises due to approximations in the analysis. m_{xh} and m_{hhh} also have small errors of 3×10^{-5} and 7×10^{-6} respectively. The discrepancies introduced by the approximations are small enough to be ignored.

simulated point from the scaling trajectory can be seen to introduce small deviations of the order 0.5% on the quantities m_{xy}, m_{xh} and m_{hhh}. The decay constants and r_0 also appear to scale well around the match point, indicating that the discretisation errors are small.

8.3 Taking the continuum limit

The matching analysis of section 8.2.1 defines a scaling trajectory at unphysical light and heavy quark masses within the range of the available data, upon which the unitary quantities m_{ll}, m_{lh} and m_{hhh} at the match point are defined to scale perfectly. Other quantities such as f_{ll}, f_{lh}, B_{lh} and r_0, retain a scale dependence, and hence require an extrapolation to the continuum limit. The discussion in this section focuses upon the continuum extrapolation of the decay constants, but the procedure for the remaining quantities is essentially the same (cf. section 8.6 for r_0 and r_1, and section 8.7 for B_K).

A conceptually simple method of taking the continuum limit of f_{ll} and f_{lh} is outlined below. Here it is convenient to discuss the light-quark interpolation on an ensemble $\mathbf{e}$ in terms of general fit ansätze:

$$\begin{aligned} f_{xy} &= f_{xy}(\tilde{m}_x^{\mathbf{e}}, \tilde{m}_y^{\mathbf{e}}, \tilde{m}_l^{\mathbf{e}}) \\ f_{xh} &= f_{xh}(\tilde{m}_x^{\mathbf{e}}, \tilde{m}_l^{\mathbf{e}})\,. \end{aligned} \tag{8.18}$$

In this section all quantities are expressed in physical units unless otherwise specified. The continuum limit can be taken via the following procedure.

1. Choose the values of $m_l^{\text{match},\,\mathbf{A}}$ and $m_h^{\text{match},\,\mathbf{A}}$ at the match point and obtain the corresponding $f_{ll}^{\text{match},\,\mathbf{A}}$ and $f_{lh}^{\text{match},\,\mathbf{A}}$.

2. Perform the matching analysis of section 8.2.1 in order to obtain the corresponding $m_l^{\text{match},\,\mathbf{B}}$ and $m_h^{\text{match},\,\mathbf{B}}$.

3. Reweight/interpolate all data for $f_{xy}^{\mathbf{B}}$ and $f_{xh}^{\mathbf{B}}$ to $m_h^{\text{match},\,\mathbf{B}}$, assuming a linear ansatz as before.

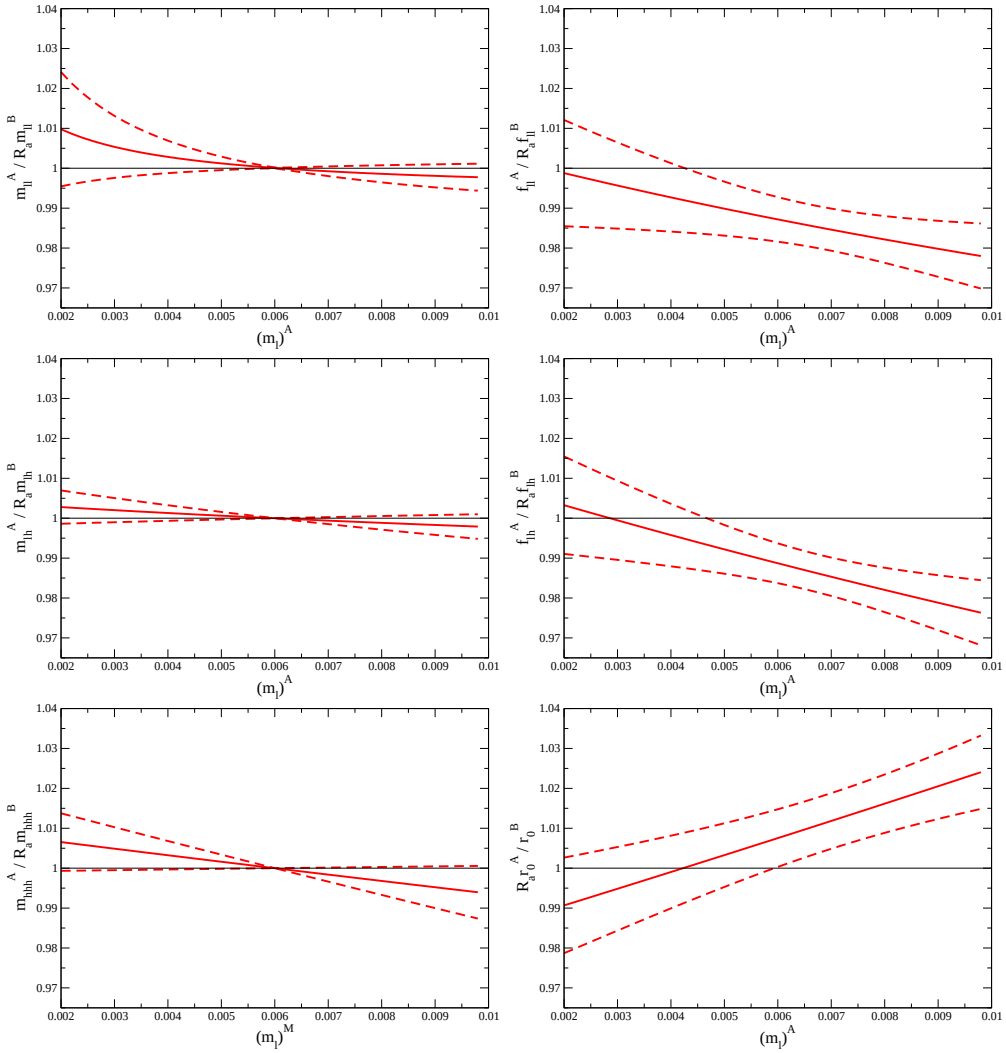

Figure 8.1: Plots of the ratio R_Q at a range of light quark masses $m_l^{\mathbf{A}}$. $R_Q = 1$ indicates perfect scaling. m_{xy}, m_{xh} and m_{hhh} are shown to scale perfectly at $m_l^{\mathbf{A}} = 0.006$ as required.

4. Fit $f_{xy}^{\mathbf{B}}$ and $f_{xh}^{\mathbf{B}}$ to the forms $f_{xy}(\tilde{m}_x^{\mathbf{B}}, \tilde{m}_y^{\mathbf{B}}, \tilde{m}_l^{\mathbf{B}})$ and $f_{xh}(\tilde{m}_x^{\mathbf{B}}, \tilde{m}_l^{\mathbf{B}})$.

5. Interpolate the quantities to $m_l^{\text{match},\mathbf{B}}$ to obtain the corresponding $f_{ll}^{\text{match}\,\mathbf{B}}$ and $f_{lh}^{\text{match},\mathbf{B}}$.

6. Extrapolate to the continuum limit.

This procedure can be repeated over a number of match points in order to build a set of continuum data at different light and heavy quark masses.

The form for the continuum extrapolation is motivated by a double-expansion of a quantity Q in a^2 and the quark mass m_q:

$$Q(a^2, m_q) = A + Bm_q + Ca^2 + Dm_q a^2 + \ldots \tag{8.19}$$

The terms $m_q a^2$ and higher are considered as higher order, and are discarded. This power counting is similar to Weinberg's scheme for ChPT, discussed in section 3.2.1, which treats the quark mass at the same chiral order as two powers of the momentum. At fixed quark mass, the continuum limit of f_{ll}^{match} and f_{lh}^{match} can therefore be taken by extrapolating with the forms

$$\begin{aligned} f_{ll}^{\text{match},\mathbf{e}} &= f_{ll}^{\text{match},(0)} + ca^2\,, \text{ and} \\ f_{lh}^{\text{match},\mathbf{e}} &= f_{lh}^{\text{match},(0)} + da^2\,, \end{aligned} \tag{8.20}$$

where the continuum values $f_{ll}^{\text{match},(0)}$ and $f_{lh}^{\text{match},(0)}$ depend on the chosen match point. Note that until the continuum data is matched to the correct physical renormalised trajectory and the scale is set, the lattice spacings are not known. As a result the extrapolation above must first be performed with estimates of the lattice spacing and requires an iterative procedure. This is described in more detail in the following section.

The simple procedure outlined above requires the matching procedure to be repeated for every mass combination in order to obtain the values of m_l and m_h on the **B** ensembles that correspond to the match point on the **A** ensembles. This can be avoided by recalling that to a good approximation, quark masses on scaling trajectories that are sufficiently close together can be related using Z_l and Z_h determined at a single representative match point. In addition, as $\mathcal{O}(a^2 m_q)$ terms are treated as higher order in the power counting scheme, the coefficients c and d of eqn. 8.20 can be assumed to have negligable mass dependence. As a result the procedure of interpolating each quantity in the quark masses and extrapolating to the continuum over a number of match points can be simplified, while also allowing c and d to be constrained by the data on both ensembles, by performing a simultaneous fit over both ensemble sets as in section 8.2.2, using fit forms that include an a^2 scaling dependence.

For f_{xy} and f_{xh}, this simultaneous continuum extrapolation proceeds as follows. First f_{xy} and f_{xh} are reweighted/interpolated to a single unitary strange quark mass, $m_h^{\text{match},\mathbf{A}}$, which corresponds to $m_h^{\text{match},\mathbf{B}} = Z_h m_h^{\text{match},\mathbf{A}}$ on the **B** ensembles. The quantities are then simultaneously fit over both ensemble sets, using the following mass dependence:

$$f_{xy}^{\mathbf{A}} = f_{xy}(\tilde{m}_x^{\mathbf{A}}, \tilde{m}_y^{\mathbf{A}}, \tilde{m}_l^{\mathbf{A}}) + ca^2, \tag{8.21}$$

$$f_{xy}^{\mathbf{B}} = f_{xy}(Z_l\tilde{m}_x^{\mathbf{B}}, Z_l\tilde{m}_y^{\mathbf{B}}, Z_l\tilde{m}_l^{\mathbf{B}}) + ca^2, \tag{8.22}$$

and

$$f_{xh}^{\mathbf{A}} = f_{xh}(Z_l\tilde{m}_x^{\mathbf{A}}, Z_l\tilde{m}_l^{\mathbf{A}}) + da^2, \tag{8.23}$$

$$f_{xh}^{\mathbf{B}} = f_{xh}(Z_l\tilde{m}_x^{\mathbf{B}}, Z_l\tilde{m}_l^{\mathbf{B}}) + da^2. \tag{8.24}$$

The fit needs only to be repeated if a different heavy quark mass is required.

Used in this way, the ratios Z_l and Z_h can be considered to be the renormalisation coefficients of a *matching scheme* which renormalises the quark masses, and the fit parameters multiplying them, in a lattice regularisation dependent scheme defined by unit renormalisation factors on a 2.3 GeV cutoff.

8.4 Chiral extrapolation and setting the scale

The process described in the previous section requires an iterative procedure to obtain the self-consistent lattice spacings on each ensemble set. As described in section 8.1, this is achieved by first tuning the light and heavy quark masses in the continuum such that m_{ll}/m_{hhh} and m_{hl}/m_{hhh} match their physical values. The lattice spacings are then determined by repeating the extrapolation procedure while varying the lattice spacing estimates until the simulated continuum m_{hhh} matches its physical value. In practise, as the data obtained from the continuum extrapolation are already in physical units, the equivalent conditions that m_{ll}, m_{hl} and m_{hhh} match their physical values are used instead.

As discussed previously, a chiral extrapolation is required to reach the physical light quark mass. This is performed using a simultaneous chiral/continuum fit to both ensemble sets in order to minimise the statistical error. The fit forms are obtained as before, by performing a double-expansion in a^2 and the quark masses. This analysis uses forms obtained by expanding about a fixed unphysical quark mass and also about the chiral limit. These are discussed further in the following sections.

For the cutoff-dependent quantities f_{xy} and f_{xh}, the continuum results can be extrapolated to the physical quark masses by using the chiral ansatz for the

simultaneous fit that is performed in order to take the continuum limit (eqns. 8.22 and 8.24). The fits for the artefact-free quantities m_{xy}, m_{xh} and m_{hhh} are performed using the following generic forms over both ensemble sets:

$$\begin{aligned}(m_{xy}^2)^{\mathbf{e}} &= m_{xy}^2(Z_l^{\mathbf{e}}\tilde{m}_x^{\mathbf{e}}, Z_l^{\mathbf{e}}\tilde{m}_y^{\mathbf{e}}, Z_l^{\mathbf{e}}\tilde{m}_l^{\mathbf{e}})\,,\\ m_{xh}^{\mathbf{e}} &= m_{xh}(Z_l^{\mathbf{e}}\tilde{m}_x^{\mathbf{e}}, Z_l^{\mathbf{e}}\tilde{m}_l^{\mathbf{e}})\,,\\ m_{hhh}^{\mathbf{e}} &= m_{hhh}(Z_l^{\mathbf{e}}\tilde{m}_l^{\mathbf{e}})\,.\end{aligned} \tag{8.25}$$

Here the definition $Z_l^{\mathbf{A}} = Z_h^{\mathbf{A}} = 1$ has been used to simplify the equations.

In practise, some of the chiral fit functions share parameters with others. In order to maximally constrain the fit, the chiral/continuum procedure is therefore implemented as a simultaneous fit over all quantities on both ensemble sets at once. This is referred to as a *global fit*. A step-by-step summary of the global fit procedure is given in section 8.4.4.

8.4.1 Analytic ansatz

The simplest ansatz for the chiral behaviour is obtained by performing a Taylor expansion about an unphysical quark mass $\tilde{m}^m$. In order to remain consistent with the linear a^2 dependence assumed in the continuum extrapolations, the power counting scheme restricts the Taylor expansion to first order. For the pion mass the expansion has the form

$$m_{xy}^2 = C_0^{m_\pi} + C_1^{m_\pi}\left(\frac{1}{2}(\tilde{m}_x + \tilde{m}_y) - \tilde{m}^m\right) + C_2^{m_\pi}(\tilde{m}_l - \tilde{m}^m)\,, \tag{8.26}$$

which has no scale dependence as the pions are defined to scale perfectly along the scaling trajectory. At this order, the above can be rewritten as

$$m_{xy}^2 = C_0^{m_\pi} + \frac{1}{2}C_1^{m_\pi}(\tilde{m}_x + \tilde{m}_y) + C_2^{m_\pi}\tilde{m}_l\,. \tag{8.27}$$

In a similar way the other scale-independent quantities behave as

$$\begin{aligned}m_{xh}^2 &= C_0^{m_K} + C_1^{m_K}\tilde{m}_x + C_2^{m_K}\tilde{m}_l\,, \text{ and}\\ m_{hhh} &= C_0^{m_\Omega} + C_2^{m_\Omega}\tilde{m}_l\,,\end{aligned} \tag{8.28}$$

and the scale-dependent quantities f_{xy} and f_{xh} are fit to the chiral/continuum forms

$$\begin{aligned}f_{xy} &= C_0^{f_\pi}[1 + C_f a^2] + \frac{1}{2}C_1^{f_\pi}(\tilde{m}_x + \tilde{m}_y) + C_2^{f_\pi}\tilde{m}_l\,, \text{ and}\\ f_{xh} &= C_0^{f_K}[1 + C_{f_K} a^2] + C_1^{f_K}\tilde{m}_x + C_2^{f_K}\tilde{m}_l\,.\end{aligned} \tag{8.29}$$

8.4.2 Partially-quenched ChPT

Traditionally, chiral extrapolations are guided by (partially-quenched) chiral perturbation theory. The fit forms for the second chiral ansatz are therefore derived from the formulae given in sections 3.2.4 and 3.2.5. This analysis is restricted to $SU(2)$ (PQ)ChPT following the discussion in section 3.2. The kaons are coupled into the theory by the procedure described in section 3.2.5. In this chapter, the prefix 'PQ' is dropped for convenience.

The next-to-leading order ChPT fit forms for the pion mass and the kaon mass are given in equations 3.79 and 3.84 respectively. The chiral/continuum forms for f_{xy} and f_{xh} are obtained from eqns. 3.80 and 3.86 by including an a^2 coefficient as a correction to the leading-order LECS. For unitary data, this gives

$$f_{ll} = f\left[1 + c_f a^2\right] + f \cdot \left\{ \frac{8}{f^2}(2l_4 + l_5)\chi_l - \frac{\chi_l}{8\pi^2 f^2} \log \frac{\chi_l}{\Lambda_\chi^2} \right\} \text{ and} \tag{8.30}$$

$$f_{lh} = f^{(K)}\left[1 + c_{f^{(K)}} a^2\right] + f^{(K)} \left\{ \frac{\lambda_3 + \lambda_4}{f^2}\chi_l - \frac{1}{(4\pi f)^2}\,\frac{3}{4}\,\chi_l \log \frac{\chi_l}{\Lambda_\chi^2} \right\}. \tag{8.31}$$

Here the low-energy constants B and f are simultaneously constrained by m_{xy}, m_{xh}, f_{xy} and f_{xh} in the global fit.

The fit form for the Omega baryon mass m_{hhh} is linear in the light sea quark mass:

$$m_{hhh} = m^{(\Omega)} + m^{(\Omega)}\, c_{m_\Omega, m_l}\, \chi_l \,. \tag{8.32}$$

8.4.3 Finite-volume ChPT

In addition to the ChPT fit forms given in the previous section, the analysis is also performed using finite-volume ChPT [155][156][157][158][159][160][1], in which the chiral logarithms are corrected by the Bessel functions that appear in loop integrals when the loop-momenta are discretised in a finite volume. The finite-volume ChPT fit forms for m_{xy}, f_{xy} and f_{xh} are given in ref. [1]. For the decay constants, a scaling term linear in a^2 is included as above. The NLO ChPT fit forms for m_{xh} and m_{hhh}, given in eqns. 3.84 and 8.32 respectively, do not contain logarithmic corrections and thus receive no finite volume corrections. An example of a finite-volume ChPT fit form is given for B_K in section 8.7.2.

Infinite-volume results are obtained using these forms by first fitting the data with the full form, including the Bessel function corrections, and subsequently removing the Bessel function contributions.

8.4.4 Summary of the global fit procedure

The full global fit procedure is summarised as follows:

1. Perform the fixed trajectory matching analysis to obtain Z_l, Z_h and R_a.
2. Estimate the lattice spacings on both ensemble sets.
3. Estimate the physical up/down and strange quark masses in the matching scheme; $m_{u/d}$ and m_s respectively.
4. Convert all simulated quantities to physical units using the lattice spacings obtained previously.
5. Reweight/interpolate all quantities on the **A** ensembles to the physical strange quark mass $\tilde{m}_h^{\mathbf{A}} = m_s$.
6. Reweight/interpolate all quantities on the **B** ensembles to the physical strange quark mass $\tilde{m}_h^{\mathbf{B}} = m_s/Z_h$.
7. Simultaneously fit m_{xy}, m_{xh}, f_{xy}, f_{xh} and m_{hhh} to the forms obtained for the chosen ansatz.
8. Obtain predictions for the physical values of m_{ll}, m_{lh} and m_{hhh} by setting $m_x = m_y = m_l = m_{u/d}$ and $a = 0$ in the fit formulae.
9. Comparing the predicted value of m_{ll} with the true physical value, suggest a new value for $m_{u/d}$.
10. Comparing the predicted value of m_{lh} with the true physical value, suggest a new value for m_s.
11. Comparing the predicted value of m_{hhh} with the true physical value, and using the pre-determined $R_a = a^{\mathbf{A}}/a^{\mathbf{B}}$, suggest new values for the lattice spacings.
12. With the updated lattice spacings and quark masses, return to step 4. Repeat until the procedure converges.

The updated value of the light quark mass is obtained by numerically inverting the (unitary) chiral fit form upon the physical pion mass. The heavy quark mass is updated using an estimate of dm_{xh}/dm_h obtained by repeating steps 4–10 with a slightly shifted strange quark mass.

Parameter	Value	Parameter	Value
$C_0^{m_\pi}$	-0.001(1) GeV^2	$C_1^{m_K}$	3.68(4) GeV
$C_1^{m_\pi}$	7.46(9) GeV	$C_2^{m_K}$	0.6(1) GeV
$C_2^{m_\pi}$	0.43(8) GeV	$C_0^{f_K}$	0.147(2) GeV
$C_0^{f_\pi}$	0.121(2) GeV	C_{f_K}	0.13(5) GeV^2
C_{f_π}	0.16(6) GeV^2	$C_1^{f_K}$	0.35(1)
$C_1^{f_\pi}$	0.85(2)	$C_2^{f_K}$	0.53(10)
$C_2^{f_\pi}$	0.57(9)	$C_0^{m_\Omega}$	1.666(2) GeV
$C_0^{m_K}$	0.2354(9) GeV^2	$C_2^{m_\Omega}$	2.7(9)

Table 8.4: Fit parameters obtained from the simultaneous chiral-continuum fit using the analytic ansatz. The parameters are defined in section 8.4.1.

8.5 Continuum results for quark masses and pseudoscalar decay constants

The simultaneous chiral-continuum extrapolation is performed over both ensemble sets using the analytic and NLO $SU(2)$ ChPT chiral ansätze (with and without finite volume corrections) to fit the following quantities: $m_{xy}, f_{xy}, m_{xh}, f_{xh}$ and m_{hhh}. The results obtained using the finite-volume NLO ChPT ansatz are labelled 'ChPT-fv', and those with the continuum chiral perturbation theory ansatz as 'ChPT'. As in ref. [1], the fits are performed with a cut on the heaviest pion mass of ~ 420 MeV, which equates to including partially-quenched light-quark data up to $m_q = 0.01$ on the **B** ensembles and $m_q = 0.008$ on the **A** ensembles. The fits are all uncorrelated, i.e. performed assuming a unit correlation matrix, as the data are not precise enough to reliably estimate the true correlation matrix. As a result, the χ^2 per degree of freedom of the fits most likely underestimates the 'true' deviation of the data from the fit.

The results for the fit parameters obtained using the analytic ansatz are given in table 8.4, and those obtained using the ChPT and ChPT-fv ansätze in table 8.5. The χ^2 per degree of freedom of the fits are given in table 8.5. Finally the lattice spacings and the bare quark masses in lattice units are given in table 8.7, and the quark masses in physical units are given in table 8.8. The quark masses are given in the intermediate matching scheme, in which the renormalisation coefficients for light and heavy quarks are Z_l and Z_h respectively on the **B** ensembles, and are both unity on the **A** ensembles. In section 8.5.2, these results are combined with the non-perturbative renormalisation conditions calculated in chapter 7 to obtain values in the $\overline{\text{MS}}$-scheme. Note that the errors on the quark masses, which are obtained in physical units from the extrapolations, become inflated when converting back into lattice units (compare tables 8.7 and 8.8). This is because the quark masses, particularly the heavy quark mass, are highly correlated with the lattice spacings as a result of the fit procedure.

Parameter	No FV Corrections	With FV Corrections
B	4.13(7) GeV	4.03(7) GeV
f	0.107(2) GeV	0.110(2) GeV
c_f	0.18(7) GeV^2	0.18(7) GeV^2
$L_4^{(2)}$	0.00000(7)	-0.00004(7)
$L_5^{(2)}$	0.00048(4)	0.00046(4)
$L_6^{(2)}$	-0.00003(4)	-0.00005(4)
$L_8^{(2)}$	0.00055(2)	0.00060(2)
$m^{(K)}$	0.4857(4) GeV	0.4855(4) GeV
$f^{(K)}$	0.139(2) GeV	0.140(2) GeV
$c_{f^{(K)}}$	0.13(5) GeV^2	0.13(5) GeV^2
λ_1	0.0037(9)	0.0040(10)
λ_2	0.022(1)	0.023(1)
λ_3	-0.0017(9)	-0.0016(10)
λ_4	0.0057(2)	0.0056(2)
$m^{(\Omega)}$	1.666(2) GeV	1.666(2) GeV
c_{m_Ω,m_l}	0.20(6) GeV^{-2}	0.20(7) GeV^{-2}

Table 8.5: Fit parameters obtained from the simultaneous chiral-continuum fit using the NLO ChPT ansatz with and without finite-volume corrections. The fit parameters are defined in sections 8.4.2 and 8.4.3. The only statistically significant differences between the fits occur on the leading order LECs, B and f.

Ansatz	χ^2/dof
NLO	0.82(49)
NLO-fv	1.23(51)
Analytic	0.63(45)
Analytic	1.06(46)

Table 8.6: The uncorrelated χ^2/dof obtained from the global fits to the various ansatze. There are 109 degrees of freedom in the fit.

	NLO	NLO fv	Analytic
$\tilde{m}_l(\mathbf{A})$	0.00099(3)	0.00101(3)	0.00105(6)
$m_l(\mathbf{A})$	0.00033(3)	0.00035(3)	0.00038(6)
$\tilde{m}_s(\mathbf{A})$	0.0278(7)	0.0278(7)	0.0277(7)
$m_s(\mathbf{A})$	0.0272(7)	0.0271(7)	0.0271(7)
$a^{-1}(\mathbf{A})$	2.283(29) GeV	2.284(29) GeV	2.285(28) GeV
$\tilde{m}_l(\mathbf{B})$	0.00134(4)	0.00136(4)	0.00141(9)
$m_l(\mathbf{B})$	-0.00174(7)	-0.00171(7)	-0.00166(11)
$\tilde{m}_s(\mathbf{B})$	0.0377(11)	0.0376(11)	0.0376(11)
$m_s(\mathbf{A})$	0.0346(11)	0.0346(11)	0.0345(11)
$a^{-1}(\mathbf{B})$	1.731(25) GeV	1.732(25) GeV	1.733(25) GeV

Table 8.7: Inverse lattice spacings and unrenormalised quark masses in lattice units for the **A** and **B** ensembles. Here, as always, $\tilde{m}_q = m_q + m_{\text{res}}$.

	NLO	NLO fv	Analytic
m_l^{phys}	0.00227(4) GeV	0.00231(4) GeV	0.00240(13) GeV
m_h^{phys}	0.0636(9) GeV	0.0635(9) GeV	0.0634(9) GeV

Table 8.8: Quark masses in physical units, renormalised in the intermediate matching scheme in which the renormalisation coefficient is Z_l on the **B** ensembles and unity on the **A** ensembles.

8.5.1 Global fit results

In order to display the quality of the fits to the data over this many-parameter space, it is useful to consider each fitted quantity in turn. In the following sections, the partially-quenched data on the lightest ensembles of both ensemble sets are overlaid by the fitted curves (apart from for m_{hhh} which has only a single data point per ensemble). The combined unitary extrapolation to the physical light quark mass is shown overlaying the data corrected to the continuum using the fitted a^2 dependence.

Pion mass

The partially-quenched pion data are fitted to the forms detailed in sections 8.4.1, 8.4.2 and 8.4.3.

Figures 8.2 and 8.3 show the partially-quenched pion data on the lightest ensembles of the **A** and **B** ensemble sets respectively, overlaid by the ChPT fit curves. Figures 8.4 and 8.5 contain the same for the ChPT-fv fits. The figures are plotted with the ratio of square of the pion mass to the average valence quark mass on the y-axis in an attempt to enhance the visibility of the non-analytic behaviour of the data resulting from the chiral logarithms. The plots clearly show that the ChPT and ChPT-fv fit curves diverge rapidly from the data at large masses - this behaviour motivated the introduction of the 420 MeV pion-mass cut in ref. [1].

Figures 8.6 and 8.7 show the results of the leading-order analytic fit overlaying the partially-quenched data on the **A** and **B** ensemble sets respectively. Here the apparent curvature of the fit forms arises due to the division by the average valence-quark mass:

$$\frac{2m_{xy}^2}{(\tilde{m}_x+\tilde{m}_y)} = \frac{2C_0^{m_\pi}}{(\tilde{m}_x+\tilde{m}_y)} + C_1^{m_\pi} + \frac{C_2^{m_\pi}\tilde{m}_l}{(\tilde{m}_x+\tilde{m}_y)}. \tag{8.33}$$

Clearly it is entirely possible to explain the apparent curvature of the data in these plots without requiring non-analytic logarithmic terms. The apparent non-analyticity of the data is therefore misleading. The analytic form appears to describe the data at the simulated quark masses somewhat better than the ChPT and ChPT-fv forms, and continues to describe the data quite well far above the 420 MeV cut.

Figure 8.8 shows the chiral extrapolations of the unitary data on both ensemble

sets. Here the data are displayed in physical units, and in the ChPT-fv case are corrected to the infinite volume. Although the extrapolated continuum values of m_π are constrained to match the physical values, the extrapolated points in these figures, which show m_π^2/m_l, differ due to the different physical light-quark masses obtained in the analyses.

The pole at zero quark mass on the analytic curve is allowed by the inclusion of a constant term $C_0^{m_\pi}$ in the analytic fit forms. The result, $C_0^{m_\pi} = -0.001(1)$ GeV, is in fact consistent with zero, and thus satisfies Goldstone's theorem in the unitary direction. Goldstone's theorem also applies in the limit of vanishing average valence quark mass, $\frac{1}{2}(\tilde{m}_x + \tilde{m}_y)$, at finite m_l. In order to be completely consistent with the theorem, the coefficient $C_2^{m_\pi}$, which parameterises the dependence of m_{xy}^2 on m_l, must also be zero. The analytic global fit gives $C_2^{m_\pi} = 0.43(8)$, which is clearly inconsistent with Goldstone's theorem in the partially-quenched chiral limit. It is possible that the magnitude of this term is a result of the mass-dependence of m'_{res}, which occurs mainly due to the difference of the PCAC current renormalisation from unity (cf. section 4.1.3). The largest mass dependence occurs in the partially-quenched direction on the **B** ensembles, but can at most generate only a 1% dependence of the valence quark masses on $\tilde{m}_l$. In addition, the effect that this has on $C_2^{m_\pi}$ will be reduced, as the term is also constrained by the **A** ensembles, for which the residual chiral symmetry breaking is significantly smaller. The analytic fit results give strong evidence for the existence of some form of non-analytic behaviour in the partially-quenched direction, likely due to partially-quenched chiral logarithms that are expected to be larger than those in the unitary direction. However, the proof of logarithmic behaviour would require the quark mass to be varied substantially on a logarithmic scale and/or a substantial increase in statistics to be able to identify non-analytic behaviour, which cannot yet be achieved.

It should be noted that the consistency of the analytic fit and the chiral limit is not necessary to extract physical predictions. It is only necessary for the analytic expansion to be valid from the range of simulated data down to the physical pion mass (~ 130 MeV). Although it has been shown that some non-analyticity is required before the chiral limit is reached, it cannot be known at what scale this behaviour enters - it may occur at scale lower than the physical pion mass, in which case it is irrelevant to this study.

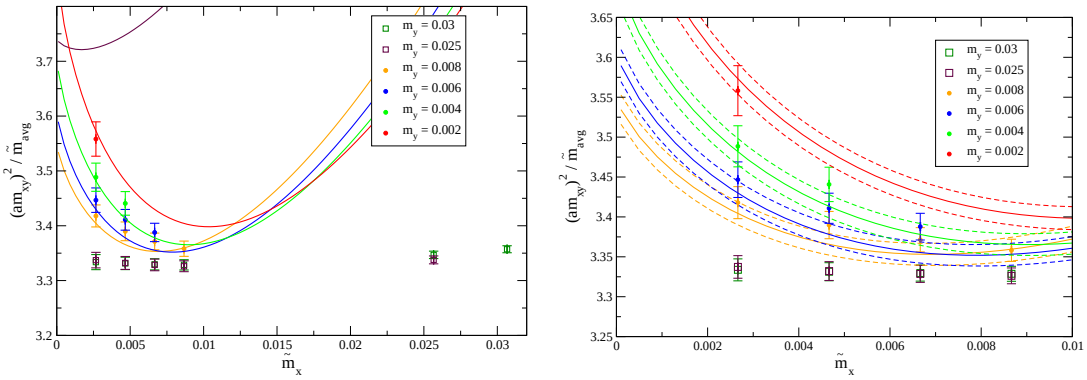

Figure 8.2: Partially-quenched pion data on the $m_l = 0.004$ ensemble of set **A** overlaid by the results of the global fit using the ChPT ansatz. Points marked by full circles were included in the fit, and those marked with unfilled squares were not. The right panel shows the region containing the fitted data at a smaller scale and includes error bands on the curves.

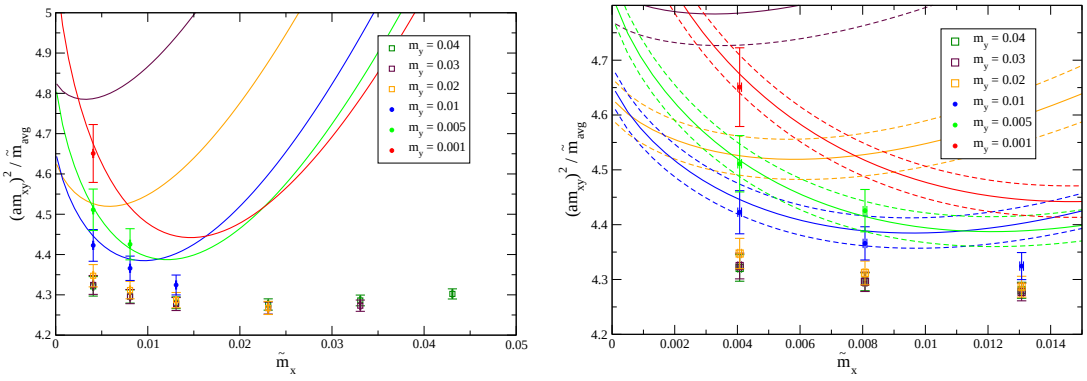

Figure 8.3: Partially-quenched pion data on the $m_l = 0.005$ ensemble of set **B** overlaid by the results of the global fit using the ChPT ansatz. Points marked by full circles were included in the fit, and those marked with unfilled squares were not. The right panel shows the region containing the fitted data at a smaller scale and includes error bands on the curves.

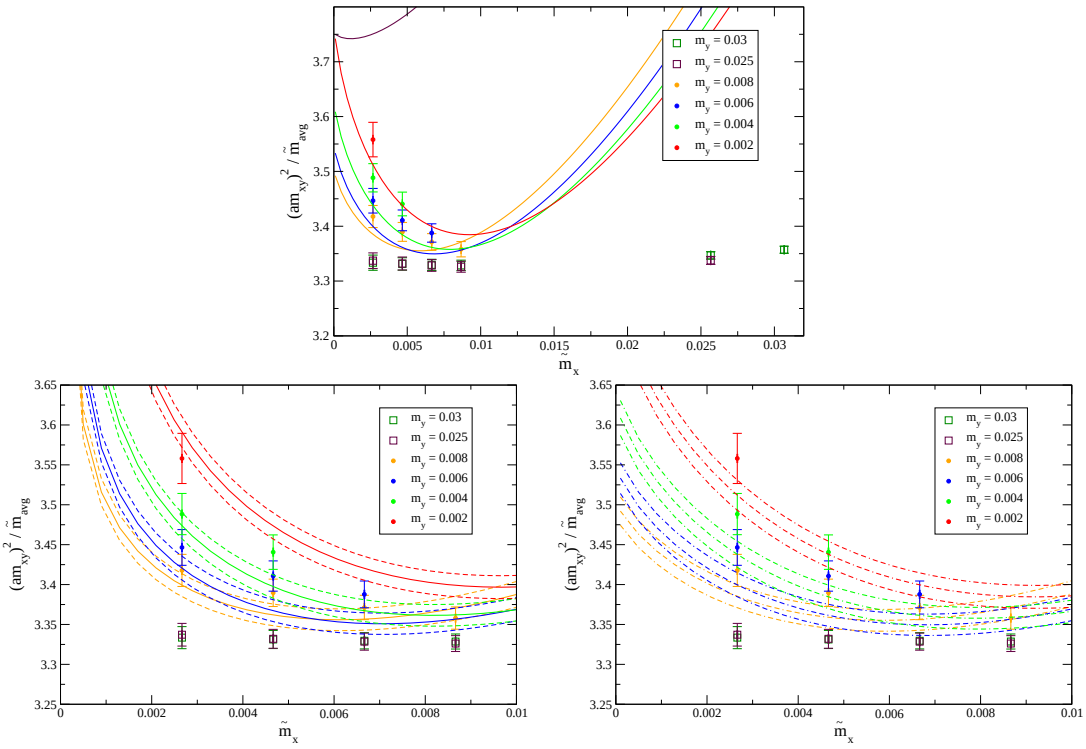

Figure 8.4: Partially-quenched pion data on the $m_l = 0.004$ ensemble of set **A** overlaid by the results of the global fit using the ChPT-fv ansatz. Points marked by full circles were included in the fit, and those marked with unfilled squares were not. The upper panel shows the data overlaid by the infinite volume fit curves. The lower-left and lower-right panels show the region containing the fitted data at a smaller scale, overlaid by the finite and infinite volume curves respectively.

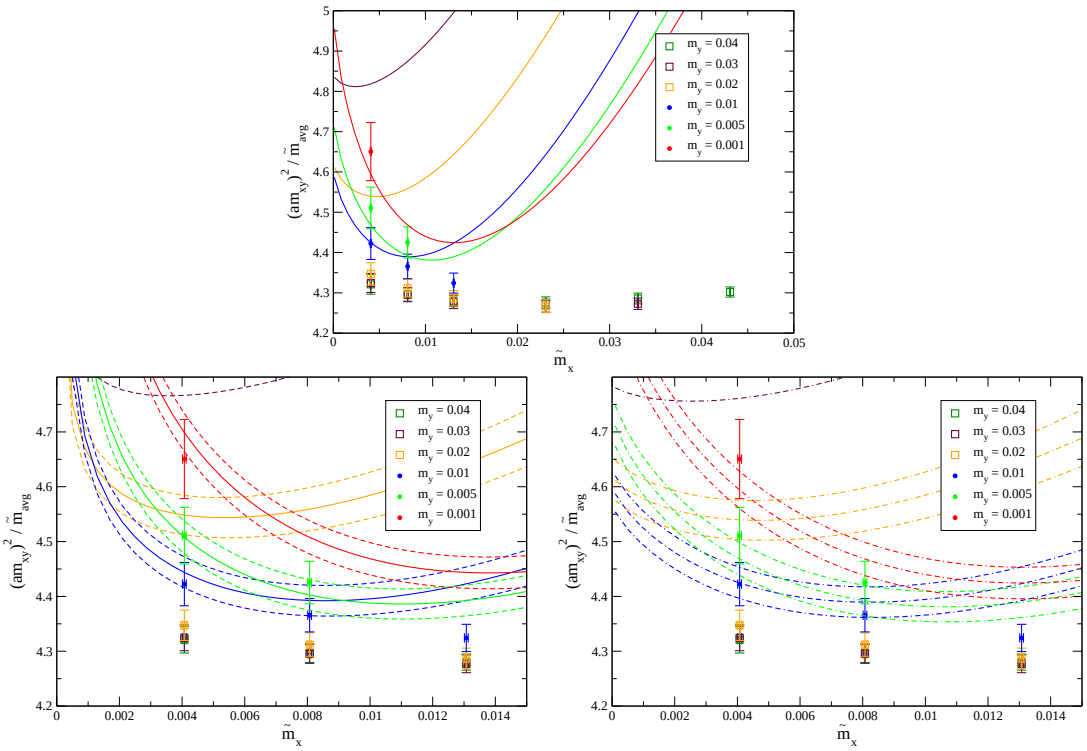

Figure 8.5: Partially-quenched pion data on the $m_l = 0.005$ ensemble of set **B** overlaid by the results of the global fit using the ChPT-fv ansatz. Points marked by full circles were included in the fit, and those marked with unfilled squares were not. The upper panel shows the data overlaid by the infinite volume fit curves. The lower-left and lower-right panels show the region containing the fitted data at a smaller scale, overlaid by the finite and infinite volume curves respectively.

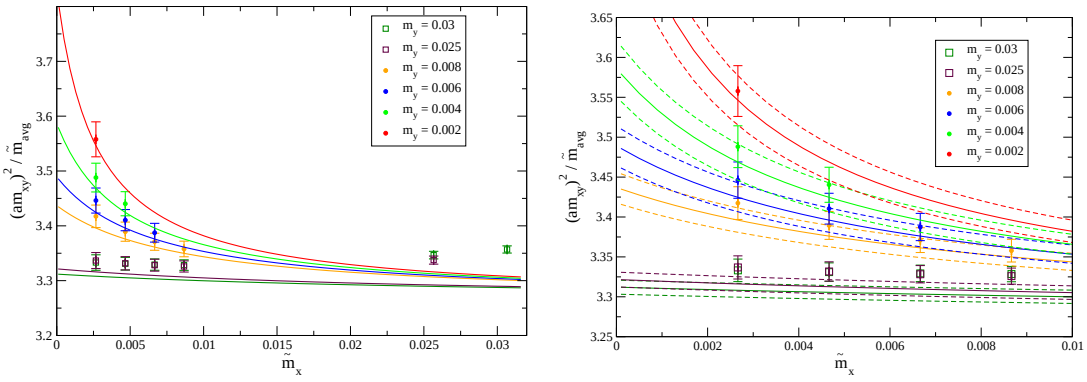

Figure 8.6: Partially-quenched pion data on the $m_l = 0.004$ ensemble of set **A** overlaid by the results of the global fit using the analytic ansatz. Points marked by full circles were included in the fit, and those marked with unfilled squares were not. The right panel shows the region containing the fitted data at a smaller scale and includes error bands on the curves.

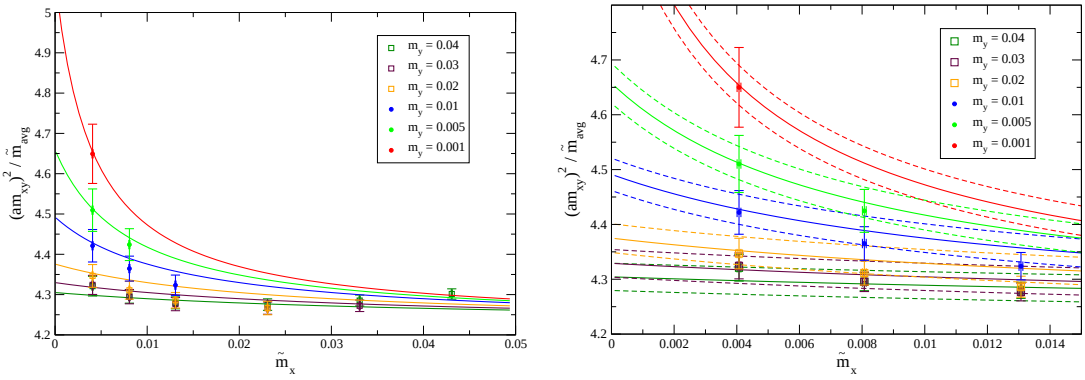

Figure 8.7: Partially-quenched pion data on the $m_l = 0.005$ ensemble of set **B** overlaid by the results of the global fit using the analytic ansatz. Points marked by full circles were included in the fit, and those marked with unfilled squares were not. The right panel shows the region containing the fitted data at a smaller scale and includes error bands on the curves.

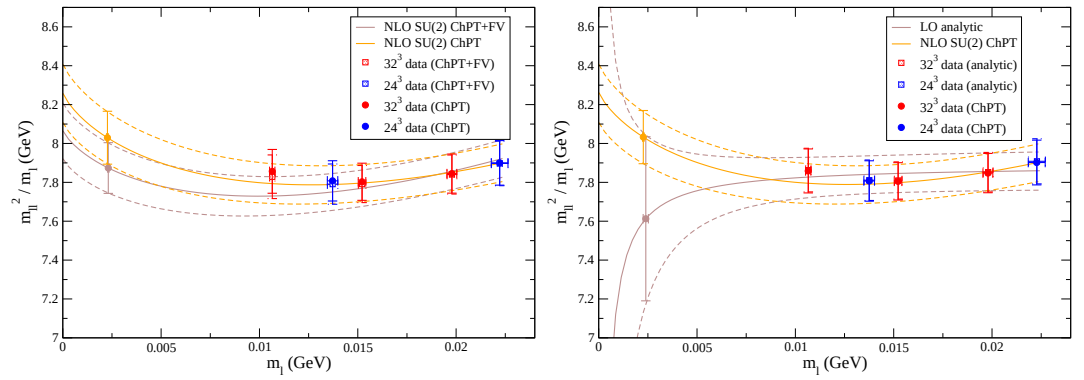

Figure 8.8: Unitary pion data in physical units on both ensemble sets. In the left panel this is overlaid by the unitary chiral extrapolation curves of the ChPT and ChPT-fv fits. Here the data represented by unfilled square points has been corrected to the infinite volume using the results of the ChPT-fv fit and the curve is plotted at infinite volume. The right panel shows a comparison of the chiral extrapolation using the analytic ansatz and the ChPT form. Here the small differences in the data represented by squared and circled points arise due to the different values of the final lattice spacings.

Pion decay constant

Following the layout of the previous section, the partially-quenched data on the lightest ensembles of the **A** and **B** ensembles are shown overlaid by the fit curves of the three ansätze in figures 8.9–8.14. Using the fit ansätze, the unitary data are adjusted to the continuum limit and are displayed with the extrapolations to the physical light quark mass in figure 8.15. For comparison, the uncorrected data are shown in figure 8.16 overlaid by the same curve, as well as the corresponding curves at non-zero lattice spacing.

The predictions for f_π in the continuum limit and at each finite lattice spacing, obtained from each of the three ansätze, are given in table 8.9. For use in the following discussion, the predictions for f_K and the ratio f_K/f_π are given in tables 8.10 and 8.11 respectively.

The known physical value of $f_\pi \sim 130.7$ MeV [29] is significantly larger than the continuum value predicted using the ChPT and ChPT-fv ansätze ($\sim 12\%$ and $\sim 10\%$ resp.). Even at the simulated lattice spacings the predicted value is too low. These disparities are consistent with the expected size of NNLO ChPT contributions: The data are typically between $20 - 40\%$ larger than the determined LO coefficient f. Squaring this gives an estimate of $5 - 15\%$ for NNLO corrections within the range of simulated data. In ref. [3], NNLO simultaneous fits to these ensembles were attempted, with the conclusion that the data does not significantly constrain the fits without the introduction of a strong model dependence.

The analytic ansatz gives a result that is much closer to the known value, only $\sim 5.4\%$ too low, and it appears that the inconsistency only arises after the a^2-extrapolation: at both finite lattice spacings the data extrapolate close to the known value (cf. fig. 8.16). The fact that the analytic ansatz underestimates f_π is interesting, as NLO ChPT predicts that the leading non-analytic behaviour results in a *downwards* shift. It is also interesting that only a small amount of non-linearity is allowed over the leading-order linear behaviour while retaining consistency with the known physical value.

In order to further test the consistency of the ansätze with the known physical value, for each ansatz an artificial data point is generated on both ensemble sets, set to the value of the physical pion decay constant offset by the a^2 coefficients obtained previously. The fits are repeated with fixed lattice spacings and physical quark masses. The aim is to test whether each ansatz can be consistent with both the data and the physical value. The results of this analysis are shown in figure 8.17. It is found that the analytic ansatz could be consistent but the NLO $SU(2)$ ChPT ansatz could not.

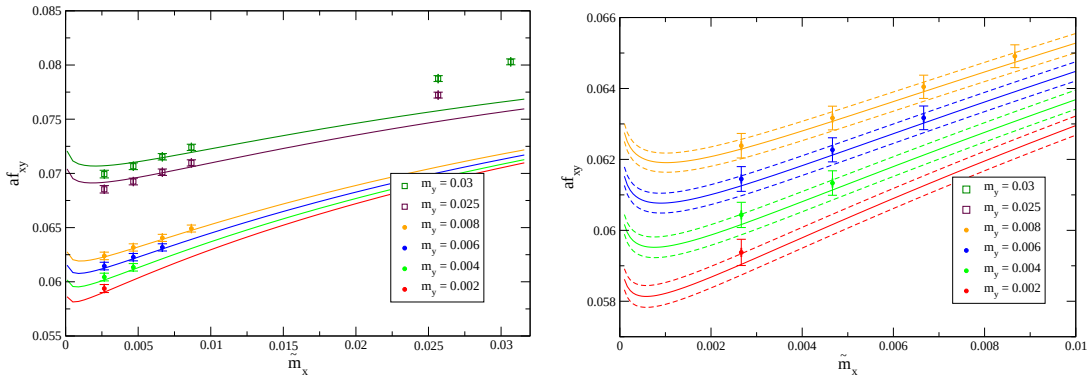

Figure 8.9: Partially-quenched pion decay constant data on the $m_l = 0.004$ ensemble of set **A** overlaid by the results of the global fit using the ChPT ansatz. Points marked by full circles were included in the fit, and those marked with unfilled squares were not. The right panel shows the region containing the fitted data at a smaller scale and includes error bands on the curves.

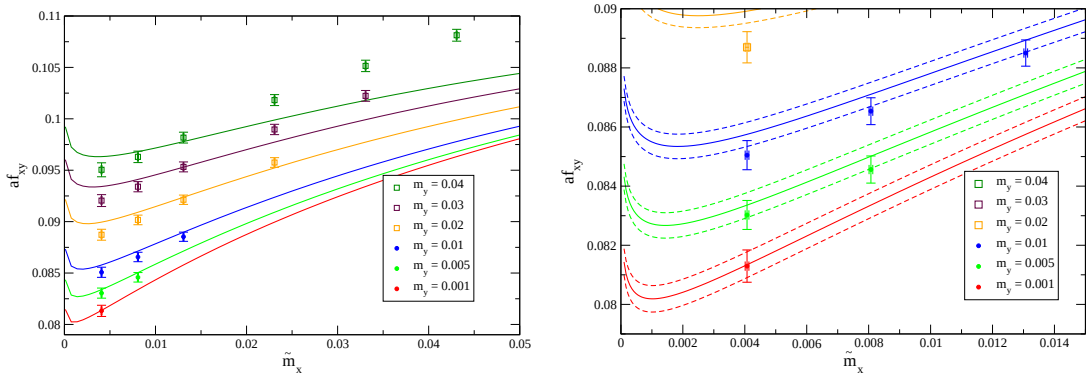

Figure 8.10: Partially-quenched pion decay constant data on the $m_l = 0.005$ ensemble of set **B** overlaid by the results of the global fit using the ChPT ansatz. Points marked by full circles were included in the fit, and those marked with unfilled squares were not. The right panel shows the region containing the fitted data at a smaller scale and includes error bands on the curves.

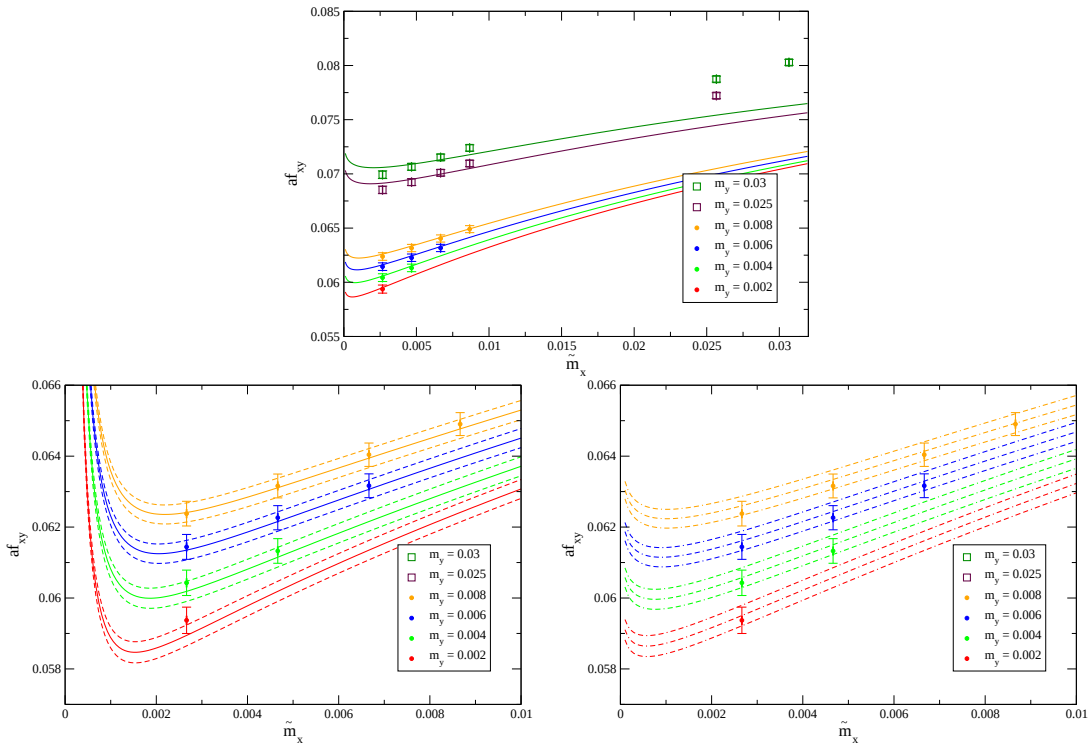

Figure 8.11: Partially-quenched pion decay constant data on the $m_l = 0.004$ ensemble of set **A** overlaid by the results of the global fit using the ChPT-fv ansatz. Points marked by full circles were included in the fit, and those marked with unfilled squares were not. The upper panel shows the data overlaid by the infinite volume fit curves. The lower-left and lower-right panels show the region containing the fitted data at a smaller scale, overlaid by the finite and infinite volume curves respectively.

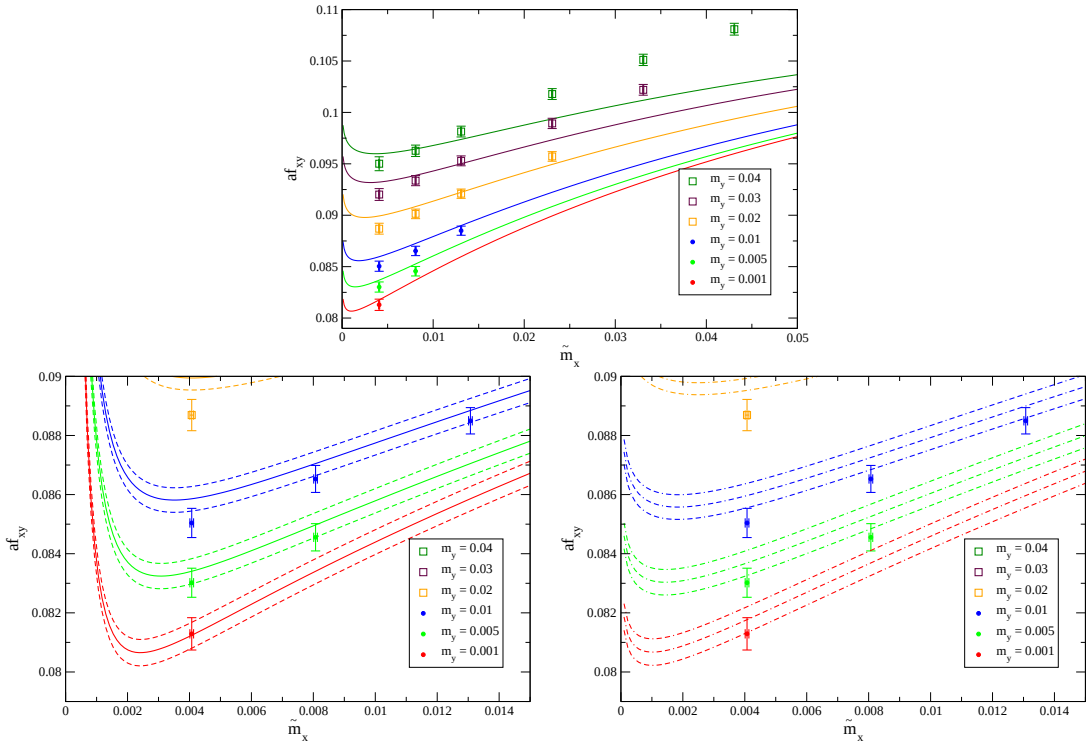

Figure 8.12: Partially-quenched pion decay constant data on the $m_l = 0.005$ ensemble of set **B** overlaid by the results of the global fit using the ChPT-fv ansatz. Points marked by full circles were included in the fit, and those marked with unfilled squares were not. The upper panel shows the data overlaid by the infinite volume fit curves. The lower-left and lower-right panels show the region containing the fitted data at a smaller scale, overlaid by the finite and infinite volume curves respectively.

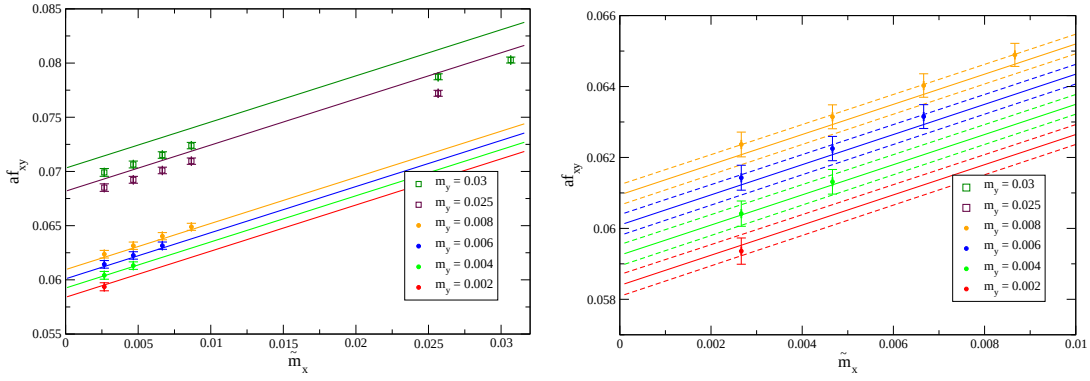

Figure 8.13: Partially-quenched pion decay constant data on the $m_l = 0.004$ ensemble of set **A** overlaid by the results of the global fit using the analytic ansatz. Points marked by full circles were included in the fit, and those marked with unfilled squares were not. The right panel shows the region containing the fitted data at a smaller scale and includes error bands on the curves.

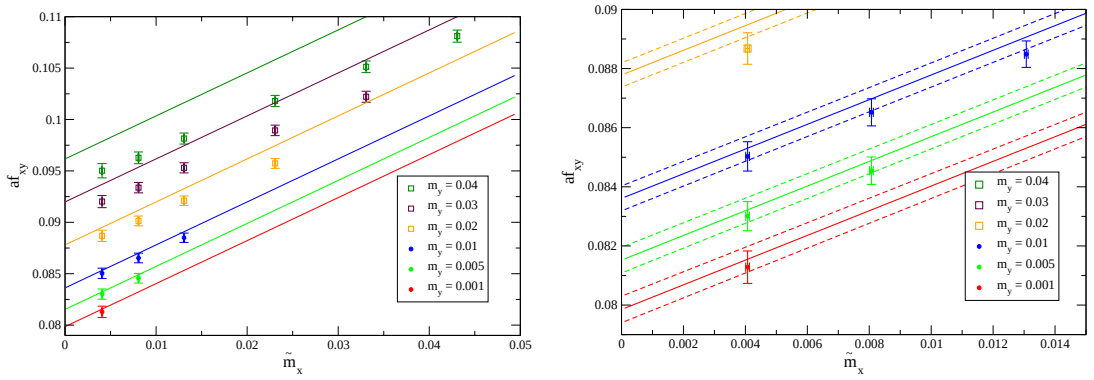

Figure 8.14: Partially-quenched pion decay constant data on the $m_l = 0.005$ ensemble of set **B** overlaid by the results of the global fit using the analytic ansatz. Points marked by full circles were included in the fit, and those marked with unfilled squares were not. The right panel shows the region containing the fitted data at a smaller scale and includes error bands on the curves.

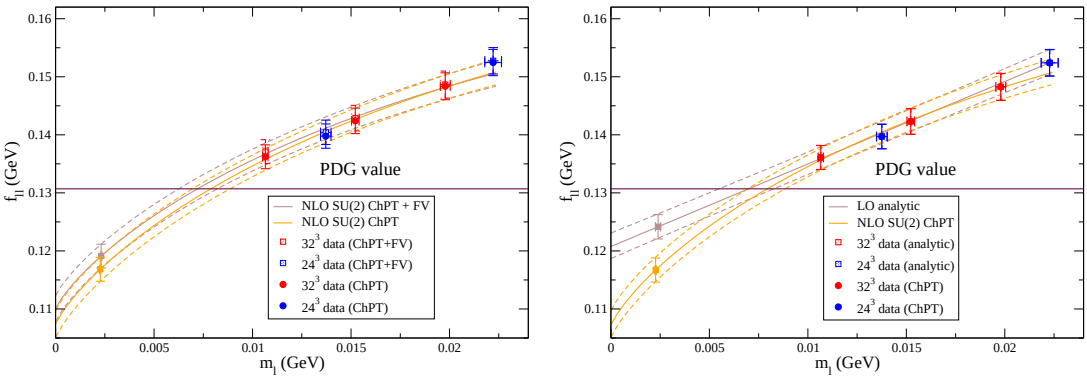

Figure 8.15: Unitary pion decay constant data in physical units on both ensemble sets corrected to the continuum using the a^2 dependence of the fit forms. In the left panel the data is overlaid by the unitary chiral extrapolation curves of the ChPT and ChPT-fv fits. Here the data represented by square points has been corrected to the infinite volume using the results of the ChPT-fv fit and the curve is plotted at infinite volume. The right panel shows a comparison of the chiral extrapolation using the analytic ansatz and the ChPT form.

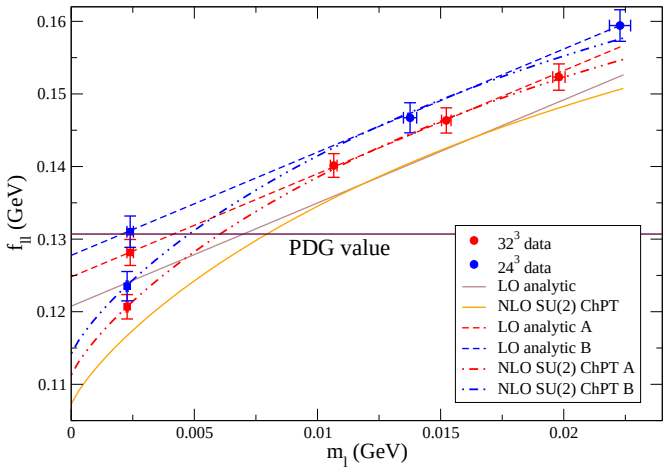

Figure 8.16: Unitary pion decay constant data in physical units on both ensemble sets that is not corrected to the continuum. These are overlaid by the mass dependence at each lattice spacing and in the continuum limit inferred from the ChPT and analytic ansatze.

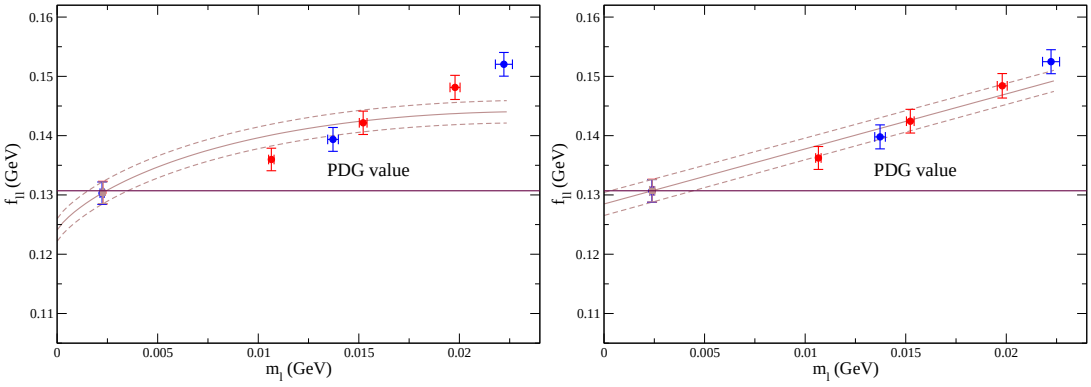

Figure 8.17: Unitary pion decay constant data in physical units on both ensemble sets corrected to the continuum using the a^2 dependence of the fit forms. The data include an artificial data point on each ensemble set that has a value equal to the physical f_π shifted by the a^2-dependence. The data is overlaid by the unitary chiral extrapolation curves of the ChPT fit (left) and the analytic fit (right).

	ChPT	ChPT-fv	Analytic
$f_\pi^{24^3}$	0.123(2)	0.126(2)	0.131(2)
$f_\pi^{32^3}$	0.121(2)	0.123(2)	0.128(2)
$f_\pi^{\text{continuum}}$	0.117(2)	0.119(2)	0.124(2)

Table 8.9: Physical predictions for the pion decay constant f_π in GeV at the simulated lattice spacings and in the continuum limit, obtained from the simultaneous chiral-continuum fits.

	ChPT	ChPT-fv	Analytic
$f_K^{24^3}$	0.150(2)	0.151(2)	0.155(2)
$f_K^{32^3}$	0.147(2)	0.149(2)	0.152(2)
$f_K^{\text{continuum}}$	0.144(2)	0.145(2)	0.149(2)

Table 8.10: Physical predictions for the kaon decay constant f_K in GeV at the simulated lattice spacings and in the continuum limit, obtained from the simultaneous chiral-continuum fits.

	ChPT	ChPT-fv	Analytic
$(f_K/f_\pi)^{24^3}$	1.215(9)	1.204(9)	1.182(9)
$(f_K/f_\pi)^{32^3}$	1.222(6)	1.210(6)	1.188(6)
$(f_K/f_\pi)^{\text{continuum}}$	1.233(8)	1.219(7)	1.196(8)

Table 8.11: Physical predictions for ratio of the kaon and pion decay constants f_K/f_π at the simulated lattice spacings and in the continuum limit, obtained from the simultaneous chiral-continuum fits.

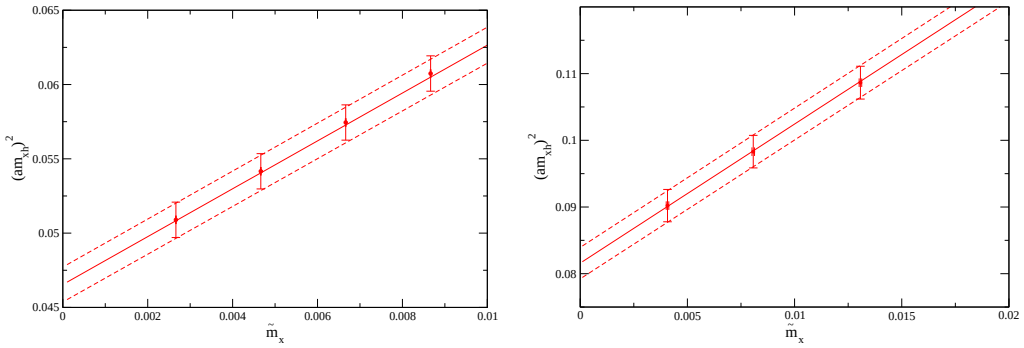

Figure 8.18: Partially-quenched kaon data on the $m_l = 0.004$ ensemble of set **A** (left) and the $m_l = 0.005$ ensemble of set **B** (right). These are overlaid by the results of the global fit using the ChPT ansatz. Points marked by full circles were included in the fit, and those marked with squares were not.

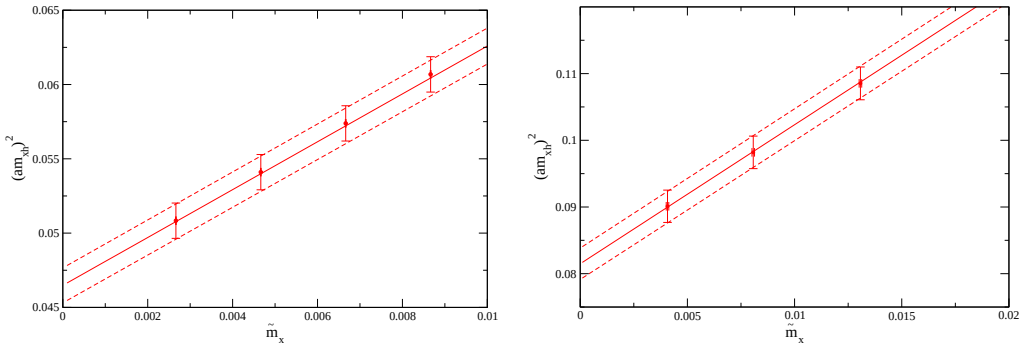

Figure 8.19: Partially-quenched kaon data on the $m_l = 0.004$ ensemble of set **A** (left) and the $m_l = 0.005$ ensemble of set **B** (right). These are overlaid by the results of the global fit using the ChPT-fv ansatz. The kaon ChPT fit form contains no logarithms, thus the infinite volume and finite volume curves are the same. Points marked by full circles were included in the fit, and those marked with squares were not.

Kaon mass

The fit results to the kaon mass are presented as before.

The partially-quenched fit curves for the ChPT and ChPT-fv fits are shown in figures 8.18 and 8.19 respectively, and those of the analytic fit are shown in figure 8.20. Figure 8.21 shows the unitary extrapolation curve overlaying the continuum-corrected data. Here the figures clearly show the extrapolated continuum value being constrained to the physical value, as required by the definition of the scaling curve.

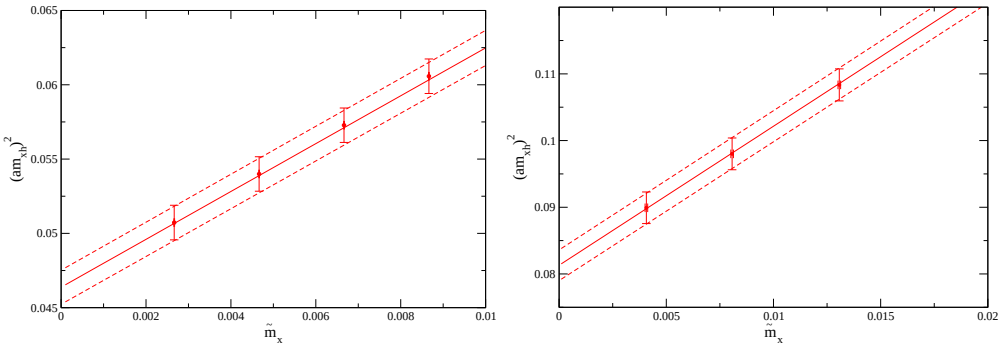

Figure 8.20: Partially-quenched kaon data on the $m_l = 0.004$ ensemble of set **A** (left) and the $m_l = 0.005$ ensemble of set **B** (right). These are overlaid by the results of the global fit using the linear analytic ansatz. Points marked by full circles were included in the fit, and those marked with squares were not.

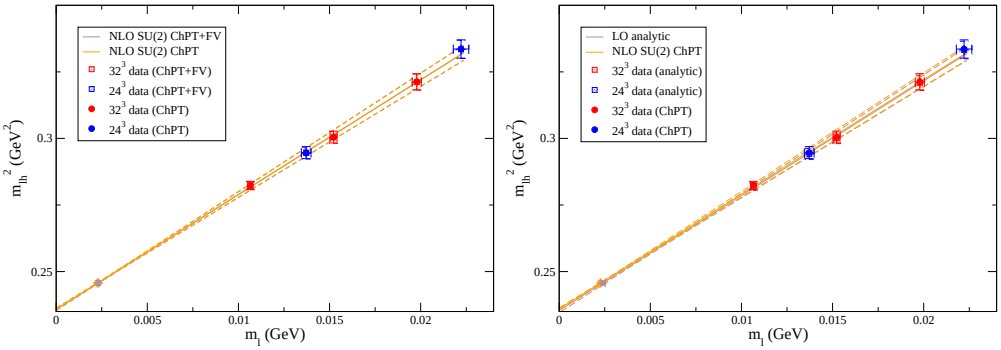

Figure 8.21: Unitary kaon data in physical units on both ensemble sets. In the left panel this is overlaid by the unitary chiral extrapolation curves of the ChPT and ChPT-fv fits. The right panel shows a comparison of the chiral extrapolation using the analytic ansatz and the ChPT form. Here the small differences in the data represented by squared and circled points arise due to the different values of the final lattice spacings.

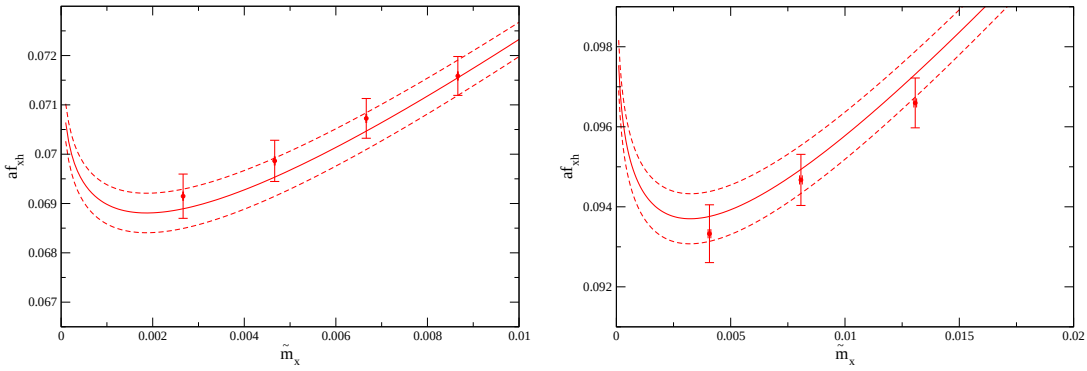

Figure 8.22: Partially-quenched kaon decay constant data on the $m_l = 0.004$ ensemble of set **A** (left) and the $m_l = 0.005$ ensemble of set **B** (right). These are overlaid by the results of the global fit using the ChPT ansatz.

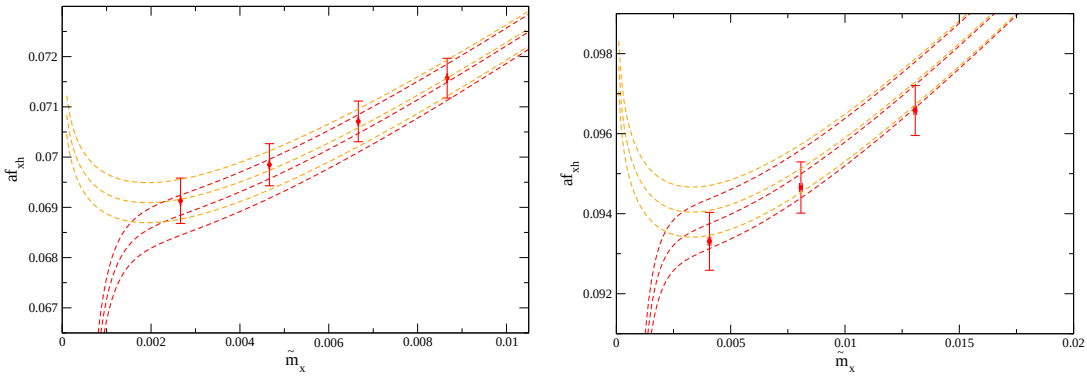

Figure 8.23: Partially-quenched kaon decay constant data on the $m_l = 0.004$ ensemble of set **A** (left) and the $m_l = 0.005$ ensemble of set **B** (right). These are overlaid by the results of the global fit using the ChPT-fv ansatz. Here the red curve shows the fit in the finite volume, and the orange curve shows the fit at infinite volume.

Kaon decay constant

The partially-quenched curves for the fits to the kaon decay constant using the three chiral ansätze are shown in figures 8.22–8.24. As in the case of f_π, data are corrected to the continuum limit using the fit ansätze, and are displayed in figure 8.25 overlaid by the continuum unitary extrapolation. For comparison, the uncorrected data is shown in figure 8.26 alongside the mass dependence at non-zero lattice spacings and in the continuum.

The resulting values of f_K and the ratio of f_K to f_π are given in tables 8.10 and 8.11 respectively. Here the differences between the results for f_K obtained from the ChPT and analytic ansätze are $\sim 3\%$, which is significantly smaller than for f_π.

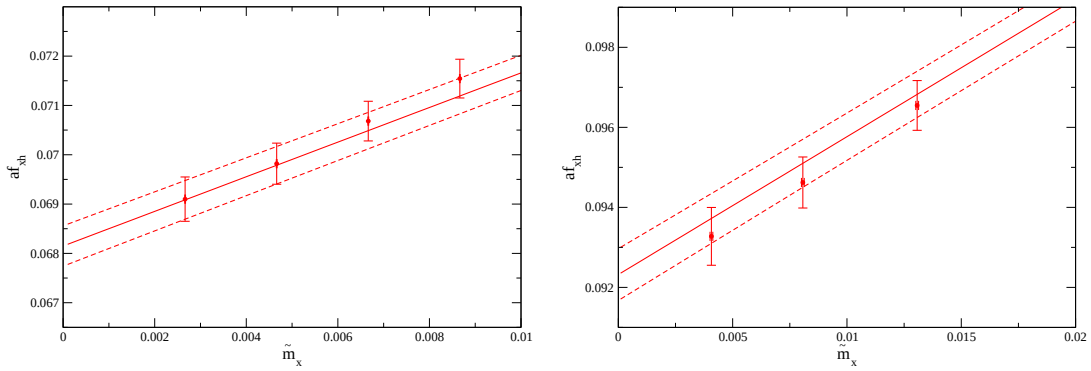

Figure 8.24: Partially-quenched kaon decay constant data on the $m_l = 0.004$ ensemble of set **A** (left) and the $m_l = 0.005$ ensemble of set **B** (right). These are overlaid by the results of the global fit using the linear analytic ansatz.

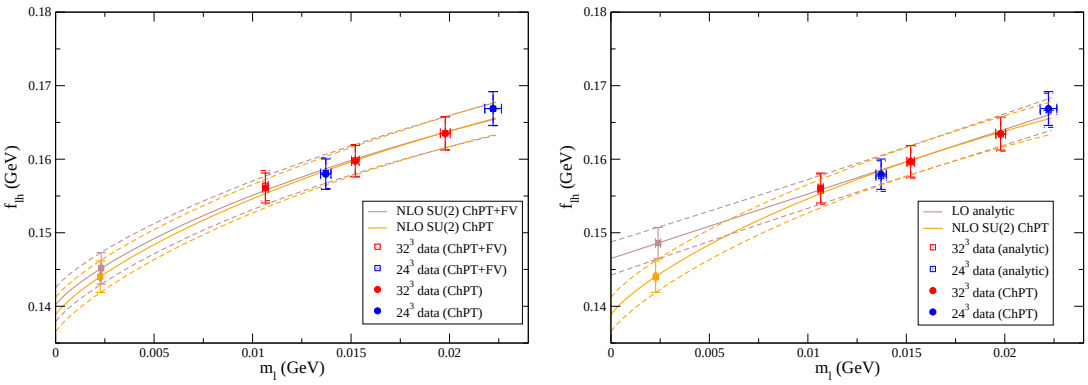

Figure 8.25: Unitary kaon decay constant data in physical units on both ensemble sets corrected to the continuum using the a^2 dependence of the fit forms. In the left panel the data is overlaid by the unitary chiral extrapolation curves of the ChPT and ChPT-fv fits. Here the data represented by square points has been corrected to the infinite volume using the results of the ChPT-fv fit and the curve is plotted at infinite volume. The right panel shows a comparison of the chiral extrapolation using the analytic ansatz and the ChPT form.

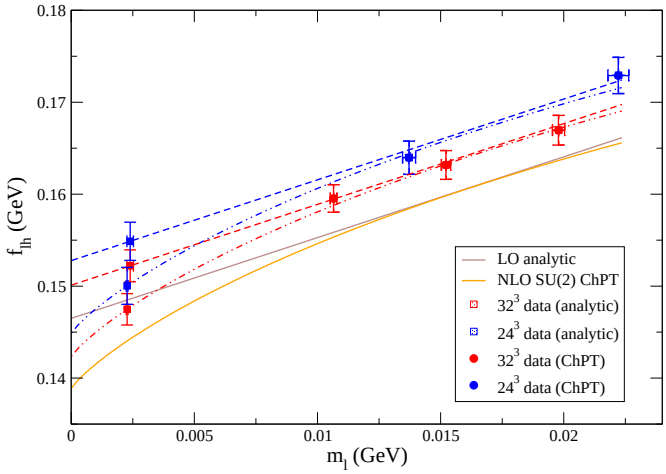

Figure 8.26: Unitary kaon decay constant data in physical units on both ensemble sets that is not corrected to the continuum. These are overlaid by the mass dependence at each lattice spacing and in the continuum limit inferred from the ChPT and analytic ansatze.

Omega baryon mass

The unitary extrapolations of the Ω baryon mass are shown in figure 8.27. The plots are very similar as the fit form is the same for all three ansätze. The small differences arise due to the differing values of the quark masses and lattice spacings. As in the case of the kaon mass, these figures clearly show the extrapolated continuum value being constrained to the physical value.

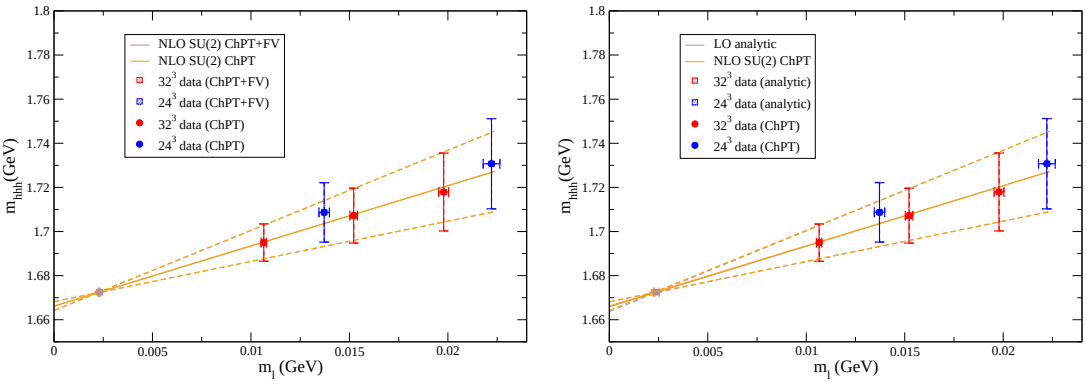

Figure 8.27: Omega baryon data in physical units on both ensemble sets. In the left panel the data is overlaid by the unitary chiral extrapolation curves of the ChPT and ChPT-fv fits, and in the right panel by the ChPT and analytic curves. For all three ansatze the fit form is the same. The small differences arise only due to the differing lattice spacings and quark masses obtained in the analyses.

8.5.2 Predictions

Systematic error estimation

In section 8.5.1 it was shown that the predictions for f_π obtained from the ChPT-fv and analytic results are lower than the known value by approximately 10% and 5% respectively. In the case of the analytic fits, the values at each finite β are statistically consistent with the physical value, whereas this is not true for the ChPT or ChPT-fv fits. In addition, it was shown that the analytic fits could be consistent with the physical point whereas the ChPT fit would fail to fit both the data and the continuum limit. On the other hand the differences between the physical value and the ChPT and ChPT-fv fits is of the order of magnitude expected for NNLO effects.

For quantities such as B_K and the quark masses, the luxury of being able to compare the prediction to the physical value is not available. In light of the discussion above, it is decided to estimate the chiral extrapolation systematic error on these quantities as the difference between the results obtained using the ChPT-fv and analytic ansätze, and to take the central value as the average of the two. The statistical error on the final number is taken from the larger of the statistical errors on the two determinations. An estimate of the finite volume error is obtained from the difference between the ChPT-fv and ChPT results. Although this estimate is not ideal in light of the observed difficulties with the ChPT fits, it is the best that can be achieved without generating additional lattice ensembles. In any case the finite volume error is dwarfed by the systematic error on the chiral extrapolations, hence even a doubling of the finite volume error estimate will not have a significant impact on the total error.

The procedure outlined above allows predictions to be made for these unknown

quantities with a robust systematic error that does not rely on the convergence of $SU(2)$ ChPT in this region of masses. Note that by its nature, the global fit procedure generates strong correlations between output quantities such as the quark masses and lattice spacings. As a result the averaging procedure should only be applied at the last stage of the analysis.

The final values for the lattice spacings are

$$\begin{aligned} a^{-1}(\mathbf{A}\ ) &= 2.285(29)_{\rm stat}(1)_{\rm FV}\,{\rm GeV}\,, \\ a^{-1}(\mathbf{B}\ ) &= 1.733(25)_{\rm stat}(1)_{\rm FV}\,{\rm GeV}\,, \end{aligned} \tag{8.34}$$

where the errors are statistical and finite-volume respectively. The remaining predictions of the analysis are presented in the following sections.

Pseudoscalar decay constants

The predictions for f_π, f_K and the ratio f_K/f_π for each chiral ansatz are given in tables 8.9, 8.10 and 8.11 respectively. Using the procedure outlined above, the following predictions are obtained:

$$f\pi = 122(2)_{\rm stat}(5)_\chi(2)_{\rm FV}\,{\rm MeV} \tag{8.35}$$

$$f_K = 147(2)_{\rm stat}(4)_\chi(1)_{\rm FV}\,{\rm MeV} \tag{8.36}$$

$$f_K/f_\pi = 1.208(8)_{\rm stat}(23)_\chi(14)_{\rm FV}\,. \tag{8.37}$$

Quark masses in the $\overline{\rm MS}$-scheme

The physical quark masses in the $\overline{\rm MS}$-scheme are obtained by renormalising the results given in table 8.8. The global fit produces quark masses that are already renormalised in the mass-dependent *matching scheme*, which are related to the bare quark masses $m^{\mathbf{e}}$ as

$$m^{{\rm match},\mathbf{e}} = Z_m^{{\rm match},\mathbf{e}}(m^{\mathbf{e}}) \times m^{\mathbf{e}} \tag{8.38}$$

on the ensemble $\mathbf{e}$. As explained in section 8.2.1, the renormalisation coefficients are constant within the ranges of 'light' and 'heavy' quark masses to a good approximation. Consequently, the following values are taken:

$$\begin{aligned} Z_{m_l}^{{\rm match},\mathbf{A}} &= 1\,, \\ Z_{m_h}^{{\rm match},\mathbf{A}} &= 1\,, \\ Z_{m_l}^{{\rm match},\mathbf{B}} &= Z_l\,, \\ Z_{m_h}^{{\rm match},\mathbf{B}} &= Z_h\,. \end{aligned} \tag{8.39}$$

The mass-independent non-perturbative renormalisation coefficients $Z_m^{\overline{\rm MS},\mathbf{e}}$, ob-

tained in chapter 7, relate bare quark masses to their values in the $\overline{\text{MS}}$ scheme at 2 GeV according to the relation

$$m^{\overline{\text{MS}},\mathbf{e}} = Z_m^{\overline{\text{MS}},\mathbf{e}} \times m^{\mathbf{e}} \,. \tag{8.40}$$

Combining this with eqn. 8.38 gives

$$m_f^{\overline{\text{MS}},\mathbf{e}} = Z_m^{\overline{\text{MS}},\mathbf{e}} \left(\frac{m_f^{\text{match},\mathbf{e}}}{Z_{m_f}^{\text{match},\mathbf{e}}} \right) , \tag{8.41}$$

where $f \in \{l, h\}$. The conversion factor relating the matching scheme to the $\overline{\text{MS}}$ scheme is henceforth denoted as

$$\hat{Z}_{m_f}^{\mathbf{e}} \equiv \frac{Z_m^{\overline{\text{MS}},\mathbf{e}}}{Z_{m_f}^{\text{match},\mathbf{e}}} \,. \tag{8.42}$$

The factor relating the *physical* quark masses in the matching scheme to those in the $\overline{\text{MS}}$ scheme is obtained by extrapolating $\hat{Z}_{m_f}^{\mathbf{e}}$ to the continuum limit. This is performed with a linear ansatz,

$$\hat{Z}_{m_f}^{\mathbf{e}} = \hat{Z}_{m_f}^{\text{cont.}} + B(a_0^{\mathbf{e}})^2 \,. \tag{8.43}$$

In section 7.5 it was shown that the renormalisation coefficients determined from the two schemes differ quite considerably due to the presence of several systematic error sources. When performing the continuum extrapolation, it is important to separate out the sources of error that are correlated between the two ensemble sets, as a naive uncorrelated treatment of these errors leads to the incorrect inflation of the error on the extrapolated result. The following systematic errors fall into this category:

1. The error associated with the truncation of the perturbative expansion.
2. The SSB error associated with the residual chiral symmetry breaking.
3. The m_s error associated with the treatment of data near the physical strange sea quark as mass independent.
4. The a error associated with the lattice spacing determination. The lattice spacings are correlated because their ratio is fixed to R_a.

These errors are applied only after the continuum limit has been taken. The best estimate of the magnitude of each error on the continuum quantities is taken from the finest ensemble set, **A**. The statistical and 'spread' errors on the renormalisation coefficients must be included in the continuum extrapolation, but should be kept separate from the uncorrelated statistical errors on the matching factors Z_l and Z_h. This is achieved by combining these errors in quadrature and placing them on a fictitious

ensemble in the superjackknife distribution that is orthogonal to those of the matching factors.

Up to the error already included in the renormalisation coefficients, $\hat{Z}^{\text{cont.}}_{m_f}$ is independent of the chiral ansatz used in the determination of the lattice spacings. To see this, consider two determinations of the lattice spacing on the **B** ensembles, $a_0^{\mathbf{B}}$ and $a_1^{\mathbf{B}}$. The mass renormalisation on the **B** ensembles can then be written

$$\hat{Z}^{\mathbf{B}}_{m_f} = \hat{Z}^{\text{cont.}}_{m_f,0} + B_0(a_0^{\mathbf{B}})^2 = \hat{Z}^{\text{cont.}}_{m_f,1} + B_1(a_1^{\mathbf{B}})^2\,, \tag{8.44}$$

where the subscript $i \in \{0,1\}$ indexes the chiral ansatz. The gradient of the fit has the value

$$B_i = \frac{(\hat{Z}^{\mathbf{B}}_{m_f} - \hat{Z}^{\mathbf{A}}_{m_f})}{(a_i^{\mathbf{B}})^2 - (a_i^{\mathbf{A}})^2} = \frac{(\hat{Z}^{\mathbf{B}}_{m_f} - \hat{Z}^{\mathbf{A}}_{m_f})}{(1-R_a^2)(a_i^{\mathbf{B}})^2}\,, \tag{8.45}$$

which when multiplied by $(a_i^{\mathbf{B}})^2$ is independent of i. Inserting this into eqn. 8.44 gives $\hat{Z}^{\text{cont.}}_{m_f,0} = \hat{Z}^{\text{cont.}}_{m_f,1}$. As a result, no further error associated with the lattice spacing need be applied.

The values of $\hat{Z}_{m_f}$ on each ensemble are given in table 8.12, and the continuum extrapolations are shown in figure 8.28.

As discussed in section 7.5, the magnitude of the truncation error cannot be estimated at finite lattice spacing due to the presence of discretisation errors. Instead a slope error is obtained that is only proportional to the truncation error. Now the continuum limit has been taken, an estimate of the truncation error can be determined as follows. The slope error, along with the other systematic errors, is added in quadrature to the statistical and spread error on $Z^{\text{cont.}}_{m_f}$. Then, for each mass type $m_f \in \{m_l, m_h\}$, a fit to a constant is performed over $Z^{\text{cont.}}_{m_f}(\text{SMOM}_{\gamma_\mu})$ and $Z^{\text{cont.}}_{m_f}(\text{SMOM}_{\not{q}})$. The total errors are then inflated by a PDG scale factor obtained from the square-root of the χ^2/d.o.f of this fit, ensuring that the two schemes are consistent. Surprisingly the χ^2/d.o.f are close to unity,

$$\begin{aligned} \chi^2/\text{d.o.f}(\hat{Z}_{m_l}) &= 1.102\,, \text{ and} \\ \chi^2/\text{d.o.f}(\hat{Z}_{m_h}) &= 1.363\,, \end{aligned} \tag{8.46}$$

which indicates that the error obtained by including the slope error is actually a reasonable estimate of the total error. The truncation error is isolated by removing

Scheme	$\hat{Z}^{\mathbf{A}}_{m_l}$	$\hat{Z}^{\mathbf{A}}_{m_h}$	$\hat{Z}^{\mathbf{B}}_{m_l}$	$\hat{Z}^{\mathbf{B}}_{m_h}$
SMOM_{γ_μ}	1.599(5)	1.599(5)	1.617(15)	1.629(12)
$\text{SMOM}_{\not{q}}$	1.539(8)	1.539(8)	1.546(17)	1.557(15)

Table 8.12: The conversion factor relating the matching scheme quark masses to $\overline{\text{MS}}$ via the intermediate lattice scheme given in the first column. Here the errors comprise the statistical errors on $Z_m^{\overline{\text{MS}}}$ and Z_f and the 'spread' errors associated with the $O(4)$ symmetry breaking effects.

the known sources of error. This gives

$$\begin{aligned} Z^{\text{cont.}}_{m_l}(\text{SMOM}_{\gamma_\mu}) &= 1.574(23)_{\text{stat+spread}}(10)_{\text{trunc}}(10)_{\text{other sys}} \\ Z^{\text{cont.}}_{m_h}(\text{SMOM}_{\gamma_\mu}) &= 1.558(19)_{\text{stat+spread}}(14)_{\text{trunc}}(9)_{\text{other sys}} \\ Z^{\text{cont.}}_{m_l}(\text{SMOM}_{\not{q}}) &= 1.531(31)_{\text{stat+spread}}(15)_{\text{trunc}}(10)_{\text{other sys}} \\ Z^{\text{cont.}}_{m_h}(\text{SMOM}_{\not{q}}) &= 1.515(28)_{\text{stat+spread}}(22)_{\text{trunc}}(10)_{\text{other sys}} . \end{aligned} \tag{8.47}$$

The largest of these errors is still somewhat small, at around $\sim 1.5\%$. Given that only two schemes are available, a more conservative estimate of 4.7% is obtained from the relative magnitude of the 1-loop corrections. As discussed in section 7.5, this is taken for the final value.

Due to the scatter of points in the $\text{SMOM}_{\not{q}}$ scheme (fig. 7.6), the determination of $Z^{\text{cont.}}_{m_f}$ with the SMOM_{γ_μ} intermediate scheme is deemed more reliable, and is therefore used as the final value:

$$\begin{aligned} Z^{\text{cont.}}_{m_l} &= 1.574(23)_{\text{stat+spread}}(74)_{\text{trunc}}(10)_{\text{other sys}} , \\ Z^{\text{cont.}}_{m_h} &= 1.558(19)_{\text{stat+spread}}(73)_{\text{trunc}}(9)_{\text{other sys}} , \end{aligned} \tag{8.48}$$

for which the total errors are $\sim 5\%$.

For each of the chiral ansätze, the renormalisation coefficients are applied to the quark masses (table 8.8), and the results are listed in table 8.13. Taking the quark masses from the average of the analytic and NLO-fv results as before, the renormalised physical quark masses in the $\overline{\text{MS}}$ scheme at 2 GeV are obtained:

$$\begin{aligned} m_{u/d}(\overline{\text{MS}}, 2\,\text{GeV}) &= 3.71(21)_{\text{stat+spread}}(7)_{\text{FV}}(17)_{\text{trunc}}(2)_{\text{other sys}}\,\text{MeV} , \\ m_s(\overline{\text{MS}}, 2\,\text{GeV}) &= 98.9(1.8)_{\text{stat+spread}}(0.1)_{\text{FV}}(4.6)_{\text{trunc}}(0.6)_{\text{other sys}}\,\text{MeV} . \end{aligned} \tag{8.49}$$

	Analytic	ChPT	ChPT-fv
$m_{u/d}$	3.77(21) MeV	3.57(8) MeV	3.64(8) MeV
m_s	98.8(2) MeV	99.0(2) MeV	98.9(2) MeV

Table 8.13: Physical quark masses in the $\overline{\text{MS}}$ scheme at 2 GeV obtained for each of the chiral ansatz. Here the errors comprise the statistical and 'spread' errors.

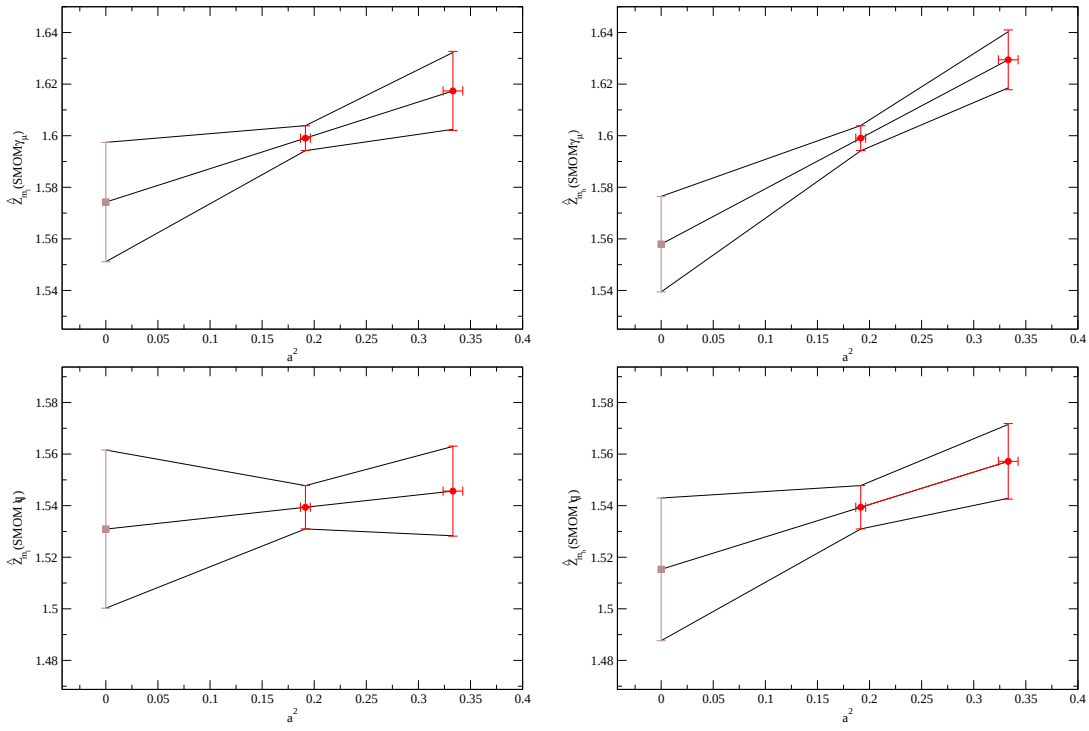

Figure 8.28: The continuum extrapolation of $\hat{Z}_{m_f}$. The upper panels show the extrapolation of $\hat{Z}_{m_l}$ (top-left) and $\hat{Z}_{m_h}$ (top-right) with the SMOM$_{\gamma_\mu}$ intermediate scheme, and the lower panels show the same for the SMOM$_{\not{q}}$ intermediate scheme.

(a) r_0

Parameter	ChPT	ChPT-fv	Analytic
c_{r_0}	2.465(42) GeV^{-1}	2.464(42) GeV^{-1}	2.463(42) GeV^{-1}
$c_{r_0,a}$	-0.26(14) GeV	-0.26(14) GeV	-0.26(14) GeV
c_{r_0,m_l}	0.50(1.25) GeV^{-2}	0.52(1.25) GeV^{-2}	0.55(1.25) GeV^{-2}

(b) r_1

Parameter	ChPT	ChPT-fv	Analytic
c_{r_1}	1.692(30) GeV^{-1}	1.691(30) GeV^{-1}	1.690(30) GeV^{-1}
$c_{r_1,a}$	-0.15(12) GeV	-0.15(12) GeV	-0.15(12) GeV
c_{r_1,m_l}	-1.75(64) GeV^{-2}	-1.75(64) GeV^{-2}	-1.75(64) GeV^{-2}

Table 8.14: Parameters of the chiral/continuum fits to r_0 and r_1.

Quantity	ChPT	ChPT-fv	Analytic
r_0	1.29(1.62)	1.27(1.60)	1.25(1.60)
r_1	2.64(2.33)	2.63(2.33)	2.61(2.31)

Table 8.15: χ^2/d.o.f of the chiral/continuum fits to r_0 and r_1.

8.6 Continuum results for r_0 and r_1

The scales r_0 and r_1 were calculated on the **A** and **B** ensembles in section 6.7. In this section the chiral/continuum fit procedure is applied to these quantities.

Assuming a linear dependence on the light sea-quark mass and including a leading order a^2 term, the scales are independently fit to the form

$$r_i = c_{r_i} + c_{r_i,a}a^2 + c_{r_i,m_l}\tilde{m}_l \,, \tag{8.50}$$

where $i = 0, 1$. Prior to the fit, the data are linearly interpolated to each of the physical strange quark masses obtained from the global fits in section 8.5.1, and the fit and the subsequent extrapolation are performed using the corresponding light quark mass and lattice spacings.

The parameters and χ^2/d.o.f of the fits are given in table 8.14 and table 8.15 respectively, and plots of the data, both corrected and uncorrected to the continuum limit, overlaid by the three chiral extrapolations, are given in figures 8.29 and 8.30.

The fits to r_0 appear to describe the data well by eye, and have a reasonable (uncorrelated) χ^2/d.o.f for the central value but with a large deviation across the superjackknife distribution. The fits to r_1 also appear to describe the data reasonably well, although there does seem to be a tension with the heaviest point on the **B** ensembles, which is likely responsible for the larger χ^2/d.o.f. As there are only five data points it is difficult to reach any stronger conclusions regarding the data:

Quantity	ChPT	ChPT-fv	Analytic
r_0	2.466(41) GeV^{-1}	2.465(41) GeV^{-1}	2.464(41) GeV^{-1}
r_1	1.688(30) GeV^{-1}	1.687(30) GeV^{-1}	1.686(30) GeV^{-1}
r_1/r_0	0.6844(98)	0.6844(98)	0.6843(98)

Table 8.16: Continuum values of r_0 and r_1 and the ratio r_1/r_0 obtained from a chiral/continuum fit using the lattice spacings and quark masses obtained from the global fits.

more ensembles and better statistics are needed. For the purposes of quoting a final result, a PDG scale factor of $\sqrt{\chi^2/\text{d.o.f}}$ is applied to the statistical errors on each of the results. In order to retain the correlations between these quantities when the ratio is taken, the scale factor is applied to the difference of each jackknife sample from the mean.

The results for the continuum extrapolations are given in table 8.16. Using the procedure for combining the data outlined in section 8.5.2 and applying the PDG scale factor as above, gives:

$$\begin{aligned} r_0 &= 2.465(47)_{\text{stat}}(1)_{\chi}(1)_{\text{FV}}\,\text{GeV}^{-1} = 0.4864(81)_{\text{stat}}(2)_{\chi}(2)_{\text{FV}}\,\text{fm}\,, \\ r_1 &= 1.688(49)_{\text{stat}}(1)_{\chi}(1)_{\text{FV}}\,\text{GeV}^{-1} = 0.3331(59)_{\text{stat}}(2)_{\chi}(2)_{\text{FV}}\,\text{fm}\,, \text{ and} \\ r_1/r_0 &= 0.684(15)_{\text{stat}}(1)_{\chi}(0)_{\text{FV}}\,, \end{aligned} \tag{8.51}$$

where the finite volume error arising from the different determinations of the lattice spacings and quark masses is smaller than the quoted precision on the ratio.

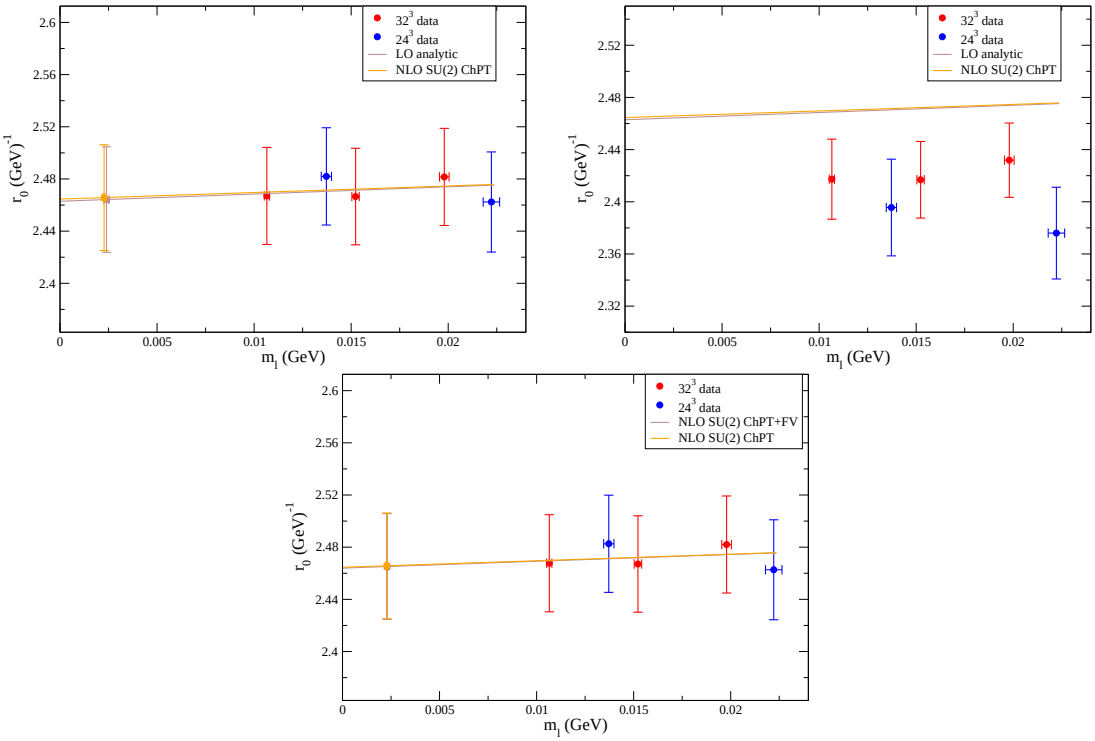

Figure 8.29: The Sommer scale r_0 overlaid by the chiral fits to the continuum data. The upper panels show the data both corrected to the continuum limit (top-left) and uncorrected (top-right), overlaid by the ChPT and analytic chiral fits. The lower panel shows the corrected data overlaid by the ChPT-fv and ChPT chiral fits. Note that the fit forms for all three ansätze are the same, it is only the values of the lattice spacings and quark masses that differ.

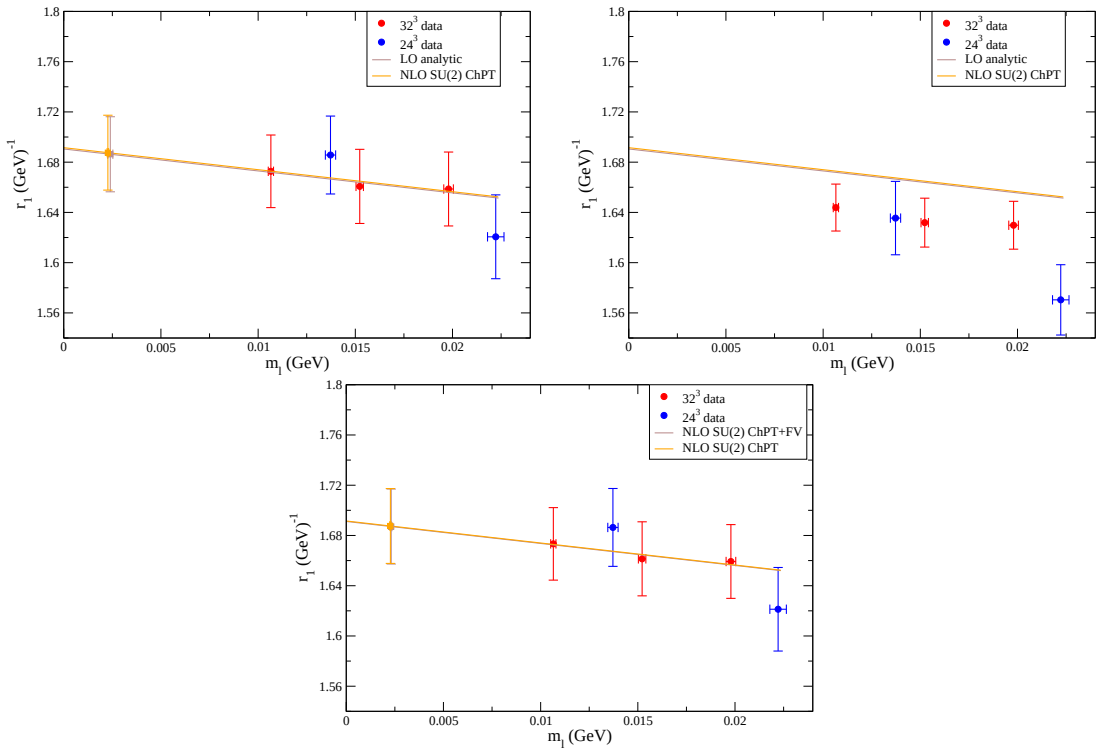

Figure 8.30: The scale r_1 overlaid by the chiral fits to the continuum data. The upper panels show the data both corrected to the continuum limit (top-left) and uncorrected (top-right), overlaid by the ChPT and analytic chiral fits. The lower panel shows the corrected data overlaid by the ChPT-fv and ChPT chiral fits. Note that the fit forms for all three ansätze are the same, it is only the values of the lattice spacings and quark masses that differ.

8.7 Continuum results for B_K

The combined chiral/continuum extrapolation of B_K is also performed separately from the main body of the analysis. As before, the fit is performed using the ChPT, ChPT-fv and analytic ansätze, allowing for an estimate of the error on the chiral extrapolation to be obtained according to the procedure discussed in section 8.5.2. For each chiral ansatz, the lattice spacings and physical quark masses are fixed to those obtained from the corresponding analysis in section 8.5.1. For the ChPT and ChPT-fv ansätze, the LO LECs B and f are also fixed to those in table 8.5 in order to improve the quality of the fit. This follows the strategy employed in the analysis of B_K on the **B** ensembles (ref. [128]).

8.7.1 Renormalisation

As B_K is a renormalisation scheme dependent quantity, the fits must be performed to renormalised data. Unlike the quark masses, B_K is not defined to scale perfectly along the scaling curve, therefore one cannot renormalise into an intermediate matching scheme in which the ratio $B_K^{\mathbf{A}}/B_K^{\mathbf{B}}$ at a chosen match point renormalises the data on the **B** ensembles. Instead the data are renormalised using the non-perturbative renormalisation coefficients Z_{B_K} in the NDR scheme at 2 GeV that were determined in section 7.4.

As in the section 8.5.2, the systematic errors that are correlated between the two ensembles are applied only after the continuum limit is taken, in order to avoid double-counting. The statistical and spread error are again included on a fictitious ensemble in the superjackknife distribution in order to keep them separate from the errors on the data.

8.7.2 Fit strategy

For a given scheme and chiral ansatz, the chiral/continuum fit procedure is as follows. The data on each ensemble set are first renormalised into the chosen scheme by applying the corresponding renormalisation coefficient, with the associated errors treated as above. The data are then reweighted such that the valence and sea strange quark masses are equal, and interpolated to the physical strange quark masses determined from the global fit with the chiral ansatz in question. The fit is then performed, and the physical result is determined. The slope, a, $V-A$ and m_s errors are then applied in quadrature to obtain a final value for that scheme and chiral ansatz. Finally, the results are combined using a similar procedure to that used in section 8.5.2. This is discussed in more detail in section 8.7.4.

Type	RIMOM	SMOM($\gamma^\mu, \not{q}$)	SMOM(γ^μ, γ^μ)	SMOM($\not{q}, \not{q}$)	SMOM($\not{q}, \gamma^\mu$)
ChPT	0.57(37)	0.18(13)	0.55(36)	0.47(32)	0.24(17)
ChPT-fv	1.09(42)	0.37(15)	1.07(42)	0.92(36)	0.49(19)
Analytic	0.17(36)	0.06(12)	0.17(35)	0.15(31)	0.07(15)

Table 8.17: χ^2/d.o.f. for the global fits to B_K.

The chiral/continuum fit form for the ChPT ansatz is

$$B_K^{xh} = B_K^0 \Big[1 + c_a a^2 + \frac{c_0 \chi_l}{f^2} + \frac{\chi_x c_1}{f^2} - \frac{\chi_l}{32\pi^2 f^2} \log\left(\frac{\chi_x}{\Lambda_\chi^2}\right) \Big] , \tag{8.52}$$

and for the analytic ansatz is

$$\begin{aligned} B_K &= c_0(1 + c_a a^2) + c_l(\tilde{m}_l - \tilde{m}^m) + c_v(\tilde{m}_x - \tilde{m}^m) \\ &\equiv c_0(1 + c_a a^2) + c_l \tilde{m}_l + c_v \tilde{m}_x \,. \end{aligned} \tag{8.53}$$

The ChPT-fv form is obtained by applying the rules for associating Bessel function corrections to a particular chiral logarithm given in the appendix of ref. [1]. The result is

$$B_K^{xh} = B_K^0 \Big[1 + c_a a^2 + \frac{c_0 \chi_l}{f^2} + \frac{\chi_x c_1}{f^2} - \frac{\chi_l}{32\pi^2 f^2} \left\{ \log\left(\frac{\chi_x}{\Lambda_\chi^2}\right) + \delta_1\left(aL\sqrt{\chi_x}\right) \right\} \Big] , \tag{8.54}$$

where

$$\delta_1(x) = \frac{4}{x} \sum_{\vec{r} \neq \vec{0}} \frac{K_1(|\vec{r}|x)}{|\vec{r}|} \,. \tag{8.55}$$

Here K_1 is a modified Bessel function of the second kind. As discussed in ref. [1], the value of δ_1 is obtained by summing over lattice vectors $\vec{r}$ of increasing size until the changes in the sum become negligable.

8.7.3 Results

The results of the reweight/interpolation of the data on both ensemble sets to the physical strange quark mass obtained from the analytic fits are given in tables 6.24 and 6.26. The data at the physical strange quark mass obtained from the other two ansätze are essentially the same as the there is only a small difference between the masses (cf. table 8.7). Of course the fit is performed using the correct strange quark mass for each chiral ansatz.

The fit coefficients obtained from the global fits for each chiral ansatz and renormalisation scheme are given in tables 8.18–8.20, and the χ^2/d.o.f. are given in table 8.17.

Parameter	RIMOM	SMOM($\gamma^\mu, \not{q}$)	SMOM(γ^μ, γ^μ)	SMOM($\not{q}, \not{q}$)	SMOM($\not{q}, \gamma^\mu$)
B_K^0	0.518(5)	0.544(14)	0.516(5)	0.531(6)	0.502(11)
c_a	-0.00(4) GeV^2	0.1(1) GeV^2	0.02(4) GeV^2	0.07(4) GeV^2	-0.04(9) GeV^2
c_0	-0.0060(7)	-0.0063(9)	-0.0060(8)	-0.0061(8)	-0.0062(9)
c_1	0.0060(3)	0.0063(4)	0.0060(3)	0.0061(3)	0.0062(3)

Table 8.18: Global fit parameters for B_K using the ChPT ansatz.

Parameter	RIMOM	SMOM($\gamma^\mu, \not{q}$)	SMOM(γ^μ, γ^μ)	SMOM($\not{q}, \not{q}$)	SMOM($\not{q}, \gamma^\mu$)
B_K^0	0.516(5)	0.540(14)	0.514(5)	0.528(6)	0.499(11)
c_a	-0.01(4) GeV^2	0.1(1) GeV^2	0.01(4) GeV^2	0.06(5) GeV^2	-0.05(9) GeV^2
c_0	-0.0062(8)	-0.0066(9)	-0.0062(8)	-0.0063(8)	-0.0064(9)
c_1	0.0070(3)	0.0076(4)	0.0070(3)	0.0071(4)	0.0074(4)

Table 8.19: Global fit parameters for B_K using the ChPT-fv ansatz.

Figures 8.31, 8.32 and 8.33 show the fit on both ensemble sets for each of the three ansätze in the SMOM($\not{q}, \not{q}$) scheme. This is the scheme that is chosen for the central value of the final result in section 8.7.5. One notable feature is the tension between ChPT fit and the data at the lightest points on the $m_l = 0.006$ ensemble of set **A** and the $m_l = 0.01$ ensemble of set **B** in figure 8.31. The analytic fits again appear to describe the data very well, and there is no evidence for chiral curvature.

Figure 8.34 shows a comparison of the chiral extrapolations in the continuum limit obtained using all three chiral ansätze, and figure 8.35 shows the data at finite β for comparison. Again these are for the data renormalised into the SMOM($\not{q}, \not{q}$) scheme. It is clear that the difference between the ChPT and analytic ansätze is considerably smaller than for the decay constants, at around 3%.

The results for the global fits using all five schemes and all three chiral ansätze are given in table 8.21. These results include the a, $V-A$, m_s and slope systematic errors.

Parameter	RIMOM	SMOM($\gamma^\mu, \not{q}$)	SMOM(γ^μ, γ^μ)	SMOM($\not{q}, \not{q}$)	SMOM($\not{q}, \gamma^\mu$)
c_0	0.539(6)	0.565(15)	0.537(6)	0.552(7)	0.522(11)
c_a	-0.00(4) GeV^2	0.13(10) GeV^2	0.02(4) GeV^2	0.07(4) GeV^2	-0.03(8) GeV^2
c_l	0.2(3) GeV^{-1}	0.3(3) GeV^{-1}	0.2(3) GeV^{-1}	0.2(3) GeV^{-1}	0.3(3) GeV^{-1}
c_v	0.8(1) GeV^{-1}	0.9(1) GeV^{-1}	0.9(1) GeV^{-1}	0.9(1) GeV^{-1}	0.8(1) GeV^{-1}

Table 8.20: Global fit parameters for B_K using the analytic ansatz.

Type	RIMOM	SMOM($\gamma^\mu, \not{q}$)	SMOM(γ^μ, γ^μ)	SMOM($\not{q}, \not{q}$)	SMOM($\not{q}, \gamma^\mu$)
ChPT	0.529(5)(9)	0.555(14)(13)	0.527(5)(8)	0.541(6)(2)	0.512(11)(19)
ChPT-fv	0.526(5)(9)	0.552(14)(13)	0.524(5)(8)	0.539(6)(2)	0.509(11)(19)
Analytic	0.542(5)(9)	0.568(14)(13)	0.540(5)(8)	0.555(7)(2)	0.524(11)(19)

Table 8.21: Continuum values for $B_K(\overline{\text{MS}}, 2\text{ GeV})$ obtained using three chiral ansätze and five non-perturbative renormalisation schemes. Here the first error contains the statistical error on the B_K data and the renormalisation coefficients, and also the spread error associated with the breaking of the $O(4)$-symmetry under discretisation. The second is the systematic error associated with the a, $V-A$, m_s and *slope* error sources.

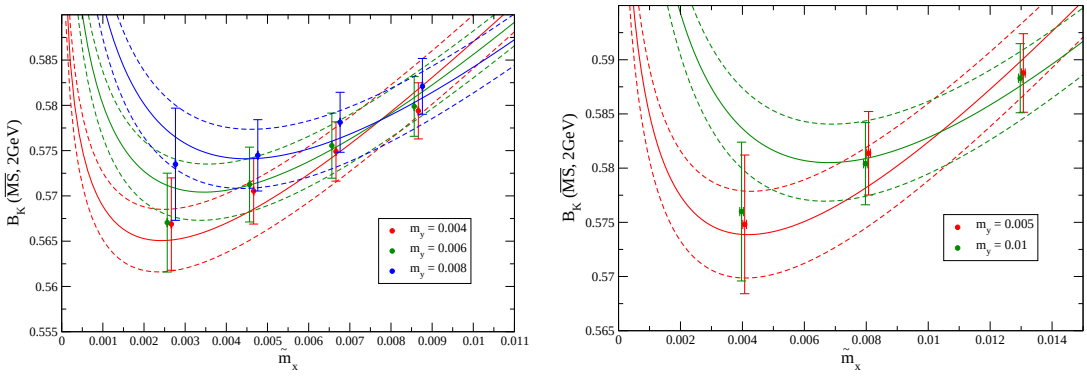

Figure 8.31: Partially-quenched B_K data in the SMOM($\not{q}, \not{q}$) scheme for all ensembles of set **A** (left) and **B** (right). These are overlaid by the results of the global fit using the ChPT ansatz. The datasets have been shifted slightly for clarity.

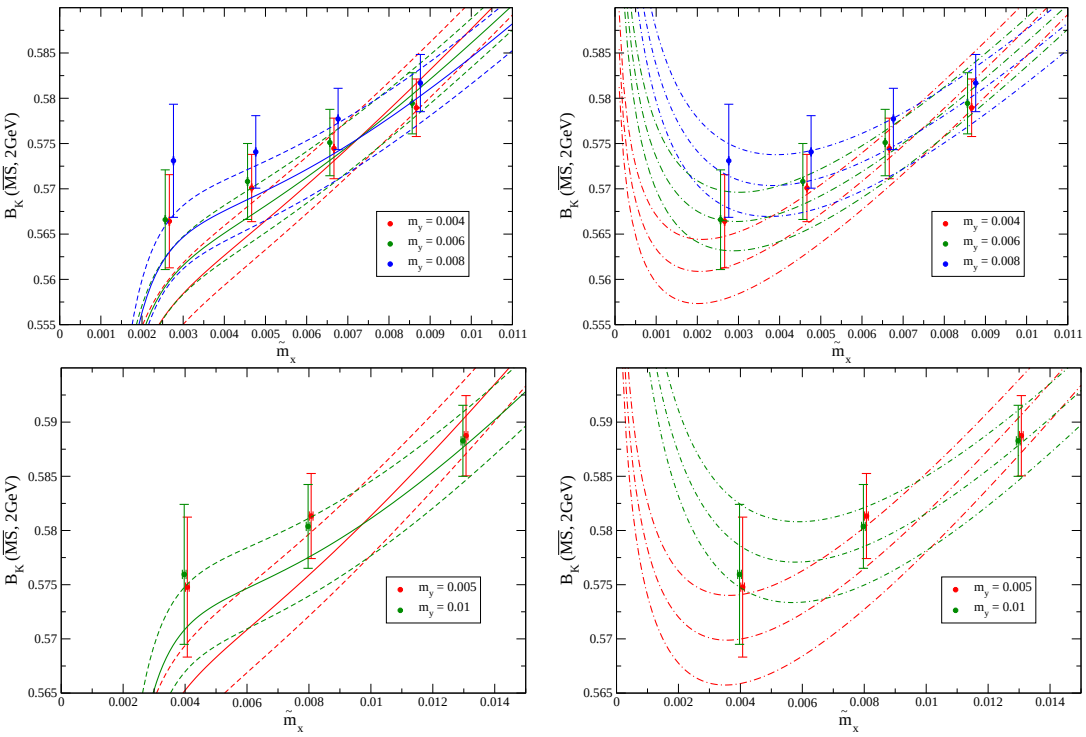

Figure 8.32: Partially-quenched B_K data in the SMOM($\not{q},\not{q}$) scheme for all ensembles overlaid by the results of the global fit using the ChPT-fv ansatz. The upper-left and upper-right panels are the data on the **A** ensembles at finite volume and infinite volume respectively. The lower panels show the same on the **B** ensembles. The datasets have been shifted slightly for clarity.

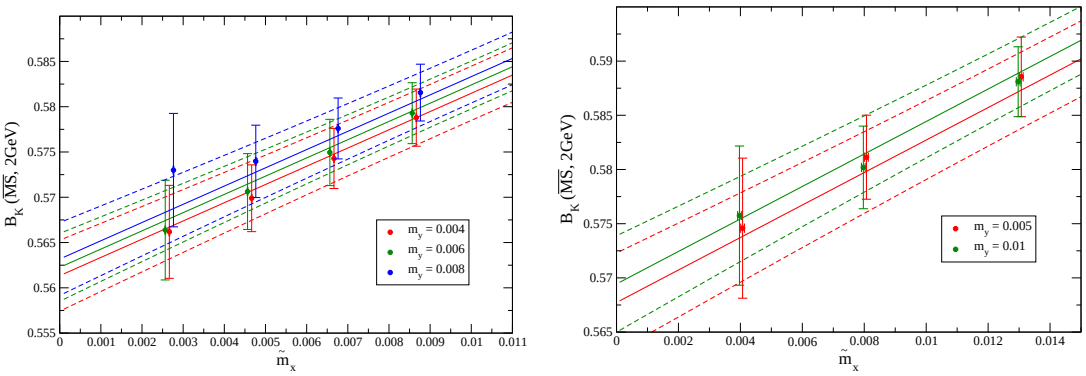

Figure 8.33: Partially-quenched B_K data in the SMOM($\not{q},\not{q}$) scheme for all ensembles of set **A** (left) and **B** (right). These are overlaid by the results of the global fit using the analytic ansatz. The datasets have been shifted slightly for clarity.

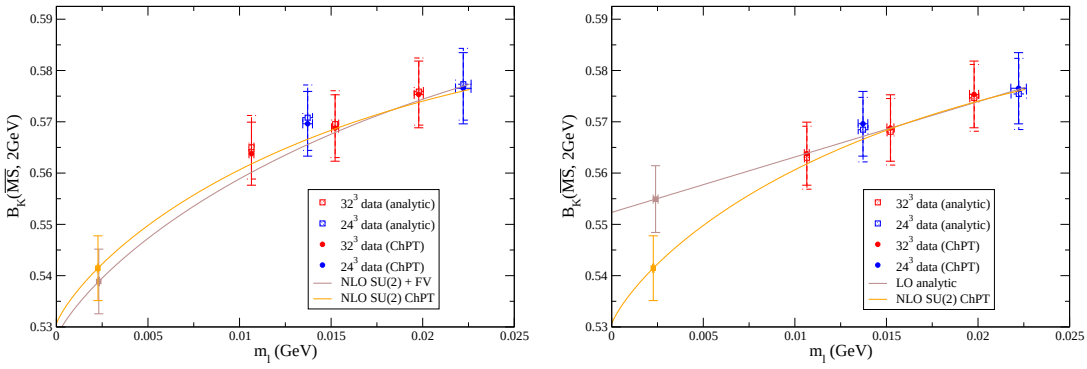

Figure 8.34: Unitary B_K data in the SMOM($\not{q}, \not{q}$) scheme on both ensemble sets corrected to the continuum using the a^2 dependence of the fit forms. In the left panel the data is overlaid by the unitary chiral extrapolation curves of the ChPT and ChPT-fv fits. Here the data represented by square points has been corrected to the infinite volume using the results of the ChPT-fv fit and the curve is plotted at infinite volume. The right panel shows a comparison of the chiral extrapolation using the analytic ansatz and the ChPT form.

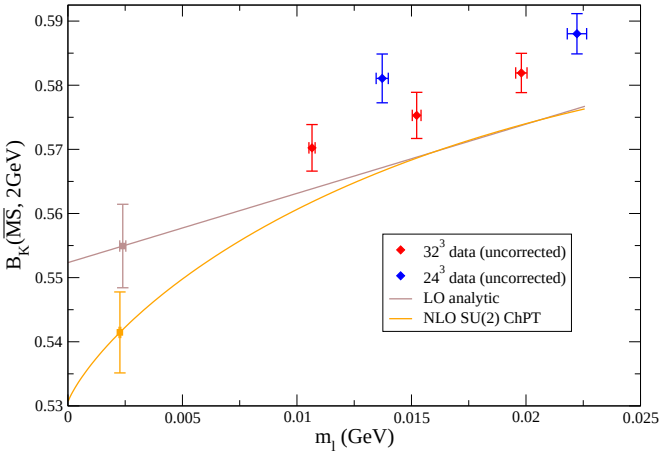

Figure 8.35: Unitary B_K data in the SMOM($\not{q}, \not{q}$) scheme on both ensemble sets that is not corrected to the continuum. These are overlaid by the mass dependence at each lattice spacing and in the continuum limit inferred from the ChPT and analytic ansatze.

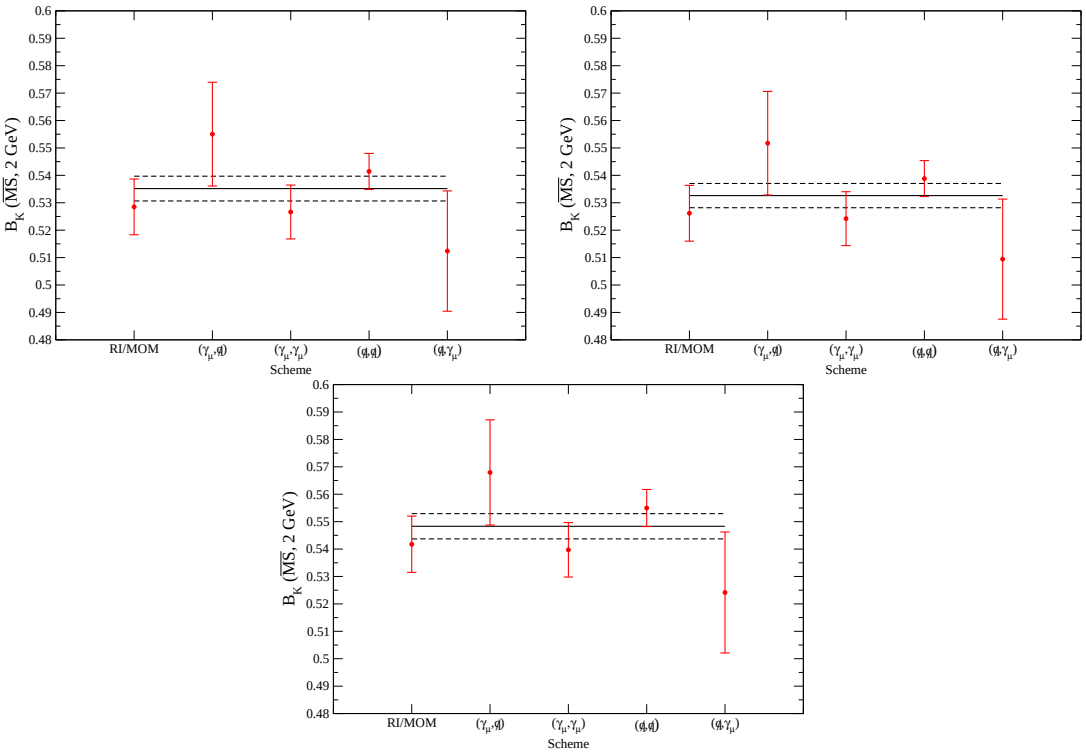

Figure 8.36: Plots of the continuum predictions for B_K obtained for each of the five schemes, overlaid by a fit to a constant. The upper-left and upper-right panels contain the ChPT and ChPT-fv predictions respectively, and the lower plot contains the analytic predictions.

8.7.4 Systematic errors

The results given in table 8.21 differ over a range of roughly 2.5% as a result of the various systematic errors. For the SMOM schemes, the dominant systematic is the slope error arising from the truncation of the perturbative series. The truncation error was crudely estimated at finite lattice spacing from the difference of the renormalisation constants in the NDR-scheme at 2 GeV obtained from the RI/(S)MOM data at $p^2 = 2$ GeV and $p^2 = 0$ GeV (section 7.6). A better estimate is now obtained following the procedure outlined in section 8.5.2, in which the errors are inflated by a PDG scale factor obtained from the square-root of the χ^2/d.o.f of a constant fit over all five schemes.

The results of the fits are given in table 8.22. The fits all have an uncorrelated χ^2/d.o.f that is roughly unity, indicating that the systematic error estimate, particularly of the slope error, is surprisingly robust. The agreement between the predicted values can be seen in the plots in figure 8.36.

Type	Fitted constant	χ^2/d.o.f
ChPT	0.535(5)	1.07(5)
ChPT-fv	0.533(4)	1.04(5)
Analytic	0.548(5)	1.09(5)

Table 8.22: The results of a fit of B_K to a constant form over the five renormalisation schemes. The χ^2/d.o.f is intended to be used to estimate a PDG scale factor for inflating the systematic error on a chosen result that is representative of the range of values.

8.7.5 Final result

In ref. [143], a trial analysis of the five renormalisation schemes for B_K was performed on two $16^3 \times 32$ DWF ensembles using twisted boundary conditions to allow the quark momenta to be varied while maintaining a fixed direction. This removes the systematic error resulting from the breaking of the $O(4)$ symmetry under discretisation, revealing very clearly the effects of the truncation of the perturbative series on the running of the coefficients. It shows that the SMOM($\not{q}, \not{q}$) scheme is best described by the perturbation theory in the scaling window associated with the present analysis. This is reflected in the magnitude of the slope error for this scheme (table 7.23). As a result, the SMOM($\not{q}, \not{q}$) result is chosen as the central 'best' determination of B_K for each chiral ansatz. Although the constant fit in the previous section shows that the results all agree, it is prudent to increase the systematic error on the result. This is performed by taking the difference between the SMOM($\not{q}, \not{q}$) and the SMOM(γ^μ, γ^μ) results. As before the central value is taken to be the average of the analytic and ChPT-fv determinations, and the difference between them is used to estimate the size of the chiral extrapolation error. Applying this procedure gives a final result for the continuum value of B_K:

$$B_K(\overline{\text{MS}}, 2\,\text{GeV}) = 0.547(7)_{\text{stat+spread}}(16)_{\chi}(2)_{FV}(14)_{\text{ren}}\,, \tag{8.56}$$

where the first error includes the statistical and spread errors on B_K and its renormalisation coefficient, the second is the error on the chiral extrapolation, the third is the finite-volume error, and the last is the remaining systematic error on the renormalisation coefficients.

8.8 Conclusions

Using a scaling trajectory that passes through the simulated data, the continuum and chiral limit of two $2+1$ flavour domain wall fermion ensembles was taken. The trajectory determines all quark masses with reference to the values of $m_{u/d}(\beta)$ and $m_s(\beta)$ that give ratios $(m_\pi/m_\Omega)(\beta)$ and $(m_K/m_\Omega)(\beta)$ that match those at a chosen

unphysical simulated point. The quantities m_π, m_K and m_Ω at these chosen masses are then necessarily free of lattice artefacts. Nearby masses were considered in a double-expansion in the mass and lattice spacing. The physical quark masses and the lattice spacings were determined by requiring that the predictions for m_π, m_K and m_Ω, obtained in the continuum limit, match their physical values.

This procedure was applied using a simultaneous fit to m_π, m_K, m_Ω, f_π and f_K over both ensemble sets. Three chiral fit ansätze were investigated, the first of which was obtained by an analytic expansion around an unphysical quark mass, and the others using $SU(2)$ partially-quenched chiral perturbation theory, with and without finite volume corrections. A chiral cutoff of $m_\pi = 420$ MeV was applied to all fit ansätze following ref. [1].

The fit procedure made use of reweighting in the strange sea quark mass in order to allow a post-simulation interpolation to the physical strange quark mass.

It was shown that the predictions for f_π obtained using the ChPT and ChPT-fv ansätze were 12% and 10% lower than the physical value respectively. These differences are of the magnitude expected for NNLO contributions within the range of the data, as obtained from the square of the size of the typical NLO corrections. However it was noted that NNLO ChPT fits could not be sufficiently constrained by the data without introducing a strong model dependence. The result for the analytic ansatz was significantly closer, at around 4% lower in the continuum limit. The results at the physical quark masses at finite lattice spacing are both consistent with the physical point within statistical errors, and only after continuum extrapolation did the discrepancy arise in a statistically significant form. This was possible because the (truncated) double-expansion in a^2 and the quark masses imposes a simultaneous constraint on the a^2 dependence of all data within a large partially-quenched data set. It is worth noting that there is a slightly different slope of f_π with respect to the quark mass between the **A** and **B** ensembles. The mass dependent terms in the fit ansätze are assumed to have no a^2 dependence, so this is inconsistent with the power counting scheme. The power counting suggests that the inclusion of mass dependent terms will have little effect on the central value, however it is possible that some error inflation on the extrapolation would occur with their inclusion.

The analytic fits to m_π gave a light quark mass dependence of $C_2^{m_\pi} = 0.43(8)$, which is inconsistent with Goldstone's theorem in the partially-quenched direction, which states that the pion mass vanishes in the limit of vanishing average valence quark mass. It was demonstrated that the result could not be explained by the mass dependence of m'_{res} arising due to the difference between the PCAC renormalisation $Z_{\mathcal{A}}$ and unity, indicating that non-analytic behaviour is required to reach the partially-quenched chiral limit. However it was noted that the analytic ansatz appears to be

valid above the pion mass, describing the data well far past the chiral cutoff.

In light of these difficulties it was decided take the central value of the physical predictions as the average of the analytic and ChPT-fv results, and to include a systematic error for the chiral extrapolation taken from the difference of the two results.

Applying the above procedure to the fit results gave the following predictions:

$$f\pi = 122(2)_{\text{stat}}(5)_{\chi}(2)_{\text{FV}}\,\text{MeV}\,, \tag{8.57}$$

$$f_K = 147(2)_{\text{stat}}(4)_{\chi}(1)_{\text{FV}}\,\text{MeV}\,, \tag{8.58}$$

$$f_K/f_\pi = 1.208(8)_{\text{stat}}(23)_{\chi}(14)_{\text{FV}}\,\text{MeV}\,, \tag{8.59}$$

for the decay constants,

$$\begin{aligned} r_0 &= 2.465(47)_{\text{stat}}(1)_{\chi}(1)_{\text{FV}}\,\text{GeV}^{-1} = 0.4864(81)_{\text{stat}}(2)_{\chi}(2)_{\text{FV}}\,\text{fm}\,, \\ r_1 &= 1.688(49)_{\text{stat}}(1)_{\chi}(1)_{\text{FV}}\,\text{GeV}^{-1} = 0.3331(59)_{\text{stat}}(2)_{\chi}(2)_{\text{FV}}\,\text{fm}\,, \\ r_1/r_0 &= 0.684(15)_{\text{stat}}(1)_{\chi}(0)_{\text{FV}}\,, \end{aligned} \tag{8.60}$$

for the Sommer scale r_0 and the related scale r_1, and

$$\begin{aligned} m_{u/d}(\overline{\text{MS}},\,2\,\text{GeV}) &= 3.71(21)_{\text{stat+spread}}(7)_{\text{FV}}(17)_{\text{trunc}}(2)_{\text{other sys}}\,\text{MeV}\,, \\ m_s(\overline{\text{MS}},\,2\,\text{GeV}) &= 98.9(1.8)_{\text{stat+spread}}(0.1)_{\text{FV}}(4.6)_{\text{trunc}}(0.6)_{\text{other sys}}\,\text{MeV}\,. \end{aligned} \tag{8.61}$$

for the physical quark masses in the $\overline{\text{MS}}$-scheme. The renormalisation of the quark masses was performed non-perturbatively, using two intermediate RI/SMOM lattice schemes (chapter 7) with volume source propagators for improved statistics. Here the 'stat' error is statistical, the 'FV' error is the finite volume systematic and the 'χ' error is associated with the systematic error on the chiral extrapolation. The 'spread', 'trunc' and 'other sys' errors on the quark masses are associated with the renormalisation coefficients. They arise, in turn, from the breaking of the $O(4)$ rotational symmetry under discretisation, the truncation of the perturbative expansion, and from the other minor systematic errors described in section 7.5, the most notable of which is the error due to the residual effect of the spontaneous breaking of the chiral symmetry, which is now a small effect due to the use of symmetric momentum configurations.

The chiral/continuum fit procedure was also applied to B_K. The fits were performed over data renormalised in the NDR-scheme using non-perturbative renormalisation coefficients obtained with the RI/MOM and four RI/SMOM intermediate lattice schemes. A robust strategy for estimating the truncation error on the renormalisation coefficients was employed, in which the errors were inflated by a PDG scale factor obtained from a constant fit over the five determinations. It was shown that the errors did not require significant inflation in order to be made consistent, but it was

considered prudent to assign a larger error by hand as the difference between the two best determinations. The prediction obtained for the continuum value of B_K is reproduced below:

$$B_K(\overline{\mathrm{MS}},\, 2\,\mathrm{GeV}) = 0.547(7)_{\mathrm{stat+spread}}(16)_{\chi}(2)_{FV}(14)_{\mathrm{ren}}\,. \tag{8.62}$$

This is the first determination of the continuum limit of B_K with a chirally-symmetric lattice action. The result is consistent with that determined in the analysis of the **B** ensembles [128].

8.9 Outlook

Using the combined chiral/continuum procedure, the leading discretisation errors and the systematic error associated with an unphysical strange quark mass have been reduced considerably. The dominant systematic effect is now that of the chiral extrapolation. This can be reduced by increasing statistics and going to lighter quark masses. As the physical point is approached, the chiral and analytic ansätze *must* converge. As a result the difference between the two will remain a robust estimate of the chiral extrapolation systematic error, allowing for predictions to be made with confidence.

RBC&UKQCD are in the process of generating a new ensemble set using the DSDR gauge action [161] at a different lattice spacing. This procedure allows for lighter quark masses to be reached while retaining sufficient sampling of topological configurations in the Monte Carlo procedure. Combining this ensemble set with the **A** and **B** sets analysed in this thesis will allow for a significant reduction of the systematic errors.

8.10 Prospects

In the longer term a number of significant improvements can be expected. Using the step-scaling procedure [143], the errors on the non-perturbative renormalisation factors can be reduced dramatically, in principle to $< 1\%$, by allowing the lattice scheme data to be matched to perturbation theory at a much larger scale at which the perturbation theory is more applicable. The relentless advance of computing power will allow these to be combined with data generated at the physical point with sub-percent scale statistical errors, and as a result percent-scale total errors on the decay constants, quark masses and B_K can be envisioned within a timescale of 2–3 years.

Bibliography

[1] C. Allton *et al.* [RBC-UKQCD Collaboration], "Physical Results from 2+1 Flavor Domain Wall QCD and SU(2) Chiral Perturbation Theory," Phys. Rev. D **78**, 114509 (2008) [arXiv:0804.0473 [hep-lat]].

[2] P. A. Boyle, A. Juttner, C. Kelly and R. D. Kenway, "Use of stochastic sources for the lattice determination of light quark physics," JHEP **0808** (2008) 086 [arXiv:0804.1501 [hep-lat]].

[3] Y. Aoki *et al.* [RBC Collaboration and UKQCD Collaboration], Provisionally entitled "Continuum Limit Physics from 2+1 Flavor DomainWall QCD" (2010)

[4] C. Kelly, P. A. Boyle and C. T. Sachrajda [RBC Collaboration and UKQCD Collaboration], "Continuum results for light hadrons from 2+1 flavor DWF ensembles," PoS **LAT2009** (2009) 087 [arXiv:0911.1309].

[5] Y. Aoki *et al.* [RBC Collaboration and UKQCD Collaboration], Provisionally entitled "Continuum Limit of B_K from 2+1 Flavor Domain Wall QCD" (2010)

[6] C. Kelly, [RBC Collaboration and UKQCD Collaboration], "Scaling of B_K for 2+1 flavour domain wall fermions from 24^3 and $32^3 \times 64$ lattices," PoS **LATTICE 2008** (2008) 270.

[7] P. A. Boyle *et al.*, "The pion's electromagnetic form factor at small momentum transfer in full lattice QCD," JHEP **0807** (2008) 112 [arXiv:0804.3971 [hep-lat]].

[8] P. A. Boyle *et al.*, "$K \to \pi$ form factors with reduced model dependence," [arXiv:1004.0886 [hep-lat]] .

[9] G. 't Hooft, "Symmetry breaking through Bell-Jackiw anomalies," Phys. Rev. Lett. **37** (1976) 8.

[10] C. Vafa and E. Witten, "Restrictions On Symmetry Breaking In Vector-Like Gauge Theories," Nucl. Phys. B **234** (1984) 173.

[11] T. Banks and A. Casher, "Chiral Symmetry Breaking In Confining Theories," Nucl. Phys. B **169** (1980) 103.

[12] M. F. Atiyah and I. M. Singer, "The Index of elliptic operators. 1," Annals Math. **87**, 484 (1968).

[13] Y. Nambu, "Quasi-particles and gauge invariance in the theory of superconductivity," Phys. Rev. **117**, 648 (1960).

[14] J. Goldstone, "Field Theories With Superconductor Solutions," Nuovo Cim. **19**, 154 (1961).

[15] J. Goldstone, A. Salam and S. Weinberg, "Broken Symmetries," Phys. Rev. **127**, 965 (1962).

[16] S. L. Glashow, "Partial Symmetries Of Weak Interactions," Nucl. Phys. **22** (1961) 579.

[17] S. Weinberg, "A Model Of Leptons," Phys. Rev. Lett. **19**, 1264 (1967).

[18] A. Salam, "Weak And Electromagnetic Interactions," *Originally printed in *Svartholm: Elementary Particle Theory, Proceedings Of The Nobel Symposium Held 1968 At Lerum, Sweden*, Stockholm 1968, 367-377*

[19] P. W. Higgs, "Broken symmetries, massless particles and gauge fields," Phys. Lett. **12**, 132 (1964).

[20] P. W. Higgs, "Spontaneous Symmetry Breakdown without Massless Bosons," Phys. Rev. **145**, 1156 (1966).

[21] F. Englert and R. Brout, "Broken Symmetry and the Mass of Gauge Vector Mesons," Phys. Rev. Lett. **13**, 321 (1964).

[22] G. S. Guralnik, C. R. Hagen and T. W. B. Kibble, "Global Conservation Laws and Massless Particles," Phys. Rev. Lett. **13** (1964) 585.

[23] A. J. Buras, "Weak Hamiltonian, CP violation and rare decays," [arXiv:hep-ph/9806471].

[24] J. H. Christenson, J. W. Cronin, V. L. Fitch and R. Turlay, "Evidence For The 2 Pi Decay Of The K(2)0 Meson," Phys. Rev. Lett. **13** (1964) 138.

[25] M. Kobayashi and T. Maskawa, "CP Violation In The Renormalizable Theory Of Weak Interaction," Prog. Theor. Phys. **49**, 652 (1973).

[26] J. R. Ellis, S. Ferrara and D. V. Nanopoulos, "CP Violation And Supersymmetry," Phys. Lett. B **114** (1982) 231.

[27] O. W. Greenberg, "CPT violation implies violation of Lorentz invariance," Phys. Rev. Lett. **89** (2002) 231602 [arXiv:hep-ph/0201258].

[28] L. L. Chau, "Quark Mixing In Weak Interactions," Phys. Rept. **95** (1983) 1.

[29] C. Amsler *et al.* [Particle Data Group], "Review of particle physics," Phys. Lett. B **667** (2008) 1.

[30] H. Burkhardt *et al.* [NA31 Collaboration], "First Evidence For Direct CP Violation," Phys. Lett. B **206**, 169 (1988).

[31] V. Fanti *et al.* [NA48 Collaboration], "A new measurement of direct CP violation in two pion decays of the neutral kaon," Phys. Lett. B **465** (1999) 335 [arXiv:hep-ex/9909022].

[32] A. Alavi-Harati *et al.* [KTeV Collaboration], "Observation of direct CP violation in K(S,L) $\to$ pi pi decays," Phys. Rev. Lett. **83** (1999) 22 [arXiv:hep-ex/9905060].

[33] C. Bagnuls and C. Bervillier, "Exact renormalization group equations: An introductory review," Phys. Rept. **348**, 91 (2001) [arXiv:hep-th/0002034].

[34] Yu. M. Ivanchenko, A. A. Lisyansky and A. E. Filippov, "Structure of the correlation function of a fluctuating system at the critical point," Theor. Math. Phys. **84**, 829 (1991) [Teor. Mat. Fiz. **84**, 223 (1990)].

[35] B. Delamotte, "A hint of renormalization," Am. J. Phys. **72** (2004) 170 [arXiv:hep-th/0212049].

[36] D. V. Shirkov and V. F. Kovalev, "The Bogoliubov renormalization group and solution symmetry in mathematical physics," Phys. Rept. **352**, 219 (2001) [arXiv:hep-th/0001210].

[37] B. Delamotte, "An introduction to the nonperturbative renormalization group," [arXiv:cond-mat/0702365].

[38] K. G. Wilson and J. B. Kogut, "The Renormalization group and the epsilon expansion," Phys. Rept. **12**, 75 (1974).

[39] D. J. Gross and F. Wilczek, "Ultraviolet Behaviour of Non-Abelian Gauge Theories," Phys. Rev. Lett. **30** (1973) 1343.

[40] Y. Nambu, "Magnetic And Electric Confinement Of Quarks," Phys. Rept. **23** (1976) 250.

[41] G. 't Hooft, "On The Phase Transition Towards Permanent Quark Confinement," Nucl. Phys. B **138**, 1 (1978).

[42] G. 't Hooft, "A Property Of Electric And Magnetic Flux In Nonabelian Gauge Theories," Nucl. Phys. B **153**, 141 (1979).

[43] S. Mandelstam, "Vortices and Quark Confinement in Nonabelian Gauge Theories," Phys. Lett. B **53**, 476 (1975).

[44] S. Mandelstam, "Charge - Monopole Duality And The Phases Of Non-abelian Gauge Theories," Phys. Rev. D **19**, 2391 (1979).

[45] T. R. Morris, "Elements of the continuous renormalization group," Prog. Theor. Phys. Suppl. **131** (1998) 395 [arXiv:hep-th/9802039].

[46] J. Polchinski, "Renormalization And Effective Lagrangians," Nucl. Phys. B **231** (1984) 269.

[47] W. Bietenholz, R. Brower, S. Chandrasekharan and U. J. Wiese, "Progress on perfect lattice actions for QCD," Nucl. Phys. Proc. Suppl. **53** (1997) 921 [arXiv:hep-lat/9608068].

[48] K. Symanzik, "Continuum Limit And Improved Action In Lattice Theories. 1. Principles And Phi**4 Theory," Nucl. Phys. B **226** (1983) 187.

[49] K. Symanzik, "Continuum Limit And Improved Action In Lattice Theories. 2. O(N) Nonlinear Sigma Model In Perturbation Theory," Nucl. Phys. B **226** (1983) 205.

[50] H. Lehmann, K. Symanzik and W. Zimmermann, "On the formulation of quantized field theories," Nuovo Cim. **1** (1955) 205.

[51] J. Zinn-Justin, "Quantum field theory and critical phenomena," Int. Ser. Monogr. Phys. **92** (1996) 1.

[52] G. M. Shore, "New methods for the renormalization of composite operator Green functions," Nucl. Phys. B **362** (1991) 85.

[53] C. Kopper and W. Pedra, "Irrelevant interactions without composite operators: A remark on the universality of second order phase transitions," J. Phys. A **34** (2001) 2681 [arXiv:cond-mat/0007476].

[54] C. P. Burgess, "Introduction to effective field theory," Ann. Rev. Nucl. Part. Sci. **57** (2007) 329 [arXiv:hep-th/0701053].

[55] D. J. Gross and S. B. Treiman, "Light cone structure of current commutators in the gluon quark model," Phys. Rev. D **4** (1971) 1059.

[56] S. A. Gottlieb, "Contribution Of Twist Four Operators To Deep Inelastic Scattering," Nucl. Phys. B **139** (1978) 125.

[57] E. L. Berger, "Higher Twist Effects In Deep Inelastic Scattering," Phys. Lett. B **89** (1980) 241.

[58] R. L. Jaffe, "Parton Distribution Functions For Twist Four," Nucl. Phys. B **229** (1983) 205.

[59] E. L. Berger, "Quark Structure Functions Of Mesons, Fragmentation Functions, Higher Twist Effects In QCD, Deep Inelastic Scattering, And The Drell-Yan Process," Z. Phys. C **4** (1980) 289.

[60] G. Cynolter and E. Lendvai, "Symmetry preserving regularization with a cutoff," [arXiv:1002.4490].

[61] M. Oleszczuk, "A Symmetry preserving cutoff regularization," Z. Phys. C **64** (1994) 533.

[62] V. Bernard, T. R. Hemmert and U. G. Meissner, "Cutoff schemes in chiral perturbation theory and the quark mass expansion of the nucleon mass," Nucl. Phys. A **732** (2004) 149 [arXiv:hep-ph/0307115].

[63] G. 't Hooft and M. J. G. Veltman, "Regularization And Renormalization Of Gauge Fields," Nucl. Phys. B **44** (1972) 189.

[64] W. A. Bardeen, R. Gastmans and B. Lautrup, "Static Quantities In Weinberg's Model Of Weak And Electromagnetic Interactions," Nucl. Phys. B **46**, 319 (1972).

[65] M. S. Chanowitz, M. Furman and I. Hinchliffe, "The Axial Current In Dimensional Regularization," Nucl. Phys. B **159**, 225 (1979).

[66] H. Georgi, "Effective field theory," Ann. Rev. Nucl. Part. Sci. **43** (1993) 209.

[67] M. E. Luke, "Effects Of Subleading Operators In The Heavy Quark Effective Theory," Phys. Lett. B **252** (1990) 447.

[68] T. Inami and C. S. Lim, "Effects Of Superheavy Quarks And Leptons In Low-Energy Weak Processes K(L) → Mu Anti-Mu, K+ → Pi+ Neutrino Anti-Neutrino And K0 ¡—¿ Anti-K0," Prog. Theor. Phys. **65**, 297 (1981) [Erratum-ibid. **65**, 1772 (1981)].

[69] S. L. Glashow, J. Iliopoulos and L. Maiani, "Weak Interactions with Lepton-Hadron Symmetry," Phys. Rev. D **2**, 1285 (1970).

[70] A. J. Buras, M. Jamin and P. H. Weisz, "Leading and Next-to-leading QCD Corrections to Epsilon Parameter and B0 - anti-BO Mixing in the presence of a Heavy Top Quark," Nucl. Phys. B **347** (1990) 491.

[71] A. J. Buras and P. H. Weisz, "QCD Nonleading Corrections to Weak Decays in Dimensional Regularization and 't Hooft-Veltman Schemes," Nucl. Phys. B **333** (1990) 66.

[72] J. Urban, F. Krauss, U. Jentschura and G. Soff, "Next-to-leading order QCD corrections for the B0 anti-B0 mixing with an extended Higgs sector," Nucl. Phys. B **523** (1998) 40 [arXiv:hep-ph/9710245].

[73] S. Herrlich and U. Nierste, "Enhancement of the K(L) - K(S) mass difference by short distance QCD corrections beyond leading logarithms," Nucl. Phys. B **419** (1994) 292 [arXiv:hep-ph/9310311].

[74] S. Herrlich and U. Nierste, "Indirect CP violation in the neutral kaon system beyond leading logarithms," Phys. Rev. D **52** (1995) 6505 [arXiv:hep-ph/9507262].

[75] S. Herrlich and U. Nierste, "The Complete —Delta S—=2 Hamiltonian in the Next-To-Leading Order," Nucl. Phys. B **476** (1996) 27 [arXiv:hep-ph/9604330].

[76] A. Donini, V. Gimenez, L. Giusti and G. Martinelli, "Renormalization group invariant matrix elements of Delta(S) = 2 and Delta(I) = 3/2 four-fermion operators without quark masses," Phys. Lett. B **470** (1999) 233 [arXiv:hep-lat/9910017].

[77] S. Weinberg, "Phenomenological Lagrangians," Physica A **96** (1979) 327.

[78] S. Scherer and M. R. Schindler, "A chiral perturbation theory primer," [arXiv:hep-ph/0505265].

[79] J. Gasser and H. Leutwyler, "Chiral Perturbation Theory: Expansions In The Mass Of The Strange Quark," Nucl. Phys. B **250**, 465 (1985).

[80] J. Gasser and H. Leutwyler, "Chiral Perturbation Theory To One Loop," Annals Phys. **158** (1984) 142.

[81] C. W. Bernard and M. F. L. Golterman, "Partially quenched gauge theories and an application to staggered fermions," Phys. Rev. D **49** (1994) 486 [arXiv:hep-lat/9306005].

[82] A. Morel, "Chiral Logarithms In Quenched QCD," J. Phys. (France) **48** (1987) 1111.

[83] S. R. Sharpe, "Applications of chiral perturbation theory to lattice QCD," [arXiv:hep-lat/0607016].

[84] A. Roessl, "Pion kaon scattering near the threshold in chiral SU(2) perturbation theory," Nucl. Phys. B **555** (1999) 507 [arXiv:hep-ph/9904230].

[85] K. G. Wilson, "Confinement of Quarks," Phys. Rev. D **10**, 2445 (1974).

[86] D. J. Antonio *et al.* [RBC and UKQCD Collaborations], "First results from 2+1-flavor domain wall QCD: Mass spectrum, topology change and chiral symmetry with L(s) = 8," Phys. Rev. D **75** (2007) 114501 [arXiv:hep-lat/0612005].

[87] Y. Iwasaki, "Renormalization Group Analysis Of Lattice Theories And Improved Lattice Action. 2. Four-Dimensional Nonabelian SU(N) Gauge Model," UTHEP-118;

[88] Y. Iwasaki, "Renormalization Group Analysis of Lattice Theories and Improved Lattice Action: Two-Dimensional Nonlinear O(N) Sigma Model," Nucl. Phys. B **258** (1985) 141.

[89] Y. Iwasaki and T. Yoshie, "Renormalization Group Improved Action For SU(3) Lattice Gauge Theory And The String Tension," Phys. Lett. B **143**, 449 (1984).

[90] D. J. Antonio *et al.* [RBC Collaboration and UKQCD Collaboration], "Localization and chiral symmetry in 3 flavor domain wall QCD," Phys. Rev. D **77**, 014509 (2008) [arXiv:0705.2340 [hep-lat]].

[91] R. Sommer, "A New way to set the energy scale in lattice gauge theories and its applications to the static force and alpha-s in SU(2) Yang-Mills theory," Nucl. Phys. B **411**, 839 (1994) [arXiv:hep-lat/9310022].

[92] R. G. Edwards, U. M. Heller and T. R. Klassen, Nucl. Phys. B **517** (1998) 377 [arXiv:hep-lat/9711003].

[93] M. Guagnelli, R. Sommer and H. Wittig [ALPHA collaboration], "Precision computation of a low-energy reference scale in quenched lattice QCD," Nucl. Phys. B **535**, 389 (1998) [arXiv:hep-lat/9806005].

[94] Y. Shamir, "Chiral fermions from lattice boundaries," Nucl. Phys. B **406** (1993) 90 [arXiv:hep-lat/9303005].

[95] V. Furman and Y. Shamir, "Axial Symmetries In Lattice QCD With Kaplan Fermions," Nucl. Phys. B **439**, 54 (1995) [arXiv:hep-lat/9405004].

[96] D. B. Kaplan, Phys. Lett. B **288** (1992) 342 [arXiv:hep-lat/9206013].

[97] P. M. Vranas, "Chiral symmetry restoration in the Schwinger model with domain wall fermions," Phys. Rev. D **57** (1998) 1415 [arXiv:hep-lat/9705023].

[98] M. Golterman, Y. Shamir and B. Svetitsky, "Localization properties of lattice fermions with plaquette and improved gauge actions," Phys. Rev. D **72**, 034501 (2005) [arXiv:hep-lat/0503037].

[99] S. R. Sharpe, "Future of Chiral Extrapolations with Domain Wall Fermions,"]arXiv:0706.0218 [hep-lat]].

[100] T. Blum *et al.*, "Quenched lattice QCD with domain wall fermions and the chiral limit," Phys. Rev. D **69**, 074502 (2004) [arXiv:hep-lat/0007038].

[101] S. Aoki and Y. Taniguchi, "One loop renormalization for the axial Ward-Takahashi identity in domain-wall QCD," Phys. Rev. D **59** (1999) 094506 [arXiv:hep-lat/9811007].

[102] N. Christ [RBC and UKQCD Collaborations], "Estimating domain wall fermion chiral symmetry breaking," PoS **LAT2005**, 345 (2006).

[103] T. Blum *et al.*, "Non-perturbative renormalisation of domain wall fermions: Quark bilinears," Phys. Rev. D **66** (2002) 014504 [arXiv:hep-lat/0102005].

[104] M. F. Lin [RBC and UKQCD Collaborations], "Chiral extrapolations in 2+1 flavor domain wall fermion simulations," PoS **LAT2006**, 185 (2006) [arXiv:hep-lat/0610052].

[105] M. A. Clark and A. D. Kennedy, "The RHMC algorithm for 2 flavors of dynamical staggered fermions," Nucl. Phys. Proc. Suppl. **129** (2004) 850 [arXiv:hep-lat/0309084].

[106] M. Luscher and F. Palombi, "Fluctuations and reweighting of the quark determinant on large lattices," PoS **LATTICE2008** (2008) 049 [arXiv:0810.0946 [hep-lat]].

[107] A. Hasenfratz, R. Hoffmann and S. Schaefer, "Reweighting towards the chiral limit," Phys. Rev. D **78** (2008) 014515 [arXiv:0805.2369 [hep-lat]].

[108] G. C. Wick, "The Evaluation of the Collision Matrix," Phys. Rev. **80** (1950) 268.

[109] L. Del Debbio, L. Giusti, M. Luscher, R. Petronzio and N. Tantalo, "QCD with light Wilson quarks on fine lattices. II: DD-HMC simulations and data analysis," JHEP **0702** (2007) 082 [arXiv:hep-lat/0701009].

[110] J. D. Bratt *et al.* [LHPC Collaboration], "Nucleon structure from mixed action calculations using 2+1 flavors of asqtad sea and domain wall valence fermions," [arXiv:1001.3620 [hep-lat]].

[111] A. Voigt, E. M. Ilgenfritz, M. Muller-Preussker and A. Sternbeck, "Coulomb gauge studies of SU(3) Yang-Mills theory on the lattice," PoS **LAT2007** (2007) 338 [arXiv:0709.4585 [hep-lat]].

[112] Y. Nakagawa *et al.*, "Coulomb-gauge ghost and gluon propagators in SU(3) lattice Yang-Mills theory," Phys. Rev. D **79** (2009) 114504 [arXiv:0902.4321 [hep-lat]].

[113] J. C. Vink and U. J. Wiese, "Gauge fixing on the lattice without ambiguity," Phys. Lett. B **289** (1992) 122 [arXiv:hep-lat/9206006].

[114] M. Luscher, "Volume Dependence of the Energy Spectrum in Massive Quantum Field Theories.2. Scattering States," Commun. Math. Phys. **105**, 153 (1986).

[115] M. Luscher, "Two particle states on a torus and their relation to the scattering Nucl. Phys. B **354**, 531 (1991).

[116] S. R. Beane, P. F. Bedaque, A. Parreno and M. J. Savage, "Two Nucleons on a Lattice," Phys. Lett. B **585**, 106 (2004) [arXiv:hep-lat/0312004].

[117] J. Flynn, A. Juttner, C. Sachrajda and G. Villadoro, "Partially twisted boundary conditions in lattice simulations," PoS **LAT2005** (2006) 352 [arXiv:hep-lat/0509093].

[118] S. J. Dong and K. F. Liu, "Stochastic estimation with Z(2) noise," Phys. Lett. B **328** (1994) 130, [arXiv:hep-lat/9308015].

[119] N. Eicker *et al.* [TXL Collaboration], "Evaluating sea quark contributions to flavour-singlet operators in lattice QCD," Phys. Lett. B **389**, 720 (1996), [arXiv:hep-lat/9608040].

[120] M. Foster and C. Michael [UKQCD Collaboration], "Quark mass dependence of hadron masses from lattice QCD," Phys. Rev. D **59** (1999) 074503, [arXiv:hep-lat/9810021].

[121] A. O'Cais, K. J. Juge, M. J. Peardon, S. M. Ryan and J. I. Skullerud [TrinLat Collaboration], "Improving algorithms to compute all elements of the lattice quark propagator," [arXiv:hep-lat/0409069].

[122] J. Foley, K. J. Juge, A. O'Cais, M. Peardon, S. M. Ryan and J. I. Skullerud, "Practical all-to-all propagators for lattice QCD," Comput. Phys. Commun. **172** (2005) 145, [arXiv:hep-lat/0505023].

[123] C. McNeile and C. Michael [UKQCD Collaboration], "Decay width of light quark hybrid meson from the lattice," Phys. Rev. D **73** (2006) 074506, [arXiv:hep-lat/0603007].

[124] Ph. Boucaud *et al.* [ETM Collaboration], "Dynamical twisted mass fermions with light quarks," Phys. Lett. B **650** (2007) 304, [arXiv:hep-lat/0701012].

[125] B. Blossier *et al.* [European Twisted Mass Collaboration], "Light quark masses and pseudoscalar decay constants from Nf=2 Lattice QCD with twisted mass fermions," JHEP **0804**, 020 (2008) [arXiv:0709.4574 [hep-lat]].

[126] P. Boucaud *et al.* [ETM collaboration], "Dynamical Twisted Mass Fermions with Light Quarks: Simulation and Analysis Details," Comput. Phys. Commun. **179**, 695 (2008) [arXiv:0803.0224 [hep-lat]].

[127] S. Simula [ETMC Collaboration], "Pseudo-scalar meson form factors with maximally twisted Wilson fermions at Nf = 2," PoS **LAT2007**, 371 (2007) [arXiv:0710.0097 [hep-lat]].

[128] D. J. Antonio *et al.* [RBC Collaboration], "Neutral kaon mixing from 2+1 flavor domain wall QCD," Phys. Rev. Lett. **100** (2008) 032001, [arXiv:hep-ph/0702042].

[129] J. Viehoff *et al.* [TXL Collaboration], "Improving stochastic estimator techniques for disconnected diagrams", Nucl. Phys. Proc. Suppl. **63** (1998) 269, [arXiv:hep-lat/9710050].

[130] C. Allton *et al.* [RBC and UKQCD Collaborations], "2+1 flavor domain wall QCD on a $(2\ \mathrm{fm})^3$ lattice: light meson spectroscopy with Ls = 16," Phys. Rev. D **76** (2007) 014504, [arXiv:hep-lat/0701013].

[131] C. Aubin, J. Laiho and R. S. Van de Water, "The kaon B^- parameter from unquenched mixed action lattice QCD," PoS **LAT2007**, 375 (2007) [arXiv:0710.1121 [hep-lat]].

[132] P. A. Boyle, J. M. Flynn, A. Jüttner, C. T. Sachrajda and J. M. Zanotti, "Hadronic form factors in lattice QCD at small and vanishing momentum transfer," JHEP **0705** (2007) 016, [arXiv:hep-lat/0703005].

[133] G. Martinelli and C. T. Sachrajda, "A lattice study of nucleon structure," Nucl. Phys. B **316** (1989) 355.

[134] C. T. Sachrajda and G. Villadoro, "Twisted boundary conditions in lattice simulations," Phys. Lett. B **609** (2005) 73, [arXiv:hep-lat/0411033].

[135] T. A. DeGrand and S. Schaefer, "Improving meson two-point functions in lattice QCD," Comput. Phys. Commun. **159**, 185 (2004) [arXiv:hep-lat/0401011].

[136] T. A. DeGrand and S. Schaefer, "Improving meson two-point functions by low-mode averaging," Nucl. Phys. Proc. Suppl. **140** (2005) 296 [arXiv:hep-lat/0409056].

[137] M. F. Lin and E. E. Scholz [UKQCD Collaboration and RBC Collaboration], "Chiral Limit and Light Quark Masses in 2+1 Flavor Domain Wall QCD," PoS **LAT2007** (2007) 120 [arXiv:0710.0536 [hep-lat]].

[138] C. W. Bernard *et al.*, "The static quark potential in three flavor QCD," Phys. Rev. D **62** (2000) 034503 [arXiv:hep-lat/0002028].

[139] F. X. Lee and D. B. Leinweber, Nucl. Phys. Proc. Suppl. **73** (1999) 258 [arXiv:hep-lat/9809095].

[140] M. Gockeler, R. Horsley, D. Pleiter, P. E. L. Rakow, G. Schierholz, C. M. Maynard and D. G. Richards [QCDSF Collaboration and UKQCD Collaboration and LHPC Collaboration], Phys. Lett. B **532** (2002) 63 [arXiv:hep-lat/0106022].

[141] Y. Aoki *et al.*, "Non-perturbative renormalization of quark bilinear operators and B_K using domain wall fermions," Phys. Rev. D **78**, 054510 (2008) [arXiv:0712.1061 [hep-lat]].

[142] G. Martinelli, C. Pittori, C. T. Sachrajda, M. Testa and A. Vladikas, "A General Method For Nonperturbative Renormalization Of Lattice Operators," Nucl. Phys. B **445**, 81 (1995) [arXiv:hep-lat/9411010].

[143] R. Arthur and P. A. Boyle, "Step Scaling with off-shell renormalisation," [arXiv:1006.0422].

[144] C. Sturm, Y. Aoki, N. H. Christ, T. Izubuchi, C. T. C. Sachrajda and A. Soni, "Renormalization of quark bilinear operators in a momentum-subtraction scheme with a nonexceptional subtraction point," Phys. Rev. D **80** (2009) 014501 [arXiv:0901.2599 [hep-ph]].

[145] A. Grozin, "Lectures on QED and QCD: Practical calculation and renormalization of one- and multi-loop Feynman diagrams," *Hackensack, USA: World Scientific (2007) 224 p*

[146] Y. Aoki [RBC Collaboration and UKQCD Collaboration], "Quark mass renormalization with non-exceptional momenta," PoS **LATTICE2008** (2008) 222 [arXiv:0901.2595 [hep-lat]].

[147] K. G. Chetyrkin and A. Retey, "Renormalization and running of quark mass and field in the regularization invariant and MS-bar schemes at three and four loops," Nucl. Phys. B **583**, 3 (2000) [arXiv:hep-ph/9910332].

[148] R. Tarrach, "The Pole Mass In Perturbative QCD," Nucl. Phys. B **183** (1981) 384.

[149] O. V. Tarasov, "Anomalous Dimensions Of Quark Masses In Three Loop Approximation," preprint JINR P2-82-900.

[150] K. G. Chetyrkin, "Quark mass anomalous dimension to O(alpha(s)**4)," Phys. Lett. B **404** (1997) 161 [arXiv:hep-ph/9703278].

[151] J. A. M. Vermaseren, S. A. Larin and T. van Ritbergen, "The 4-loop quark mass anomalous dimension and the invariant quark mass," Phys. Lett. B **405**, 327 (1997) [arXiv:hep-ph/9703284].

[152] M. Gorbahn and S. Jager, "Precise MS-bar light-quark masses from lattice QCD in the RI/SMOM scheme," [arXiv:1004.3997].

[153] L. G. Almeida and C. Sturm, "Two-loop matching factors for light quark masses and three-loop mass anomalous dimensions in the RI/SMOM schemes," [arXiv:1004.4613].

[154] T. van Ritbergen, J. A. M. Vermaseren and S. A. Larin, "The four-loop beta function in quantum chromodynamics," Phys. Lett. B **400**, 379 (1997) [arXiv:hep-ph/9701390].

[155] J. Gasser and H. Leutwyler, "Light Quarks at Low Temperatures," Phys. Lett. B **184** (1987) 83.

[156] J. Gasser and H. Leutwyler, "Thermodynamics of Chiral Symmetry," Phys. Lett. B **188** (1987) 477.

[157] J. Gasser and H. Leutwyler, "Spontaneously Broken Symmetries: Effective Lagrangians at Finite Volume," Nucl. Phys. B **307** (1988) 763.

[158] C. Bernard [MILC Collaboration], "Chiral Logs in the Presence of Staggered Flavor Symmetry Breaking," Phys. Rev. D **65** (2002) 054031 [arXiv:hep-lat/0111051].

[159] C. Aubin and C. Bernard, "Pseudoscalar decay constants in staggered chiral perturbation theory," Phys. Rev. D **68**, 074011 (2003) [arXiv:hep-lat/0306026].

[160] C. Aubin and C. Bernard, "Pion and Kaon masses in Staggered Chiral Perturbation Theory," Phys. Rev. D **68**, 034014 (2003) [arXiv:hep-lat/0304014].

[161] D. Renfrew, T. Blum, N. Christ, R. Mawhinney and P. Vranas, "Controlling Residual Chiral Symmetry Breaking in Domain Wall Fermion Simulations," PoS **LATTICE2008** (2008) 048 [arXiv:0902.2587 [hep-lat]].